Contents

Figures

Tables

7.0 GMC Databases

In the framework of a Senior Seismic Hazard Analysis Committee (SSHAC) Level 3 study, the GMC model is developed through successive stages of evaluation and integration (see Section 2.1.2). The evaluation phase focuses on the impartial assessment of available data, methods, and models that may be of relevance to the characterization of earthquake ground-shaking at the Hanford Site. In order to conduct this evaluation, databases of existing information must be compiled and, where necessary and feasible, supplemented by new data collection. This chapter describes the databases developed for the GMC component of the Hanford PSHA model in terms of ground motion recordings from the site and surrounding region; dynamic characterization of the geological strata below the site, including target kappa and shear-wave velocity models and the potential for 3-D basin effects; available ground motion prediction equations for both crustal and subduction earthquakes; and vertical-to-horizontal (V/H) response spectral ratios.

The evaluation of these data and models informed the decisions made by the GMC Technical Integration (TI) Team in constructing the logic trees for median ground motions and their associated variability, as well as the models of the near-surface layers to be used in subsequent site-response analyses. All of these elements of the final GMC model are fully described in Chapter 9.0. The boundary between evaluation and integration is not sharply defined; this chapter discusses the TI Team's evaluation of most of the database elements; Chapter 9.0 continues the discussion for some cases.

7.1 Ground Motion Recordings

Ground motion recordings are essential for calibrating various components of the GMC model and for verifying the applicability of ground motion prediction equations (GMPEs) to the Hanford Site. The GMC Team made use of the ground motion recordings described in this section for 1) estimation of kappa values for the Hanford Site (Section 7.3), 2) estimation of potential 3-D amplification effects (Section 7.6), and 3) comparison of GMPEs with region-specific data for crustal and subduction earthquakes (Section 9.2). Ground motion recordings of interest for this project include strong-motion accelerograms from the Hanford Site, broadband seismograms recorded at a regional scale, and worldwide subduction-zone ground motion recordings.

In addition to collecting ground motion data, information about the site conditions (e.g., geology, average shear-wave velocity, surface topography) was also collected for the recording stations. All of the data related to ground motion recordings were compiled into a project-specific ground motion catalog that served several ground motion needs for the project, including the estimation of kappa for the Hanford Site and evaluation of basin effects. In addition, data used for GMPE development were compiled into two flatfiles (PNNL 2014b).

At an early stage of the project, including Workshop 1 and the first working meetings of the GMC TI Team, a decision was made to search for ground motion recordings from sites with strong near-surface velocity inversions. The purpose of this exercise would have been to obtain insight into the influence of such inversions on the surface motion, as potential analogs for the inversions associated with the basalt and sedimentary interbed layers in the Saddle Mountains basalts (SMBs). This focus reflected the original decision to define the reference baserock horizon for the GMC model and for the hazard calculations at the top of the SMBs, and the search focused on other regions with near-surface basalts

such as Iceland and Hawaii. However, no data were found that could have served as a suitable analog for the SMB stack at the Hanford Site. When the baserock was moved to the base of the SMB stack (see Section 7.2.5), the usefulness of such recordings—had any been found—could have been in providing insight into stress drop levels and ground motion amplitudes resulting from ruptures extending into near-surface basalt layers. However, no data of this nature had been found, so the documentation of these fruitless searches is limited to this introductory paragraph.

7.1.1 Strong-Motion Accelerographs at the Hanford Site

DOE owns five free-field strong-motion accelerographs at the Hanford Site (Rohay et al. 2001). The USGS and the California Institute of Technology (Caltech) operate two additional strong-motion accelerographs. Information about the seven accelerograms is given in Table 7.1. Processed ground motion data from these accelerograms were obtained from Dr. Alan Rohay at PNNL. All of these data are compiled in the project-specific ground motion catalog (PNNL 2014a) that is discussed more extensively in Section 7.1.2. Additional ground motion data from these instruments were obtained from the Incorporated Research Institutions for Seismology (IRIS) website (these data, along with additional data obtained from the IRIS website, are discussed in Section 7.1.2). The processing of the data obtained from the accelerographs is described by Rohay (2014).

Table 7.1. Strong-motion accelerographs at the Hanford Site.

Station Name	Owner	Instrument Type	V_{S30} (m/s)
H1K	DOE	ETNA SM accelerographs	515[(a)]
H2E	DOE	ETNA SM accelerographs	371[(a)]
H2W	DOE	ETNA SM accelerographs	394[(a)]
H4A	DOE	ETNA SM accelerographs	381[(a)]
H3A	DOE	ETNA SM accelerographs	409[(a)]
LTH	Caltech	Episensor accelerographs	400[(b)]
HAWA	USGS	Episensor accelerographs	596[(a)]

(a) From spectral analysis of shear waves measurement at the recording stations.
(b) Estimated from National Earthquake Hazards Reduction Program (NEHRP) V_{S30} maps for Washington State (Palmer et al. 2004).

7.1.2 Ground Motion Data from the IRIS Website

Selected strong-motion seismograms curated by IRIS were incorporated into the project-specific catalog. The various application programming interfaces offered by the IRIS web services interface product (http://service.iris.edu/, last accessed 04/22/2014) were used to download data from 2,771 earthquakes recorded at 839 sites within Washington State. The data cover earthquakes from January 2000 to January 2013, with magnitudes ranging from 2.0 to 6.8, including both crustal and subduction earthquakes. The entire database was made available online (PNNL 2014a). The online project-specific catalog included all the metadata available through IRIS, as well as a link to unprocessed recordings and instrument response information for all stations for which recordings are available. Users can browse the data either grouped by earthquake or recording station. The strong-motion accelerograms recorded by instruments owned by DOE (Section 7.1.1) were also merged into the project-specific catalog.

The USGS SeismoTectonic Regime Earthquake Calculator (STREC; USGS 2014) was used to classify each earthquake as a crustal or subduction earthquake. The classification scheme embedded in the STREC algorithm is explained by Garcia et al. (2012). The classification uses the Flinn-Engdahl regionalization scheme, seismotectonic information related to plate boundaries, and source parameters of each earthquake to determine earthquake type. For some tectonic settings additional criteria based on hypocentral depth and regional seismicity are applied. This scheme was validated by Garcia et al. (2012) against a large database of historical earthquakes. The STREC implementation is available in an open-source software repository (USGS 2014) and it includes some minor updates to the Garcia et al. (2012) publication; these updates are documented in the open-source code (D. Garcia, personal communication, 2014). We note that the SSC earthquake catalog analysis used a different algorithm for earthquake classification. The Garcia et al. (2012) algorithm was selected for GMC applications because it is specifically targeted at GMPE selection. Because the objectives of earthquake classification for the SSC catalog and the GMC ground motion catalog, there are no implications of using different algorithms on the computed hazard.

The project-specific catalog included several metadata parameters along with the ground motion recordings. Some of these parameters were downloaded from IRIS servers along with the recorded time histories. These parameters included earthquake magnitude, magnitude type, earthquake date and time, latitude/longitude/depth of the hypocenter, name of the recording station and network that reported the data, and the latitude/longitude/elevation of the recording station. These parameters were used to compute the epicentral and hypocentral distances for each record. The moment magnitudes of several earthquakes were obtained from the project SSC catalog (Chapter 6.0). The hypocenter location and earthquake time reported by IRIS and those in the SSC catalog were used to match the earthquakes in the two databases.

The project-specific catalog was used to create subsets of recordings to estimate kappa, evaluate basin effects, and to compare the performance of crustal and subduction GMPEs developed using data from different regions. The criteria used to select the subset of data from the project-specific catalog to prepare the smaller catalogs are described below:

1. Kappa catalog: A set of stations that were potential analogs to the SMB, and stations that were analogs for Wanapum Basalt (WB) were pre-selected by the GMC TI Team and a final group of stations was agreed upon through email communication with Dr. Walter Silva and Dr. Alan Rohay. Table 7.2 lists the stations selected for the kappa study. All earthquakes where at least one recording within 100 km of the epicenter was made at any of the selected stations were considered. These earthquakes were then sorted according to the number of recordings within 100 km of the epicenter at the selected stations. The time history recordings from the selected station-earthquake pairs were extracted from the project-specific catalog to create the catalog of data used for kappa estimation. The catalog for kappa estimation is available by clicking on the link titled “Walt” on the online catalog (PNNL 2014a).

2. Basin database: A subset of the master database was created to aid in the evaluation of basin effects. The following criteria were followed to create this subset:

   – Stations within the latitude and longitude limits of the geological model for basin effects (Thorne et al. 2014). This includes stations within the latitude/longitude bounding box defined by (-120.75768°E, 45.89084°N) and (-118.52584°E, 47.04380°N).

– Earthquakes that occurred after 1/1/2000 with magnitudes greater than 2, and occurring within Washington State, Oregon, and the Cascadia region of Canada. Earthquakes occurring offshore near the Mendocino Triple Junction were excluded and recordings from the Denali earthquake on DOE instruments were kept. The Mendocino Triple Junction earthquakes were excluded because of the uncertainty with respect to the earthquake type for earthquakes occurring in this region.

– Only stations that recorded more than 10 samples per second were considered.

The catalog compiled for basin effects estimation can be accessed by clicking on the link titled "Basin" on the project-specific catalog (PNNL 2014a). As noted in Section 7.6, only a subset of this database was used by Dr. Frankel in the evaluation of basin effects.

3. Crustal and subduction flatfiles: Earthquakes with magnitudes greater than 3 were selected to be included in two flatfiles, one for crustal and one for subduction earthquakes. As indicated above, the STREC algorithm (USGS 2014) was used to classify the earthquakes in the project-specific catalog into crustal or subduction earthquakes. The flatfiles also include the geometric mean of 5% damped pseudo-acceleration response spectra. We used the Nigam and Jennings algorithm (Nigam and Jennings 1969) to compute the pseudo-acceleration response spectra of the processed time histories. Along with the pseudo-acceleration response spectra, the metadata from the project-specific catalog were included in the flatfiles. In addition to these metadata parameters, several other parameters were computed for the crustal and subduction flatfiles. These parameters included an aftershock flag computed using the Reasenberg (1985) declustering algorithm, National Earthquake Hazards Reduction Program (NEHRP) site class extracted from maps prepared by the Washington State Department of Natural Resources (Palmer et al. 2004), and estimated closest distance (R_{rup}) and Joyner-Boore distance (R_{jb}) for each recording. The R_{rup} and R_{jb} distances were estimated by simulating several possible rupture scenarios using a method similar to the one used by Chiou and Youngs (2008b). The Wells and Coppersmith (1994) relationships were used to simulate rupture lengths and widths, and the USGS STREC was used to find the possible strike and dips for the ruptures needed for the computation.

Table 7.2. Stations included in the Kappa database along with site information for each station.

Station Name	Surface Geology	Depth to Basalt	Basalt Formation	Analogy to …	V_s Profile available?
HAWA	Ql (Quaternary loess) cemented gravel	28 ft (8.5 m)	Saddle Mts.	SMB	YES
E07A/CCRK	Ql (Quaternary loess)	124 ft (38 m)	Saddle Mts.	SMB	YES
E08A/DDRF	Saddle Mts. Basalt; Elephant Mt. Member	2 ft (0.6 m)	Saddle Mts.	SMB	YES
F07A/PHIN	Pleistocene ?[(a)]	25 (16-32) ft (7.6 [4.9–9.7] m)	Saddle Mts.	SMB	YES
D08A/WOLL	Pleistocene ?[(a)]	12 ft (3.6 m)	Wanapum	Wanapum	YES
E09A/TUCA	Quaternary alluvium dune sand loess	11 (3.4 m)	Grande Ronde Basalt	Wanapum	YES
EBG	Wanapum Basalt	0	Wanapum	Wanapum	NO
VT2	Wanapum Basalt	0	Wanapum	Wanapum	NO
WRD	Wanapum Basalt	0	Wanapum	Wanapum	NO

(a) Pleistocene continental glacial glaciolacustrine and outburst flood deposits

The time histories downloaded from the IRIS servers reported raw "counts," and the project-specific catalog has a link to the raw (unprocessed) recordings. The processing of ground motion data used for kappa estimates is described by Rohay (2014). The processing of the data used for estimation of basin effects is described by Frankel et al. (2013). The data incorporated into the flatfiles were also processed by the GMC TI Team to filter out the noise from the recordings and correct for instrument response to convert the data from counts to appropriate units of acceleration or velocity. The following steps were taken to process the recordings incorporated into the flatfiles:

1. The records were automatically screened for noisy and clipped records. A record was labeled as clipped if a threshold of 99% of the maximum value of the record was exceeded more than 20 times. This requirement filtered most of the records that were clipped by the instrument. Figure 7.1 shows an example of a clipped record. To filter noisy records we used the STA/LTA algorithm (described in next paragraph) to find the trigger point of the record. The 40 sec of the record following the trigger point were used to represent the signal (which also includes noise, hence is labeled as signal+noise), and the last 40 sec of the record were used to represent the noise. The two time series were tapered using a cosine taper and then their Fourier spectrum was computed to represent the noise and (signal + noise) spectrum. We smoothed the spectrum using the Konno-Ohmachi smoothing filter (Konno and Ohmachi 1998) and computed the smooth (signal + noise)/noise ratio. Any record with a (signal + noise)/noise ratio lower than 3 at all frequencies was classified as a noisy record (Boore and Bommer 2005). Figure 7.2 shows an example of a noisy record and its (signal + noise)/noise ratio.

   The STA/LTA algorithm computes average motion in two moving time windows— a short time window (STA) and a long time window (LTA). The LTA measures the level of seismic noise, while the STA gives an estimate of amplitude of the signal. A ratio of the STA and LTA value is compared against a threshold value to find the trigger point. We used the STA/LTA algorithm implemented in the python library Obspy (Beyreuther et al. 2010; Megies et al. 2011).

2. The first and the last frequencies where the (signal + noise)/noise ratio crossed the value of 3 were used as potential corner frequencies. Another set of corner frequencies was computed using the frequency response of the instrument. The range of frequencies where the instrument response was relatively flat was used as the second set of potential corner frequencies. The intersection of the range of bandwidths described by the two sets of corner frequencies was used to select the final corner frequencies used for processing the record. Figure 7.3 describes the process of determining the corner frequencies.

3. An 8th order acausal bandpass Butterworth filter with the corner frequencies determined above (Step 2) was applied to the record.

4. The frequency response of the instrument downloaded from IRIS was used to perform the instrument correction. The instrument correction was performed after filtering the motion to avoid amplifying the noise in this step.

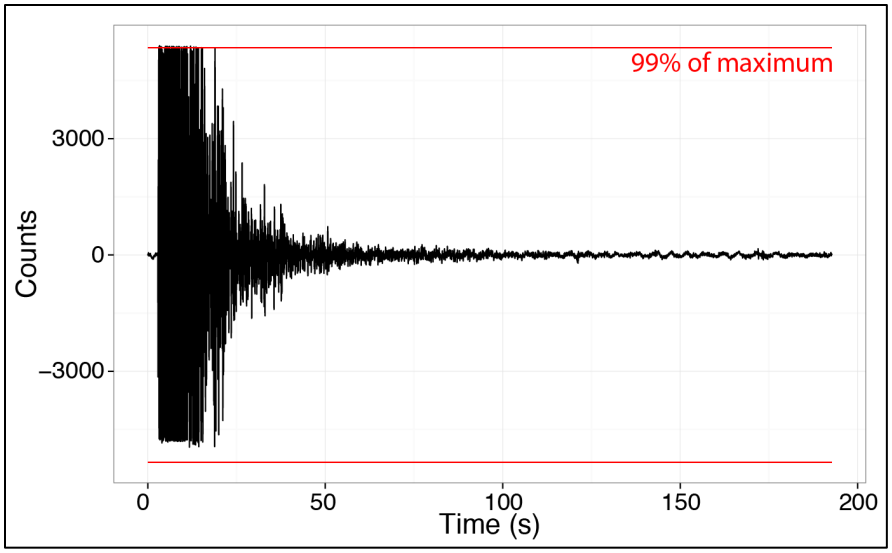

Figure 7.1. A clipped record along with the threshold used for classification.

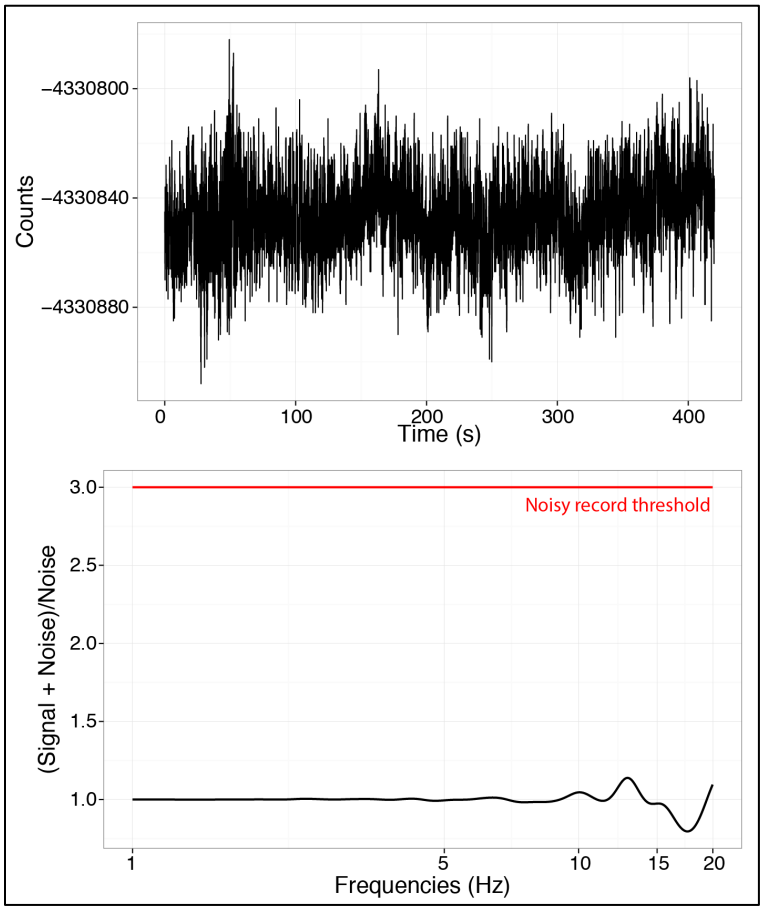

Figure 7.2. A noisy record with the smooth (signal + noise)/noise ratio that never crosses the threshold value of 3.

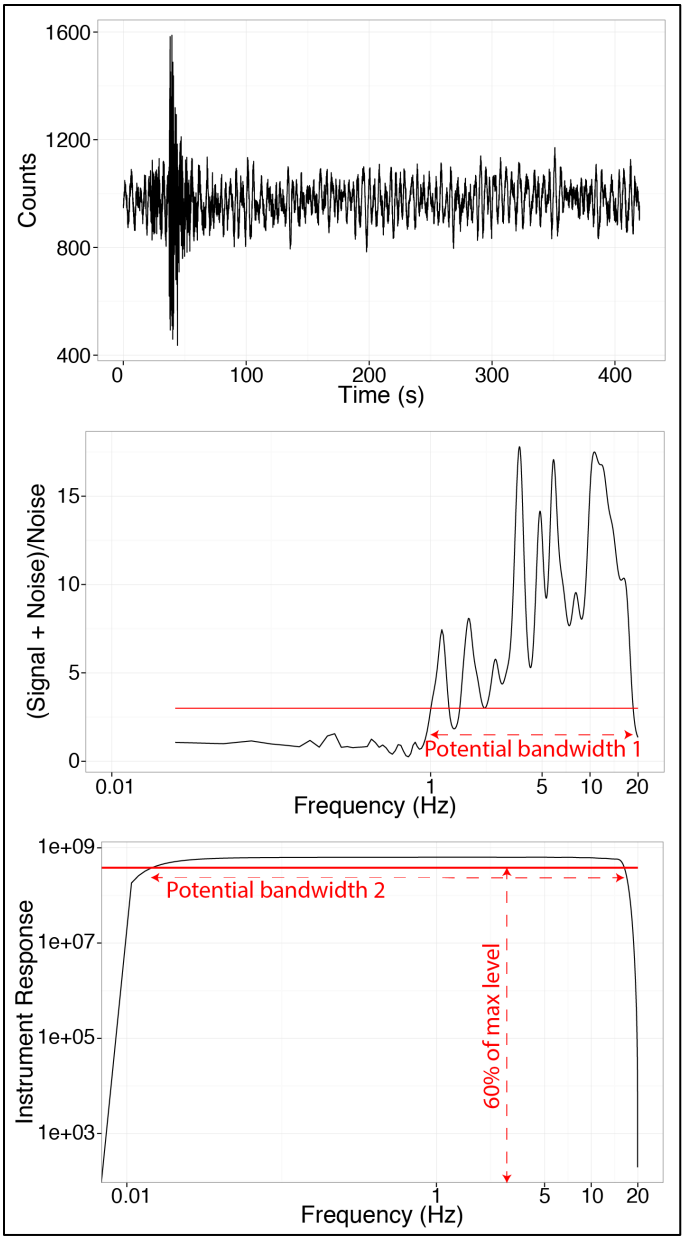

Figure 7.3. A raw time history record along with the two methods used to compute the potential corner frequencies. The intersection of Potential bandwidth 1 and Potential bandwidth 2 is used to compute the final corner frequency used with the Butterworth filter.

7.1.3 Subduction-Zone Ground Motion Recordings

Subduction-zone ground motion recordings were used to develop a GMPE for subduction earthquakes. The ground motion database was compiled into a flatfile containing all relevant metadata and pseudo-spectral accelerations (5% damping). The flatfile is available at PNNL (2014b) The flatfile was built using the BC Hydro project flatfile (BC Hydro 2012) as a starting point. Data from IRIS, as described in Section 7.1.2, were also included in this flatfile. Data from the Japanese KiK-net network, from Arango et al. (2011) for Central America, and for the **M** 8.8 February 27, 2010, Maule earthquake were added to the BC Hydro data. Each of these sources of data is discussed separately below.

7.1.3.1 BC Hydro Data

The BC Hydro flatfile is described in detail by BC Hydro (2012) and Abrahamson et al. (2014a). The BC Hydro data set was an effort to compile a global data set of subduction ground motions from data used in earlier studies, as well as ground motion data collected in recent years. The data set includes data from Atkinson and Boore (2003, 2008), which included a compilation of data from earlier studies (Crouse et al. 1988; Crouse 1991; Youngs et al. 1997) and data that were collected as part of the BC Hydro study (these data are described by BC Hydro 2012). Overall, the BC Hydro data set includes ground motions from Alaska, Central America, Chile, Cascadia, Japan, Mexico, Peru, Solomon Island, and Taiwan.

The BC Hydro data set compiled processed acceleration time histories when available, but for older records only peak ground acceleration (PGA) and 5% damped response spectra at selected periods were available (0.1, 0.2, 0.4, 1.0, 2.0, and 3.0 sec). These periods were assumed to fall within the usable range of the data. This assumption was verified through residual analyses (BC Hydro 2012). The available acceleration time histories were used to compute 5% damped response spectra at 105 periods and the usable period range was determined from the filters used to process each recording. The flatfile includes the geometric mean of the two horizontal components for all the records except the Taiwan data. For these data, the GMRotI (Boore et al. 2006) was used. Beyer and Bommer (2006) showed that the difference between the two measures of horizontal motion is negligible (albeit using recordings from crustal earthquakes), and it was ignored in the derivation of the BC Hydro ground motion model.

Most of the metadata were obtained directly from the original sources for the ground motion data (Atkinson and Boore 2003, 2008), but some metadata were corrected and/or updated. Table 7.3 summarizes the updates of the original data. Table 7.3 also includes the most relevant information about the source of the metadata in the BC Hydro flatfile.

Table 7.3. Summary of metadata compiled in the BC Hydro flatfile.

Metadata Parameter	Comment
Earthquake magnitude	Moment magnitude (**M**) was used. Preference was given to Harvard Centroid Moment Tensor catalog solutions over regional Centroid Moment Tensor (CMT) solutions.
Hypocentral location and depth	ISC (http://www.isc.ac.uk) or CMT solution locations were used to replace missing or erroneous locations in the original data sets. Depth estimates from pP seismic phase were given preference.
Earthquake classification	Earthquakes were classified as intraslab or interface using preferred ISC hypocentral depths, CMT solution, and/or first motion fault-plane solutions. Earthquakes with hypocentral depth less than 30 km were assumed to be interface events.
Aftershock/foreshock identification	Earthquakes within a year of each other and within approximately 100 to 200 km of each other were considered to be dependent.
Station site classification	Older studies used the Geomatrix classification or NEHRP categories. A mapping was established between these classifications and V_{S30} (Table 7.4). When conflicting V_{S30} existed for a station, the most recent value was used. For Taiwan data, V_{S30} values from the next-generation attenuation (NGA) database were used over values reported by Lee and Tsai (2008) due to concerns regarding the latter values.
Forearc or backarc station location	Based on the relative location of observed volcanic fronts for each subduction region.
Distance metrics	Older data sets did not report the type of distance metric used. For these records, it is assumed that the distance were hypocentral distances. For more recent earthquakes, both hypocentral distance and rupture distance were computed.

Table 7.4. Mapping between site classes and V_{S30} in the BC Hydro database (BC Hydro 2012).

Geomatrix 3rd Letter	*Average* V_{S30} (m/sec)
A	659.6
B	424.8
C	338.6
D	274.5
E	191.3
NEHRP Class	***Average*** V_{S30} (m/sec)
A	1745.3
B	967.6
C	450.5
D	258.2
E	152.2

7.1.3.2 KiK-net Data

KiK-net is one of several seismic networks established in Japan following the devastating Kobe earthquake (January 17, 1995) to better monitor the seismic activity around the country (Okada et al. 2004). As of December 2011, the KiK-net network consisted of 692 stations. Each KiK-net station consists of two strong ground motion seismographs, one at the ground surface and the other in a borehole, and each instrument records three components of motion. The seismic velocity profile for 655 of these stations is reported on the KiK-net website (http://www.kyoshin.bosai.go.jp/). The velocity profiles at these stations were obtained from downhole PS logging (Oth et al. 2011). Details regarding the KiK-net network and the specifications of the instruments are given by Aoi et al. (2011) and Okada et al. (2004).

Dawood et al. (2014) processed data from the Japanese KiK-net network using an automated processing protocol. Data were downloaded from the KiK-net website for earthquakes up to December 2011. In addition to the information contained in the KiK-net records, data from the F-Net seismic catalog (Okada et al. 2004) were used to compute associated metadata. F-Net is a broadband seismograph network installed in Japan (Okada et al. 2004). The F-Net website (http://www.fnet.bosai.go.jp/) provides a searchable database of earthquakes recorded by the F-Net network. The catalog includes the origin time, location (latitude, and longitude), M_{JMA} magnitude, Japan Meteorological Agency depth, region, and mechanism from the National Research Institute for Earth Science and Disaster Prevention moment tensor solution (strike, dip, rake, seismic moment, **M**, moment tensor solution, variance reduction and number of stations used).

The automated processing protocol applies first a zeroth order baseline correction to the record by first subtracting the mean of the first 100 points from the whole acceleration time series and then subtracting the mean of the pre-event noise window using an automated algorithm to detect the first arrival. The first arrival is defined as the first automatically detected arrival time for the six components (three components of the surface instrument and three components of the borehole instrument). The records are first tapered and zero-padded and then an 8th order acausal Butterworth filter is applied. The low-cut frequency is selected iteratively to satisfy several criteria to ensure zero displacement and zero velocity at the end of the time history. The minimum usable frequency of the records is taken to be 70% of the low-cut corner frequency of the filter (f_c; Akkar and Bommer 2006). The maximum frequency is defined by a built-in

anti-aliasing filter in the instruments and is 30 Hz (Aoi et al. 2011). A signal-to-noise ratio (SNR) check is also applied to all records. A noise window is defined using the last $2/f_c$ second of the record. The Fourier amplitude spectra (FAS) for the whole record and the noise window are calculated and smoothed, and the ratio between the two is calculated and defined as the SNR. Frequencies outside the range where the SNR is above 3 are not used (Boore and Bommer 2005).

Dawood et al. (2014) processed both crustal and subduction records. Dawood (2014) compared the common records processed using the automated protocol and the NGA-West2 database (Ancheta et al. 2013). The comparison showed that, in most cases, the automated protocol resulted in records with a narrower usable frequency bandwidth compared to NGA-West2 records. This is the result of applying multiple (and possibly redundant) checks in the automated protocol with conservative threshold values. These checks were necessary, in the absence of a record-by-record processing with manual input, to obtain a set of high-quality records from the automated protocol. The loss of usable frequency bandwidth is a trade-off that we accepted for the benefit of automating the processing of such a large data set.

Most of the earthquake metadata were obtained from the F-Net catalog. Earthquakes identified in the KiK-net record files were matched to earthquakes in the F-Net catalog using spatial and temporal windows. The moment magnitude and hypocentral location from the F-Net catalog were used for each earthquake. Not all earthquakes in the KiK-net records could be matched to an earthquake in the F-Net catalog, and the records without a matching earthquake were discarded. A notable exception to the source of moment magnitude was the March 11, 2011, Tohoku earthquake. For this earthquake, the moment magnitude reported in the F-Net catalog is 8.7. We used instead a moment magnitude of 9.0 as reported by the USGS (Hayes 2011).

The identification of dependent and independent earthquakes was done by declustering the F-Net catalog. The F-Net seismic catalog was declustered using the algorithms by Gardner and Knopoff (1974) and Reasenberg (1985). The Gardner and Knopoff algorithm was implemented using three different sets of input parameters (see Dawood et al. 2014 for more information). This implementation was conducted independently from the declustering conducted as part of the development of the SSC catalog (Chapter 6.0). However, this choice has no implication on hazard results because the proposed GMPE (Chapter 9.0) did not differentiate between dependent and independent events. None of the applications of the declustering algorithms resulted in a Poissonian catalog. The algorithm results using the typical input parameters of Gardner and Knopoff's algorithm were used.

The database compiled by Dawood et al. (2014) includes crustal and subduction earthquakes. The algorithms by Allen et al. (2008) and Garcia et al. (2012) were used to classify the earthquakes in the F-Net catalog into tectonic categories. The latter algorithm was validated by automatically classifying a catalog of earthquakes that also were manually classified. For most earthquake types, the validation showed a considerable improvement in the number of correctly classified earthquakes using this algorithm in comparison to the Allen et al. (2008) algorithm. However, for intraslab earthquakes the number of misclassified earthquakes increased. This was attributed to the lack of slab models for about half of the misclassified earthquakes. Additional details are given by Garcia et al. (2012). The results of applying both algorithms to the F-Net catalog are shown in Table 7.5. The 951 earthquakes that were not classified using the algorithm by Allen et al. (2008) are earthquakes with $\mathbf{M} \leq 7.7$ and depth greater than 50 km. Allen et al. (2008) do not provide a classification for earthquakes that fall within these depth-magnitude combinations. The number of earthquakes classified as interface earthquakes using both algorithms are very different. This is consistent with the Garcia et al. (2012) finding that the Allen et al.

(2008) algorithm misclassified about 54% of the interface earthquakes. For this project we use the Garcia et al. (2012) classification. Figure 7.4 shows the location of the earthquakes in the four main categories as classified by Garcia et al. (2012).

Table 7.5. Classification of F-net earthquakes in the Dawood et al. (2014) database using the algorithms by Allen et al. (2008) and Garcia et al. (2012).

Class[(a)]	Number of Earthquakes Classified by Allen et al. (2008)	Number of Earthquakes Classified by Garcia et al. (2012)
SZ intraslab	1161	1123
SZ interface	5	873
SZ outer	-	16
Shallow active crustal	1093	-
ACR deep	-	112
ACR shallow	-	1083
OBR	-	3
Not classified	951	-
Total	3210	3210

(a) SZ = subduction zone; ACR = active crustal region; and OBR = oceanic boundary region.

The epicentral and hypocentral distances were computed by Dawood et al. (2014). For earthquakes with published finite-fault solutions, the published finite fault was used to compute the closest distance to the rupture plane (R_{rup}). For other earthquakes, the method of Chiou and Youngs (2008b, Appendix B) was used. This method uses the published hypocenter location and the two fault-plane solutions from the F-Net catalog to simulate fault planes from which R_{rup} is computed. For interface earthquakes, the plane with the shallower dip was used; for intraslab earthquakes, distances were computed for the two planes and the geometric mean from both planes was used. For additional information, see Dawood et al. (2014).

7.1.3.3 Central America Data

Arango et al. (2011) compiled a data set of subduction earthquakes along the Pacific Coast of Central America, including data from Guatemala, El Salvador, Nicaragua, and Costa Rica. The final database consists of 554 ground motion recordings from earthquakes of moment magnitudes between 5.0 and 7.7, including 22 interface and 58 intraslab earthquakes for the time period 1976 to 2006. The spectral acceleration (5% damping) of processed ground motion data is included in an electronic supplement of Arango et al. (2011) along with relevant metadata. The ground motion processing is described by Arango et al. (2011). Earthquake metadata include moment magnitude and earthquake classification into interface or intraslab earthquake. The latter was done on the basis of focal mechanism, epicentral location, and depth and position with respect to the trench axis. Hypocentral depth is relevant to this classification; for earthquakes where the hypocentral depth varied between catalogs the depth was compared with models of the slab geometry. This classification scheme is consistent in principle with the classification system by Garcia et al. (2012); however, Arango et al. (2011) used a more detailed description of the subducting slab geometry and an exhaustive analysis of hypocentral depth errors considering various earthquake catalogs and the subducting slab geometry. For this reason, we chose to use the Arango et al. (2011) classification for the earthquakes included in their publication. Source-to-site

distances were characterized in terms of the closest distance to the fault plane (R_{rup}). Published fault-plane geometries were available only for the January 13, 2001, El Salvador earthquake. For other earthquakes estimated fault planes were obtained from the literature or were modeled using an approach described by Arango et al. (2011). This approach is similar to the Chiou and Youngs (2008b) approach applied to the KiK-net database.

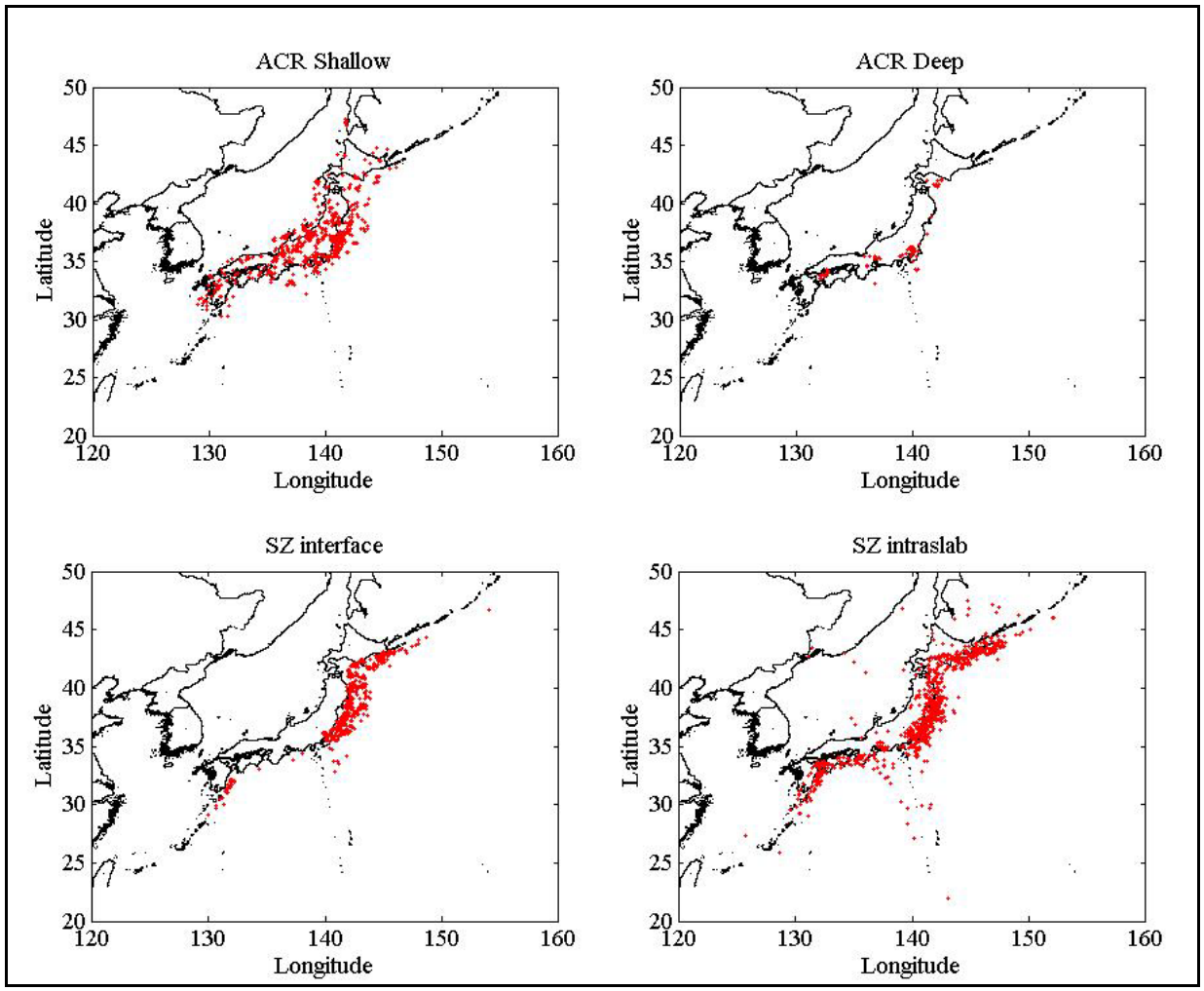

Figure 7.4. Location of the earthquakes classified as active crustal region (ACR) shallow (top left), ACR deep (top right), source zone (SZ) interface (bottom left), and SZ intraslab (bottom right) on the Japanese map using the algorithm by Garcia et al. (2012).

7.1.3.4 Data from the 2011 Maule Earthquakes

The February 27, 2010, Maule earthquake (**M** 8.8) occurred after the BC Hydro data set was compiled and was not included in the BC Hydro flatfile. However, ground motions were obtained as part of the BC Hydro project and were made available to this project (Nick Gregor, personal communication, 2013). The fault model of Hayes (2010) was used to compute rupture distances. Ground motion data and station information (estimated V_{S30} values) were provided by the National University of Chile.

7.1.3.5 Summary of Data

The database of subduction ground motion for this project is compiled in a flatfile (PNNL 2014b). The database comprises 9,500 records from 398 earthquakes; 2,976 records are from 184 interface earthquakes and 6,524 records are from 215 intraslab earthquakes. The magnitude-distance distribution of the data is shown in Figure 7.5 and Figure 7.6. The histogram of V_{S30} values is given in Figure 7.7. For stations outside of Japan, the V_{S30} is inferred from site classification (see Abrahamson et al. 2014a). For stations in the Japanese KiK-net and K-net arrays measured V_{S30} values are available.

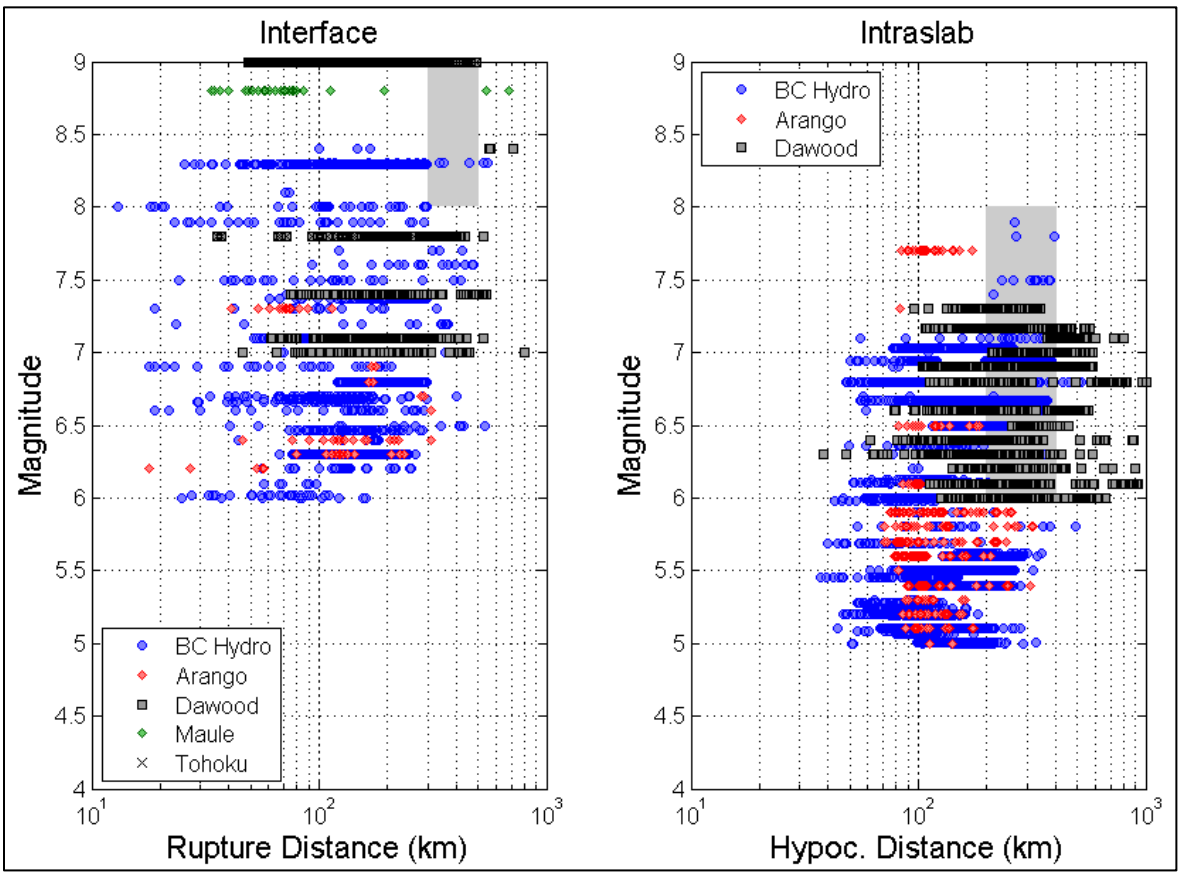

Figure 7.5. Magnitude-distance distribution of the subduction data, differentiated by the source of the data.

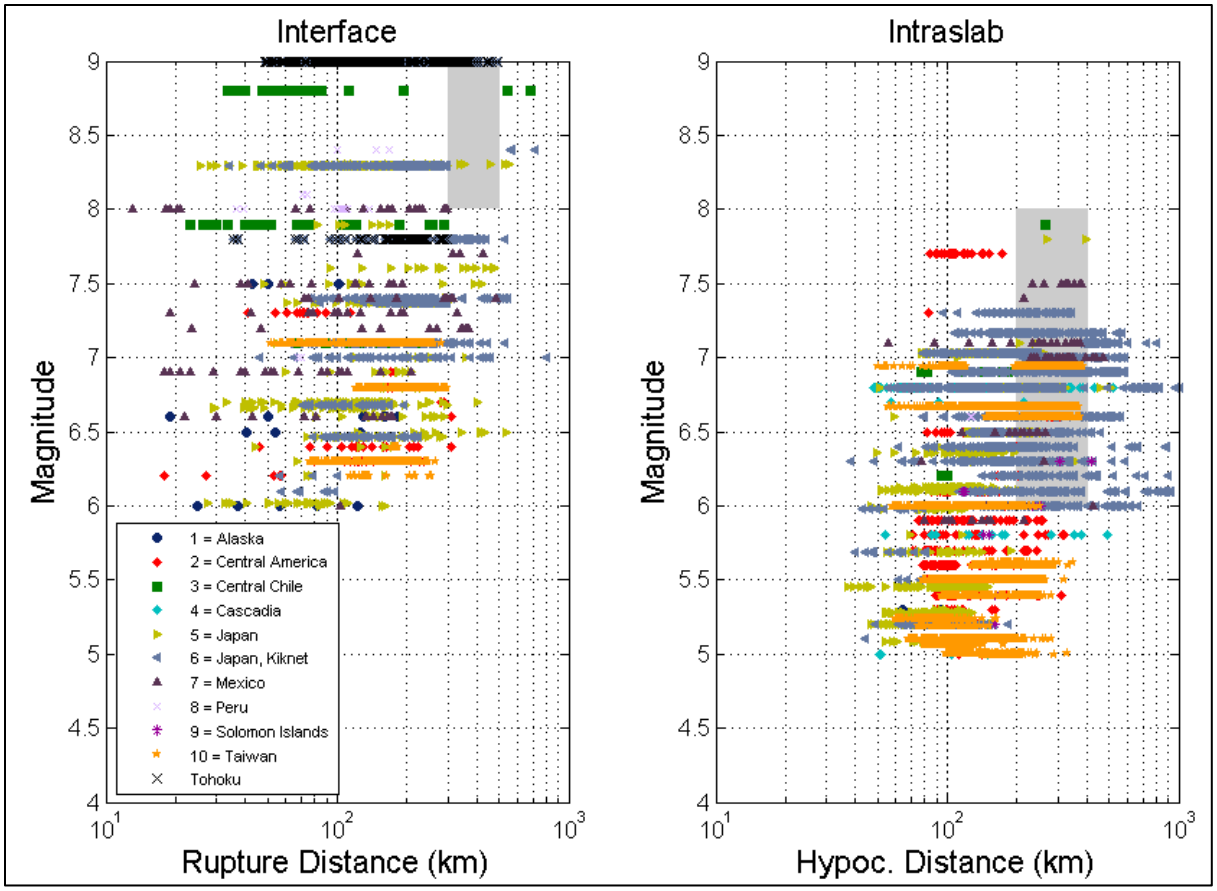

Figure 7.6. Magnitude-distance distribution of the subduction data, differentiated by the region of each recording.

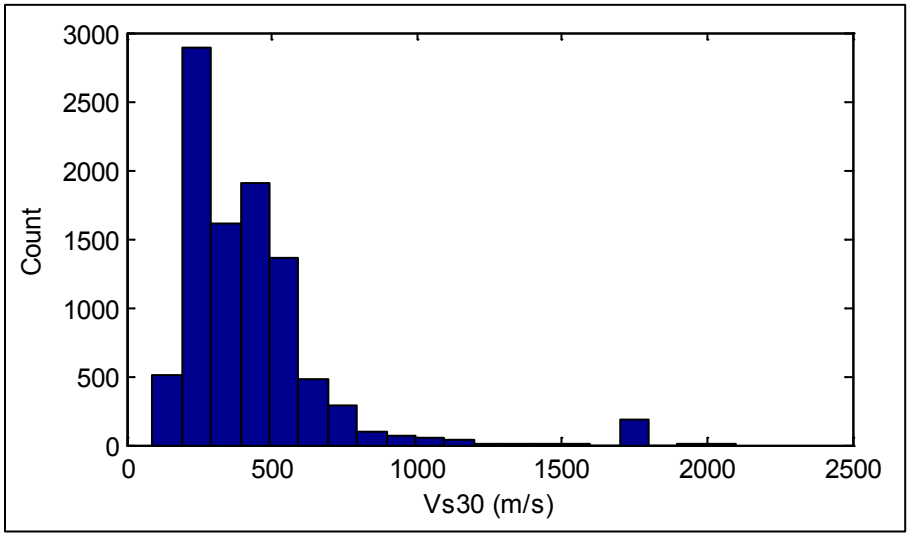

Figure 7.7. Histogram of V_{S30} values for all recording stations in the subduction database.

7.2 Site Profiles and Dynamic Characteristics of Stratigraphic Layers

The ultimate purpose of the Hanford PSHA is to provide estimates of the ground motions at the surface to be used in engineering analyses of facilities on the Hanford Site. As explained in Chapter 1.0, this is to be achieved by combining the results of the PSHA at a defined "baserock" horizon below the site with site-response analyses of the overlying near-surface layers. The site-response analyses are outside the scope of the PSHA study, but a key component of the GMC deliverables is guidance on how these analyses should be performed and combined with the baserock hazard estimates. To select the baserock level and to adjust the selected GMPEs to this horizon, it is necessary to develop a model for the dynamic properties—such as shear-wave velocity, V_S, and mass density, ρ—at the five selected locations at which seismic hazard is calculated. Although the site-response analyses to estimate the amplification factors associated with the layers above the baserock horizon is beyond the scope of the PSHA project, to ensure consistency in terms of the characterization of the site and the treatment of uncertainties, the GMC TI Team also agreed to develop models of the layers from the baserock to the top of the SMBs required as input to the site-response analyses (Section 9.7).

7.2.1 Existing V_S, V_P, and Density Measurements

The most detailed site characterization measurements, in terms of dynamic properties, on the Hanford Site were those made at the Waste Treatment Plant (WTP) site following the Defense Nuclear Facilities Safety Board (DNFSB) review of the 2005 assessment of the seismic design basis for this facility. The review raised questions about the adequacy of the site-specific geotechnical data. This prompted a series of measurements in three boreholes at the WTP site (Figure 7.8), as summarized by Rohay and Brouns (2007) and used in the updated site-response analyses by Youngs (2007).

The measurements in each of the three boreholes included two sets of velocity measurements, using PS suspension logging and downhole measurements, using both a vibratory and impulsive source for the latter; the impulsive source did not penetrate beyond the first three layers of the SMB stack (a total depth of about 225 m from the ground surface). For both the suspension logging and downhole measurements, both V_S and V_P (compressional wave velocity) were measured. To combine the results from the three boreholes at which measurements were obtained (C4993, C4996, C4997), Rohay and Brouns (2007) calculated the geometric mean velocities in each layer. The measurements were made through the suprabasalt sediments layers (of the Hanford and Ringold Formations) and the stack comprising the interbedded SMBs and Ellensburg sediments, as well as the uppermost units of Wanapum basalts (WBs) (Figure 7.9).

Mass densities were also measured using two techniques, namely a borehole gravity meter and a compensated density log run using a gamma-gamma density logging tool. Rohay and Brouns (2007) used arithmetic means to combine the gravity measurements from the three boreholes.

The two sets of density measurements gave very similar results. The two sets of V_S measurements (suspension logging and downhole) yielded similar values of shear-wave velocity in the Ellensburg Formation sedimentary interbeds but distinctly different values in the basalts; as can be seen in Table 7.6, the velocities estimated from the PS suspension logging are about 25% larger than those obtained using downhole measurements. In the table it may be noted that apart from the Elephant Mountain Member, all

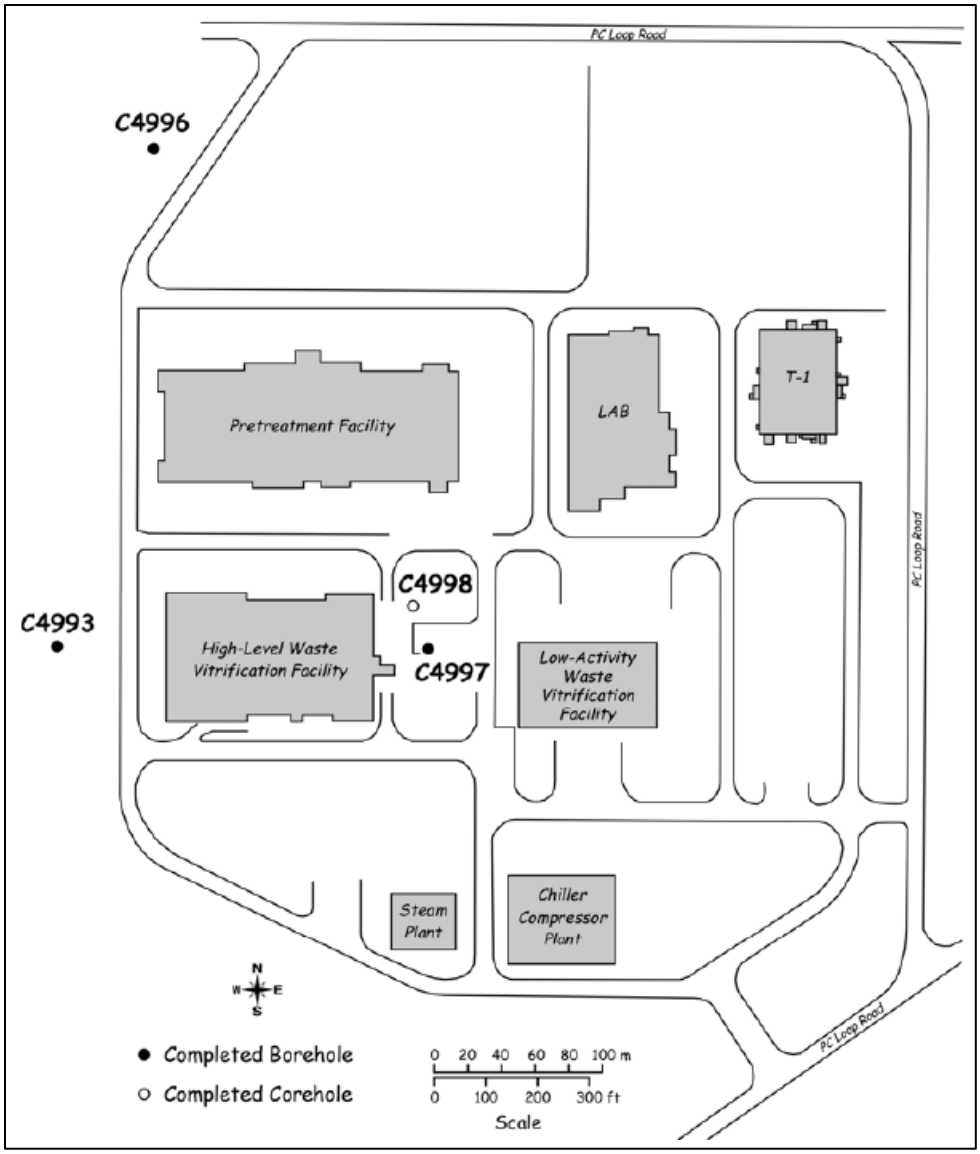

Figure 7.8. Seismic boreholes drilled at WTP site in 2006 (Rohay and Brouns 2007).

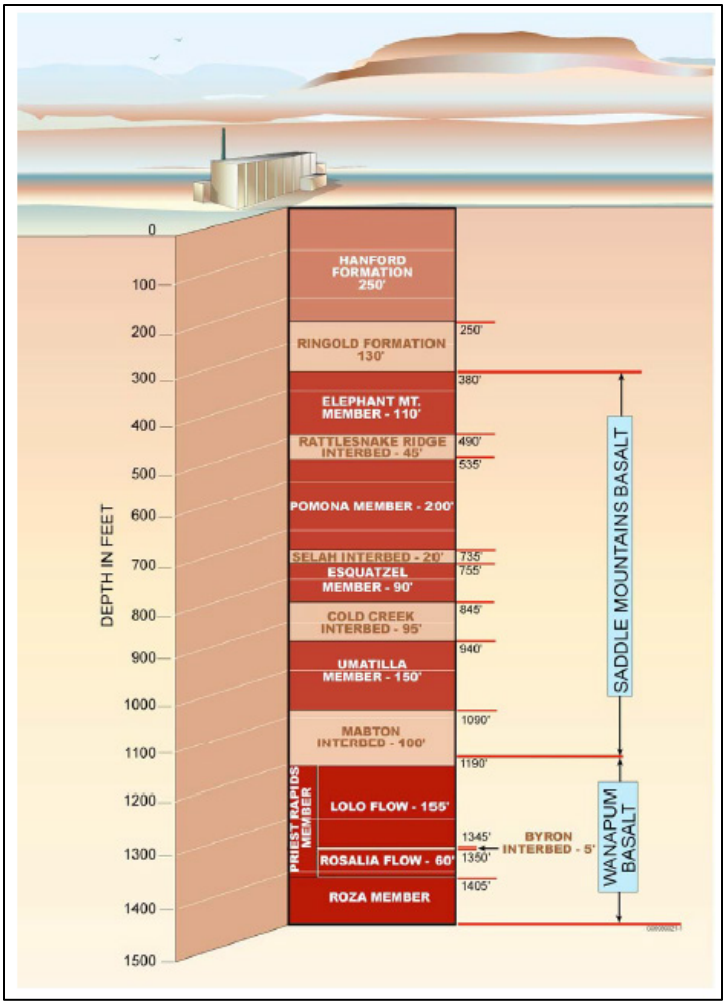

Figure 7.9. General stratigraphy at the WTP site (Rohay and Brouns 2007).

Table 7.6. Shear-wave velocities and mass densities measured at WTP (Rohay and Brouns 2007).

		V_S (m/s)		ρ
Symbol	Stratigraphic Unit	Downhole V_S	PS Logging	(g/cm^3)
Tem	Elephant Mt. Member (SMB)	2,308.6	2,910.7	2.806
Telr	Rattlesnake Ridge Interbed	838.8	832.0	1.891
Tp	Pomona Member (SMB)	2,519.5	3,119.8	2.812
Tels	Selah Interbed	879.9	972.6	2.129
Te	Esquatzel Member (SMB)	2,519.5	2,953.4	2.735
Telc	Cold Creek Interbed	822.0	759.8	1.947
Tu	Umatilla Member (SMB)	2,519.5	2,871.0	2.656
Telm	Mabton Interbed	830.0	782.3	2.035
Tpr	Lolo Flow[(a)] (Wanapum)	2,519.5	3,013.4	2.826
Tpr	Rosalia Flow[(a)] (Wanapum)	2,519.5	2,696.0	2.688

(a) These two basalt flows together form the Priest Rapids Member of the Wanapum Basalt.
SMB = Saddle Mountains Basalt.

of the basalts have the same V_S value from the downhole measurements, which reflects the recommendation of Rohay and Brouns (2007) after observing the very small layer-to-layer variations of the measured V_S values.

V_S and V_P values were also obtained for the Columbia Generating Station (CGS) site with cross-hole measurements at six boreholes (Bechtel 2013). These measurements extended only to a depth of 105 ft (~32 m) from the surface, and included only the suprabasalt sediments. Bechtel (2013) also report that cross-hole measurements were made at the WNP-1 and WNP-4 sites. A deeper V_S profile for the CGS site was developed using the shear-wave velocities in each stratigraphic layer from the WTP measurements. The cross-hole V_S measurements at CGS, WNP-1, and WNP-4 are not used in developing the velocity profiles for the SMB stacks, because they relate only to the sediment layers above the basalts.

There are no direct measurements of V_S values or density in the deeper WBs, the Grande Ronde basalts, the pre-Miocene sub-basalt sediments, or the crystalline basement. However, V_P measurements down to the top of the basement are available from a number of deep sonic logs in the region, although none are from within the boundaries of the Hanford Site (e.g., Jarchow et al. 1994; Glover 1985). In addition, V_P values for the deeper layers below the site region, including the basement, have been inferred from numerous seismic refraction surveys. Therefore, to develop deeper V_S profiles, it was necessary to assume ratios between compression- and shear-wave velocities (Section 7.2.4).

7.2.2 Spectral Analysis of Surface Waves Measurements

Within the framework of the Hanford PSHA project, spectral analysis of surface waves (SASWs) measurements were made at several locations across the site. The SASW measurements were performed by Professor Ken Stokoe and colleagues from the University of Texas at Austin, using the Liquidator vibrator truck and arrays of 1-Hz geophones. The measurements were performed at a total of 12 locations on the site (Figure 7.10), all of which were chosen to be as close as possible to the locations of the instruments from which the recordings were obtained that were analyzed for estimation of the site kappa values (Section 7.3). The key objective of the SASW measurements was to provide characterization of the recording sites for the signals analyzed to estimate kappa.

At the HAWA location, where an accelerograph is located below ground within the Nike bunker, additional measurements were performed using hammer blows, as the excitation source, and higher frequency (4.5-Hz) geophones. The measurements in the bunker were subsequently repeated using accelerometers with an operational range of 2−25 kHz.

SASW measurements were only made at Site D (100-BC Area) among the five hazard calculation sites, although several of the instrument locations are close to hazard calculation points. The SASW measurements, however, were unable to resolve the velocity inversions associated with the basalt and interbed layers within the SMBs stack; for this reason these measurements were not used in the development of the profiles presented herein. The use of these measurements in the analyses of recordings from the Hanford Site to derive a kappa model is discussed in Section 7.3.

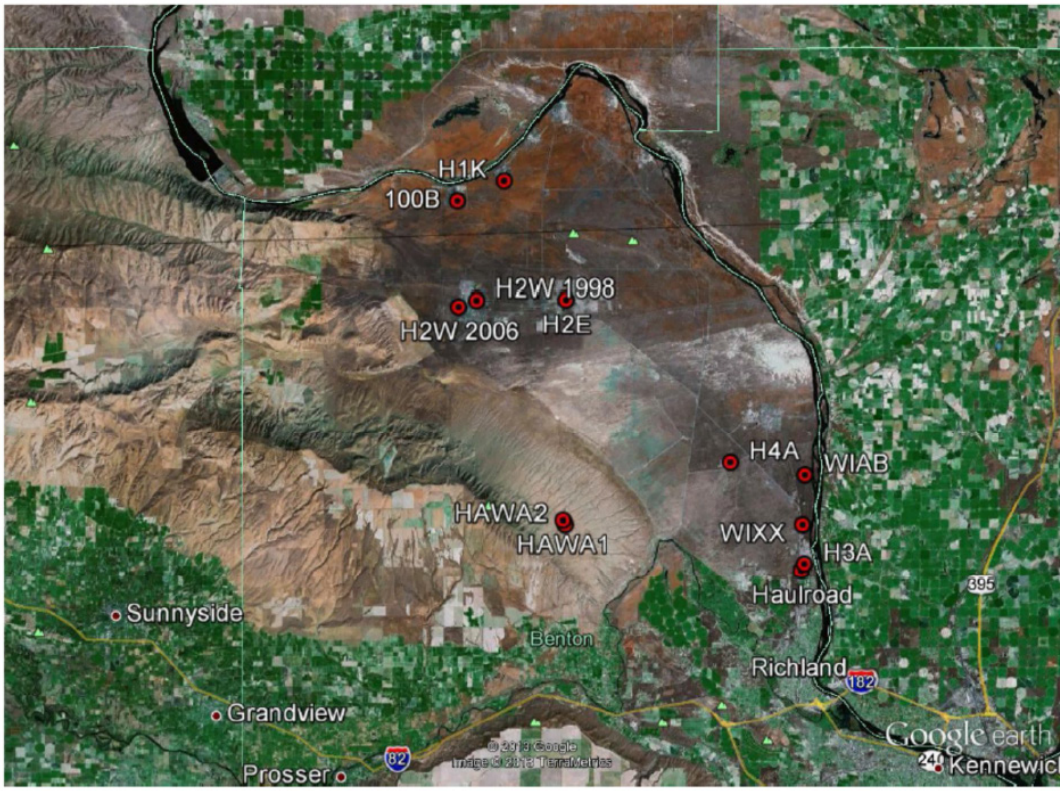

Figure 7.10. Locations of SASW measurements performed in 2013 on the Hanford Site.

7.2.3 Development of Stratigraphic Profiles

The first stage in developing the profiles for the five hazard calculation sites was to develop profiles of the stratigraphy at each location. The profiles were developed by George Last (Last 2014) of PNNL using several sources of information to construct the stratigraphy, including contour maps for the top and bottom of the basalts from seismic refraction studies (e.g., Glover 1985). A typical example of the profiles developed by Last (2014) is shown in Figure 7.11 for Site C (CGS). For the stratigraphy of the stack of SMBs and the Ellensburg Formation interbeds, the information was mainly inferred from borehole and well logs on the Hanford Site—from databases generally developed for hydrogeology studies—located near the hazard calculation sites. An important point to note here is that relatively few of the wells and boreholes extend into the basalts and it was often the case that the closest deep borehole was at some distance from the hazard calculation site (Table 7.7), leading to appreciable uncertainty regarding the thicknesses—and in some cases, even the presence—of the different stratigraphic units at each location.

An important feature of the profiles, not captured explicitly in the profiles produced by Last (2014), is the presence of "flow tops" formed by the breaking up of the basalt into pieces (brecciation) and the presence of gas bubbles (vesiculation). Rohay and Brouns (2007) developed a three-layer model for the flow top of the each of the basalts encountered in the three boreholes at the WTP site. The thicknesses of these layers were identified from the borehole gravity meter measurements, and the corresponding reductions in V_S values with respect to the main body of the basalt flow from the PS suspension logging measurements (because the downhole velocity measurements did not provide sufficient vertical

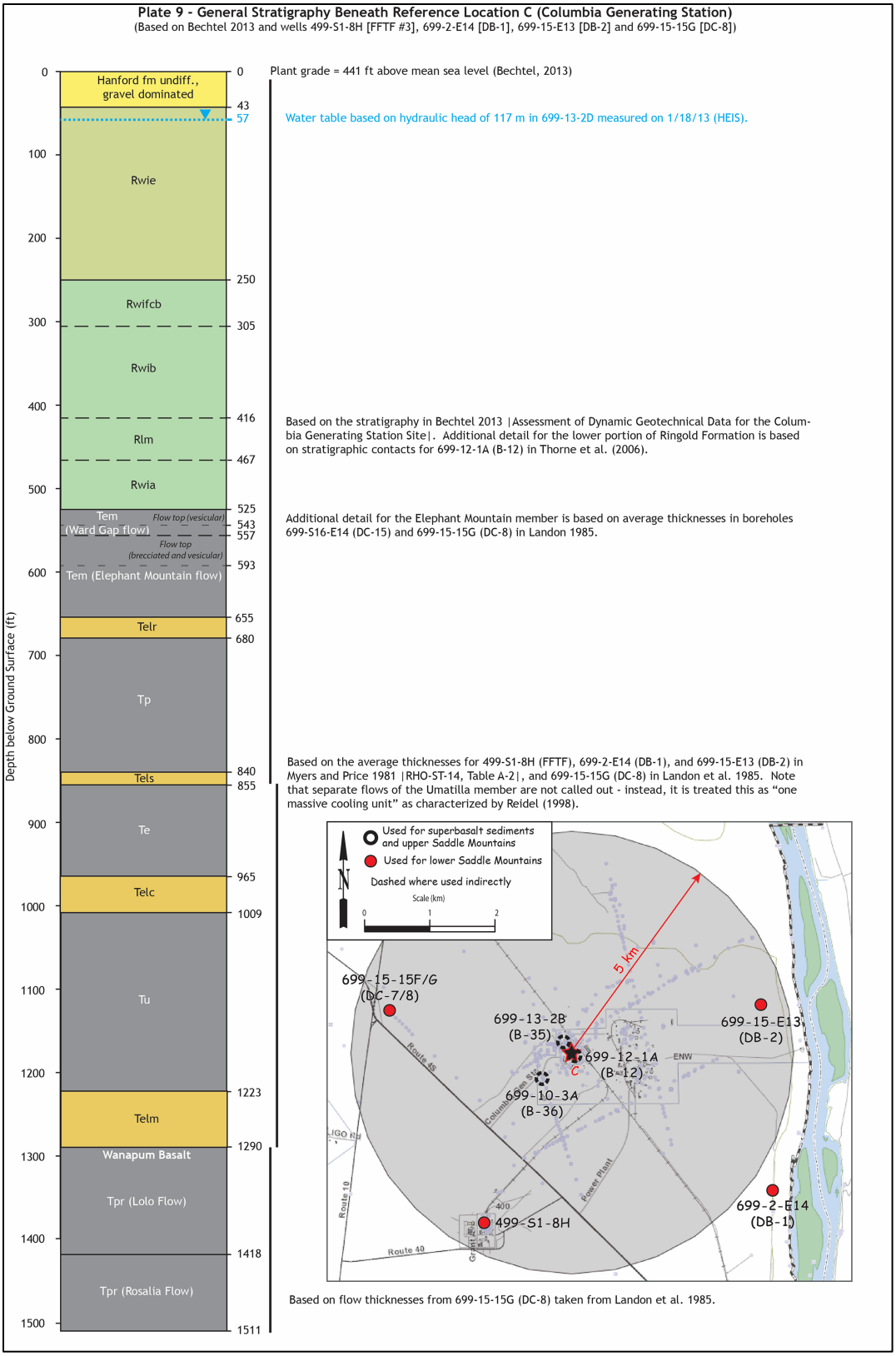

Figure 7.11. Stratigraphic profile from the surface to top of Wanapum Basalt (Last 2014).

Table 7.7. Summary of borehole information used to infer stratigraphic column at each of the hazard locations and associated uncertainties in layer characteristics (Last 2014).

Site	Number and Proximity of Boreholes for Inferring the Stratigraphy at Each Location	Uncertainty in Unit Thickness (m)
A	For the WTP site, there are deep boreholes at 45 m and 62 m from the reference location, as well as another two within about 310 m	Variations in thickness from 2.4 to 7 m in the upper part (down to Selah interbed) and 0.3 to 3.7 m below
B	Nearest borehole to top of basalts is 143 m away; thickness of SMB stack layers inferred from three deeper boreholes at distances from 1.7 to 2.5 km from reference location	Top of basalts constrained to within 3 m (as at Site A); unit thicknesses to within 3−6.7 m down through Esquatzel Member, 8.8−21 m below
C	Top of basalts from three boreholes at distances of 42 to 873 m; SMB unit thicknesses from four boreholes at distances of 4.2 to 5.5 km	Top of basalts to within 7 m; thicknesses vary by 15.2 to 26.5 m for SMB stack units
D	Upper part of SMB stack from three boreholes 7−8 km away, all in one direction (northeast) with respect to the site; lower parts of SMB from individual boreholes and isopach maps	Top of basalt constrained to within 10 m; thicknesses of units in upper part of SMB stack vary by 0.6 to 4.6 m, in lower units variation is up to 7 m. Actual uncertainty is probably higher because of the distance of boreholes.
E	Top of basalt from single borehole 176 m from the site; unit thicknesses in SMB stack from two boreholes located 1.5 and 3 km from the site.	Top of basalts may be good to within 10 m; unit thicknesses varied by up to 13 m

SMB = Saddle Mountains Basalt.

resolution). The density models for the flow tops are shown in Figure 7.12. Rohay and Brouns (2007) report the variations in the flow top thicknesses, but only the arithmetic mean thicknesses were used in building the stratigraphic profiles. The thickness of the flow top layers is considered to be a constant regardless of the thickness of the layer itself (Alan Rohay, personal communication, August 2, 2013). Therefore, wherever these same stratigraphic units were encountered, the velocities and densities in the uppermost part of the layers were modeled using the arithmetic mean values reported by Rohay and Brouns (2007).

As discussed below in Section 7.2.4, the development of the site-response profiles was based on the assumption that the dynamic properties of the units (V_S and ρ) are laterally homogeneous across the site. However, some of the units encountered at sites farther away from WTP were not present in the WTP profile (Figure 7.2), which means that assumptions had to be invoked regarding analogous units. These assumptions are summarized in Table 7.8. In most cases, this has simply involved assuming equivalence among the properties of the basalts and interbeds, respectively, which is supported by the consistency among their properties at the WTP site (Table 7.6).

A particular challenge regarded the interpretation of the thicker Umatilla Member, which is divided into the upper Sillusi flow and the underlying Umatilla flow; Figure 6.18 of Rohay and Brouns (2007) provides evidence of the presence of these two flows in the vicinity of the WTP site. The two separate flows in the Umatilla are also encountered within the stratigraphic profile at Site B (200-W). Reidel (1998) interprets the Umatilla and Sillusi flows as nearly time equivalent, with the Sillusi flow invading a still molten Umatilla flow and mixing with it. This is particularly evident in the Pasco Basin, where

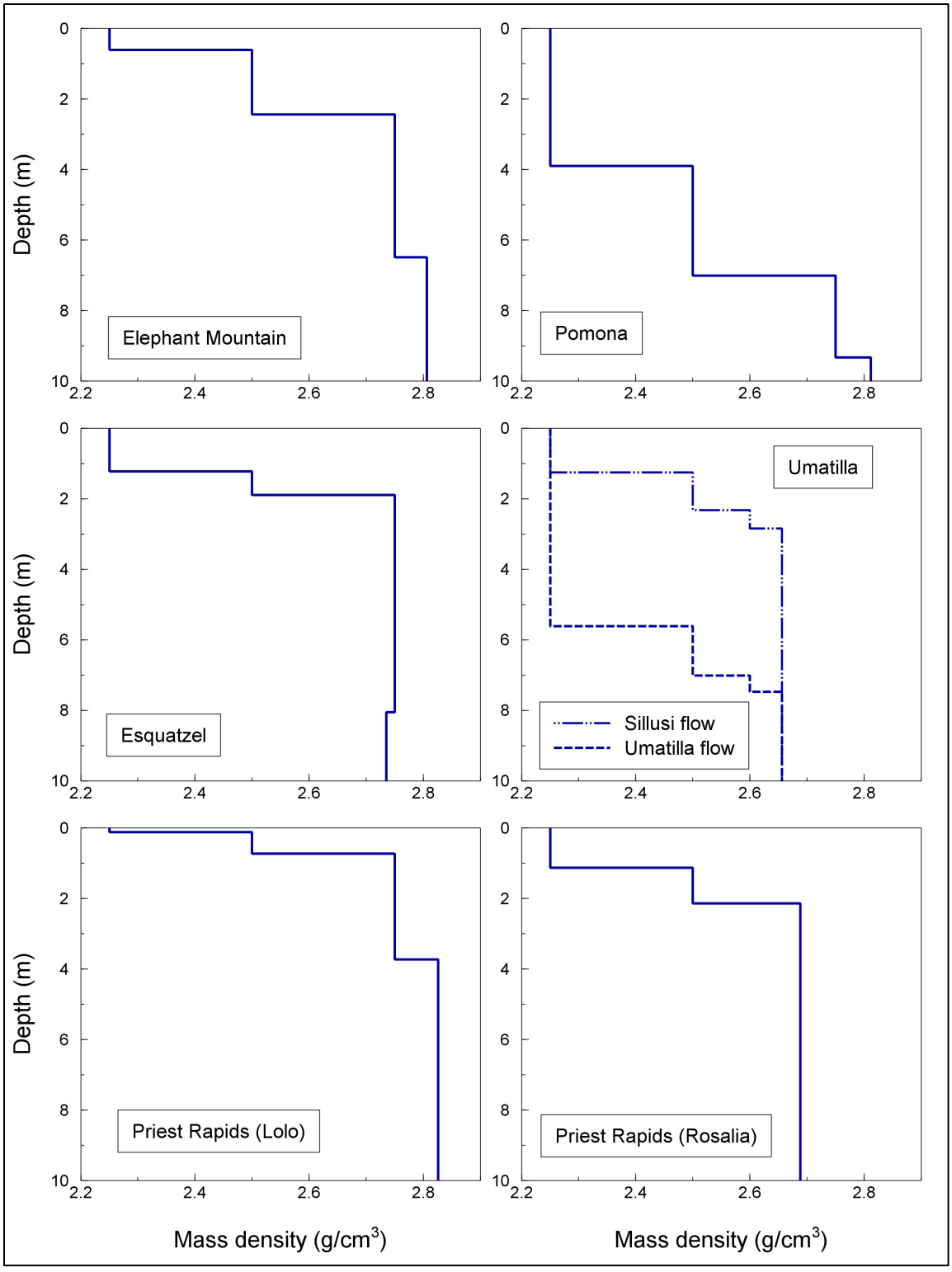

Figure 7.12. Models for the densities within the basalt flow tops proposed by Rohay and Brouns (2007).

Table 7.8. Summary of assumptions made to develop the stratigraphic profiles in terms of units and their dynamic properties.

Site	Stratigraphic Profile Construction	Unit Properties
A	Byron interbed ignored, following Rohay and Brouns (2007) who argue that it is very thin and probably discontinuous across the site. Also, thinner than density measurements interval so no meaningful density values.	None
B	None	None
C	Elephant Mountain flow top assigned also to the Ward Gap flow. Single Umatilla flow is assumed to be the Umatilla flow and not the Sillusi flow.	Ward Gap flow of Elephant Mountain unit same as the Elephant Mountain flow at WTP
D	Asotin Member not assigned flow top because none was seen in boreholes. Unnamed interbed below Asotin Member assumed to be continuation of Cold Creek Member. Single Umatilla flow is assumed to be the Umatilla flow and not the Sillusi flow.	Asotin basalt unit assigned the same properties as the Esquatzel basalt above it in the sequence.
E	Elephant Mountain flow top assigned also to the Ice Harbor Member and Ward Gap flow. Single Umatilla flow is assumed to be the Umatilla flow and not the Sillusi flow. Rosalia flow of Priest Rapids Member assumed absent because it was not encountered in all boreholes. Unnamed interbed below Lolo flow disregarded (as for Byron interbed at Site A).	Elephant Mountain properties assigned to Ice Harbor Member. Levy interbed assigned V_S of 850 m/s and ρ of 2 g/cm^3. Same assumptions as at Site C for Ward Gap flow.

Reidel (1998) states there is "*only one massive cooling unit*." He does, however, recognize that in a few cases near the flow margins, there is a compositional change that corresponds to vessicular zones (or lobes) and thus, the Umatilla Member can be separated in to two flows. Beneath the WTP site, Barnett et al. (2007) identify a breccia zone within the Umatilla Member that matches up with velocity data of Rohay and Brouns (2007), and this was used as the basis for separating the Umatilla Member into an upper (Sillusi) flow and lower (Umatilla) flow. In 200-West Area (Site B), historic data have called out two separate flows (without identifying a breccia zone). For the purposes of constructing the layers, the breccia zone identified within the Umatilla Member below the Sillusi flow is assumed to be covered by the flow top of the Umatilla flow and is not modeled separately. The available information regarding the presence of the two separate flows within the Umatilla Member at Sites C, D, and E is summarized in Table 7.8.

As noted previously, the profiles were required to extend down to the deep crystalline basement (Figure 7.13). The WBs have a total thickness on the order of 300 m. Below the Wanapum is the Grande Ronde Basalt layer, which has a thickness of around 2,200 m. The Saddle Mountain, Wanapum, and Grande Ronde basalts together form the Columbia River basalts (CRBs). Below the Grande Ronde basalts is a layer, with a thickness on the order of several kilometers, of pre-Miocene sediments, overlying the crystalline basement.

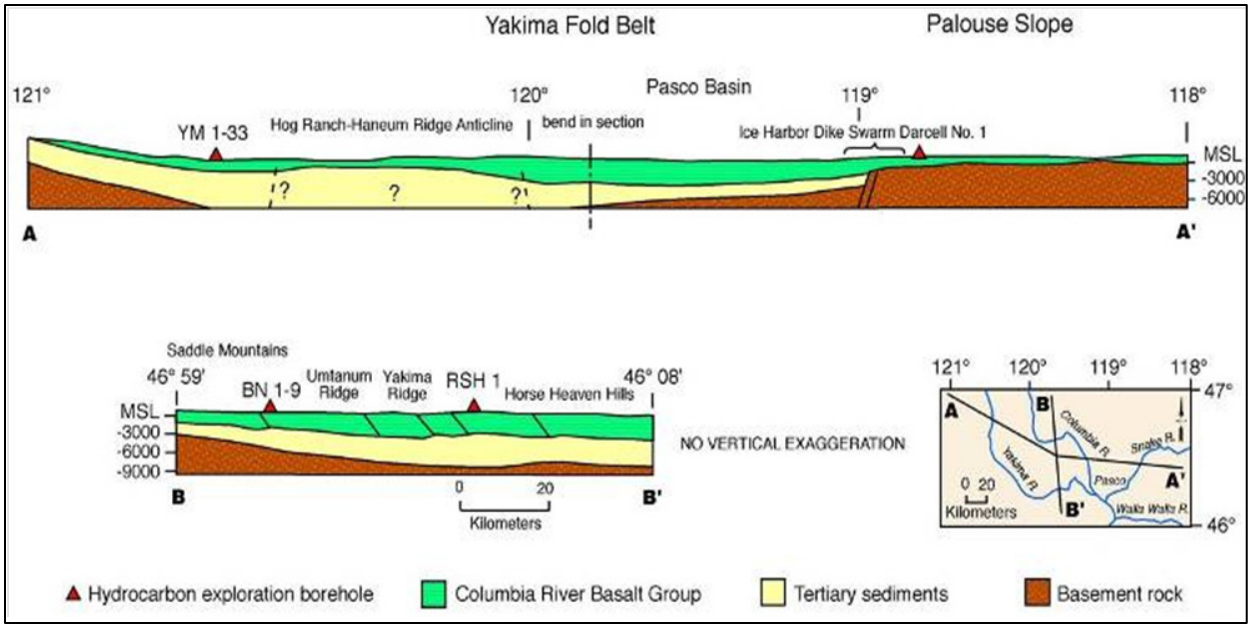

Figure 7.13. Cross sections through the upper crust in the region of the Hanford Site (Reidel et al. 2002).

In terms of the deeper stratigraphy, the information was taken from the 3-D model of the Hanford Site and surrounding region developed by Thorne et al. (2014) as input to the 3-D simulations performed by Dr. Art Frankel to explore the possible presence of basin effects. The model was developed using regional geological maps, contour maps of the depth to the top of different units, and numerous profiles from seismic refraction surveys, particularly those of Glover (1985). In this model, the crystalline basement is at a depth of between 7 and 9.5 km at the five hazard calculation sites, implying a 5 to 6-km thickness of the sub-basalt sediments. An alternative model was developed in which the depths to the basement and the deeper units were inferred from gravity measurements, which leads to much thinner sub-basalt sediments layers and depths to the crystalline basement between 3.5 and 5 km. Views of the two models are shown in Figure 7.14.

Thorne et al. (2014) note that the interpretation of the gravity data is uncertain because of a lack of information about the density of the underlying rock strata. The GMC TI Team assessment was that the refraction-based profiles were more reliable, particularly in view of the multiple reversals of velocity and density values below the Hanford Site. Moreover, a recent model developed by Blakely et al. (2013) using gravity and magnetic data, plus a single borehole, also placed the crystalline basement at depths comparable to those indicated by the seismic refraction studies. Therefore, rather than develop two models or a model representing any weighted average of the two interpretations, only the model with the thicker sub-basalt sediment layer and the crystalline basement located at depths greater than 7 km was adopted for generating the site models. This model is also consistent with the interpretation of the crustal structure by the SSC TI Team (Section 4.10).

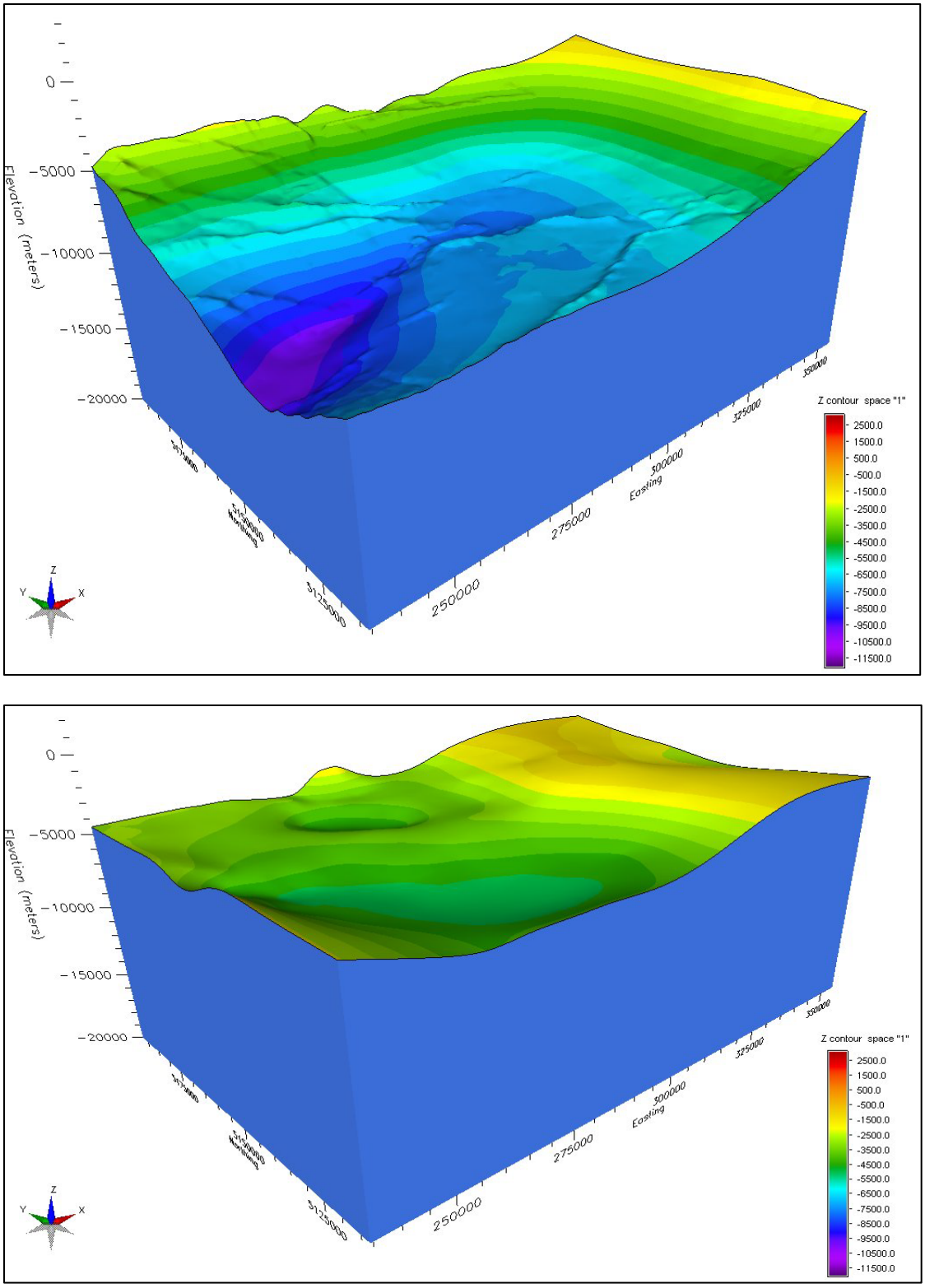

Figure 7.14. Models of the top-of-crystalline basement (3x vertical exaggeration) inferred from refraction studies (upper) and from gravity measurements (lower).

7.2.4 Development of V_S, V_P, and Density Profiles

To characterize the dynamic behavior of the Hanford Site, the stratigraphic profiles described in the previous section were transformed into profiles of shear-wave velocity (V_S) and mass density (ρ). The sequence of basalts and sedimentary interbeds of the SMB sequence has previously been shown to have a marked influence on seismic wave propagation (WCC 1981). For the development of the 3-D models for analysis of possible basin effects, Thorne et al. (2014) adopted the velocities and densities over different depths as summarized in Table 7.9.

Table 7.9. Velocity and density assignments used by Thorne et al. (2014)

Depth Below Ground Surface, m	Seismic Velocities, m/s		Density (g/cm^3)
	V_S	V_P	
Hanford sediments 0–25 m	425 m/s	800 m/s	1.75
Hanford sediments 25–50 m	550 m/s	880 m/s	1.85
Hanford sediments 50–75 m	670 m/s	1190 m/s	1.95
Cold Creek unit	670 m/s	1190 m/s	2.15
Ringold Formation	2200 m/s	3660 m/s	2.55
Saddle Mountains Basalt <125 m	2200 m/s	3600 m/s	2.55
Saddle Mountains Basalt 125–150 m	2500 m/s	4300 m/s	2.70
Saddle Mountains Basalt 150–350 m (+ Ellensburg sediments)	2000 m/s	4000 m/s	2.50
Wanapum Basalt <425 m	2600 m/s	4500 m/s	2.75
Wanapum Basalt 425–500 m	2900 m/s	5000 m/s	2.80
Basalts >500 m deep	$V_S = V_P/1.73$	$V_P = 5000$ m/s + 0.0001×(depth–500)	2.85
Sub-basalt sediments	$V_S = V_P/1.73$	$V_P = 3900$ m/s + 0.00015x depth	2.55
Crystalline basement	$V_S = 3500$ m/s	$V_P = 6100$ m/s	2.70

The information in Table 7.9 was used only to assign properties to the lower WBs and lower layers (Grande Ronde basalts, sub-basalt sediments and the crystalline basement). For the SMBs, Ellensburg sediment interbeds, and the Priest Rapids Member of the WBs, more detailed information is available from the extensive measurements made at WTP site. A key assumption was therefore that the properties of the different units are laterally homogeneous across the entire site, noting that the distances from WTP range from just over 1 km (Site A) to more than 25 km (Site E). However, as was noted previously, the consistency of the velocity and density values measured for the basalts and sedimentary interbeds vertically—see Table 7.6 and Figure 7.15 below—suggest that this is not an unreasonable assumption.

For performing earlier site-response analyses at the WTP location, Youngs (2007) followed the recommendation of Rohay and Brouns (2007) to use only the V_S values obtained from the downhole measurements because the 1,000 Hz frequency associated with the PS suspension logging measurements was so far removed from the range of frequencies of engineering interest. The GMC TI Team gave careful consideration to this issue, and also sought views from resource experts (including Professor Ken Stokoe, Dr. Walt Silva, and Dr. Carl Costantino) regarding the reliability of the two types of measurements. On the one hand, the TI Team was advised that in order to reliably measure velocities in such hard materials as the SMBs, higher frequency (5−10 kHz) signals may be required than those used at WTP. On the other hand, the TI Team was persuaded that the PS suspension logging measurements are not without value (indeed, the velocity variations within basalt flowtops could only be determined from these measurements because of their greater vertical resolution than the downhole measurements) and

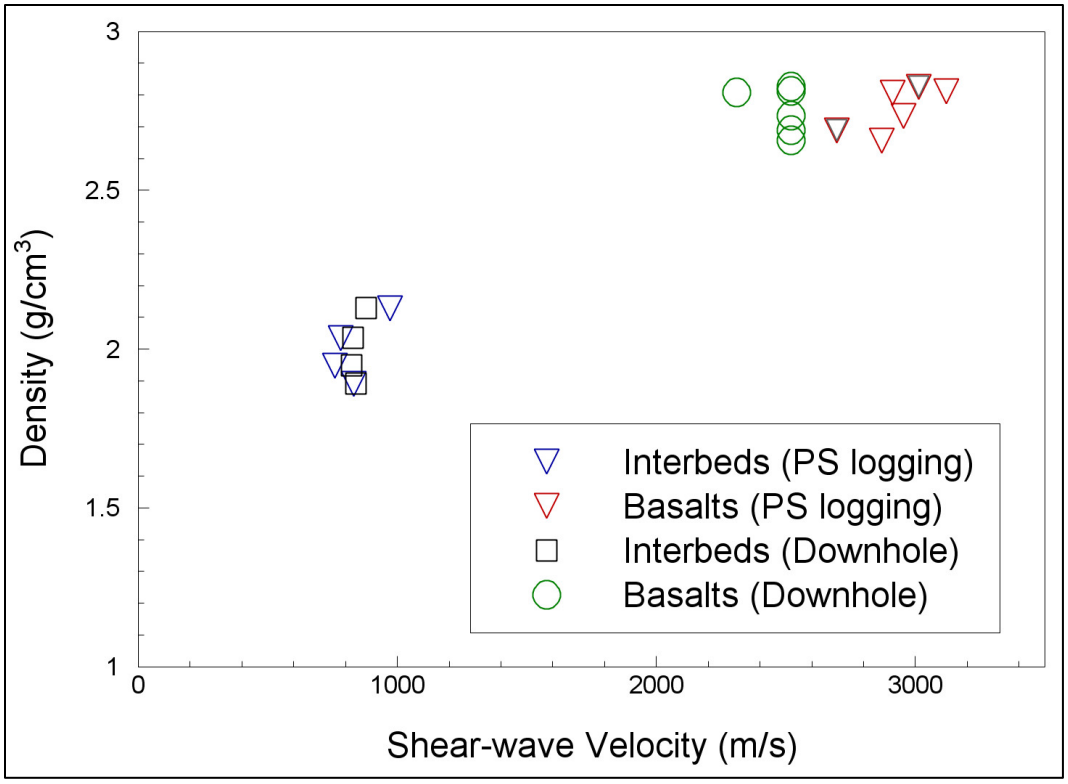

Figure 7.15. Shear-wave velocity and density values of the Saddle Mountains basalts and Ellensburg Formation sedimentary interbeds at the WTP site.

should not be rejected but rather retained as an indicator of the range of epistemic uncertainty in the velocity measurements. Professor Ken Stokoe informed the GMC TI Team that his comparisons of free-free tests with PS suspension logging measurements had suggested that the latter tended to overestimate the velocities. However, in the absence of a clear and unambiguous explanation for the differences between the two sets of velocity measurements in the basalt units, it was considered appropriate to retain both sets of V_s values, although not necessarily with equal weighting.

For the deeper layers, the information from Table 7.9 was adopted, as noted above. The depths at which the Wanapum V_S transitions from 2,600 m/s and from 2,900 m/s to the velocity gradient are taken as 325 and 400 m, respectively, because the profiles developed herein are expressed in terms of depths relative to the top of the SMBs rather than the ground surface. There is clearly and inevitably a degree of approximation here in assuming a thickness of 100 m for the suprabasalt sediments at all the sites, because the actual thickness of the near-surface sediments varies from 58 to 199 m.

The velocity gradients within the lower CRBs are given by these equations, in which velocities are in m/s and depth in meters:

$$V_S = 2900 + 0.058(depth - 400) \quad (7.1)$$

This equation is adapted very slightly from that proposed by Thorne et al. (2014) in Table 7.9 to simply make the V_S profile continuous in the transition from the constant velocity of 2,900 m/s layer to the gradient that begins immediately below (and also to be referenced to the top of SMB rather than the ground surface). The shear-wave velocities in the sub-basalt sediment layer are given by the following equation:

$$V_S = 2254 + 0.087 * depth \quad (7.2)$$

As was noted before, there are only measurements of V_P in the lower layers, V_S values being obtained from assumed ratios of V_P/V_S. The V_P and V_S values in Table 7.9 correspond to a ratio of 1.73 (i.e., the square root of 3, which corresponds to a Poisson's ratio of 0.25). There is clear uncertainty regarding the actual ratio for the sub-basalt sediments, for which reason it was decided that a second value also be considered, for which a ratio of 2 was recommended (Alan Rohay, personal communication, 2012), which would imply a Poisson's ratio of 0.33. This led to an alternative equation for the sub-basalt sediment velocities:

$$V_S = 1950 + 0.075 * depth \quad (7.3)$$

The decision was taken to build separate profiles using Equations (7.2) and (7.3) for assigning shear-wave velocities in the sub-basalt sediments. The V_S values in the Wanapum and Grande Ronde basalts were assigned in both cases using Equation (7.1); all other V_S and density values were taken from Table 7.9, except for the SMB stacks (comprising the basalt units and Ellensburg Formation interbeds), which were constructed using the WTP measurements, as explained in Section 7.2.6. Figure 7.16 shows the two different profiles developed using the two models for the velocities in the pre-Miocene sediments above the crystalline basement. The model constructed using an assumed V_P/V_S ratio of 2 leads to sharper velocity contrasts both between the basement and the sediment layer as well as between the top of the sediments and the CRBs. In Figure 7.16 it can be appreciated that the velocities in the upper layers are also different in the two profiles, which arises from the decision to retain both the downhole and PS suspension logging measurements. The treatment of the two sets of measurements, and their combinations with the two deeper profiles, is discussed in Section 7.2.6. Figure 7.17 shows the density profile, which is the same for both of the two velocity profiles shown in Figure 7.16.

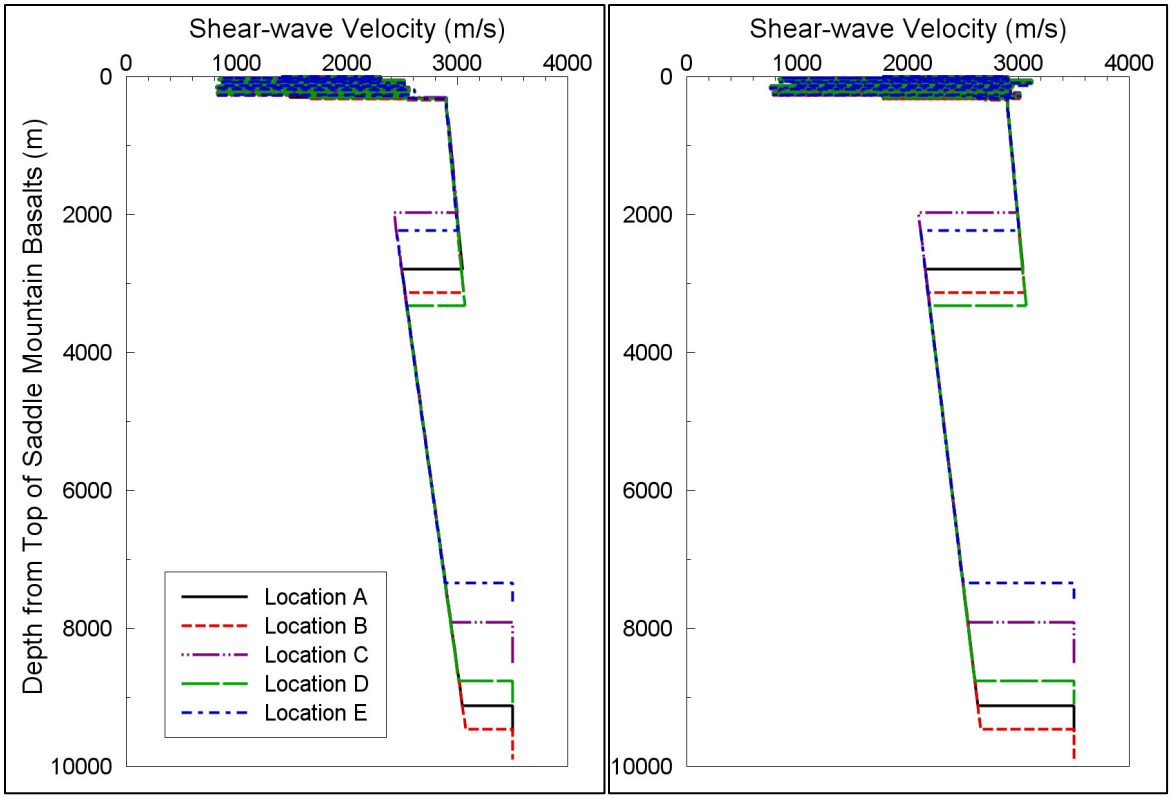

Figure 7.16. Deep V_s profiles at the five hazard calculation sites developed using V_P/V_S ratios in the sub-basalt sediments of 1.73 (left) and 2.0 (right).

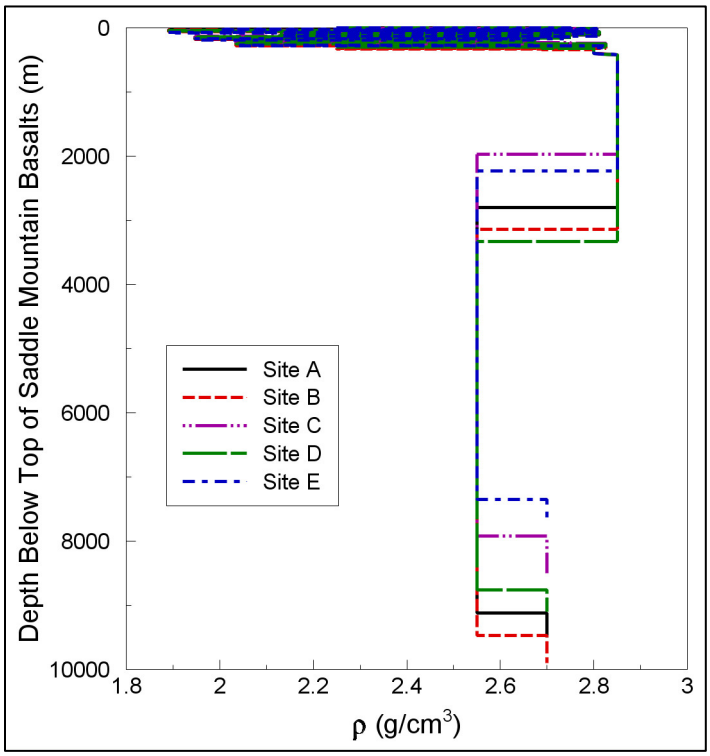

Figure 7.17. Density profiles at the five hazard calculation sites.

7.2.5 Selection of the Baserock Horizon

As noted at the beginning of this section, the ultimate goal of the Hanford PSHA is to provide a characterization of the ground motion hazard at the ground surface (or the foundation level of surface facilities on the site). One way to provide such output is to perform the hazard calculations in a way that accounts for the dynamic response of the near-surface layers so that the motions are calculated directly at the ground surface. This option was discounted for the Hanford PSHA project for the simple reason that the near-surface layers have not yet been characterized in detail at most of the facility locations on the site; the only location for which such calculations could currently be performed is the WTP location. For this reason, the approach adopted for the project was to calculate the hazard at a specified baserock elevation, so that surface motions could be subsequently calculated at each location when the characterization of the near-surface layers was obtained at some point in the future.

A key decision was therefore the selection of the baserock elevation. The natural choice would be the top of the SMBs, which would then require the downstream site-response analyses to model only the suprabasalt sediments of the Hanford and Ringold Formations (Figure 7.9). However, as has already been noted, the SMBs contain thick interbeds of the sediments of the Ellensburg Formation, which have lower densities and velocities than the basalts. If the top of the SMBs were selected as the baserock horizon, the stack of basalt and sediment interbeds would be treated as an elastic half-space in the subsequent site-response analyses. One of the assumptions regarding the behavior of an elastic half-space is that any downward propagating waves radiate away from the surface and none of the energy is reflected or refracted back toward the surface. Therefore, the question of whether the velocity reversals within the SMB stacks would undermine the assumption of an elastic half-space, and hence prevent the top of the basalts from being selected as the reference baserock horizon, had to be addressed.

This question was addressed by using the available information from the WTP site (Rohay and Reidel 2005; Rohay and Brouns 2007) to perform two sets of site-response calculations relevant to the estimation of surface motions:

1. Coupled analysis. This calculation estimates the response of the full profile (SMB stack and suprabasalt sediments) to a motion below the SMBs.
2. De-coupled analysis. This calculation is performed in two stages: a) the response of the SMB stack to a motion below the stack; and b) the response of the suprabasalt sediments to the motions at the top of the basalts, in which the SMB stack is treated as an elastic half-space.

The results of the two calculations are shown in Figure 7.18, from which it can be immediately appreciated that very different results are obtained. In particular, the de-coupled analysis leads to significant peaks in the amplification at frequencies just above 1 Hz and 5 Hz, which are not present in the amplification functions calculated from the coupled analysis using the complete profile. This leads to the clear conclusion that the SMB stack cannot be treated as an elastic half-space and therefore the baserock elevation for the interface between the hazard calculations and the subsequent site response could not be the top of the basalts.

The baserock elevation was required, therefore, to be below the SMB stack. The criterion for selecting this reference horizon was simply that it should be the first elevation encountered below the stack that could be treated as an elastic half-space. There are known flowtops at the top of both the Lolo and Rosalia flows of the Priest Rapids Member of the WBs, so it was judged appropriate to locate the

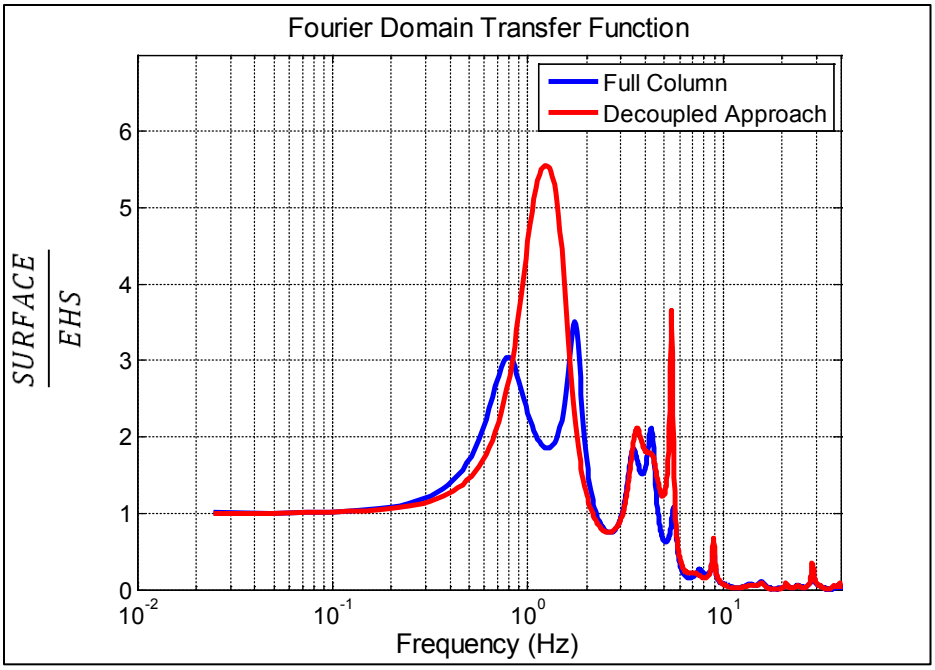

Figure 7.18. Comparison of site amplification functions (ratio of surface motions to those at the top of an elastic half-space [EHS]) using coupled and de-coupled analyses.

horizon below these flowtops, because they represent low-velocity layers and therefore create velocity reversals within the profile. However, based on the available information from boreholes in the vicinity of Site E, Last (2014) concluded that it was possible that the Rosalia flow was not present at that location. Because it was desirable to have a common reference baserock horizon across all five hazard calculation sites, the baserock elevation was defined as being at the base of the Lolo flowtop (in other words, at the top of the WBs, but not including the brecciated and vesiculated layers at the top of the uppermost Lolo basalt flow). This means, of course, that at Sites A−D, there is a known velocity reversal within the Wanapum due to the presence of the Rosalia flowtop. In reality, there are very likely to be several other flowtops within the deeper profile—see, for example, Thordarson and Self (1998)—but only those of the Lolo and Rosalia flows were penetrated by the WTP boreholes. To explore to what extent any deeper flow tops might influence the dynamic behavior of the assumed half-space, an experiment was conducted. For the WTP profile, the SMB stack and WB half-space were modified by introducing into the deeper basalts a series of flowtops, which are essentially those encountered in the SMBs introduced at arbitrary elevations (Figure 7.19). Using the modified profile, the response of the profile to the top of the SMBs with 0% damping in the WBs was calculated. The modified profile was then replaced with an equivalent layer of uniform velocity with damping, the rationale being that the baserock model would have an assigned kappa value that represents the effect of all layers below the SMBs. The response of the modified Wanapum profile was then compared with that of the equivalent uniform Wanapum half-space. As can be appreciated from Figure 7.20, the differences are small and it was concluded therefore that even if such flowtops are present, the response of the WBs can be adequately represented by an elastic half-space with kappa. The key point is that the presence of such flowtops in the WB would not influence the details of the response spectral shape.

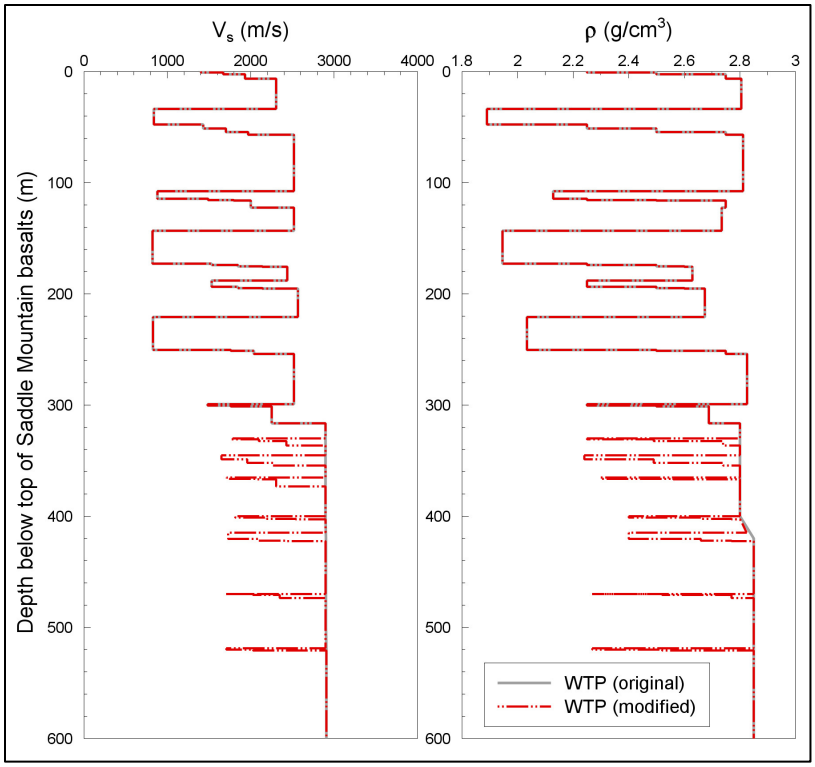

Figure 7.19. Original and modified velocity (left) and density (right) profiles at the WTP site, with "flowtops" introduced into the Wanapum basalts.

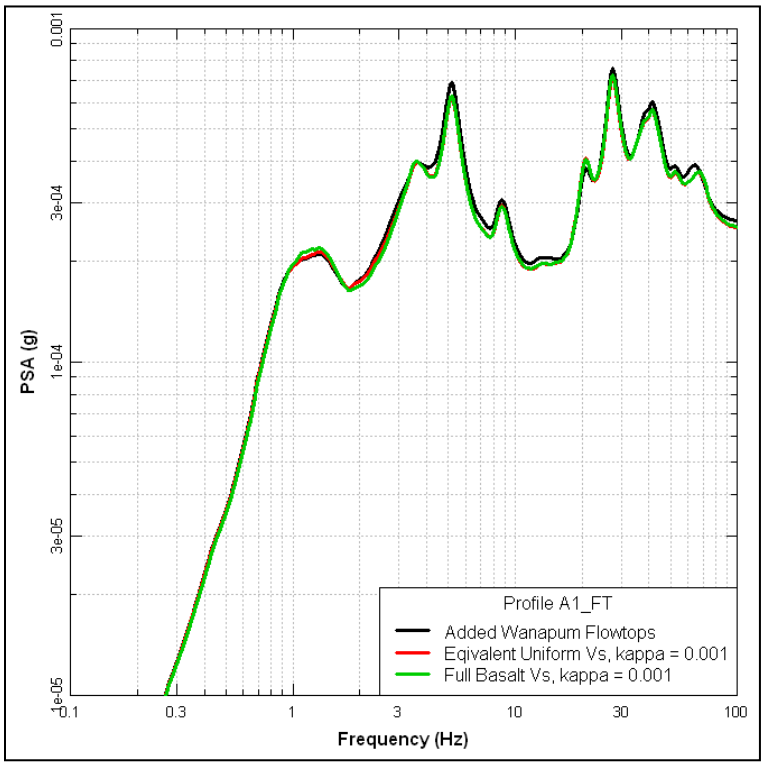

Figure 7.20. Comparison of calculated response with flowtops in Wanapum Basalt and equivalent uniform velocity layer with damping represented by baserock kappa value.

An obvious consequence of selecting the top of the WBs as the baserock elevation is that the SMB stacks need to be included in the site-response analyses that will be conducted to transform the baserock hazard characterization into surface motions. Because the original scope of the project specified that those responsible for the downstream site-response analyses would only be charged with the characterization of the suprabasalt sediment layers, the GMC TI Team decided to develop the stack models to be used in the site-response analyses as part of the handover deliverables; the development of these profiles is described below in Section 7.2.6. Another motivation for the GMC TI Team to provide these profiles was the fact that the kappa estimates obtained from analysis of ground motion recordings at the Hanford Site effectively represent kappa at the top of the SMBs; it is important that the kappa value assigned to the Wanapum baserock (Section 7.3) and the damping assigned to the basalts and sediment interbeds of the stacks (Section 9.7.2) are consistent with the kappa estimates obtained for the top of the stack.

7.2.6 Profiles for the Saddle Mountains Basalt Stacks

As noted in the previous section, the baserock horizon at which the hazard is to be calculated is the base of the Lolo flowtop at the top of the WBs. The handover includes both the ground motion hazard at this horizon and models of the layers between this elevation and the top of the SMBs for use in the subsequent site-response analyses. These models of the profiles (that start at their base with the Lolo flowtop and include the full stack of SMBs and Ellensburg interbeds) need to define layer thicknesses and V_S, ρ, and damping in each of the layers, as well as nonlinear degradation and damping curves where appropriate (i.e., for the interbeds). The layer thicknesses are defined by the stratigraphic profiles whose development was described in Section 7.2.3. The density values are assigned to the layers using the values measured at WTP, which are presented in Table 7.9. The shear-wave velocities are also assigned using the values from WTP, also summarized in Table 7.9, but using two different sets of measurements, namely those from downhole V_S measurements and those from PS suspension logging measurements. These were used to develop two separate profiles at each location, Profile 1 being based on the velocities from downhole measurements, and Profile 2 on those from PS suspension logging. The assessment of the GMC TI Team was that the V_S values from downhole measurements are more reliable than those from PS logging, because the latter would have required the use of even higher frequencies for measurements in such stiff materials, but that the PS logging data should be included as representing the range of epistemic uncertainty rather than simply being ignored. The assessment of the TI Team was that the downhole measurements could be considered twice as reliable as the PS suspension logging measurements in this environment, leading to the assignation of relative weights of 2:1 to the profiles (Section 7.3). Figure 7.21 through Figure 7.25 show the five pairs of velocity and density profiles for the hazard calculation sites.

As will be recalled from Section 7.2.4, there are also two alternatives for the deeper profiles because of different models for the velocities in the sub-basalt sediments. Combined with the alternative models for the SMB stack velocities, these result in a total of four profiles at each location. However, as shown in Section 7.3.1 below, the dynamic responses are enveloped by two profiles, namely Profile 1 that combines the downhole V_S values in the stack with the higher velocities in the sub-basalt sediments, and Profile two that combines the V_S values in the stack obtained from suspension logging with the lower sub-basalt sediment velocities. Profile 2 is therefore characterized by higher velocity contrasts than Profile 1, at all depths.

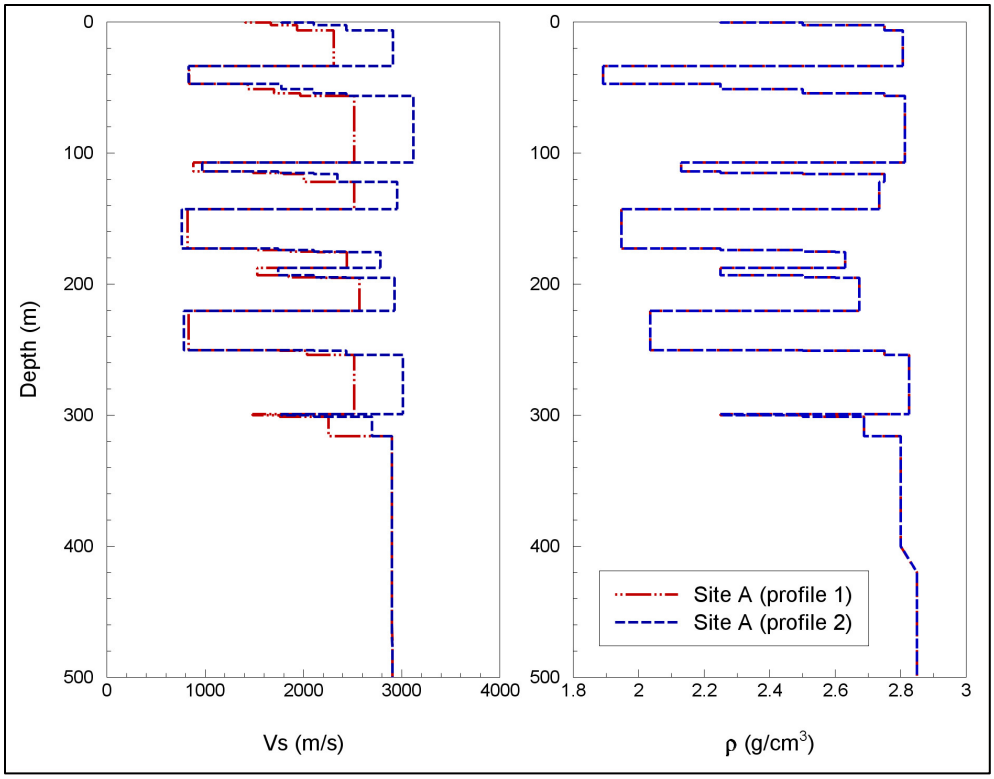

Figure 7.21. Velocity and density profiles for the Saddle Mountains Basalt stack at Site A.

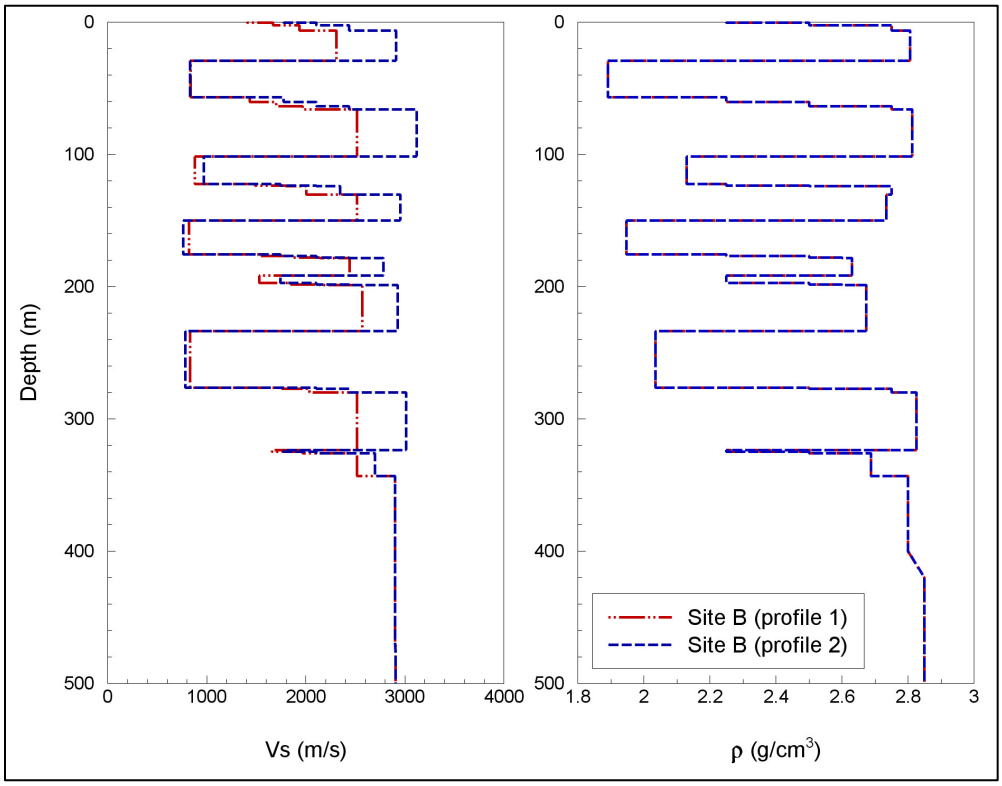

Figure 7.22. Velocity and density profiles for the Saddle Mountains Basalt stack at Site B.

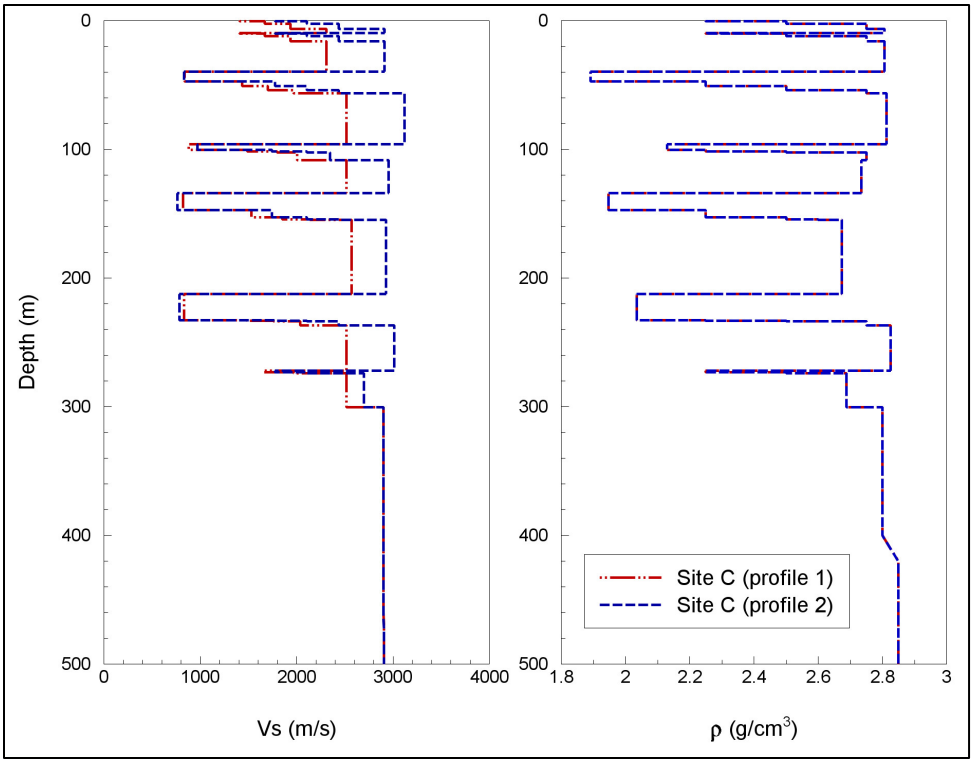

Figure 7.23. Velocity and density profiles for the Saddle Mountains Basalt stack at Site C.

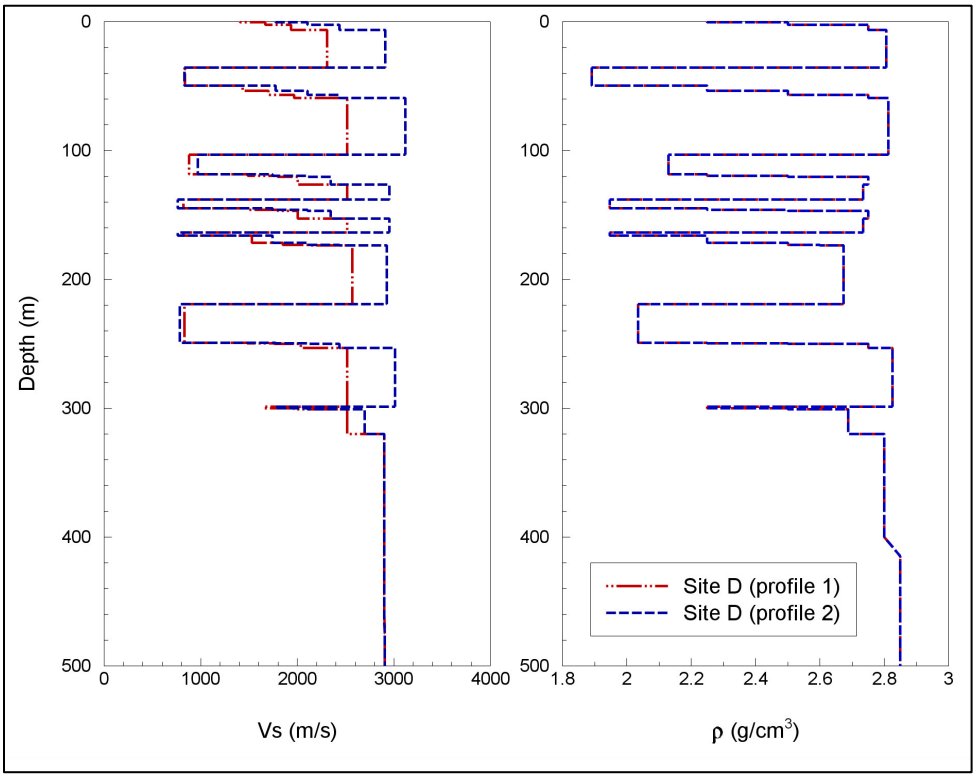

Figure 7.24. Velocity and density profiles for the Saddle Mountains Basalt stack at Site D.

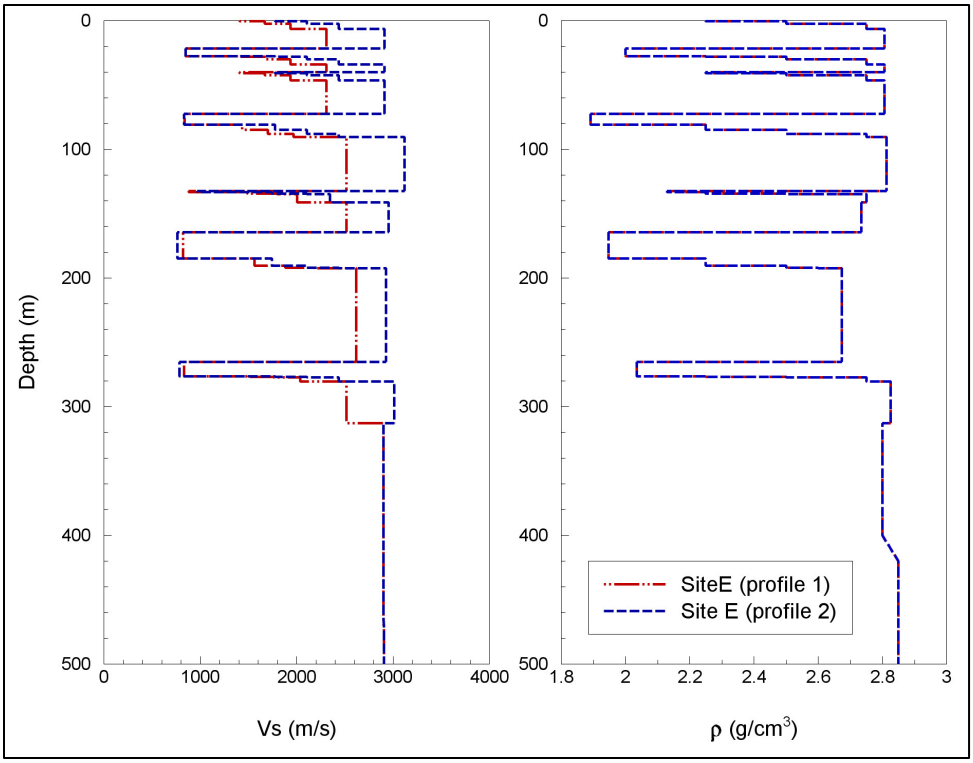

Figure 7.25. Velocity and density profiles for the Saddle Mountains Basalt stack at Site E.

The DOE consultant Dr. Carl Costantino also specified V_P profiles as part of the required handover. Because V_P values are not generally needed for site-response analyses, it is assumed that these would only be required for dynamic soil-structure interaction (SSI) calculations. It is not clear whether the profiles considered for such SSI calculations would penetrate into the SMB stacks, but recognizing that this is a possibility, the request for V_P profiles was duly considered by the GMC TI Team. The conclusion of the TI Team's deliberations is that there is considerable uncertainty in the available data. Therefore, rather than developing the V_P profiles the TI Team has opted to include herein a summary of the available information about V_P values in the SMBs and Ellensburg Formation interbeds, and also briefly discuss the implied V_P/V_S ratios. The latter are of importance because all of the V_S values assigned to units below the Priest Rapids Member of the Wanapum are estimated from V_P profiles, determined from sonic measurements in a few offsite deep boreholes (e.g., Jarchow et al. 1994), and from seismic refraction studies (Glover 1985; Ludwin et al. 1991; Jarchow et al. 1994), but also because they could be used to convert the V_S profiles provided in the handover into V_P profiles.

Rohay and Reidel (2005) used the limited information available at the time of their study to infer V_P/V_S ratios in the various units of the WTP profile. In the logic-tree formulation that they constructed for site-response estimations (Figure 3.2.1 in their report), they assigned a fixed value of 1.79 to the SMB layers. For the Ellensburg Formation interbeds, they considered ratios of 2.0, 2.3, and 2.6, which were assigned weights of 0.2, 0.3, and 0.5 respectively.

Rohay and Brouns' (2007) focus was very much on developing profiles in terms of V_S and ρ for site-response analyses, and relatively little attention was given to V_p. Figure 3.2 in their report—reproduced here as Figure 7.26—shows V_S and V_P values from suspension logging in one of the WTP boreholes;

Figures 3.3 and 3.4 in the Rohay and Brouns (2007) report show similar profiles from two other boreholes. Without the numerical data only very approximate estimates can be made from these figures, but they indicate V_P/V_S ratios of 2.5−3.0 in the interbeds and on the order of 1.8−1.9 in the basalt layers.

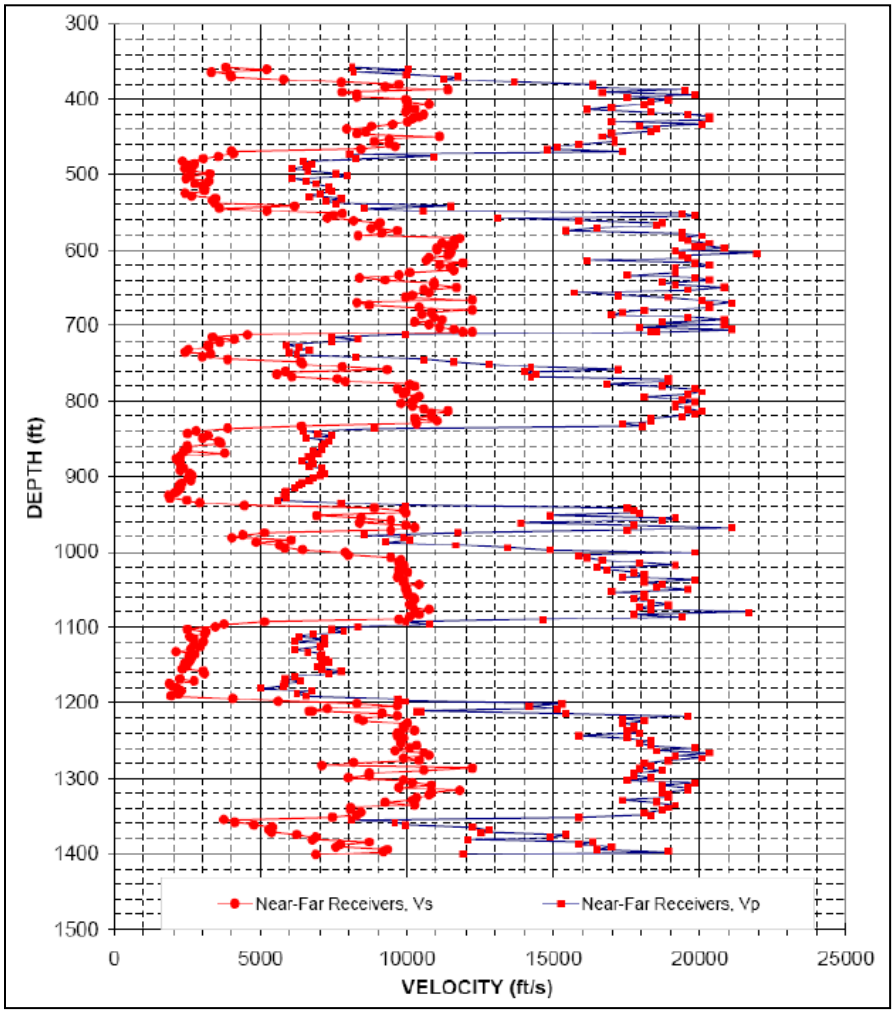

Figure 7.26. V_S and V_P suspension logging data from WTP borehole C4993 (Rohay and Brouns 2007).

Rohay and Brouns (2007) do present tabulated V_P and V_S values from downhole measurements in Tables 3.1 and 3.2 of their report. There are two sets of results, these coming from measurements with a vibratory source of excitation and an impulsive source. The latter are very incomplete and only persist down to the Pomona Basalt, with V_S results for all three boreholes and V_P results for only one of them. Therefore, only the measurements from the vibratory source are reported here, and the results are summarized in Table 7.10.

The results obtained with the average (geometric mean) velocities from the three boreholes indicate ratios in the range of 1.9−2.1 for the basalt layers, and 2.4−2.7 for the interbeds. These values are quite different from the ratios of 1.73 used to assign shear-wave velocities to the deep basalts and 1.73−2.0 for the deep sediments. Figure 7.27 shows the same information as Figure 7.15, but now with the implied V_S-ρ values for the deeper units also added, as well as the recommended relationship from Boore (2007), which is largely based on the work of Brocher (2005).

Table 7.10. Summary of V_P and V_S ratios from downhole measurements in WTP boreholes (Rohay and Brouns 2007) (velocities in m/s).

Stratigraphic Unit	Borehole-Specific V_P/V_S			Geomean Values		Ratio
	C4493	C4496	C4497	V_S	V_P	
Elephant Mountain	2.321	2.040	1.971	2308.7	4861.1	2.11
Rattlesnake Ridge IB	2.467	2.935	2.819	838.9	2292.6	2.73
Pomona	2.011	1.870	1.949	2529.6	4913.2	1.94
Selah IB	3.137	2.737	1.848	897.8	2256.3	2.51
Esquatzel	2.230	2.088	1.912	2525.9	5235.2	2.07
Cold Creek IB	2.552	2.079	2.715	822.0	1999.8	2.43
Umatilla	2.096	2.047	2.053	2548.6	5263.4	2.07
Mabton IB	2.513	2.693	3.022	830.1	2269.7	2.73
Priest Rapids	2.327	1.927	NA	2451.2	5190.3	2.12

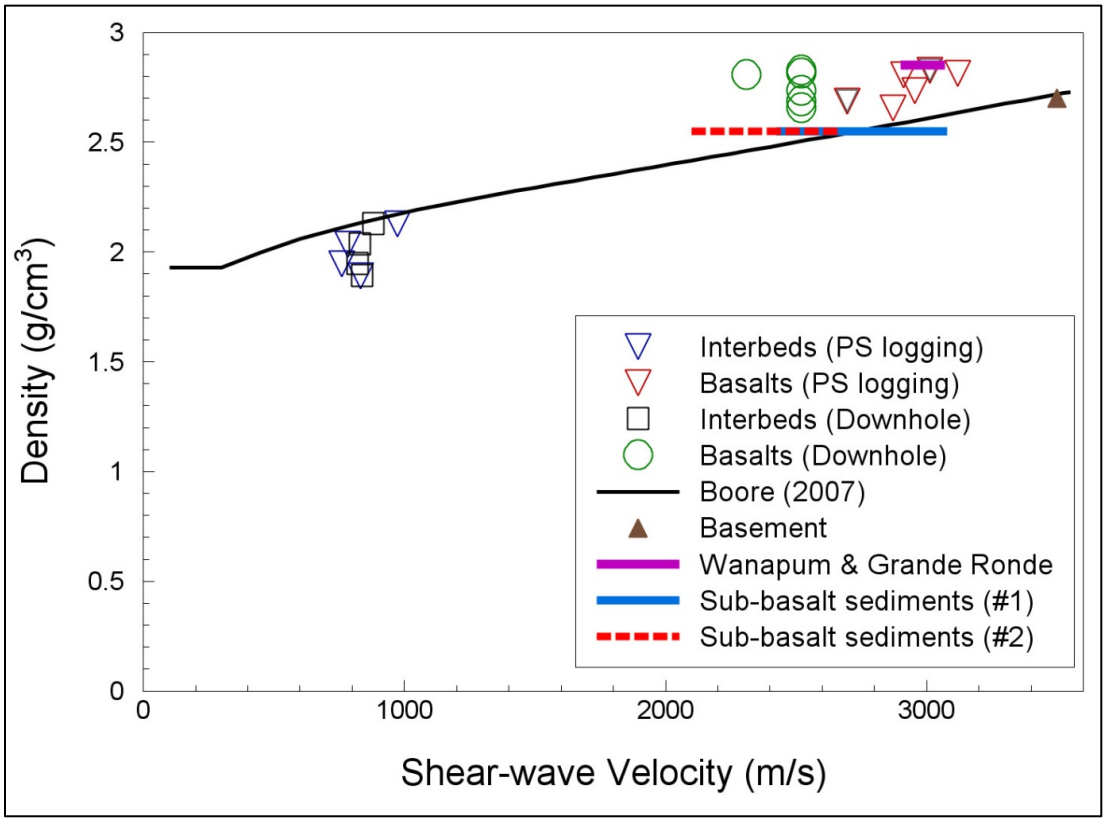

Figure 7.27. V_S-ρ values for the shallow and deep units at the Hanford Site and the recommended relationship of Boore (2007).

7.3 Kappa Model and Target V_S Profiles for the Hanford Site

The PSHA is conducted at the reference baserock horizon defined as the top of the Lolo flow at Hanford. A kappa model and target V_S profiles were developed for the five PSHA locations. The kappa model characterizes kappa at the top of SMBs referred to as κ_{site}, kappa at the reference baserock horizon referred to as $\kappa_{baserock}$, and the associated damping in the overlying layers up to the top of SMB. Target V_S profiles characterize subsurface conditions from the top of SMB to the crystalline basement and were used to develop the kappa model and the site amplification factors at the reference baserock horizon. Estimates of $\kappa_{baserock}$ and site amplification factors are used to adjust the GMPEs from their host regions to the reference baserock horizon at the five target PSHA sites at Hanford.

7.3.1 Target V_S Profiles and Site Amplification Factors for the Hanford Site

Four candidate V_S and density profiles were developed for each of the five hazard calculation sites at Hanford as discussed in Section 7.2. The V_S profiles are shown in Figure 7.16 from the top of SMB down to the crystalline basement. At each site, all four candidate profiles have the same stratigraphy and thickness of layers and only differ in their V_S values. Profiles 1 and 2 differ in the V_S values for the layers from the top of SMB down to the top of the WB layer (downhole versus PS logging) and in the V_S values for the sub-basalt sediments (different V_P/ V_S ratios). Profiles 1 and 4 share the same V_S values below the WB layer and only differ in the SMB stack. Similarly, Profiles 2 and 3 share the same V_S values below the WB layer.

Although all profile layers from the top of SMB down to the crystalline basement were used to develop the kappa model for the Hanford Site, the V_S profiles below the top of Lolo flow define the target V_S profiles for the hazard calculation sites and were used to develop target site amplification factors for the reference baserock horizon. Among the four target V_S profiles below the reference baserock at each site, Profiles 1 and 4 only differ in their V_S values in the top 63 m for Sites A, B, and C, 67 m for Site D, and 33 m for Site E. Similarly, Profiles 2 and 3 only differ in their V_S values in the relatively thin top layer above the WB. Based on these similarities for Profiles 1 and 4 and Profiles 2 and 3, only two candidate target V_S profiles (Profiles 1 and 2) were used to develop site amplification factors. Figure 7.28 presents the target V_S profiles below the reference baserock horizon at the five hazard calculation sites at Hanford.

The square-root impedance (SRI) method, also known as the quarter wavelength (QWL) method, as implemented in the computer program SMSIM (Boore 2005), was used to develop target linear site amplification factors for the two candidate V_S profiles at the five hazard calculation sites. Site amplification factors were computed at the reference baserock horizon (free surface) with respect to the half-space at the top of the crystalline basement. The factors are defined as the ratio of FAS of the ground motion at the surface of the velocity model to the ground motion that would have occurred at the surface of an equivalent constant-velocity half-space model where the layers above the reference depth are removed. The QWL method averages velocities and densities over a depth corresponding to one-quarter wavelength for each frequency. An angle of incidence of zero degrees at the source level was used in the analysis. Figure 7.29 presents the computed QWL linear site amplification factors for the two candidate target V_S profiles at the five hazard calculation sites at Hanford. Note that the site amplification factors are generally comparable for the five hazard calculation sites as well as for Profiles 1 versus Profiles 2. Profiles 1 and 2 differ at high frequencies because of the difference in the V_S values for the shallow layers of the profiles and in the low frequencies because of the difference in the sub-basalt sediments V_S values.

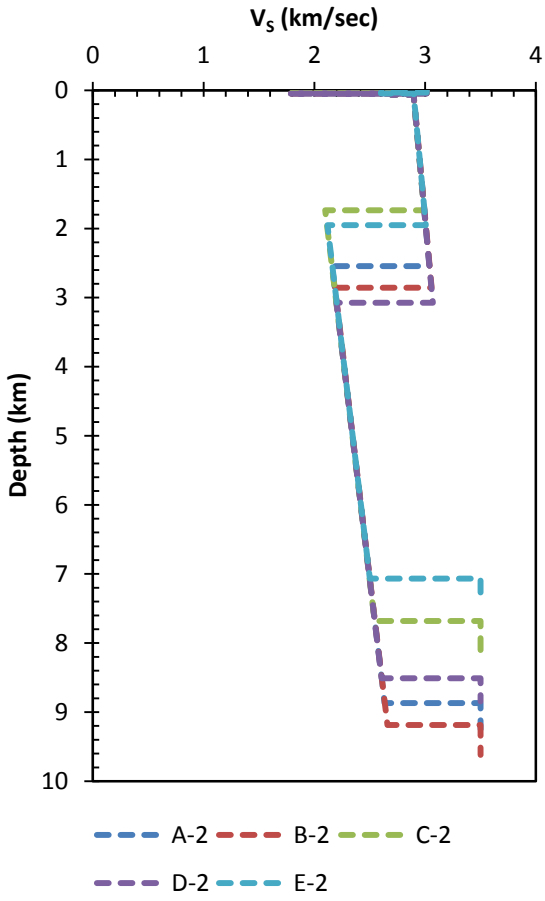

Figure 7.28. Target V_S profiles from the reference baserock horizon to the crystalline basement for the five hazard calculation sites at Hanford. Profiles 1 are shown on the left and Profiles 2 are on the right.

The sensitivity of the QWL site amplification factors to the use of a larger angle of incidence at the source was explored. Figure 7.30 presents a comparison of the QWL site amplification factors at Site A Profile 1 for an angle of incidence of zero versus 30 degrees. Using an angle of incidence of 30 degrees leads to a reduction of the site amplification factors. The maximum observed reduction is small, on the order of 4%. Despite the fact that the use of an angle of incidence of 30 degrees might be more appropriate for deep earthquakes, a zero degree angle of incidence was adopted for being more consistent with typical 1-D site-response analyses and for resulting in slightly more conservative site amplification factors and V_S scaling factors.

The use of the full-resonant method as implemented in the computer program RATTLE (Boore 2005) was explored for the development of site amplification factors. This method provides site amplification computed from theoretical simulations of shear horizontal (SH) wave propagation in layered media accounting for constructive and destructive interference of all the reverberations in the layers. Amplification is computed using the propagator-matrix of Haskell (1960). Boore (2013) provides a detailed comparison of the QWL and the full-resonant methods and their impacts on the resulting site amplification factors. Figure 7.31 presents a comparison of the site amplification factors derived using both QWL and full-resonant methods at Site A Profile 1. The RATTLE site amplification was smoothed

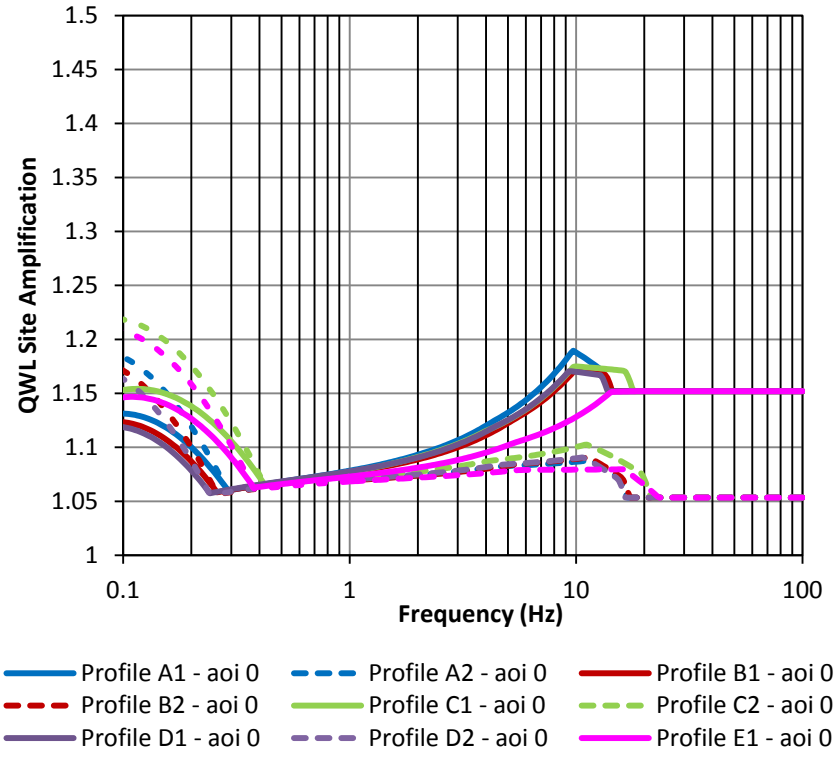

Figure 7.29. Target linear site amplification factors at the reference baserock horizon developed using the QWL method for the two candidate V_S profiles at the five hazard calculation sites at Hanford with respect to the top of the crystalline basement. An angle of incidence (aoi) of zero degrees was used.

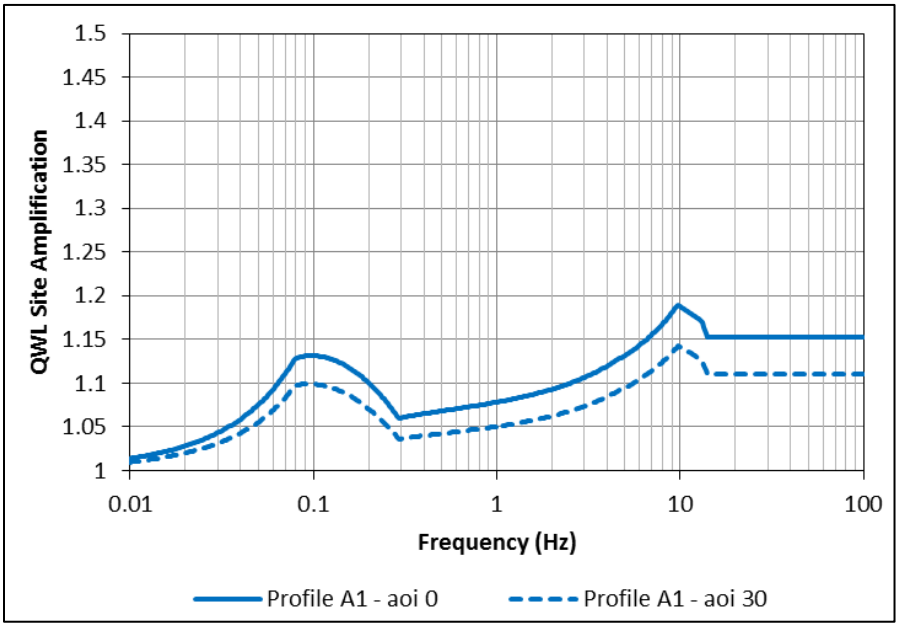

Figure 7.30. Comparison of QWL linear site amplification factors at Site A Profile 1 for an angle of incidence (aoi) at source of zero versus 30 degrees.

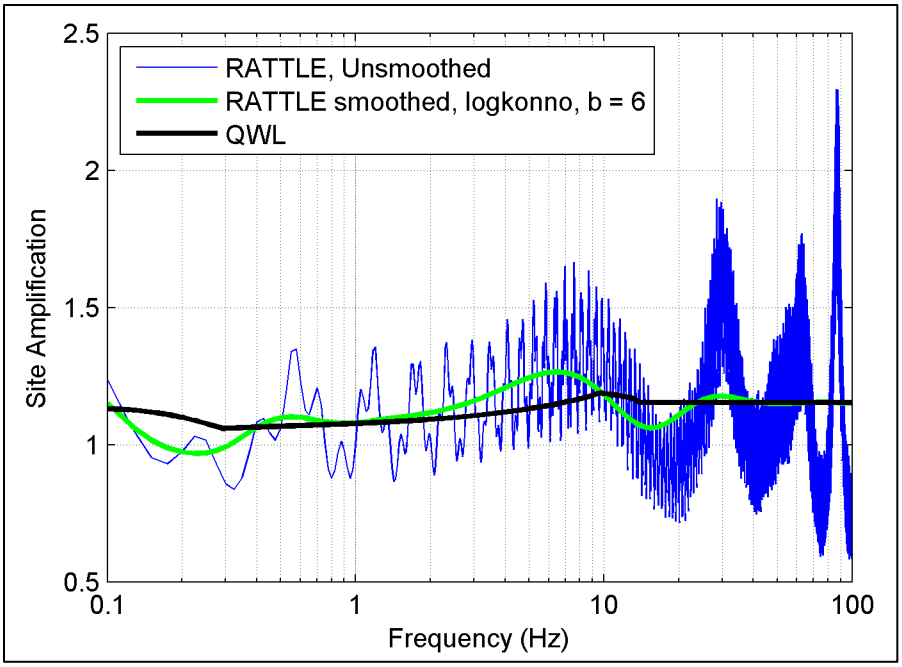

Figure 7.31. Comparison of linear site amplification factors at Site A Profile 1 using the QWL and the full-resonant RATTLE methods.

using the Konno and Ohmachi (1998) filter, smoothing the power of the spectrum over log frequency. Figure 7.31 shows that the difference in the derived site amplification factors for the two methods is small. Moreover, it is important to note that the resulting amplification from either method is only an approximation of the true amplification. Finally, because the QWL method is considered standard practice for calculating linear crustal amplification functions (e.g., Boore et al. 2013; Boore and Joyner 1997; Cotton et al. 2006; Renault et al. 2010; Bommer et al. 2014), and because the difference in amplification between the QWL method and RATTLE is small, the site amplification factors developed using the QWL method were adopted.

7.3.2 Kappa Components and Terminology

Kappa is a measure of the observed high-frequency decay of FAS of ground motion recordings. The mechanism causing the observed high-frequency fall-off has been subject to debate for the last 30 years. Detailed description of the origins of kappa can be found in Campbell (2009), Campbell et al. (2014) and Hashash et al. (2014). Here we present the terminology adopted by the TI Team to describe the different components of kappa.

Kappa estimated at a site for an individual earthquake recording is referred to as κ_{obs} and reflects the combined effects of source (κ_{source}), path (κ_{path}), and site (κ_{site}) on spectral decay:

$$\kappa_{obs} = \kappa_{source} + \kappa_{path} + \kappa_{site}. \quad (7.4)$$

Over the years, researchers studied recordings of earthquakes at multiple distances from a single station and concluded that κ_{obs} increases with source-to-site distance in a manner consistent with the effects of anelastic attenuation. The distance dependence of kappa represents the incremental attenuation due to the

horizontal propagation of shear waves through the crust. Zero-distance kappa, $\kappa(0)$, can be obtained after removing the distance or path contribution to κ_{obs} and $\kappa(0)$ becomes equal to the sum of κ_{source} and κ_{site}. Assuming that average κ_{source} is negligible (Purvance and Anderson 2003; Van Houtte et al. 2011), $\kappa(0)$ approximates κ_{site}.

κ_{site} represents the attenuation due to the propagation of shear waves through subsurface materials below and near the site within distances of hundreds meters to a few kilometers, at least for normal crust in which velocities increase monotonically with depth. κ_{site} can be further divided into two components, $\kappa_{baserock}$ and $\kappa_{profile}$, representing the combined effects of intrinsic material damping and scattering in the competent basement rock and the shallower subsurface profile, respectively. κ_{site} can be written as follows:

$$\kappa_{site} = \kappa_{baserock} + \kappa_{profile} \tag{7.5}$$

$$\kappa_{baserock} = \kappa_{damping\_b} + \kappa_{scattering\_b} \tag{7.6}$$

$$\kappa_{profile} = \kappa_{damping\_p} + \kappa_{scattering\_p} \tag{7.7}$$

$\kappa_{damping}$ represents the low strain hysteresis material damping or the frequency-independent Q in each of the underlying layers of the basement rock or the shallower profile. $\kappa_{scattering}$ is caused by the scattering and reflection of high-frequency motions in the presence of velocity contrasts. Basement rock is generally considered to be a competent material with relatively high V_S and considerable thickness. Therefore, $\kappa_{scattering\_b}$ is expected to be negligible. $\kappa_{damping}$ can be written as follows:

$$\kappa_{damping} = \sum_i \frac{H_i}{\beta_i Q_i} \tag{7.8}$$

where β_i and Q_i are the shear-wave velocity and quality factor (or energy loss parameter) for subsurface layer i with a depth H_i, respectively. Q_i is related to material damping, ξ_i by

$$\xi_i = \frac{1}{2Q_i}. \tag{7.9}$$

Kappa estimated using the Inverse Random Vibration Theory (IRVT) approach (Al Atik et al. 2013) is the average of κ_{obs} inferred from short distance scenarios (5, 10, and 20 km) and is referred to as κ_1. Assuming that the source contribution to kappa is negligible, and that the distance contribution to kappa is also negligible for the short distance scenarios considered, κ_1 approximates κ_{site}.

7.3.3 Existing Estimates of Kappa for the Hanford Site

Existing kappa estimates on SMB at Hanford are described by Rohay and Riedel (2005). These estimates are the results of Dr. Walt Silva's analyses in 2004 using recordings of 10 small and deep earthquakes located at distances of 36 to 86 km from the USGS station HAWA. These signals were recorded on the horizontal components of the broadband velocity instrument at HAWA located approximately 20 km to the south of WTP (Site A). Velocity data were sampled at 40 samples/sec resulting in a Nyquist frequency of 20 Hz. Using an anti-alias filter with a corner frequency of around 16 Hz, the highest usable frequency of these recordings was around 15 Hz, which resulted in a large uncertainty on the kappa estimates. Table 7.11 shows the catalog used in the analysis.

Table 7.11. Catalog of earthquakes recorded at station HAWA used in the 2004 kappa analysis.

Station	Magnitude	Hypocentral Distance (km)	Hypocentral Depth (km)	Year, Day	Hr	Min	Sec	Com[(a)]	EQ Nb
HAWA	1.49	45.00	10.89	1999, 266	2	24	53.790	N	1
HAWA	3.25	45.84	12.38	1999, 262	11	11	52.919	N	2
HAWA	2.55	86.37	13.48	2001, 114	13	21	29.899	N	3
HAWA	1.51	43.57	13.19	2001, 154	11	51	58.540	N	4
HAWA	2.63	66.48	20.08	2001, 158	12	45	42.639	N	5
HAWA	3.17	80.96	11.04	2003, 15	3	41	58.400	E, N	6
HAWA	1.63	44.67	17.79	2003, 35	16	33	39.580	E, N	7
HAWA	2.63	68.85	8.78	2003, 54	7	54	.140	E, N	8
HAWA	1.81	42.16	22.10	2003, 134	4	59	43.770	E, N	9
HAWA	1.58	35.80	8.72	2004, 230	19	44	51.400	E, N	10

(a) Single horizontal component available.

Dr. Walt Silva applied the inversion process to provide kappa estimates. The usable frequency bandwidth for each shear-wave FAS was determined based on visual inspection not exceeding a maximum frequency of 15 Hz. The inversion bandwidth is magnitude-dependent, generally extending to lower frequency as magnitude increases and distance decreases. The inversion process treats multiple earthquakes and sites simultaneously to constrain the common path damping parameter Q(f). Source, path, and site parameters are obtained using nonlinear least-squares fit to the FAS using the point-source model (Boore 1983; EPRI 1993). Parameters that can be determined from the inversion scheme are kappa (κ_{site}), Q_0 (value of Q(f) at a frequency of 1 Hz), η (frequency-dependent path Q), **M**, and corner frequency (stress drop). Crustal amplification is accommodated in the inversion scheme by incorporating appropriate transfer functions (source depth to surface) in estimating the point-source surface spectra. The procedure uses the Levenberg-Marquardt algorithm (Press et al. 1986) with the inclusion of the second derivative. The parameter covariance matrix was examined to determine which parameters may be resolved for the data set. Asymptotic standard errors were computed at the final iterations.

The inversions were done on log-amplitude spectra (vector sum of the two horizontal components). To reduce the potential for non-uniqueness in the inversion results, a suite of starting models were used. The final set of parameters was selected based on a visual inspection of the model fit to the FAS, the chi-square values, and the parameter covariance matrix. Because of the narrow frequency bandwidth and the limited distance, geometric spreading was fixed at 1/R and Q(f) was fixed at $500(f)^{0.6}$. The stress drop was calculated from the moment and corner frequency using the relation

$$f_c = \beta \left(\frac{\Delta\sigma}{8.44 M_0} \right)^{1/3} \tag{7.10}$$

Table 7.12 presents the results of the inversions along with the parameters starting values. The fits to the FAS are shown in Figure 7.32. Rohay and Riedel (2005) note that the small stress drop values obtained from the inversions are not considered reliable given the high-frequency limitations of the recordings. The best-estimate κ_{site} on SMB at HAWA was 0.024 sec. Sensitivity analyses varying Q(f)

and the geometrical attenuation suggested that, for reasonable values of both parameters, the κ_{site} estimate of 0.024 sec was reasonably stable. Dr. Silva assessed the sensitivity of the estimated κ_{site} to the crustal amplification function. Figure 7.33 shows the three crustal amplification functions used in the inversions. These functions result in κ_{site} values of 0.024 sec for the soil plus rock function and 0.022 sec for the remaining two functions. It came to light through discussions during Workshop 1 that Dr. Silva was supplied with a velocity profile for location other than HAWA (because the recording station lies on SMB with minimal soil cover), but that this had not been clearly communicated, so Dr. Silva had worked on the assumption of the profile being for the HAWA site.

Table 7.12. Results of kappa from the 2004 inversions (Rohay and Riedel 2005).

Magnitude		Stress Drop, bars		Hypocentral
Starting Value[(a)]	Final Value	Starting Value	Final Value	Distance, km
1.49	2.03	0.1	0.25	45
3.25	2.94	0.1	7.46	46
2.55	2.31	0.1	1.48	86
1.51	1.96	0.1	2.32	44
2.63	2.47	0.1	9.45	66
3.17	2.51	0.1	3.05	81
1.63	2.02	0.1	4.81	45
2.63	2.54	0.1	2.17	69
1.81	2.23	0.1	2.95	42
1.58	2.14	0.1	2.21	36

(a) Starting magnitudes from coda length.
Initial κ_{site} = 0.02 sec, 0.04 sec; final κ_{site} = 0.024 sec.

Given the limited quality and quantity of the analyzed recordings, Rohay and Riedel (2005) estimated the uncertainty in the mean κ_{site} estimate by applying a factor of 1.3 leading to three candidate κ_{site} values of 0.018, 0.024, and 0.031 sec with weights of 0.3, 0.4, and 0.3, respectively. This uncertainty is larger than the typical assumption that the ±30 percent factor represents a 90-percent confidence interval. Because no additional data were available, the updated site-response study for the WTP site conducted by Youngs (2007) adopted the uncertainty distribution for κ_{site} developed by Rohay and Riedel (2005).

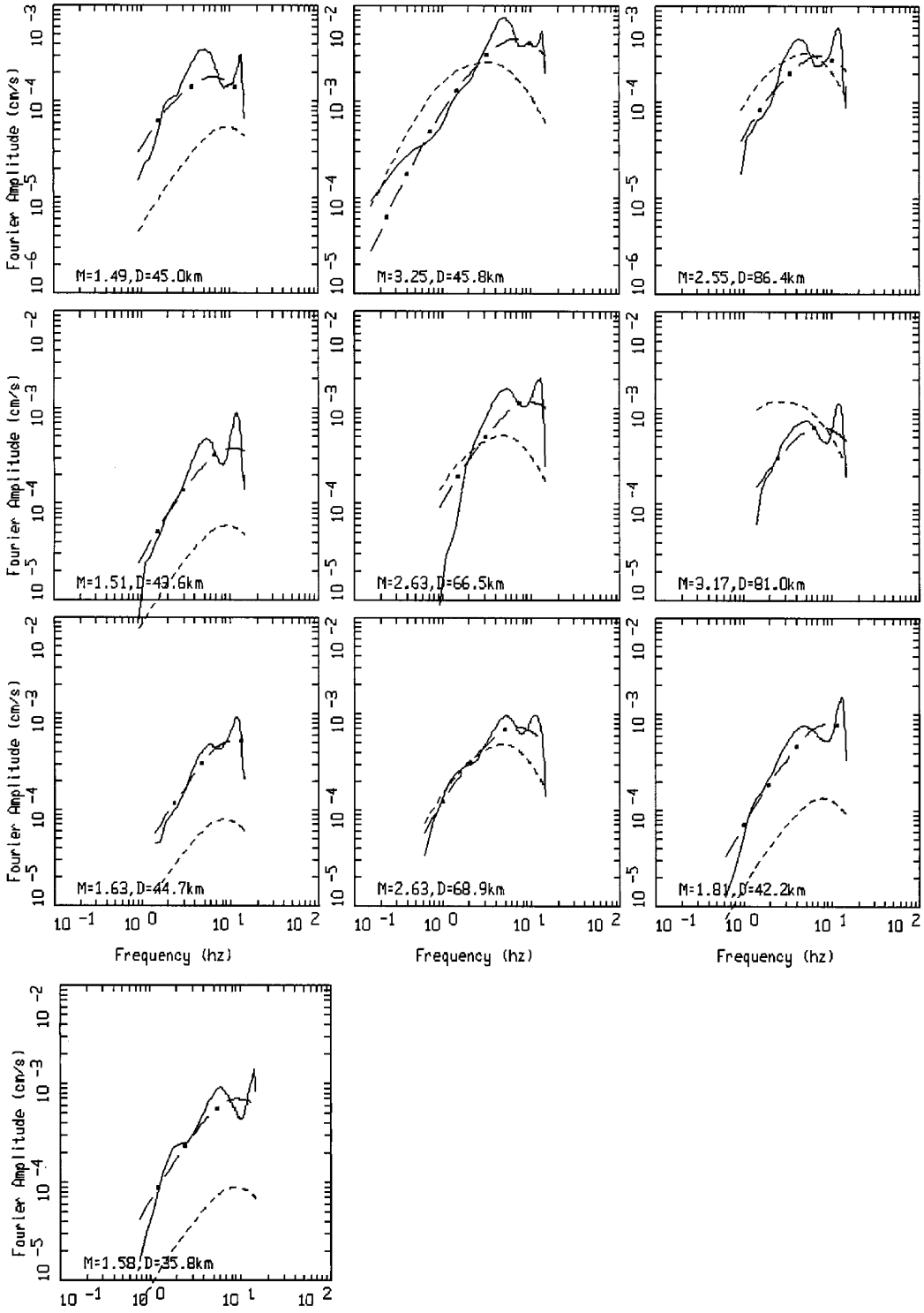

Figure 7.32. Comparison of inversions FAS (initial and final) to recordings FAS in Rohay and Riedel (2005). Recording spectra are shown as the solid lines and initial and final spectra are shown as dashed and dashed-dotted lines, respectively.

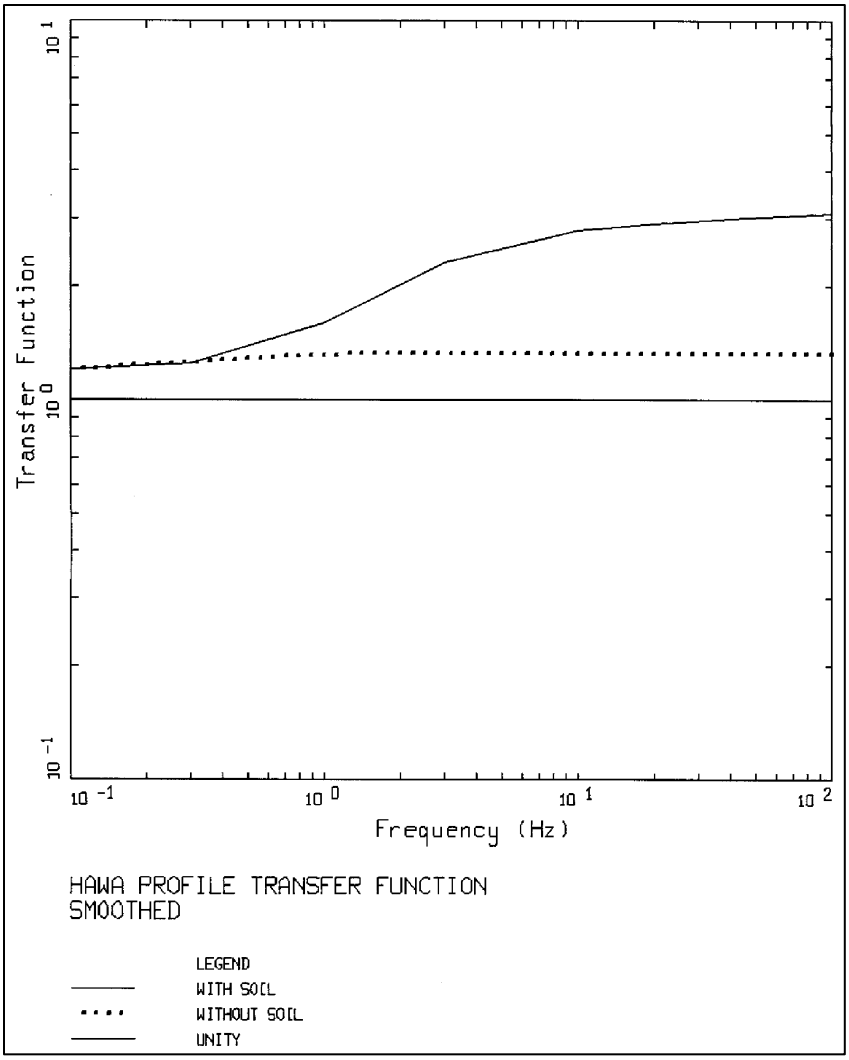

Figure 7.33. HAWA site amplification functions used in the 2004 kappa inversions.

7.3.4 New Estimates of Kappa for the Hanford Site

New estimates of κ_{site} on SMB and WBs were developed for the Hanford Site. These estimates are based on two approaches: the inversion process applied by Dr. Walt Silva and the Anderson and Hough (1984) approach applied by the TI Team. Analyzed data consist of subsets of windowed FAS provided by Dr. Alan Rohay.

The data set processed and compiled by Dr. Alan Rohay consists of windowed FAS of 59 earthquakes recorded in the 2005 to 2013 time frame at six sites within and around the Hanford Site. Table 7.13 summarizes the magnitude, distance, and hypocentral depth ranges of the processed recordings. The locations of the six recording sites are shown in Figure 7.34. Only the HAWA station is located within the Hanford Site; the E07A and E08A stations are located at relatively short distances to the west and east of the site, respectively. Stations F07A, D08A, and E09A are more remote at distances from 60 km to more than 100 km from the site.

Table 7.13. Summary of recordings compiled and processed by Dr. Alan Rohay. BB and Acc refer to recordings on the broadband velocity instrument and the accelerograph instrument, respectively.

Station Name	Number of Recordings	Magnitude Range	Epicentral Distance Range (km)	Hypocentral Depth Range (km)	Analogy for
D08A/WOLL	41	2.3–3.8	47–175	0–18	WB
E07A/CCRK	53	2–3.8	26–137	0–22	SMB
E08A/DDRF	56	2–3.8	11–165	0–22	SMB
E09A TUCA	47	2–3.8	54–221	0–22	WB
F07A/PHIN	44	2.3–3.8	42–154	0–22	SMB
HAWA	58 (BB)	2–3.8	11–148	0–22	SMB
	4 (Acc)	3.2–3.7	21–112	1–13	SMB

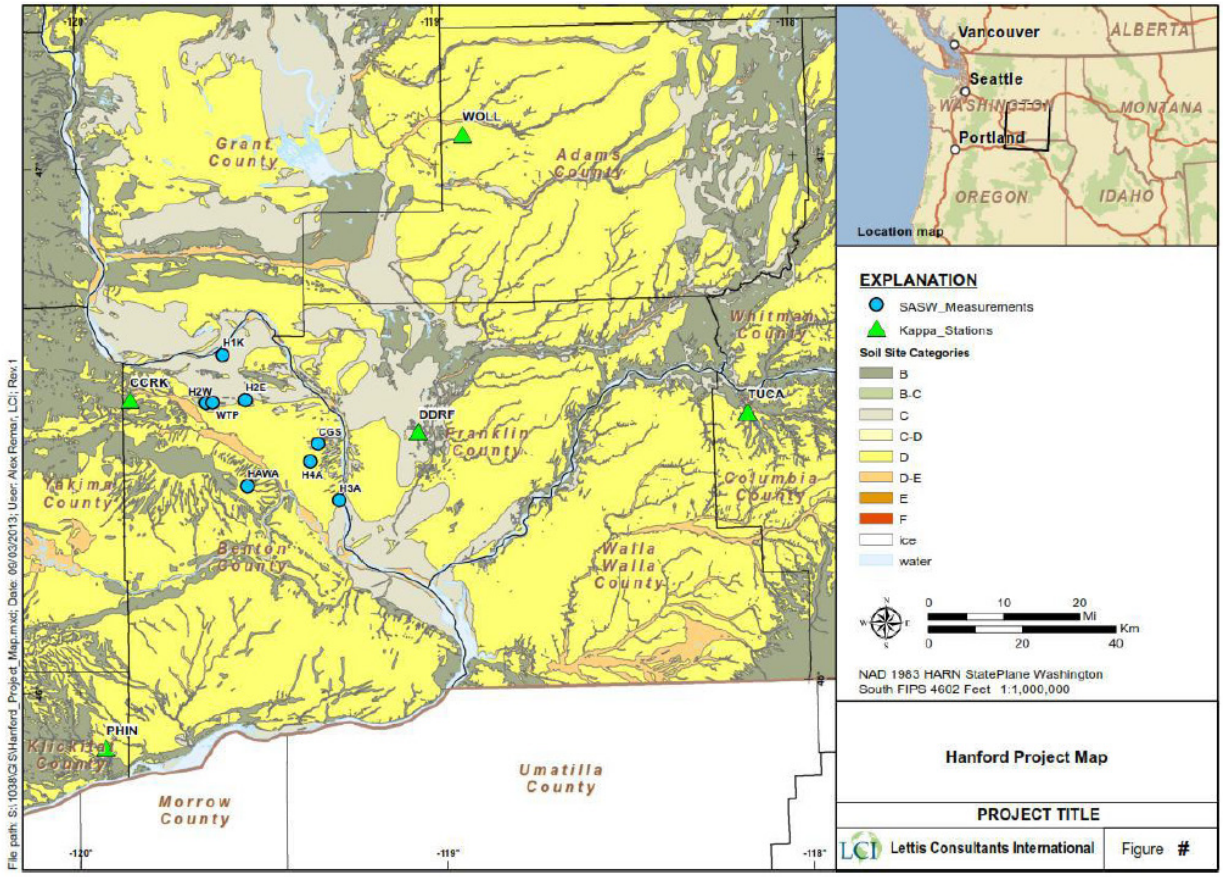

Figure 7.34. Location of broadband stations (green triangles) superimposed on the state-wide map of soil classes developed by the Washington Department of Natural Resources.

The stations were selected because they are located on basalts covered by at most a few meters of sediments, and may be considered analogs for the buried basalt horizons at the locations within the Hanford Site for which the ground motion model is being developed. Two of the stations—D08A and E09A—are analogs for the deeper WB, and the E09A station is actually located on the lower Grande

Ronde (GR) basalts. The other four stations are located on top of SMB. With the exception of four recordings at HAWA, which were recorded on both broadband velocity and accelerograph instruments, all the stations have only broadband velocity instruments (US Array or Transportable Array) with a sampling rate of 40 samples/sec and a high-frequency limit of 18 Hz, which corresponds to the corner frequency of the filter used. The accelerograph recordings have a sampling rate of 200 samples/sec and a high-frequency limit of 80 Hz.

7.3.4.1 Kappa Estimates from the Inversion Approach

Dr. Walt Silva applied the inversion approach to estimate κ_{site} at the six recording stations (HAWA, D08A, E07A, E08A, E09A, and F07A). The data set analyzed is summarized in Table 7.14 and consisted of 15 earthquakes recorded at the 6 stations in the 2005–2013 time frame in addition to the 10 recordings at HAWA from the 2004 study (Rohay and Riedel 2005). The final report provided by Dr. Silva describing the inversions analysis and the obtained results is included in Appendix I.

The 2005−2013 recordings were selected based on comparison of signal-to-noise levels while maximizing the number of stations with common recordings and only using deep earthquakes (with hypocentral depth greater than 5 km) to fully sample the supra-WB sediments and avoid double paths in the sediments from down-going paths at distance sites. The usable bandwidth for each FAS was site- and earthquake-specific, selected based on visual inspection of the pre-event FAS noise levels compared to the windowed shear-wave FAS with the maximum frequency never exceeding the estimated highest usable frequencies constrained by the filters (15 Hz for the 2004 data set, 18 Hz for the velocity instrument recordings for the 2005−2013 data set, and 80 Hz for the accelerograms). The 2004 HAWA data set suffered from problems with the response function and failure of one horizontal component. A new seismometer was installed at HAWA in 2005 and the subsequently recorded data had better quality; hence the different estimated highest usable frequencies at HAWA.

Table 7.14. Summary of recordings analyzed to provide new kappa estimates for the Hanford Site using the inversion approach.

Station Name	Number of Recordings	Magnitude Range	Hypocentral Distance Range (km)	Hypocentral Depth Range (km)	Analogy for
HAWA04[(a)]	10	1.49–3.25	36– 86	8.7–22.1	SMB
HAWA05-13[(b)]	15	2.4–3.4	32–149	5.7–21.9	SMB
E07A	10	2.4–3.4	39–138	6.4–21.9	SMB
E08A	12	2.4–3.4	25–140	6.4–21.9	SMB
F07A	9	2.4–3.4	46–118	6.4–21.9	SMB
D08A	8	2.4–3.4	48–152	6.4–18.0	WB
E09A	10	2.4–3.4	56–170	9.2–21.9	WB

(a) Recordings at HAWA analyzed in 2004 (Rohay and Riedel 2005).
(b) Earthquakes recorded at HAWA in the 2005-2013 time frame.

A feature of the inversion scheme that was used in this study is the flexibility to group stations for which kappa is determined. This feature allowed separate grouping of the SMB and WB analog stations as well as separating the recordings from the 2004 analysis to evaluate the differences between the 2004 kappa results at HAWA (HAWA04) and those of the more recent recordings (HAWA05-13). Similar to the 2004 analysis, Q(f) was fixed at $500(f)^{0.6}$ and not determined from the inversions due the frequency bandwidth limitations as well as the limited number of recordings with distance exceeding 100 km, which would lead to strong coupling between, Q_0, kappa, and R_c (cutoff distance from 1/R to $1/\sqrt{R}$ geometrical attenuation). This assumed Q(f) exceeds the estimated $Q(f) = 300(f)^{0.4}$ from Phillips et al. (2014) for the Hanford region. Dr. Silva explains that the larger assumed Q(f) in the inversions compensates for the presumed exclusion of kappa in the Phillips et al. (2014) study. The TI Team, however, is of the view that Phillips et al. (2014) did account for kappa in their study through the inclusion of a site term which accounts for both amplification and kappa effects. R_c was fixed at 80 km and inversions were done for $\Delta\sigma$ (f_c), magnitude, and kappa. Starting values for $\Delta\sigma$ and kappa were set at 5 bars and 0.04 sec, respectively.

The V_S and density profiles at the sites of the six recording stations were developed by the TI Team and provided to Dr. Silva. To construct the stratigraphic profiles, the depths from the surface to the different stratigraphic units were supplied by George Last at PNNL with input and support from Paul Thorne and Alan Rohay. The depths of deeper layers (below the top of WB) were extracted from the 3-D model constructed by Paul Thorne for use by Art Frankel in his ground motion simulations for the Hanford Site. The depth to basement was based on Glover (1985), as discussed in Section 7.2. The velocity profiles in the suprabasalt sediments were taken from the recent SASW measurements at the locations shown in Figure 7.34 and from earlier work at WTP. V_S values in deeper units were assigned according to Table 7.9.

Three crustal amplification functions from a source at a depth around 10 km to the surface were evaluated as part of the inversions process and are shown in Figure 7.35. The crustal models consist of 1) an average regional model with a shear-wave velocity of 2,080 m/sec and 3,430 m/sec at the surface and at 10-km depth, respectively, 2) smoothed site amplification of the velocity profile at HAWA from the crystalline basement with a shear-wave velocity of 3,500 m/sec to the surface concrete floor of the Nike bunker with a shear-wave velocity of 1,500 m/sec, and 3) smoothed site amplification of the velocity profile at D08A (WB site). The average regional model was provided to Dr. Silva by Alan Rohay through personal communication while the HAWA and D08A V_S and density profiles were provided the TI Team. Crustal amplification functions for HAWA and D08A shown in Figure 7.35 were computed and smoothed by Dr. Silva.

Three cases were investigated with the inversions listed in Table 7.15. Case 1 consisted of estimating eight kappa values with the corner frequencies for the 2004 data set being free and the Hanford crustal amplification function applied to all sites. Low kappa values were estimated at SMB analogs E08A and HAWA04 and WB analogs D08A and E09A. This set of inversions also resulted in inconsistent kappa values at HAWA between the 2004 data set and the 2005−2013 data set. The discrepancy in kappa values at HAWA was presumed to be due to the existence of two possible solutions for the inversions. While the best solution (minimum chi-square) resulted in corner frequencies for the 2004 data below 15 Hz and very low stress drops (<1 bar), another solution exists with corner frequencies exceeding 15 Hz and is not resolvable with the 15 Hz high-frequency limit.

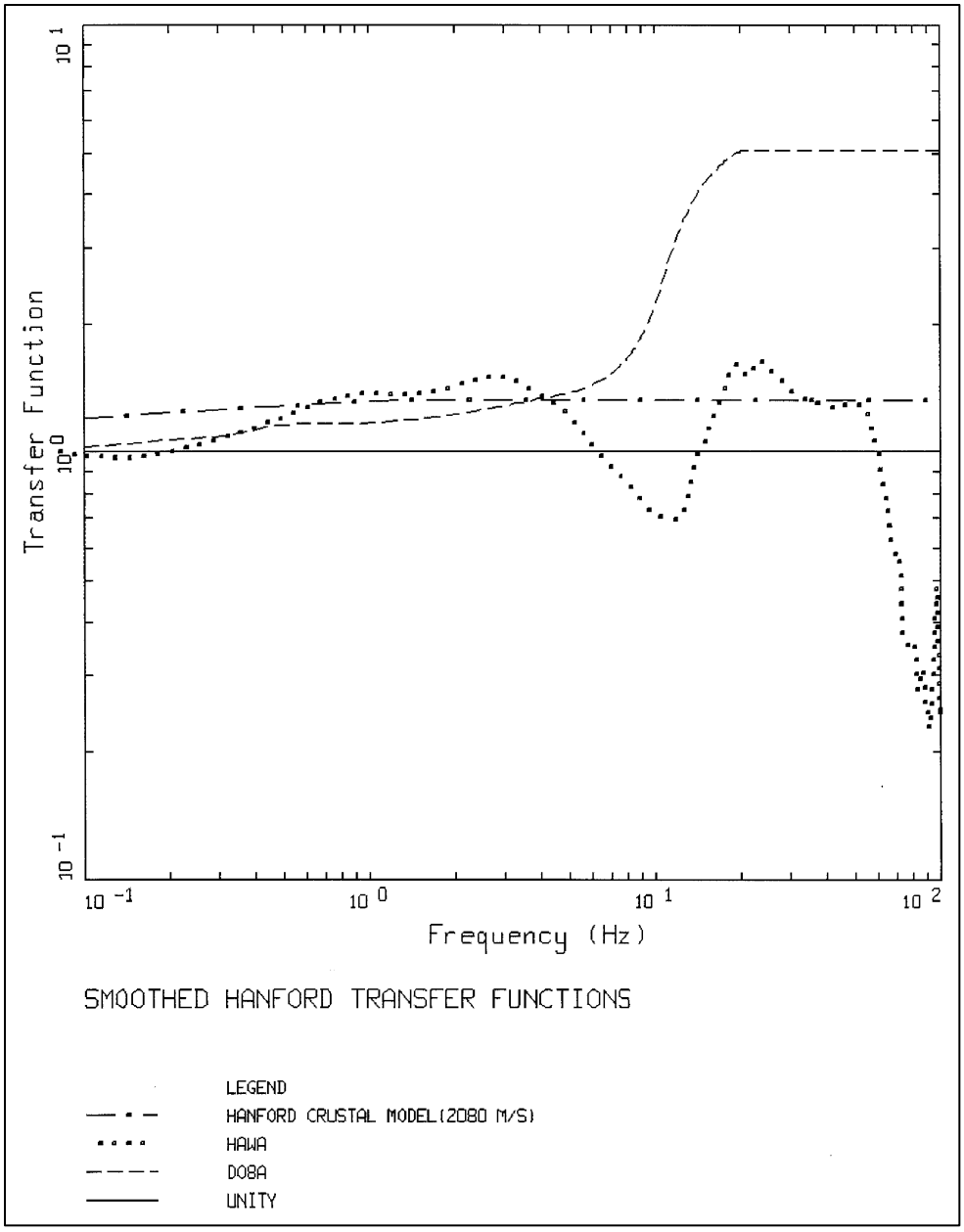

Figure 7.35. Hanford Site amplification functions used in the new kappa inversions analysis.

Table 7.15. Kappa estimates from inversions for the 2004 and the 2005−2013 data sets.

		Kappa (sec)		
	Station	Case 1	Case 2	Case 3
1	HAWA05-13	0.061	0.061	0.064
2	E07A	0.068	0.068	0.072
3	E08A	0.010	0.010	0.034
4	F07A	0.056	0.056	0.061
5	HAWA04	0.022	0.058	0.058
6	D08A	0.015	0.015	0.039

Table 7.15. (contd)

		Kappa (sec)		
	Station	Case 1	Case 2	Case 3
7	E09A	0	0	0.016
8	HAWA BB	0.056	0.056	0.058

Case 1: Hanford crustal amplification at all sites.
Case 2: Hanford crustal amplification at all sites, 2004 earthquakes, **M** < 2, f_c fixed > 15 Hz.
Case 3: WANAPUM (D08A) crustal amplification at E08A, D08A, E09A; HAWA amplification at remaining sites, 2004 earthquakes, **M** < 2, f_c fixed > 15 Hz.
HAWA05-13: HAWA recordings from the 2005-2013 period.
HAWA04: HAWA recordings from the 2004 study.
HAWA BB: Two HAWA accelerograph recordings from the 05-13 earthquake suite.

The discrepancy in kappa estimates at HAWA prompted re-evaluation of the highest usable frequency for the 2004 data. Dr. Alan Rohay advised that a maximum usable frequency for the 2004 can be extended to 16 Hz (Dr. Alan Rohay, personal communication). As a result of the high-frequency limit extension, the inconsistency in the kappa estimates at HAWA was resolved in Case 2 by fixing the corner frequencies to be greater than 15 Hz for the 2004 earthquakes with magnitude less than 2. Kappa increased for HAWA04 from 0.022 sec to 0.058 sec, now generally consistent with HAWA05-13 and HAWABB results. In addition, the stability of the remaining kappa estimates between Cases 1 and 2 suggested little coupling between sites in the inversions. It is important to note that the 2004 HAWA dataset was not used in this study to provide a kappa estimate at HAWA but simply as a consistency check with kappa estimated using the more recent dataset.

As shown in the Estimation of Kappa report (Appendix I, Figure 6), the SMB site E08A shows high-frequency characteristics that are more similar to the WB sites D08A and E09A (Appendix I, Figures 8 and 9) than to the remaining SMB sites HAWA (Appendix I, Figures 2, 3, and 4), E07A (Appendix I, Figures 5), and F07A (Appendix I, Figure 7). Therefore, for Case 3, the crustal amplification function for WB profile D08A was applied to the WB sites (D08A and E09A) as well as the SMB site E08A resulting in an increase in kappa estimates for these three sites as shown in Table 7.15. Differences in kappa between the SMB and the WB sites are apparent in Table 7.15. Kappa estimates at the sites of the recording stations obtained from Case 3 inversions were adopted by the TI Team because they show consistency in the kappa estimates at HAWA between the 2004 and the 2005-2013 recordings and because they use WB-specific crustal amplification for the WB sites (D08A and E09A) and E08A and SMB-specific crustal amplification for the rest of the SMB sites.

Figure 7.36 through Figure 7.38 show sample comparisons of the model fits to the smoothed FAS for HAWA, F07A, and D08A sites for Case 3. The complete set of comparison plots for Case 3 at all sites can be found in Appendix I. A total of 14 out of the set of 25 earthquakes analyzed were judged to have corner frequencies with potentially meaningful stress drops. The median stress drop estimate was 19.7 bars (fitting on log FAS) with a σ_{ln} of about 0.4. As a result of the inversions, earthquake magnitudes changed from their catalog values by significant amounts (≈ 0.5 unit) in some cases. It is important to note that earthquake magnitudes obtained from the inversions have no implications for the reliability of the catalog values since those were compiled separately and uniformly as described in Chapter 6.0. These magnitude changes may have impacted the kappa estimates from the inversions and this was accommodated through the large uncertainty placed on kappa in the target kappa logic tree (Figure 7.61).

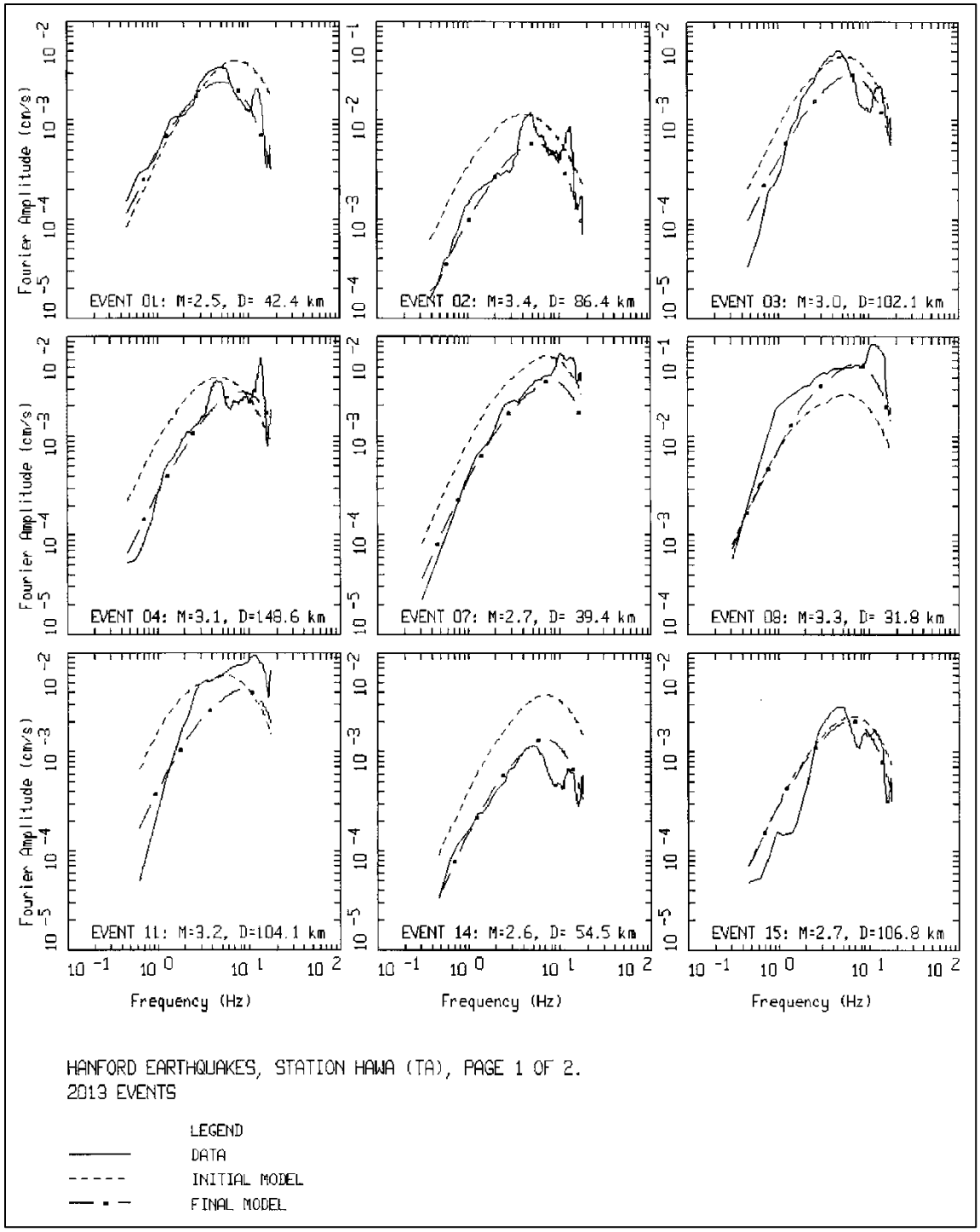

Figure 7.36. Comparison of inversions FAS (initial and final) and recording FAS at SMB site HAWA for the 15 earthquakes recorded at the Transportable Array (TA) array station in the 2005−2013 time frame.

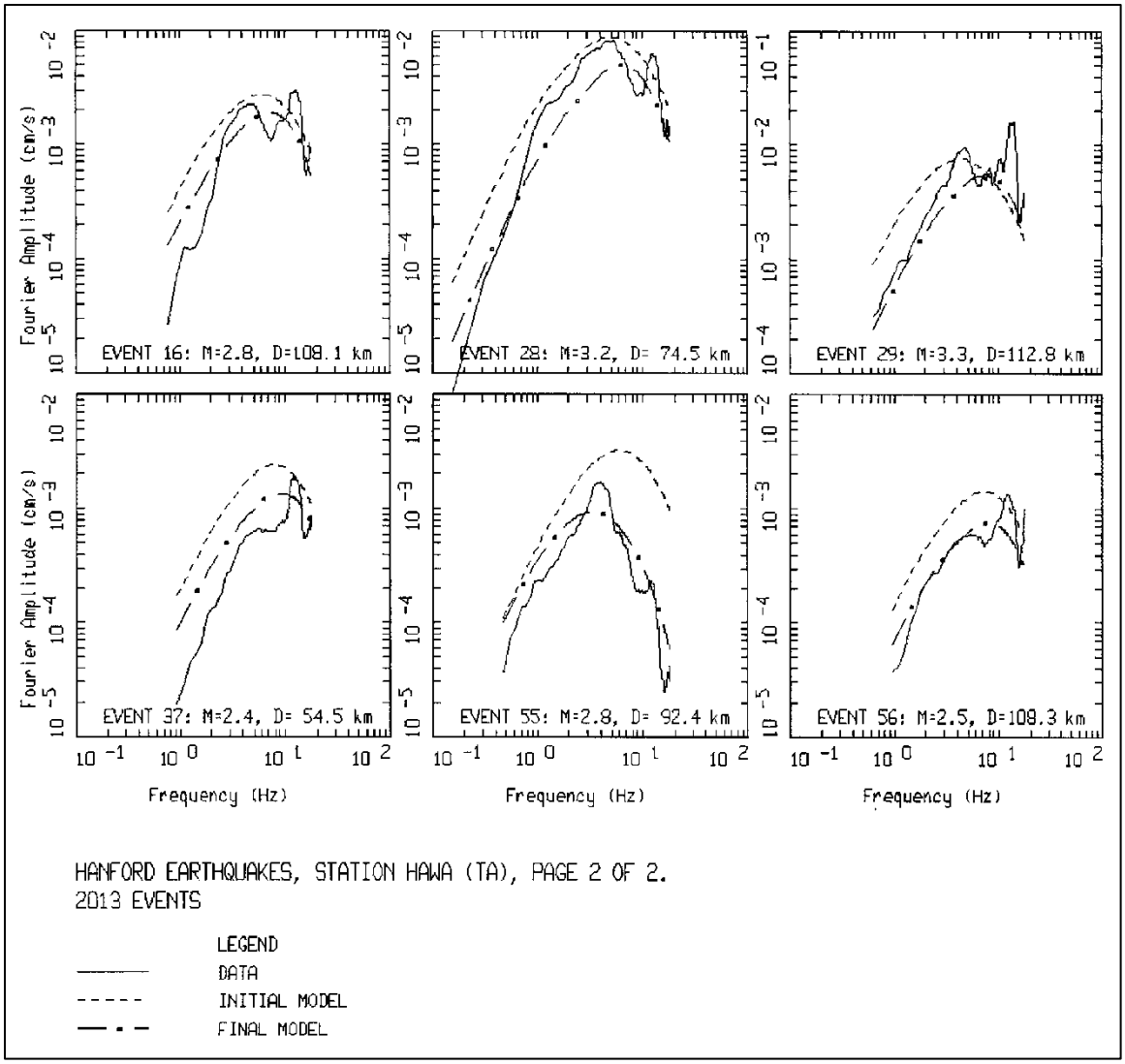

Figure 7.36. (contd)

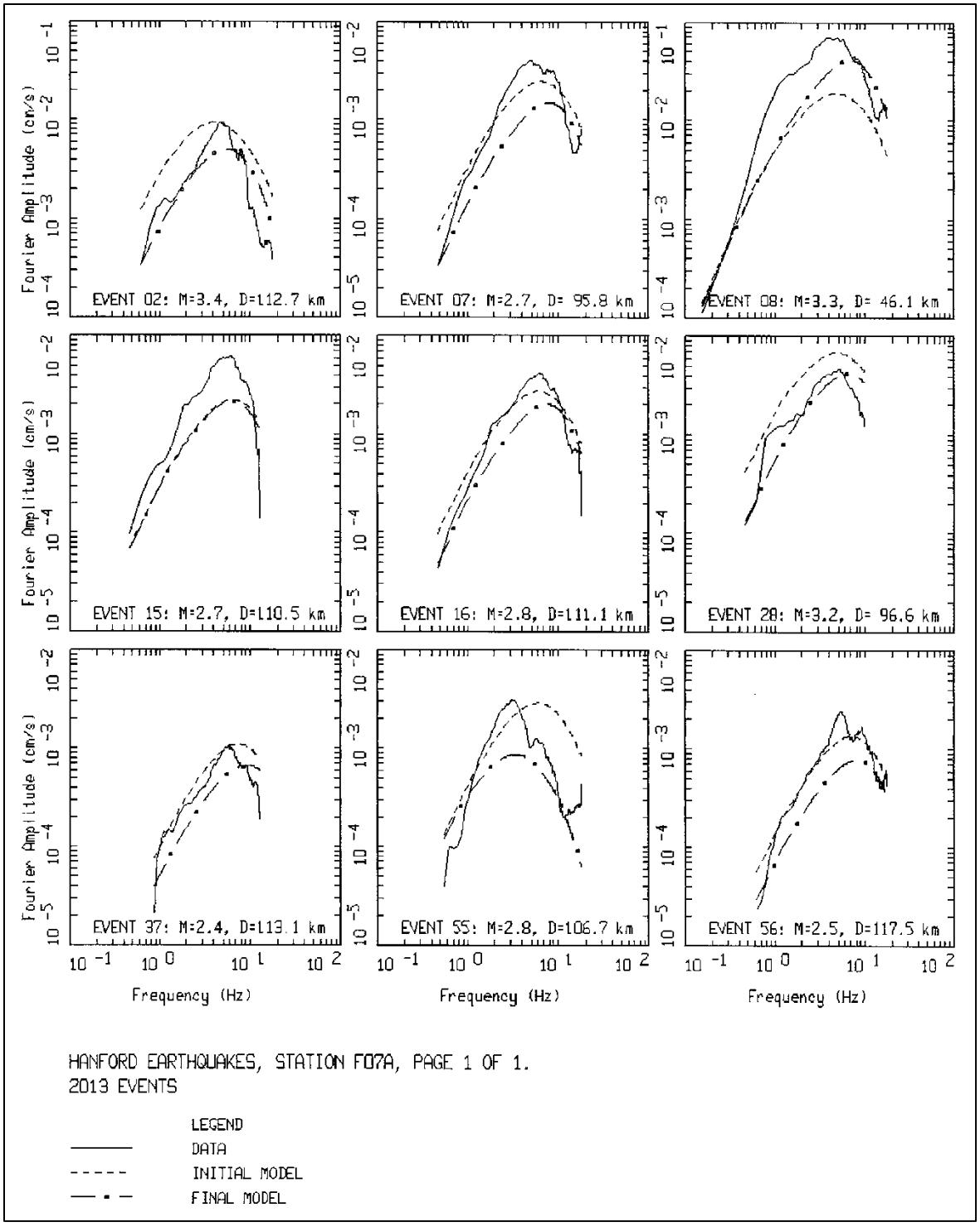

Figure 7.37. Comparison of inversions FAS (initial and final) and recording FAS at SMB site F07A.

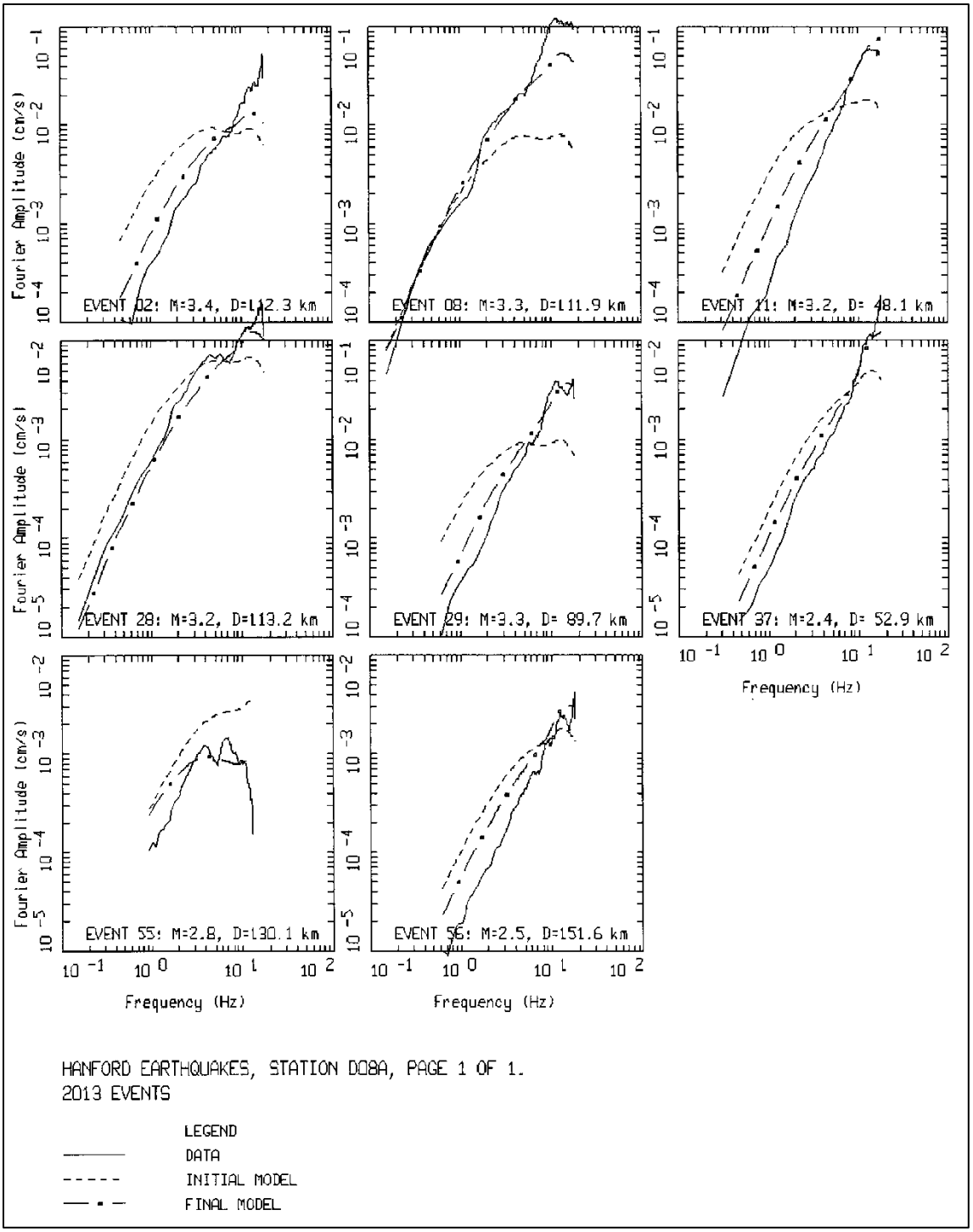

Figure 7.38. Comparison of inversions FAS (initial and final) and recording FAS at WB site D08A.

The TI Team evaluated the κ_{site} values from the inversions in relation to the stratigraphy at the sites of the recording stations. Figure 7.39 presents κ_{site} as a function of the thickness of different stratigraphic formations at the stations (suprabasalt sediments or top soil, CRBs, Ellensburg Formation interbeds, and sub-basalt sediments). A strong correlation can be observed between κ_{site} and the thicknesses of the CRBs and the sub-basalt sediments. Moreover, linear regressions of κ_{site} on the thicknesses of the different

stratigraphic formations revealed that most of κ_{site} can be explained by the thickness of sub-basalt sediments which range in depth from 1.9 to 5.2 km and in thickness from 0.7 to 6.5 km. Based on these observations, the TI Team concluded that for the deep earthquakes analyzed using the inversion approach, the entire depth of profile down to the crystalline basement contributed to the inferred κ_{site} at the stations. This conclusion contradicts the commonly accepted idea that damping in the top 1- to 2-km depth of profiles generally contributes to κ_{site} (Silva and Darragh 1995). While the 1- to 2-km profile depth assumption might be true for a typical profile with increasing shear-wave velocity with depth, it does not hold true for the unusual velocity profiles at the Hanford Site due to the velocity reversals and the presence of the deep sub-basalt sediments layer with lower V_S values. The relatively large κ_{site} values at the recording stations support the conclusion that the entire profile depth contributes to kappa. This concept of kappa being caused by damping contributions from deep sediments (i.e., 5 km or deeper) was also proposed in Campbell (2009).

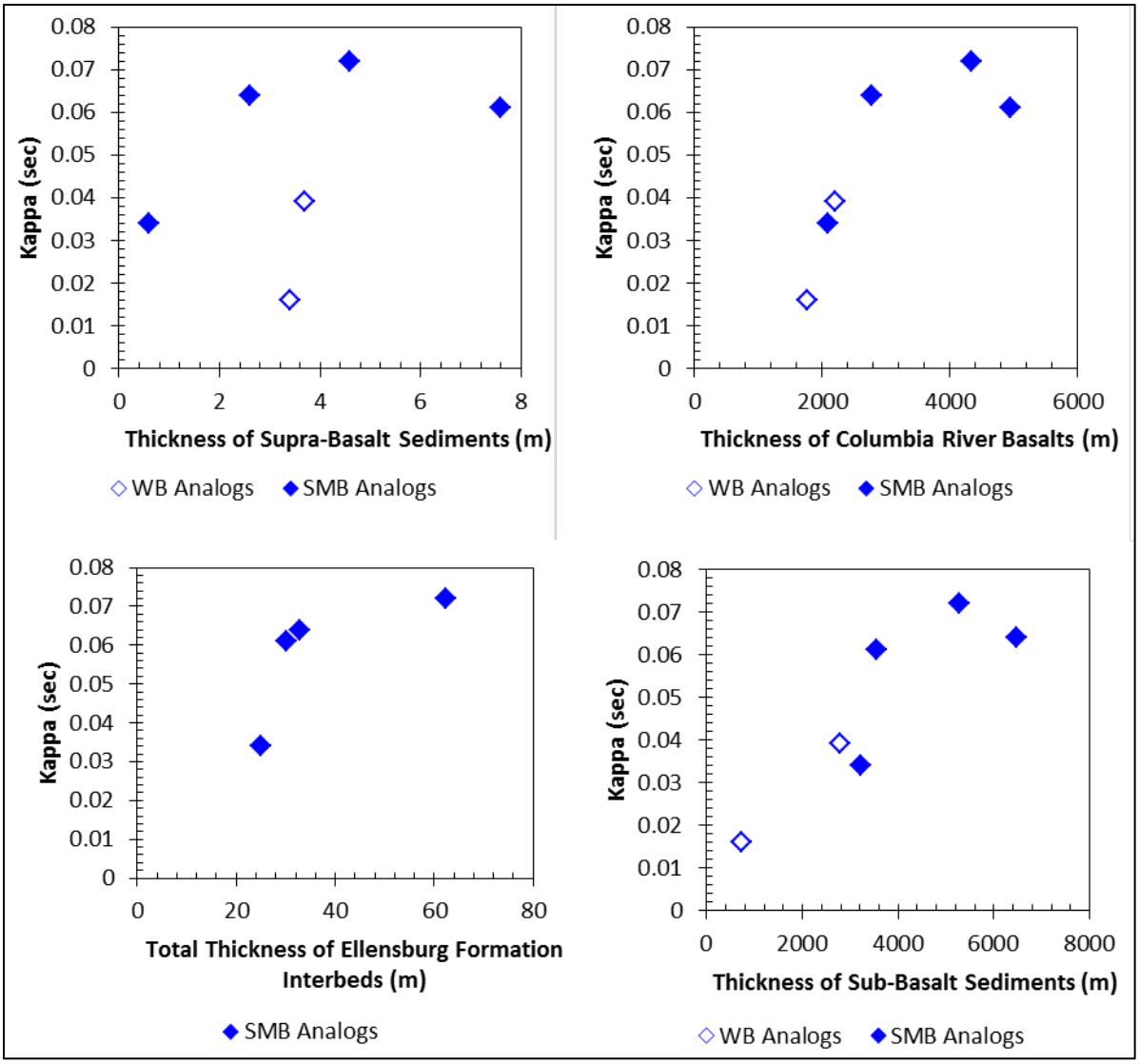

Figure 7.39. κ_{site} at the recording stations versus thickness of suprabasalt sediments, Columbia River basalts, Ellensburg Formation interbeds, and sub-basalt sediments.

Dr. Silva evaluated the epistemic uncertainty in the median kappa estimate for the eight sites by varying fixed parameters (Q_0, η, R_c, crustal amplifications) and assessing their impacts on the final kappa estimates. Table 7.16 shows the change in median kappa for a given change in each parameter as well as the starting models for $\Delta\sigma$ and kappa. Table 7.16 shows that the strongest coupling occurs between kappa and η with a reduction in median kappa by 50% when η is reduced by 40%. The kappa estimates should therefore be viewed as being strongly dependent on the assumed Q(f). Epistemic uncertainty in kappa due to analyzing different subsets of data was evaluated by considering the impact of using different subsets of data on the kappa estimates at HAWA. These results suggest a difference of 4−5% in kappa. The impact of smoothing the FAS on the resulting kappa estimates was also assessed and a difference in kappa values due to using smoothed versus unsmoothed FAS of about 2% was observed.

Based on the results of this sensitivity analysis, the TI Team adopted lower estimates of κ_{site} at the stations obtained by dividing Dr. Silva's best estimates by 1.4. Given that no parameter variation led to an increase in κ_{site} by 40%, the factor 1.4 was not applied symmetrically to obtain the upper estimates of κ_{site}. Instead, guided by the results in Table 7.16, the upper estimates were obtained by multiplying the best estimates of κ_{site} by 1.1.

Table 7.16. Impact of parameter variations in the inversions on the resulting kappa estimates.

Parameter Variations	Change in Median Kappa (sec)
Q_o/1.5	κ/1.1
Q_o * 1.5	κ * 1.1
η/1.5	κ/1.4
η * 1.5	κ * 1.1
R_C/1.5	κ * 1.01
R_C * 1.5	κ * 1.004
κ/2	κ * 1.09
κ * 2	κ * 1.004
$\Delta\sigma$ * 2	κ * 1.01
$\Delta\sigma$/2	κ/1.004
amp/1.3[(a)]	κ * 1.05

(a) Hanford crustal amplification was replaced with unity. Note relative difference for individual sites varied up to about 10%.

7.3.4.2 Kappa Estimates from the Anderson and Hough (1984) Approach

The TI Team applied the Anderson and Hough (1984) approach to estimate the κ_{site} of the locations of the six stations (HAWA, E07A, E08A, E09A, F07A, D08A) using a subset of the S-wave window FAS compiled and processed by Dr. Alan Rohay. Anderson and Hough (1984) modeled the observed high-frequency decay of FAS of ground motion recordings as follows:

$$a(f) = A_0 \exp(-\pi \kappa_{obs} f) \quad \text{for } f > f_E, \tag{7.11}$$

where f_E is the frequency above which the decay of $\ln(a(f))$ versus f is linear, A_0 is a source and propagation path dependent amplitude, and κ_{obs} is the observed spectral decay parameter controlling the rate of high-frequency amplitude decay. Using this formulation, κ_{obs} can be estimated for each ground motion recording as the high-frequency slope of ln(FAS) versus frequency where ln(FAS) versus frequency is linear. This formulation assumes that Q is frequency-independent.

The subset of recordings analyzed using this approach is summarized in Table 7.17 and consisted of 17 earthquakes with a magnitude range of 2.9 to 3.8 and epicentral distance range of 21 to 170 km. Table 7.18 shows the detailed catalog for the data set. The recordings were primarily chosen such that the high-frequency FAS of the S-wave windows show a linear trend in ln(FAS)-linear frequency space and their SNR is greater than or equal to 3. To maximize the high-frequency range used to estimate kappa and minimize the potential trade-off between kappa and corner frequency, earthquakes with magnitudes greater than or equal to 2.9 were favored. Recordings from earthquakes with smaller magnitudes were also considered for potential inclusion in the data set but were then discarded because of the absence of a clear high-frequency linear kappa slope. All the recordings in the data set were recorded on the broadband velocity instruments with the exception of the HAWA recordings, which were recorded on an accelerograph. Given the limited bandwidth of the velocity instruments recordings whereby the maximum usable frequency is 18 Hz, constraining the depth of the selected earthquakes to be greater than a few kilometers led to an insufficient usable data set for conducting the analysis. As a result, no constraints were imposed on the depth of the earthquakes in the data set with the hypocentral depth ranging from 0.3 to 18 km with a mean of 5.18 km. As shown in Table 7.17, no recordings were selected at D08A because none of the available ones displayed a linear high-frequency slope of ln(FAS) versus frequency in the limited usable frequency bandwidth. At HAWA, velocity instrument recordings were not used because of the high-frequency limitation; the accelerograph recordings were used instead.

Table 7.17. Summary of recordings analyzed using the Anderson and Hough (1984) approach to estimate kappa for the Hanford Site.

Station Name	Number of Recordings	Magnitude Range	Epicentral Distance Range (km)	Hypocentral Depth Range (km)	Analogy for
HAWA[(a)]	4	3.2–3.7	21–112	1.4–12.7	SMB
E07A	11	2.9–3.7	46–106	0.3–18	SMB
E08A	6	2.9–3.8	16–165	1–18	SMB
F07A	4	3.3–3.8	42–146	1–18	SMB
D08A	NA	NA	NA	NA	WB
E09A	7	3–3.7	67–170	0.4–18	WB

(a) HAWA accelerograph recordings.

The methodology consisted of inspecting the S-wave window FAS of the two horizontal components as well as their vector sum to visually pick the beginning and end frequencies (f1 and f2) of the high-frequency range over which the spectra are linear in log-linear space. Next, the S-wave and noise FAS of the recordings were smoothed using the Konno and Ohmachi (1998) filter before calculating the SNRs. The ends of the frequency range selected for estimating kappa for each recording were then adjusted to ensure a minimum SNR of 3. The vector sum of unsmoothed S-wave FAS of the two horizontal components were then fit with the Anderson and Hough (1984) exponential kappa function between frequencies f1 and f2 and the slope κ_{obs} of the fit was estimated. Figure 7.40 through Figure 7.44 show the high-frequency kappa fits to the FAS along with the estimated κ_{obs} values for the recordings. As shown in Figure 7.40 through Figure 7.44, the narrow frequency bandwidth of velocity instruments recordings severely limits the ability to estimate kappa.

Table 7.18. Catalog of sites and earthquakes used in the Anderson and Hough (1984) kappa analysis.

Station	Eq ID	Magnitude	Epicentral Distance (km)	Hypocentral Depth (km)	Year	Day	Hr	Min	Sec
F07A	2361118	3.4	111.83	13.6	2006	354	9	43	26.574
E07A	2738065	3.3	51.31	18	2008	139	22	19	54.7
E08A	2738065	3.3	51.81	18	2008	139	22	19	54.7
E09A	2738065	3.3	113.59	18	2008	139	22	19	54.7
F07A	2738065	3.3	42.46	18	2008	139	22	19	54.7
E07A	2787820	2.9	106.50	1	2008	197	11	19	51.25
E08A	2787820	2.9	164.58	1	2008	197	11	19	51.25
E09A	2847415	3.2	131.63	9.2	2010	84	22	31	7.149
E08A	2847579	3.8	155.46	4.2	2010	88	21	27	12.125
F07A	2847579	3.8	145.90	4.2	2010	88	21	27	12.125
E08A	2850129	2.9	61.34	3	2010	128	11	57	43
E07A	2869044	3	47.47	0.4	2009	124	10	47	42.599
E09A	2869044	3	87.32	0.4	2009	124	10	47	42.599
F07A	2874166	3.8	68.33	0.9	2010	168	14	23	24
E07A	3289031	3.3	48.97	2.6	2011	121	4	13	55.45
E09A	3289031	3.3	86.24	2.6	2011	121	4	13	55.45
HAWA	3321550	3.7	20.82	2.6	2011	247	4	13	39.525
E07A	3321550	3.7	48.38	2.6	2011	247	4	13	39.525
E09A	3321550	3.7	86.63	2.6	2011	247	4	13	39.525
HAWA	3323862	3.4	22.97	1.4	2011	288	6	11	29.1
E07A	3323862	3.4	46.32	1.4	2011	288	6	11	29.1
E08A	3323862	3.4	15.60	1.4	2011	288	6	11	29.1
HAWA	3339289	3.2	73.72	11	2012	101	4	43	35.3
E09A	3339289	3.2	67.18	11	2012	101	4	43	35.3
HAWA	3532931	3.3	112.07	12.7	2012	257	17	33	45.3
E07A	3532931	3.3	88.27	12.7	2012	257	17	33	45.3
E08A	3532931	3.3	119.57	12.7	2012	257	17	33	45.3
E09A	3532931	3.3	169.65	12.7	2012	257	17	33	45.3
E07A	3631437	2.9	47.70	1	2009	67	9	29	4.275
E07A	3639121	2.9	47.90	1	2009	77	6	39	31.874
E07A	3694554	2.9	46.70	0.3	2009	133	7	45	13.099

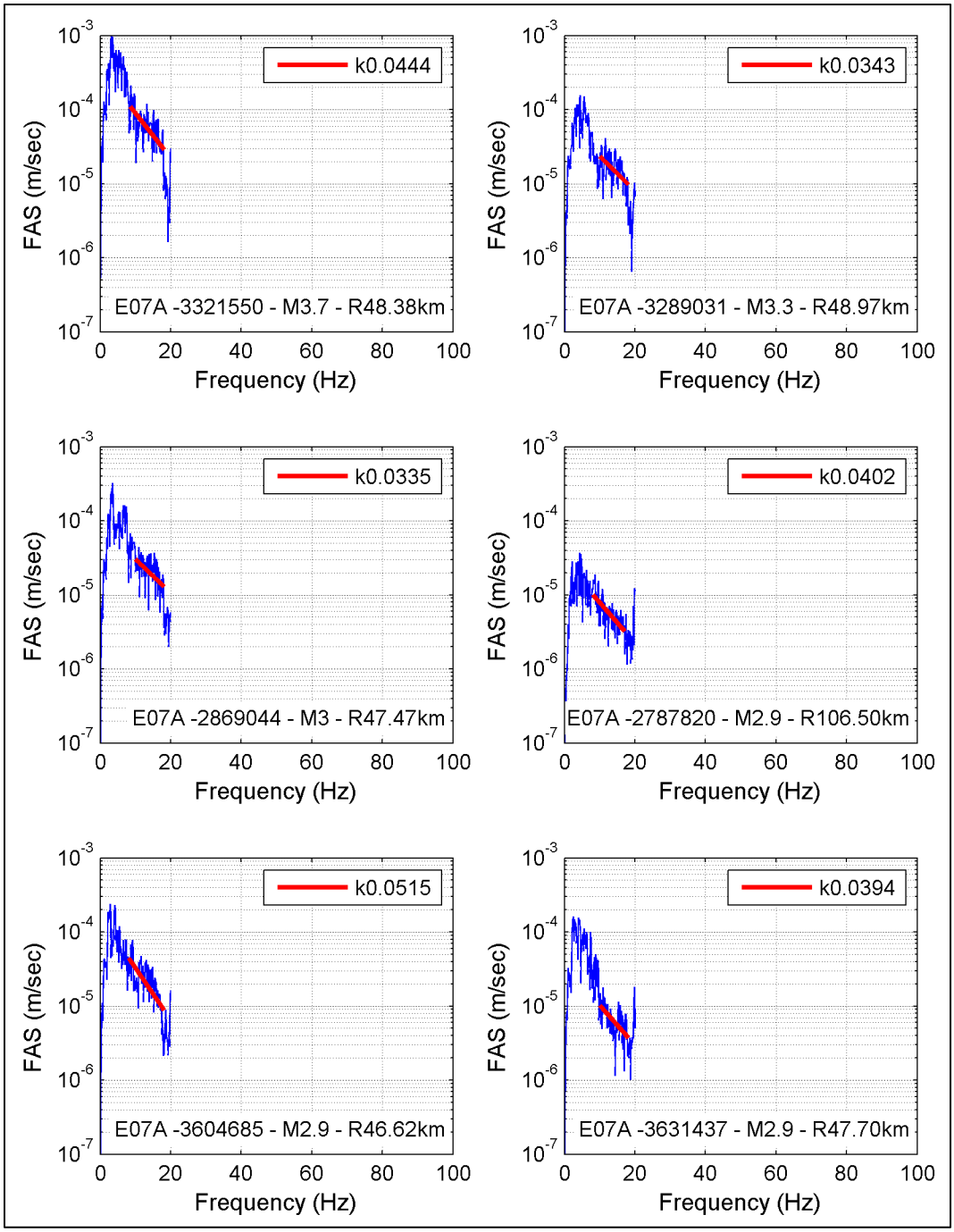

Figure 7.40. Anderson and Hough (1984) kappa fits to the FAS of recordings at SMB site E07A.

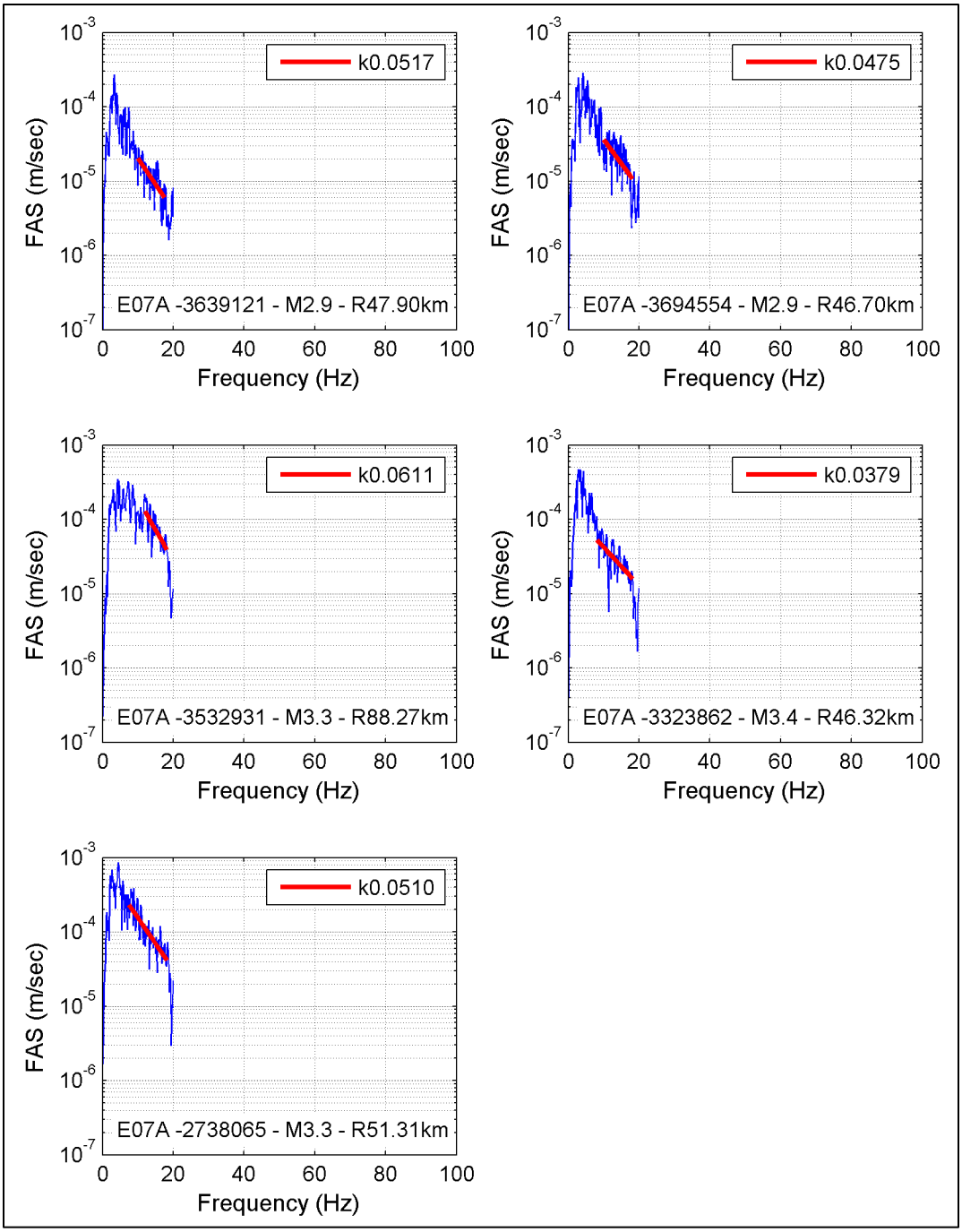

Figure 7.40. (contd)

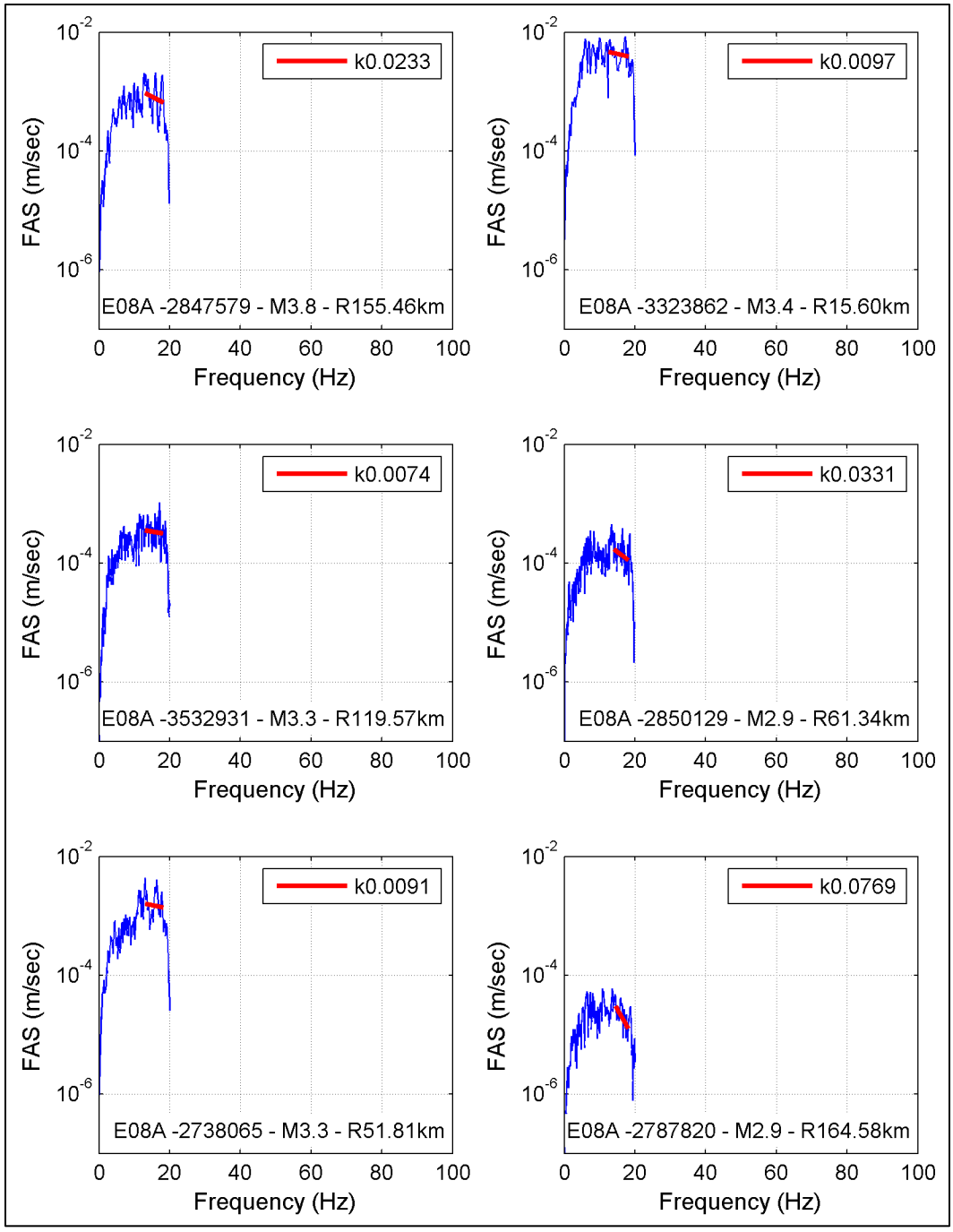

Figure 7.41. Anderson and Hough (1984) kappa fits to the FAS of recordings at SMB station E08A.

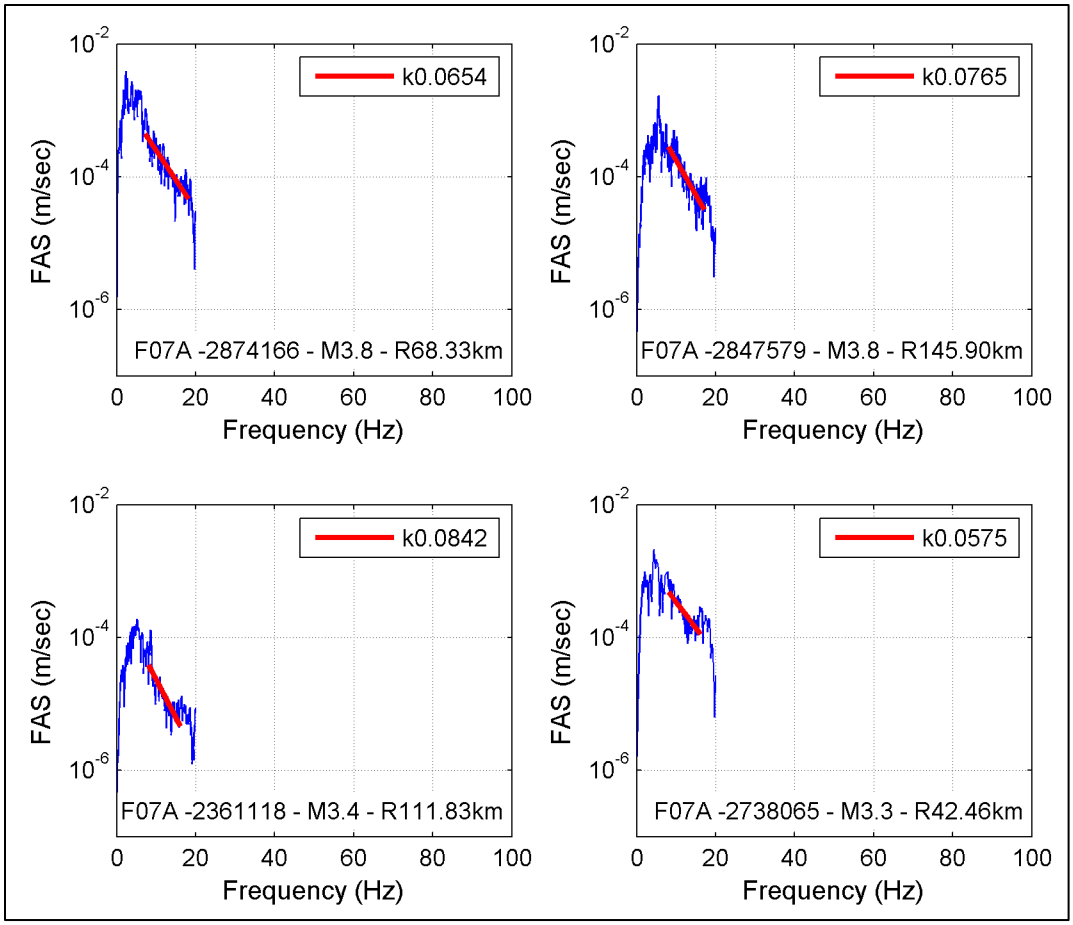

Figure 7.42. Anderson and Hough (1984) kappa fits to the FAS of recordings at SMB site F07A.

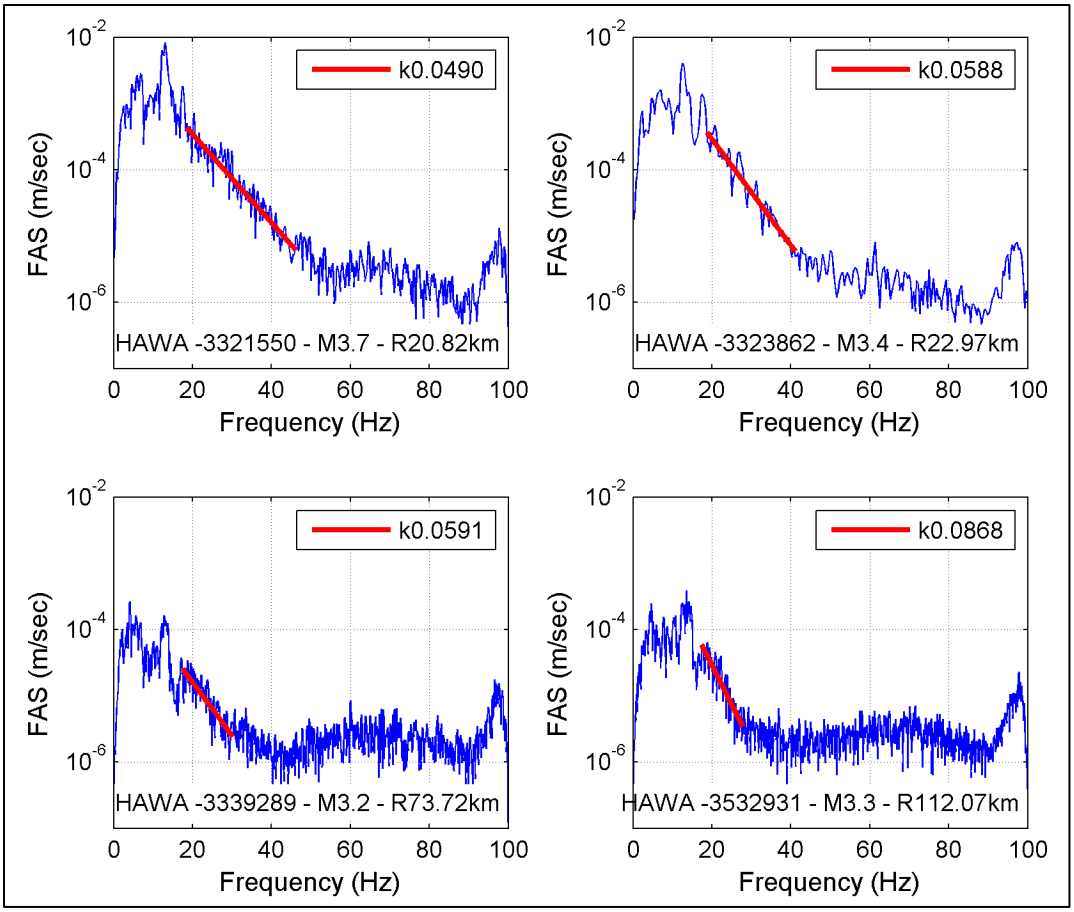

Figure 7.43. Anderson and Hough (1984) kappa fits to the FAS of recordings at SMB site HAWA.

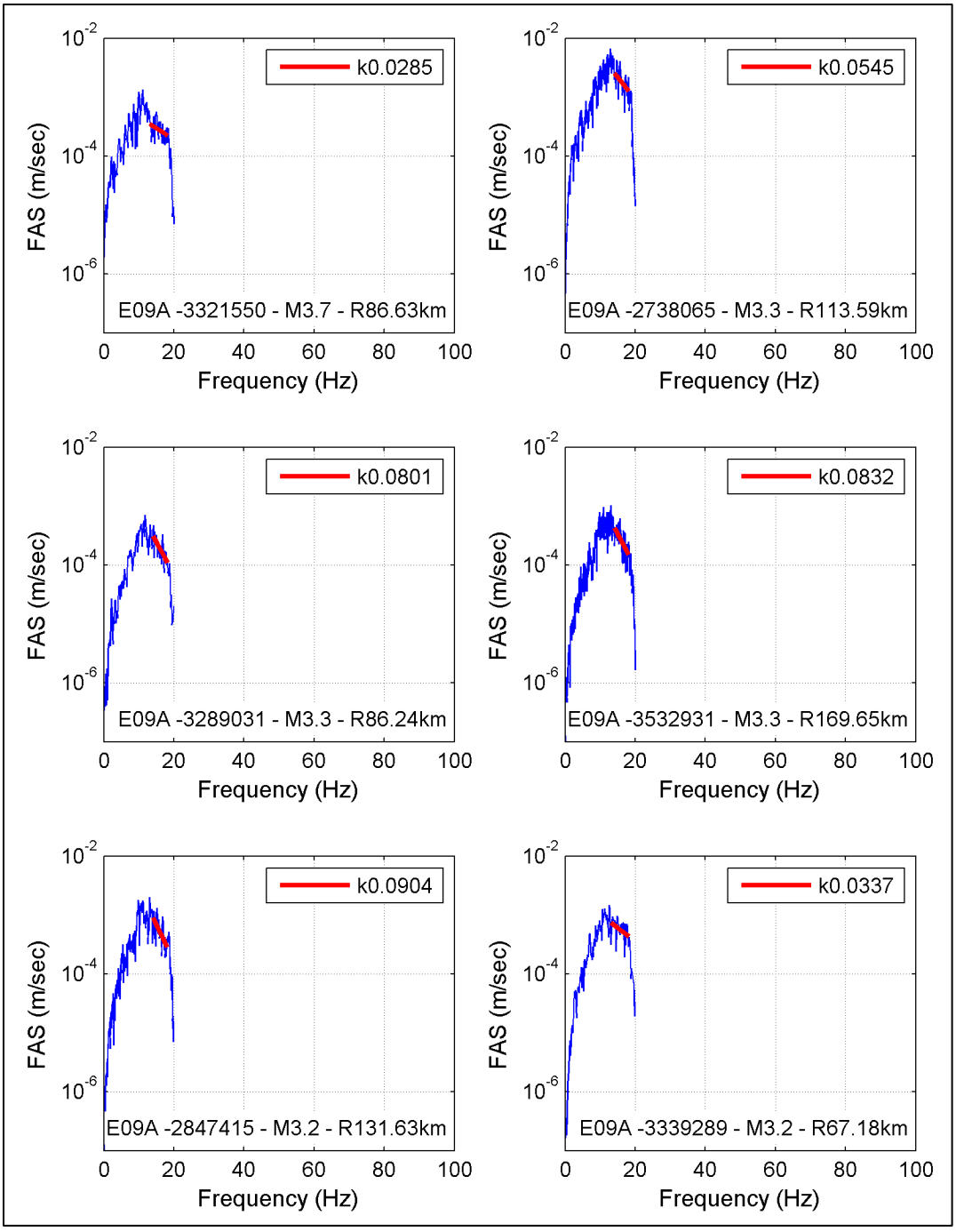

Figure 7.44. Anderson and Hough (1984) kappa fits to the FAS of recordings at WB site E09A.

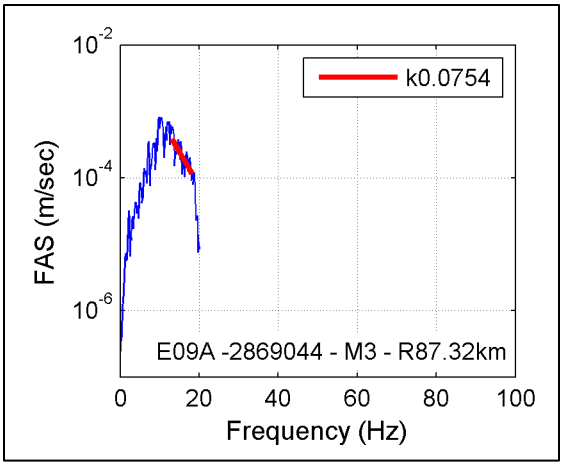

Figure 7.44. (contd)

Estimated κ_{obs} values for the recordings at each station were plotted versus epicentral distance and fitted with a linear function. The intercept of the kappa trend with distance corresponds to the zero-distance kappa, $\kappa(0)$, which approximates κ_{site} at each station location and represents the attenuation due to the vertical propagation of shear waves through subsurface materials below the site. The slope of the linear trend with distance (m) can be used to infer the average regional frequency-independent anelastic attenuation between frequencies f1 and f2 according to the relationship $Q_{ave} \approx 1/(m\beta)$ where $\beta = 3.5$ km/sec. Figure 7.45 through Figure 7.49 show the kappa trends versus distance at the sites of the five stations (HAWA, E07A, E08A, F07A, and E09A). Figure 7.45 through Figure 7.49 show the relatively limited number of recordings available at each station for estimating κ_{site} using the Anderson and Hough (1984) approach and the resulting scatter around the linear fit. Table 7.19 summarizes the estimated κ_{site} at the station locations, Q_{ave} inferred from the linear kappa versus distance fits, and estimated Q_{ave} using $Q(f) = 500(f)^{0.6}$ (Q model used in Dr. Silva's inversions) and $Q(f) = 300(f)^{0.4}$ (Phillips et al. 2014) at an average frequency in the center of f1 to f2 for each station. Table 7.19 shows that κ_{site} at the WB site (E09A) is smaller than the κ_{site} estimates at the SMB sites with the exception of the E08A site, which shows a very small κ_{site}. Q_{ave} values inferred from the Anderson and Hough (1984) approach were inconsistent among the different sites, which is a drawback of the method but they were generally smaller than Q_{ave} estimated using $Q(f) = 500(f)^{0.6}$ assumed in Dr. Silva's inversions.

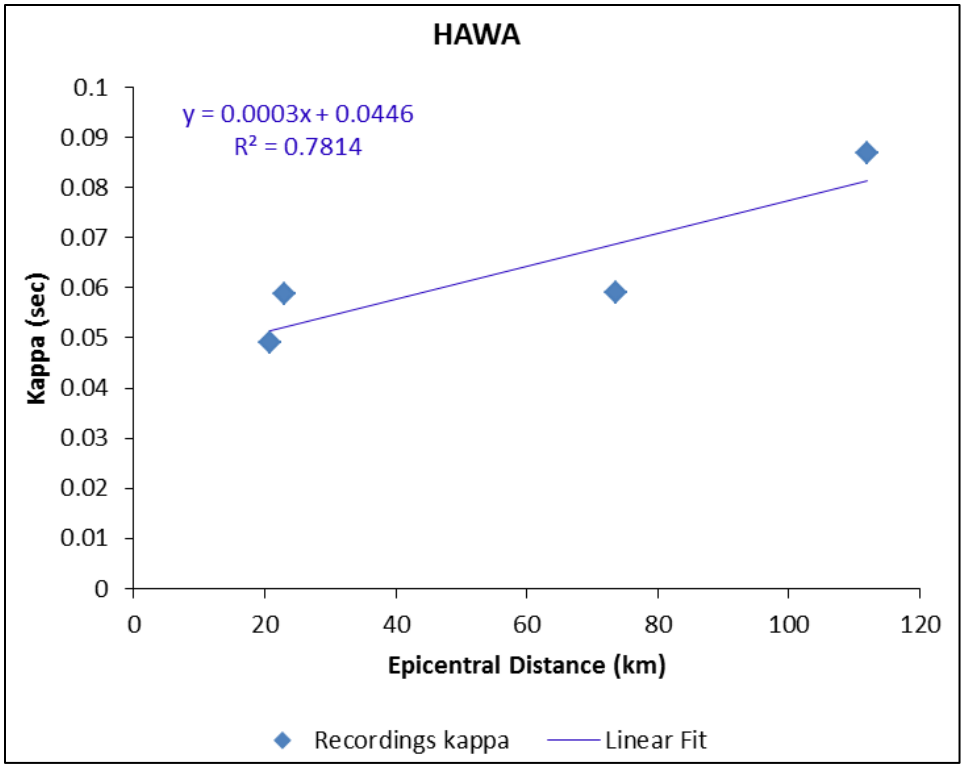

Figure 7.45. Kappa versus distance at SMB site HAWA.

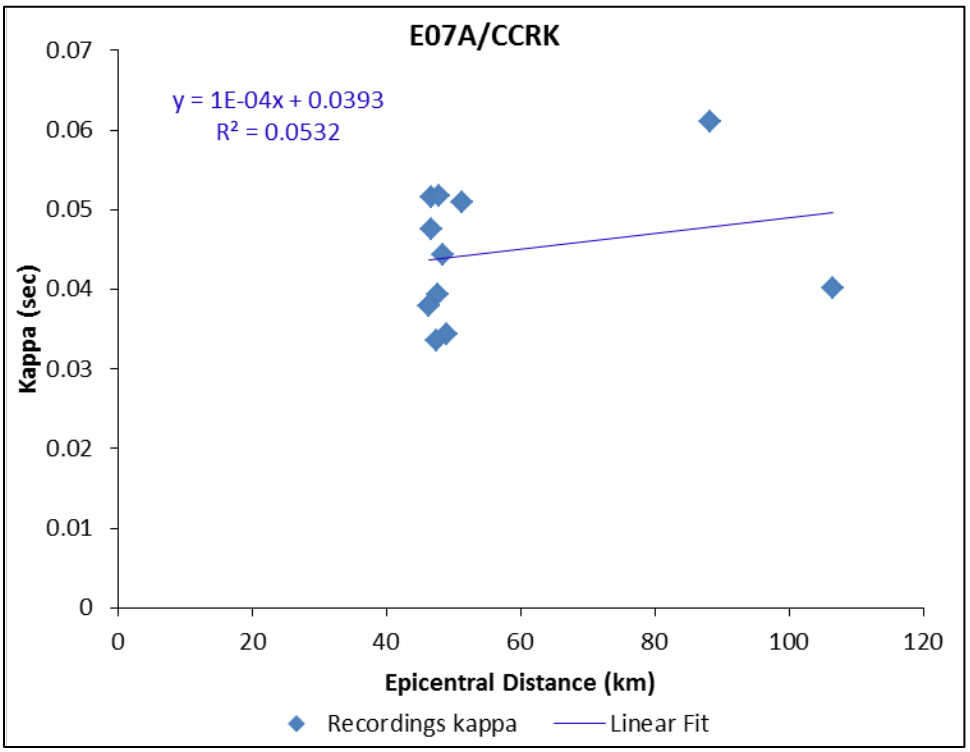

Figure 7.46. Kappa versus distance at SMB site E07A.

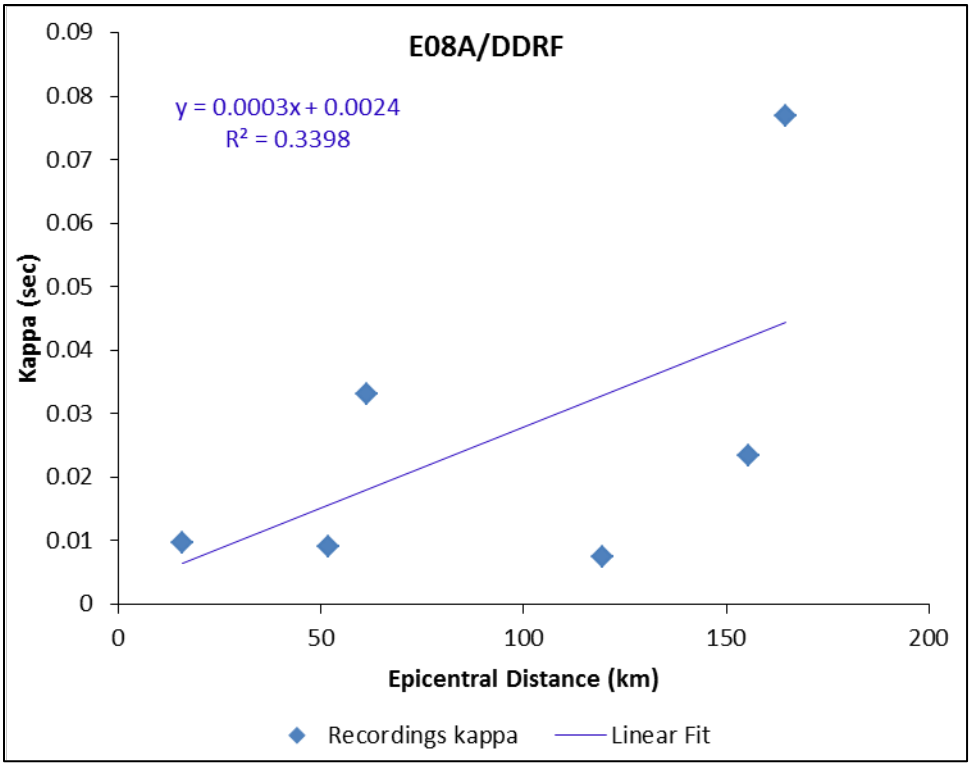

Figure 7.47. Kappa versus distance at SMB site E08A.

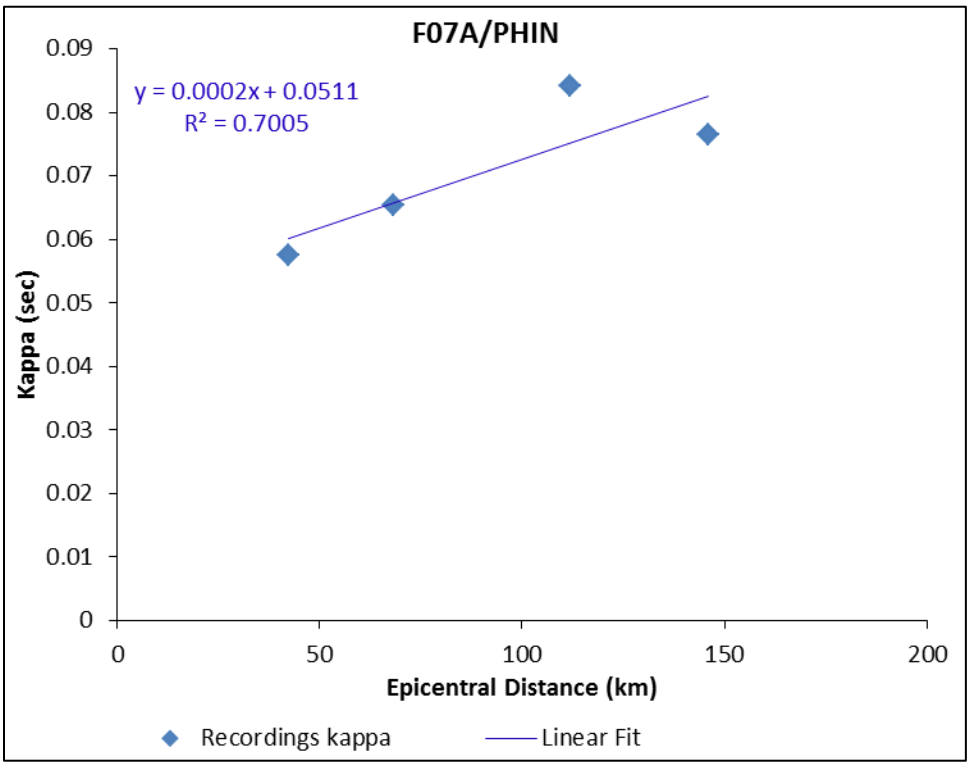

Figure 7.48. Kappa versus distance at SMB site F07A.

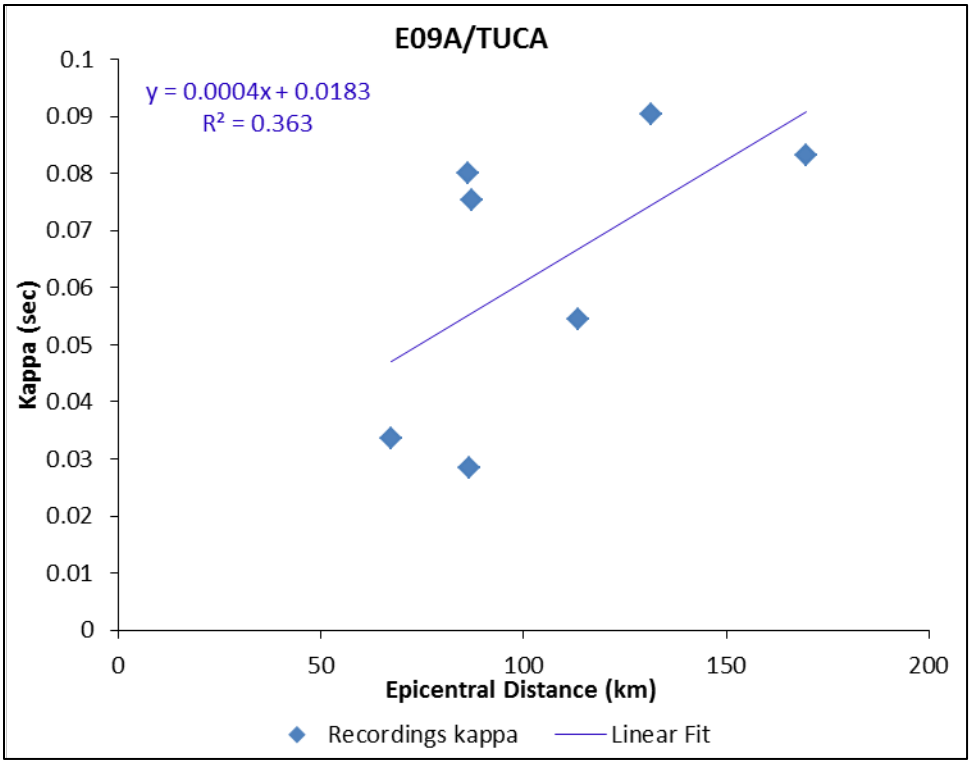

Figure 7.49. Kappa versus distance at WB site E09A.

The sensitivity of the estimated κ_{site} to the inclusion of the site amplification was evaluated for the HAWA recordings by applying the kappa fits to the FAS after first dividing them by the HAWA site amplification function. The TI Team developed V_S and density profiles for the sites of the six recording stations. To construct the stratigraphic profiles, the depths from the surface to the different stratigraphic units were supplied by George Last at PNNL with input and support from Paul Thorne and Alan Rohay. The depths of deeper layers (below the top of WB) were extracted from the 3-D model constructed by Paul Thorne for use by Art Frankel in his ground motion simulations for the Hanford Site. The depth to basement was based on Glover (1985), as discussed in Section 7.2. The V_S profile at HAWA is shown in Figure 7.50. Site amplification at HAWA was derived using the SRI method, also known as the QWL method (Boore 2005), and is shown in Figure 7.51. Dividing the FAS by the site amplification function resulted in an estimated κ_{site} at HAWA of 0.0453 sec compared to the initial κ_{site} of 0.0446 sec. Because the difference in κ_{site} is small and because it is standard practice to apply the Anderson and Hough (1984) method without correcting for the site amplification, κ_{site} estimated from the uncorrected high-frequency FAS slopes as shown in Table 7.19 were adopted. Given the relatively limited number of usable recordings at each station and their limited high-frequency bandwidth, epistemic uncertainty in the κ_{site} estimates due to the use of a different subset of data and varying f1 and f2 for the kappa fits could not be quantified. The uncertainty in the $\kappa(0)$ estimates from the κ_{obs} versus distance fits was considered for assigning epistemic uncertainty in κ_{site} at the stations but the TI Team opted to assign epistemic uncertainty on kappa estimated using the Anderson and Hough (1984) method in the derived Q model for this approach as described in Section 7.3.5. Finally, Table 7.20 summarizes the estimates of κ_{site} at the recording stations for the inversions and the Anderson and Hough (1984) approach. The best estimates of κ_{site} at the stations are considerably different for the two methods; the Anderson and Hough (1984) estimates are closer to the lower estimates of κ_{site} from the inversions.

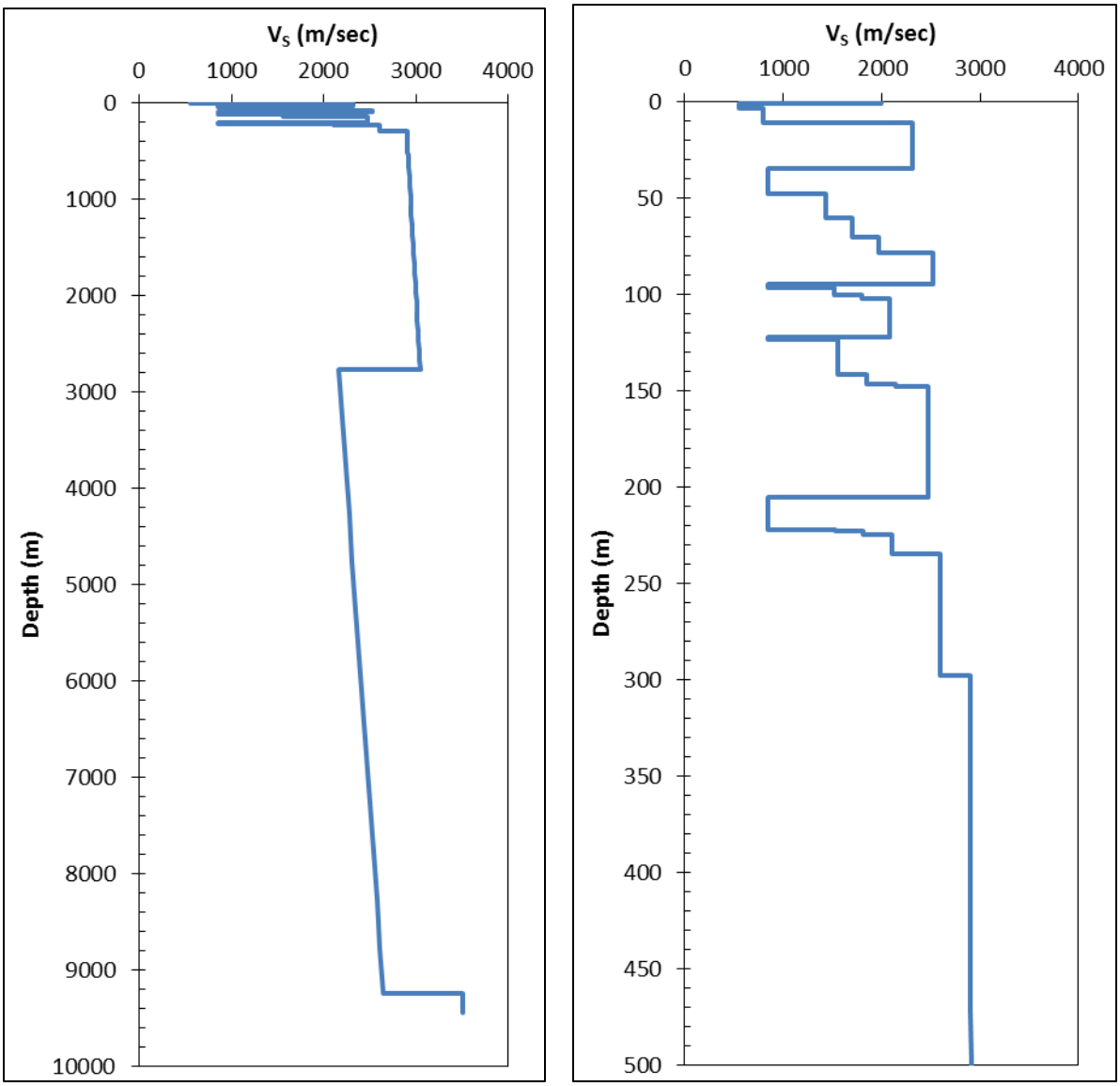

Figure 7.50. V_S profile at HAWA.

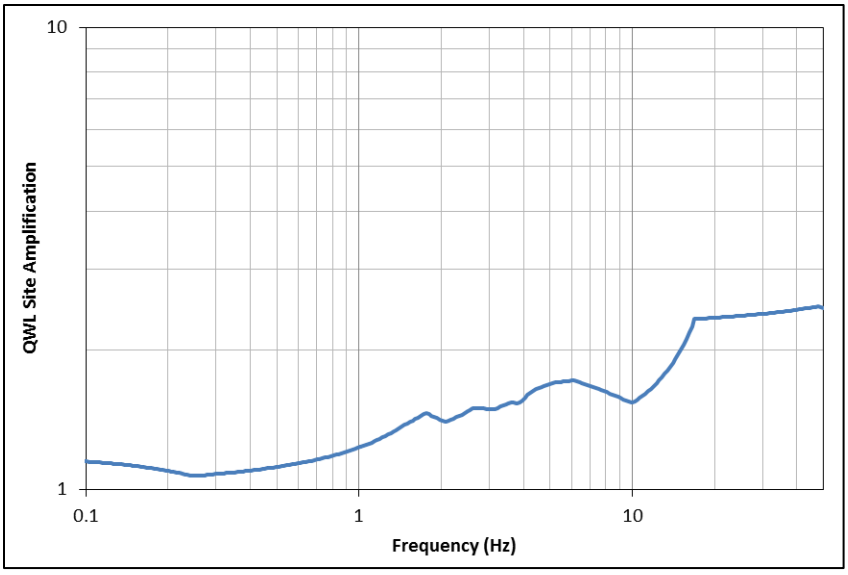

Figure 7.51. QWL site amplification at HAWA.

Table 7.19. Summary of κ_{site} and Q_{ave} estimated using the Anderson and Hough (1984) approach. Q_{ave} estimated using the Q(f) functions assumed by Dr. Silva and estimated by Phillips et al. (2014) are included for comparison.

Station Name	κ_{site} (sec)	Q_{ave} (this study)	Q_{ave} for $Q = 500(f)^{0.6}$ (Silva's Inversions)	Q_{ave} for $Q = 300(f)^{0.4}$ (Phillips et al. 2014)	Analogy for
HAWA[(a)]	0.045	952	3,731	1,146	SMB
E07A	0.039	2,947	2,383	850	SMB
E08A	0.002	1,117	2,589	898	SMB
F07A	0.051	1,327	2,248	817	SMB
D08A	NA	NA	NA	NA	WB
E09A	0.018	668	2,575	895	WB

(a) HAWA accelerograph recordings

Table 7.20. Summary of κ_{site} estimates at the recording stations using the inversion approach and the Anderson and Hough (1984) approach.

		HAWA	E07A	E08A	F07A	D08	E09A
Inversions Approach	$\kappa_{site}/1.4$	0.041	0.051	0.024	0.044	0.028	0.011
	κ_{site}	0.058	0.072	0.034	0.061	0.039	0.016
	$\kappa_{site}*1.1$	0.064	0.079	0.037	0.067	0.043	0.018
Anderson and Hough (1984) Approach	κ_{site}	0.045	0.039	0.002	0.051	NA	0.018

7.3.5 Kappa Model for the Hanford Site

Having estimates of κ_{site} at the locations of the recording stations within and around the Hanford Site, the TI Team estimated κ_{site} and $\kappa_{baserock}$ at the five hazard calculation sites (Sites A through E) at Hanford.

The approach consisted of using the two sets of κ_{site} estimates obtained from the inversions and the Anderson and Hough (1984) approach to derive Q models for the Hanford Site where $Q(z) = \gamma V_s(z)$. The simple linear Q versus V_S relationship was adopted because of the limited number of available κ_{site} estimates (six stations), which did not allow deriving more elaborate Q models. As outlined in Section 7.3.2, $\kappa_{damping}$ can be written as

$$\kappa_{\mathrm{damping}} = \sum_{\mathrm{i}} \frac{\mathrm{H_i}}{V_{S_i} \mathrm{Q_i}}. \quad (7.12)$$

Combining Equation (7.12) with the linear Q- V_S relationship, $\kappa_{damping}$ can be written as

$$\kappa_{\mathrm{damping}} = \frac{1}{\gamma} \sum_{\mathrm{i}} \frac{\mathrm{H_i}}{{V_{S_i}}^2}. \quad (7.13)$$

At each station location, $\kappa_{damping}$ can be estimated by removing the estimates of $\kappa_{scattering}$ from κ_{site}. Moreover, removing the contribution of the top few meters of relatively soft soil cover to damping at each station, $\kappa_{damping}$ can be written as

$$\kappa_{\mathrm{damping}} = \kappa_{\mathrm{site}} - \kappa_{\mathrm{scattering}} - \kappa_{\mathrm{damping\_soil}}. \quad (7.14)$$

Applying Equation (7.13) at each station location with $\kappa_{damping}$ estimated according to Equation (7.14), γ can be derived through linear regression. Derived γ can then be used in forward predictions to estimate $\kappa_{damping}$ according to Equation (7.13) at the five hazard calculation sites. This section describes the approach used to estimate $\kappa_{scattering}$ and $\kappa_{damping\_soil}$ as well as the derived γ models. The κ_{site} and $\kappa_{baserock}$ logic tree for the Hanford Site as well as the corresponding damping in the layers overlying the reference baserock horizon are presented and explained.

7.3.5.1 Damping Kappa at the Recording Sites

Shear-wave velocity profiles at the Hanford Site are characterized by the presence of velocity reversals predominantly within the SMB stack in the top 200 to 300 m of the profiles. Below the reference baserock horizon, these reversals are generally not present with the exception of the thick layer of sub-basalt sediments. Scattering kappa due to the presence of velocity contrasts was estimated at the recording sites and removed from the κ_{site} estimates in order to estimate $\kappa_{damping}$.

A SHAKE (Schnabel et al. 1972) analysis was conducted to estimate $\kappa_{scattering}$ in the SMB stack above the reference baserock horizon. The process consisted of using a base case V_S profile with zero damping and computing surface ground motions from the set of input time series used by Youngs (2007) scaled down by a factor of 0.001. The basalt/interbed sequence was then replaced with an equivalent layer with uniform velocity equal to the average velocity (travel-time average) of the basalt and interbed sequence. Levels of damping, equivalent to specific kappa values, were introduced into this uniform layer. The response of the uniform model was computed and the median surface spectrum for each case was visually compared with the median surface spectrum for the undamped basalt/interbed model. When the high-frequency levels of the two spectra were about the same, then the corresponding damping was considered to be equivalent to the scattering kappa. Figure 7.52 through Figure 7.55 show the results of the SHAKE analysis at the stations on SMB (HAWA, E07A, E08A, and F07A).

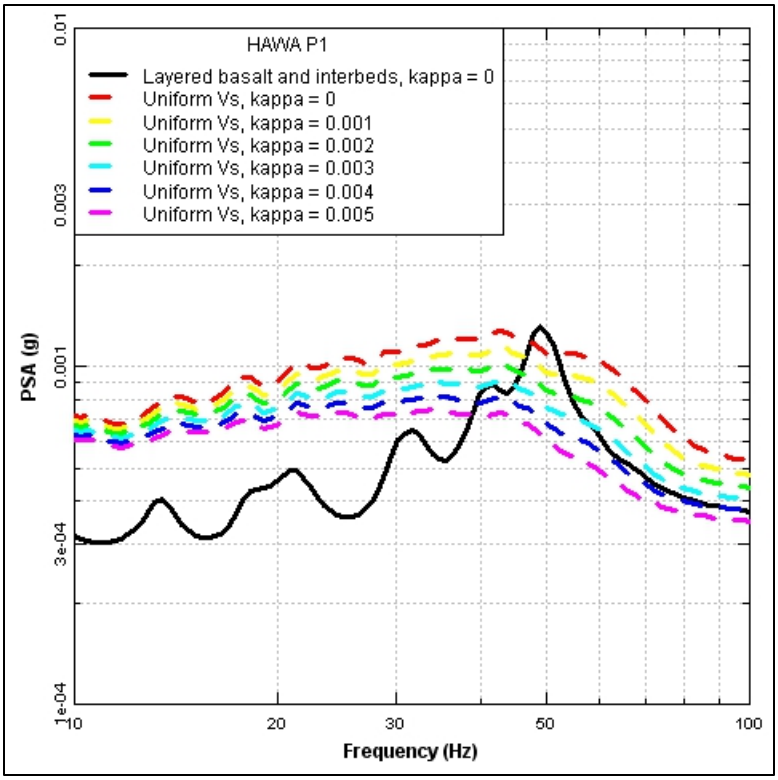

Figure 7.52. SHAKE analysis results at station HAWA. Scattering kappa is estimated to be around 0.004 sec.

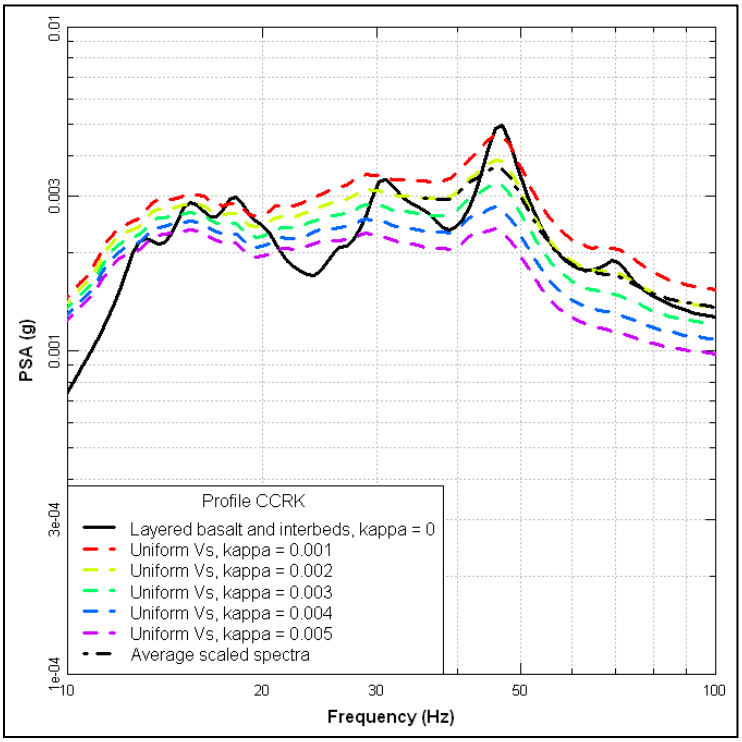

Figure 7.53. SHAKE analysis results at station E07A. Scattering kappa is estimated to be around 0.002 sec.

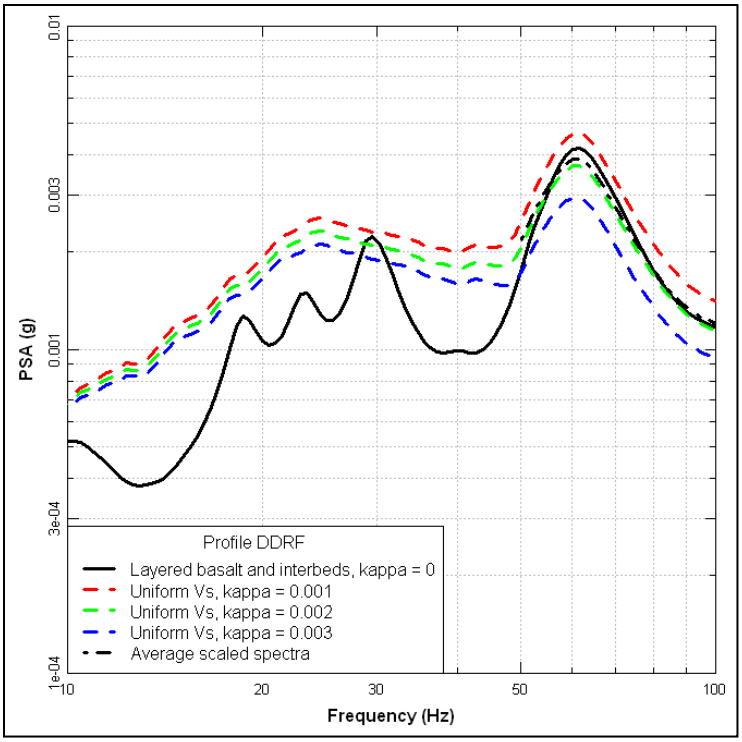

Figure 7.54. SHAKE analysis results at station E08A. Scattering kappa is estimated to be around 0.002 sec.

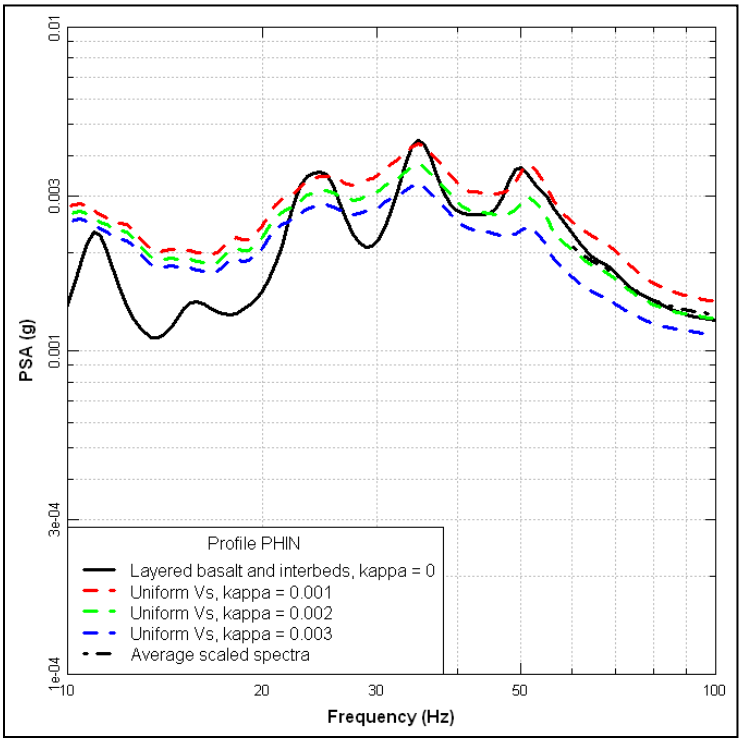

Figure 7.55. SHAKE analysis results at station F07A. Scattering kappa is estimated to be around 0.002 sec.

A similar process was applied using the full-resonant method as implemented in RATTLE (Boore 2005) to estimate $\kappa_{scattering}$ at the sites of the recording stations. A good agreement was observed between $\kappa_{scattering}$ estimated by the SHAKE and RATTLE analyses. Figure 7.56 shows a comparison of the site response (ratio of FAS at the surface to FAS at the top of the GR basalt layer) for the undamped layered profile to the equivalent uniform profile with different levels of damping at E08A and shows a $\kappa_{scattering}$ of around 0.002 sec as estimated in the SHAKE analysis. Figure 7.57 and Figure 7.58 show the RATTLE site-response comparison for the WB analog stations D08A and E09A. These plots show that scattering below the reference baserock horizon is negligible.

To develop a Q model for the Hanford Site from the top of SMB down, damping in the top few meters of soil cover at each station was estimated and removed from the κ_{site} estimates. Soil cover at the stations had V_S of less than 400 m/sec. $\kappa_{damping}$ in the soil cover was estimated according to Equation (7.12) with an assumed Q model according to Campbell (2009) (Model 3). Figure 7.59 shows the Q model used for the soil cover compared to other available Q models in the literature. The Campbell (2009) Q model was adopted because of its applicability to materials having properties similar to the soil cover. The sensitivity of $\kappa_{damping}$ in the soil cover to the choice of other Q models shown in Figure 7.59 was evaluated. Given the small thickness of the soil cover compared to the overall profile depth contributing to kappa, its $\kappa_{damping}$ is very small compared to the κ_{site} estimates, and the choice of the Q model did not make a significant impact on the analysis. Table 7.21 summarizes the estimates of $\kappa_{scattering}$ and $\kappa_{damping}$ in the soil cover at the six recording stations. $\kappa_{damping}$ at the top of SMB or WB (below the suprabasalt sediments) was calculated according to Equation (7.14) for the available κ_{site} estimates at the six recording stations.

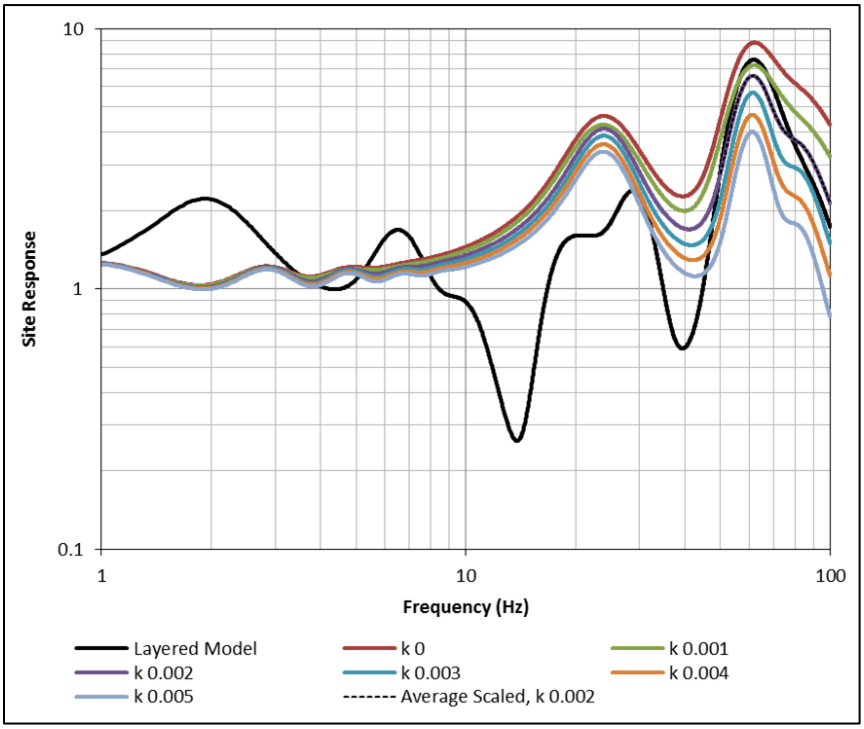

Figure 7.56. RATTLE analysis results at station F07A. Scattering kappa is estimated to be around 0.002 sec.

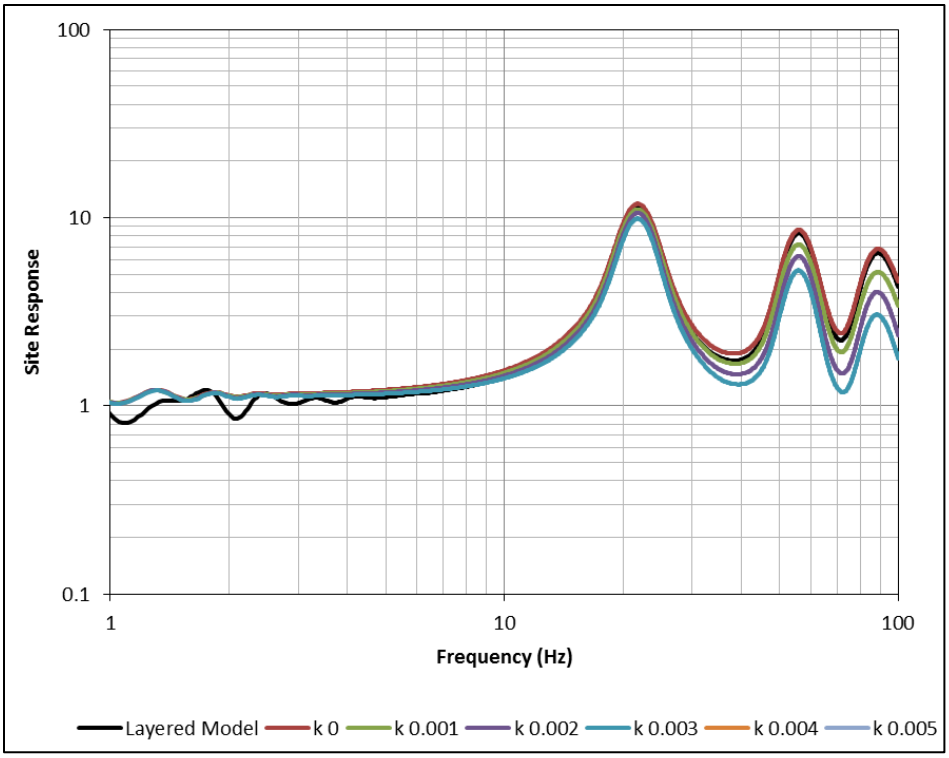

Figure 7.57. RATTLE analysis results at station E09A. Scattering kappa is estimated to be around 0.

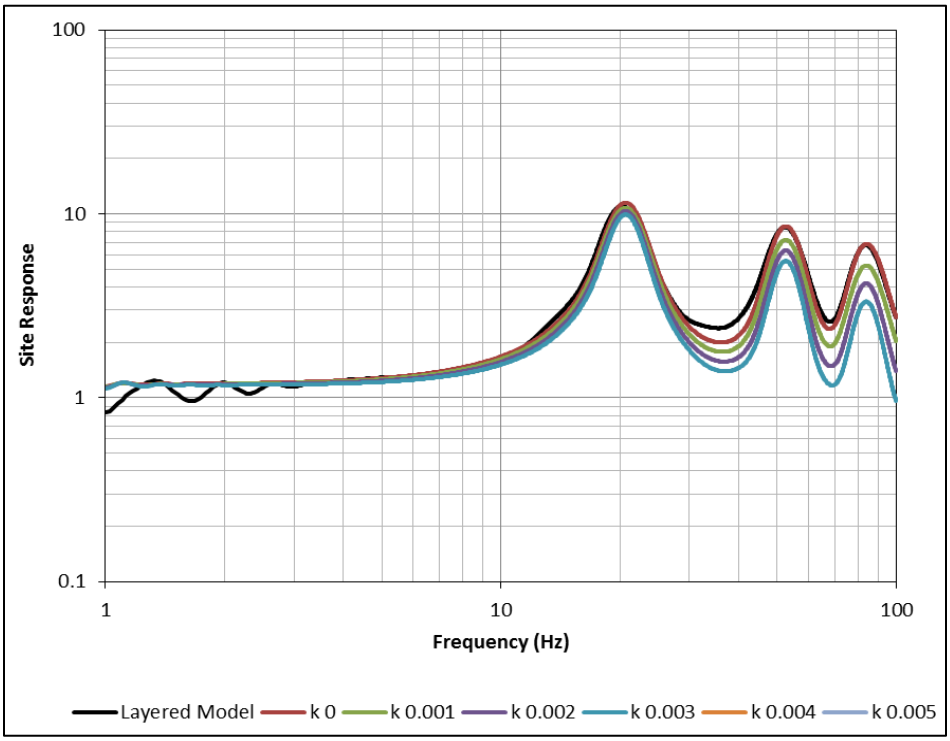

Figure 7.58. RATTLE analysis results at station D08A. Scattering kappa is estimated to be around 0.

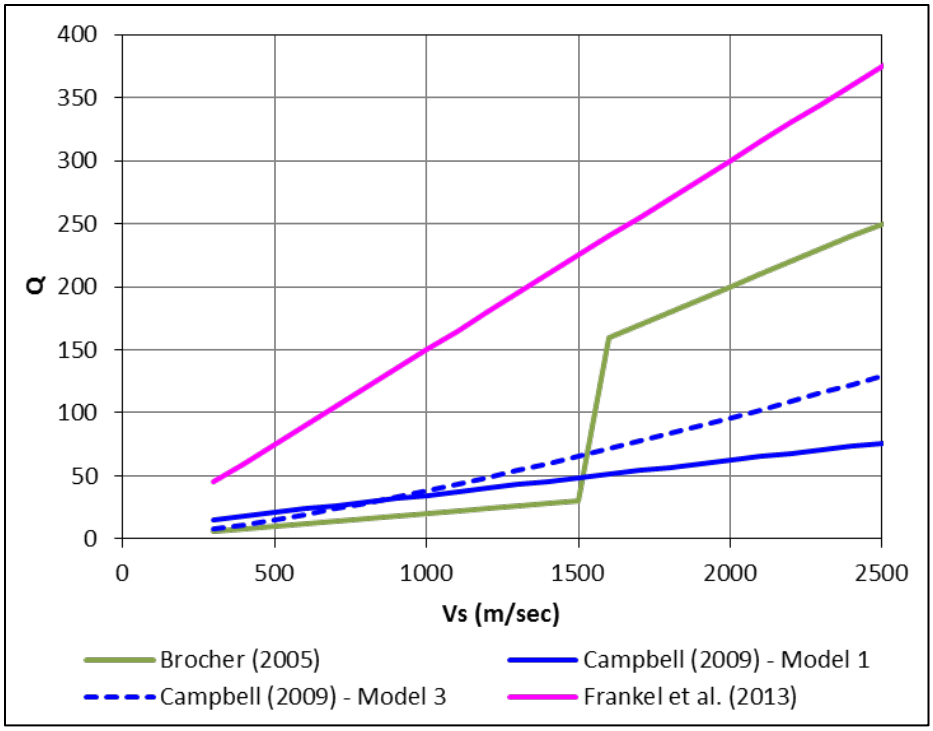

Figure 7.59. Q models from the literature. Campbell (2009) model 3 was used to estimate damping kappa in the soil cover at the sites of the recording stations.

Table 7.21. Estimates of scattering kappa and damping kappa in the suprabasalt sediments at the six recording stations

Station Name	Analog	$\kappa_{scattering}$ (sec)	$\kappa_{damping\ soil}$ (sec)
HAWA	SMB	0.004	0.0003
E07A	SMB	0.002	0.0017
E08A	SMB	0.002	0.0004
F07A	SMB	0.002	0.0023
D08A	WB	0	0.0014
E09A	WB	0	0.0014

7.3.5.2 Derived Q Models for the Hanford Site

Q models ($Q = \gamma V_s$) were developed for the Hanford Site using the three κ_{site} estimates from the inversion approach (best, upper, and lower estimates) and the best κ_{site} estimates from the Anderson and Hough (1984) approach. Four γ values were derived by regressing the $\kappa_{damping}$ estimates calculated using Equation (7.14) for the four sets of κ_{site} estimates on $\sum_i \frac{H_i}{Vs_i^2}$. As discussed in Section 7.3.4.1, the estimates of κ_{site} from the inversion analyses suggested that, for the deep earthquakes considered, the entire profile depth contributes to kappa. Therefore, $\sum_i \frac{H_i}{Vs_i^2}$ was summed over the entire profile depth down to the top of the crystalline basement. Figure 7.60 shows the four γ estimates for the Hanford Site. The derived Q models assume that γ is constant for the entire profile depth below the suprabasalt sediments. Using the derived γ values, Equation (7.13) was used in forward predictions to estimate damping kappa at the top of SMB (κ_{site}) and at the top of reference baserock horizon ($\kappa_{baserock}$) at the five hazard calculation sites.

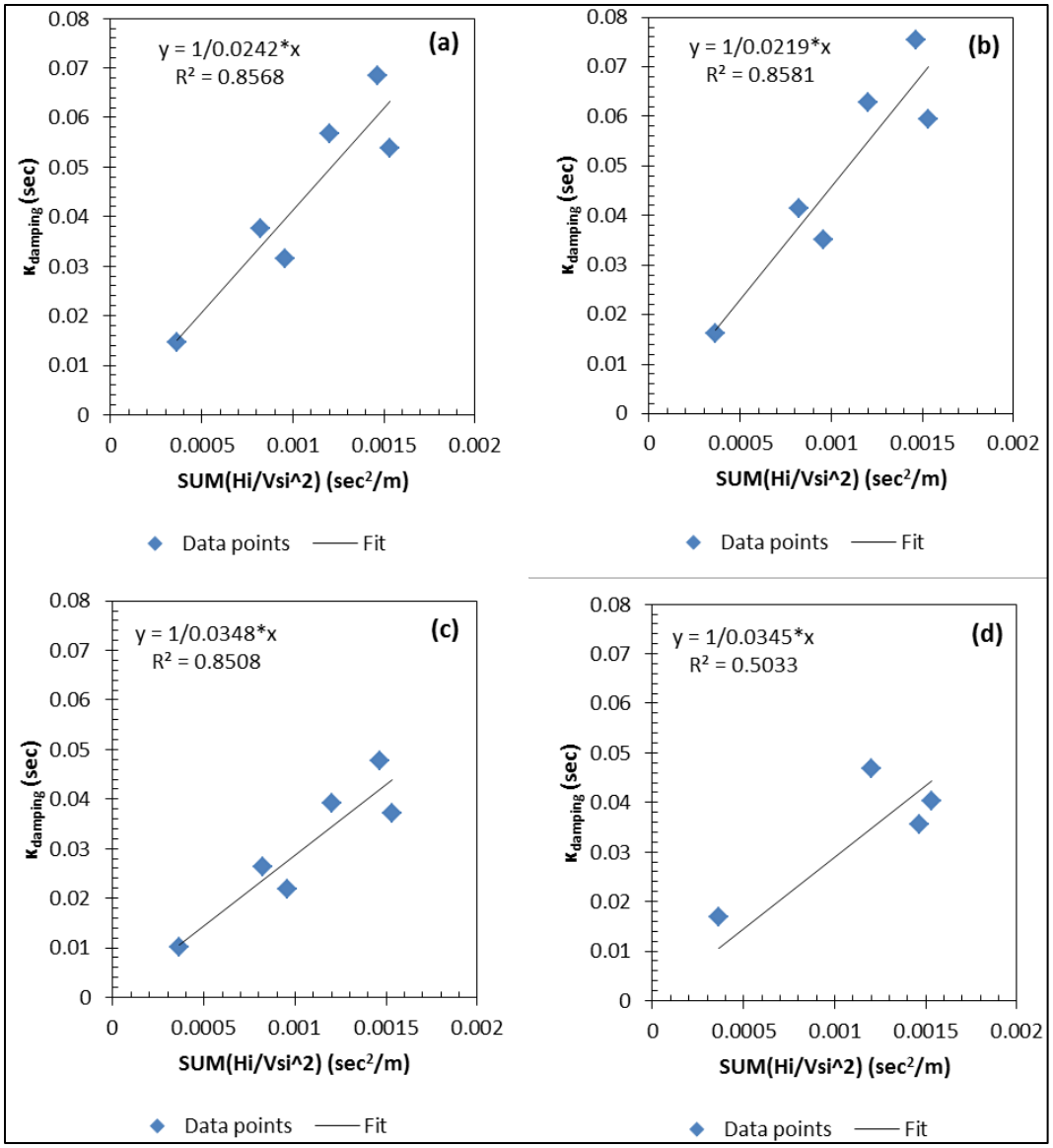

Figure 7.60. Q models for the Hanford Site derived using the inversion approach best estimates κ_{site} (a), upper estimates κ_{site} *1.1 (b), and lower estimates κ_{site} /1.4 (c) as well as κ_{site} derived using the Anderson and Hough (1984) method (d).

7.3.5.3 Kappa Logic Tree

The target kappa (κ_{site} and $\kappa_{baserock}$) logic tree for the Hanford Site is shown in Figure 7.61. The same logic-tree structure applies to all five hazard calculation sites, but different values were computed for each location. We note here that $\kappa_{baserock}$ and κ_{site} refer here to damping kappa at the baserock horizon and at the top of SMB, respectively. For the baserock horizon, scattering kappa is negligible, therefore $\kappa_{baserock}$ is equivalent to $\kappa_{damping,baserock}$. At the top of SMB, we use from this point onwards in the report κ_{site} to refer to $\kappa_{damping,site}$ with the understanding that scattering kappa in the SMB is part of the downstream site response analysis. κ_{site} was calculated using Equation (7.13) with the γ parameter estimated based on the analysis of kappa at the sites of the recording stations using the inversion approach and the Anderson and Hough (1984) approach. As shown in the logic tree, the inversions and the Anderson and Hough (1984) methods were given weights of 0.67 and 0.33, respectively. These weights were based on the fact that the

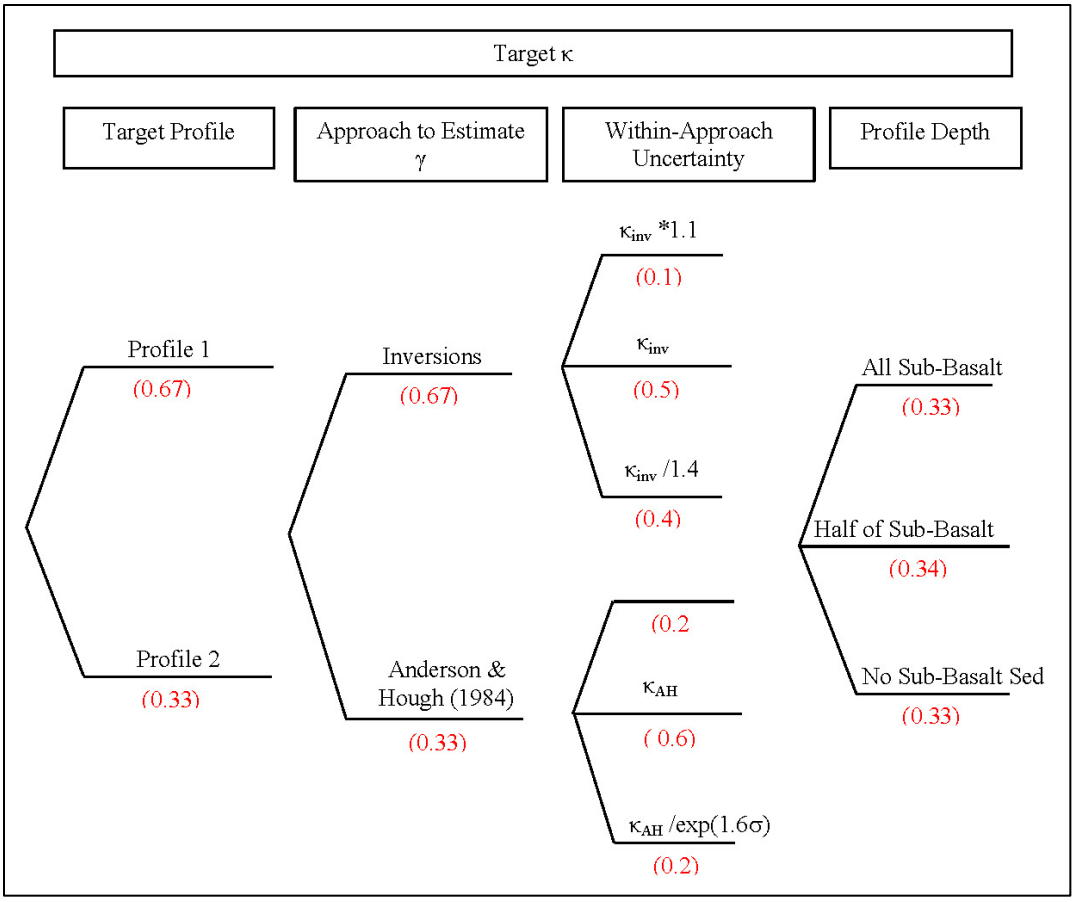

Figure 7.61. Target kappa (κ_{site} and $\kappa_{baserock}$) logic tree for the Hanford Site.

inversion approach fits the entire frequency band of the FAS and applies a common Q to all sites, while the Anderson and Hough (1984) method is more affected by the limited-frequency bandwidth due to only fitting the high-frequency part of the FAS. Moreover, the average frequency-independent Q inferred from the Anderson and Hough (1984) approach was different for the sites considered. While the inversions process only considered deep earthquakes, the Anderson and Hough (1984) data set consisted of deep and shallow earthquakes due to the limited number of usable recordings showing a linear log(FAS) versus frequency trend at high frequency. Based on these shortcomings of the Anderson and Hough (1984) approach compared to the inversion approach for the available recordings (limited-frequency bandwidth, different inferred Q values at the different sites, and mixing of deep and shallow earthquakes), the inversion method was considered more reliable and given double the weight of the Anderson and Hough (1984) method.

Epistemic uncertainty on κ_{site} derived using the inversion approach was considered by adopting the γ values derived using the inversions' best estimates, upper and lower estimates of κ_{site} at the stations. These γ values are shown in Figure 7.60 (plots a, b, and c). Because the inversions used a fixed frequency-dependent Q that is larger than Q estimated by Phillips et al. (2014) for the Hanford Site, the inversions best estimates of κ_{site} at the stations were not considered to be representative of the median of the κ_{site} distribution, but rather to be larger than the median to compensate for the large Q. Therefore, weights of 0.1, 0.5, and 0.4 for the γ values obtained from the upper, best, and lower κ_{site} estimates at the stations were judged by the TI Team to be appropriate for these branches.

The upper and lower branches of κ_{site} derived by the Anderson and Hough (1984) approach were developed assuming a lognormal distribution of kappa. The median and standard deviation of log(kappa) were estimated using Equations 3.3.34 and 3.3.35 of Benjamin and Cornell (1971) with a normal standard deviation of kappa of 0.01.. This standard deviation is the root-mean-square error of the γ fit shown in Figure 7.60d. Weights of 0.6, 0.2, and 0.2 were assigned to the median and the upper and lower branches (±1.6 standard deviation), respectively. These weights correspond to a discrete three-point representation of the assumed continuous distribution.

The application of Equation (7.13) to estimate κ_{site} requires defining the depth of profile contributing to damping at the site. The relatively large κ_{site} at the stations estimated using recordings of deep earthquakes suggested a contribution of the entire sub-basalt sediments layer to kappa. However, no further knowledge is available regarding the distribution of profile depth that would contribute to kappa for shallower earthquakes. Given the lack of knowledge on the depth of profile that would contribute to kappa for the depth distribution of future earthquakes, the TI Team adopted three branches for the profile depth: entire thickness of sub-basalt sediments layer, half of the sub-basalt sediments layer, and no sub-basalt sediments with almost equal weights of 0.33, 0.34, and 0.33, respectively. The entire sub-basalt sediments layer branch corresponds to a total profile depth of 7.3 to 9.5 km from the top of SMB at the five hazard calculation sites. Half of the sub-basalt sediments layer corresponds to a range of total profile depth from 4.8 to 6.3 km and the no sub-basalt sediments branch corresponds to the total profile depth contributing to kappa ranging from 2.0 to 3.3 km.

The four candidate V_S profiles developed at each site were considered to estimate κ_{site} according to Equation (7.13). Table 7.22 presents the κ_{site} values calculated at Site A using all branches of the logic tree along with the four candidate V_S profiles for the site. Table 7.22 shows that κ_{site} for Profiles 2 and 3 are very similar because these candidate V_S profiles only differ in the V_S values of the SMB stack, which constitutes the top 316 m of the profile depth. This V_S difference in the top 316 m does not have a significant impact on the resulting κ_{site} because the V_S values for the two profiles are identical in the larger remaining depth of profile (2.48, 5.64, and 8.81 km for the no sub-basalt sediments, half of the sub-basalt sediments, and all the sub-basalt sediments branches, respectively). Similarly, Profiles 1 and 4 only differ in the V_S values of the SMB stack, which produces similar κ_{site} estimates. Based on these similarities, the logic tree was simplified to only use Profiles 1 and 2 at the five hazard calculation sites.

Profile 1 was constructed using V_S values from downhole measurements and V_S in the sub-basalt sediments layer assigned according to a V_P/V_S ratio of 1.73. Profile 2 was constructed using V_S values from the PS logging measurements and V_S values in the sub-basalt sediments based on a V_P/V_S ratio of 2. The main difference between the downhole and the PS logging measurements is in the resulting V_S values in the basalt layers—the PS logging results in higher V_S estimates. For the interbeds, both methods provided comparable V_S values. While the PS logging generally provides higher-resolution data that allowed for a better identification of the velocity contrasts between the basalts and the interbeds, its tool dimension results in measurements of materials close to the borehole wall, which may be disturbed by the drilling. Professor Ken Stokoe informed the GMC TI Team that his comparisons of free-free tests with PS suspension logging measurements had suggested that the latter tended to overestimate the velocities. Moreover, the input source frequencies in the downhole logging are considered closer to the frequencies of interest for earthquake ground motions. For these reasons, weights of 0.67 and 0.33 were given to Profile 1 and Profile 2, respectively.

Table 7.23 presents the target κ_{site} estimates at the Hanford hazard calculation Sites A through E for all 36 branches of the logic tree in Figure 7.61. Figure 7.62 through Figure 7.64 present the histograms of κ_{site} estimates at the five hazard calculation sites where the y-axis shows the weight of each kappa bin.

Table 7.22. Comparison of κ_{site} at Site A for the four candidate V_S profiles.

		Lower κ_{inv}	Central κ_{inv}	Upper κ_{inv}	Lower κ_{AH}	Central κ_{AH}	Upper κ_{AH}
Profile 1	All Sed.	0.0322	0.0483	0.0539	0.0187	0.0313	0.0509
	Half of Sed.	0.0215	0.0328	0.0368	0.0119	0.0208	0.0346
	No Sed.	0.0083	0.0139	0.0159	0.0036	0.0080	0.0242
Profile 2	All Sed.	0.0402	0.0598	0.0666	0.0263	0.0396	0.0587
	Half of Sed.	0.0258	0.0391	0.0437	0.0164	0.0254	0.0383
	No Sed.	0.0083	0.0138	0.0158	0.0043	0.0081	0.0242
Profile 3	All Sed.	0.0403	0.0599	0.0667	0.0263	0.0396	0.0587
	Half of Sed.	0.0259	0.0392	0.0438	0.0164	0.0255	0.0384
	No Sed.	0.0083	0.0139	0.0159	0.0044	0.0082	0.0242
Profile 4	All Sed.	0.0322	0.0482	0.0538	0.0186	0.0312	0.0508
	Half of Sed.	0.0214	0.0327	0.0367	0.0118	0.0207	0.0346
	No Sed.	0.0083	0.0138	0.0158	0.0036	0.0080	0.0242

Table 7.23. Target κ_{site} at the five hazard calculation sites at Hanford.

		Profile 1			Profile 2		
Site	Case	All Sed.	Half of Sed.	No Sed.	All Sed.	Half of Sed.	No Sed.
Site A	Lower κ_{inv}	0.0366	0.0258	0.0127	0.0446	0.0302	0.0127
	Central κ_{inv}	0.0526	0.0372	0.0183	0.0642	0.0435	0.0182
	Upper κ_{inv}	0.0582	0.0411	0.0202	0.0710	0.0481	0.0202
	Lower κ_{AH}	0.0230	0.0163	0.0080	0.0307	0.0208	0.0087
	Central κ_{AH}	0.0357	0.0252	0.0124	0.0440	0.0298	0.0125
	Upper κ_{AH}	0.0552	0.0390	0.0192	0.0631	0.0427	0.0179
Site B	Lower κ_{inv}	0.0385	0.0279	0.0151	0.0463	0.0322	0.0150
	Central κ_{inv}	0.0553	0.0401	0.0217	0.0666	0.0463	0.0216
	Upper κ_{inv}	0.0612	0.0444	0.0240	0.0737	0.0512	0.0239
	Lower κ_{AH}	0.0248	0.0180	0.0097	0.0323	0.0224	0.0105
	Central κ_{AH}	0.0376	0.0273	0.0147	0.0457	0.0318	0.0148
	Upper κ_{AH}	0.0571	0.0414	0.0224	0.0647	0.0450	0.0210
Site C	Lower κ_{inv}	0.0327	0.0219	0.0088	0.0406	0.0262	0.0086
	Central κ_{inv}	0.0471	0.0315	0.0127	0.0584	0.0376	0.0124
	Upper κ_{inv}	0.0521	0.0349	0.0140	0.0647	0.0416	0.0137
	Lower κ_{AH}	0.0194	0.0130	0.0052	0.0268	0.0173	0.0057
	Central κ_{AH}	0.0316	0.0212	0.0085	0.0399	0.0257	0.0085
	Upper κ_{AH}	0.0515	0.0345	0.0138	0.0592	0.0381	0.0125
Site D	Lower κ_{inv}	0.0343	0.0250	0.0139	0.0409	0.0284	0.0136
	Central κ_{inv}	0.0493	0.0359	0.0200	0.0588	0.0409	0.0196
	Upper κ_{inv}	0.0546	0.0397	0.0221	0.0651	0.0452	0.0217
	Lower κ_{AH}	0.0209	0.0152	0.0085	0.0271	0.0188	0.0090
	Central κ_{AH}	0.0332	0.0242	0.0135	0.0401	0.0279	0.0134
	Upper κ_{AH}	0.0530	0.0386	0.0215	0.0594	0.0413	0.0198
Site E	Lower κ_{inv}	0.0305	0.0210	0.0097	0.0373	0.0245	0.0095
	Central κ_{inv}	0.0439	0.0302	0.0140	0.0536	0.0353	0.0137
	Upper κ_{inv}	0.0486	0.0334	0.0155	0.0593	0.0391	0.0151
	Lower κ_{AH}	0.0174	0.0120	0.0056	0.0237	0.0156	0.0060
	Central κ_{AH}	0.0293	0.0202	0.0094	0.0364	0.0239	0.0093
	Upper κ_{AH}	0.0493	0.0339	0.0157	0.0559	0.0368	0.0143

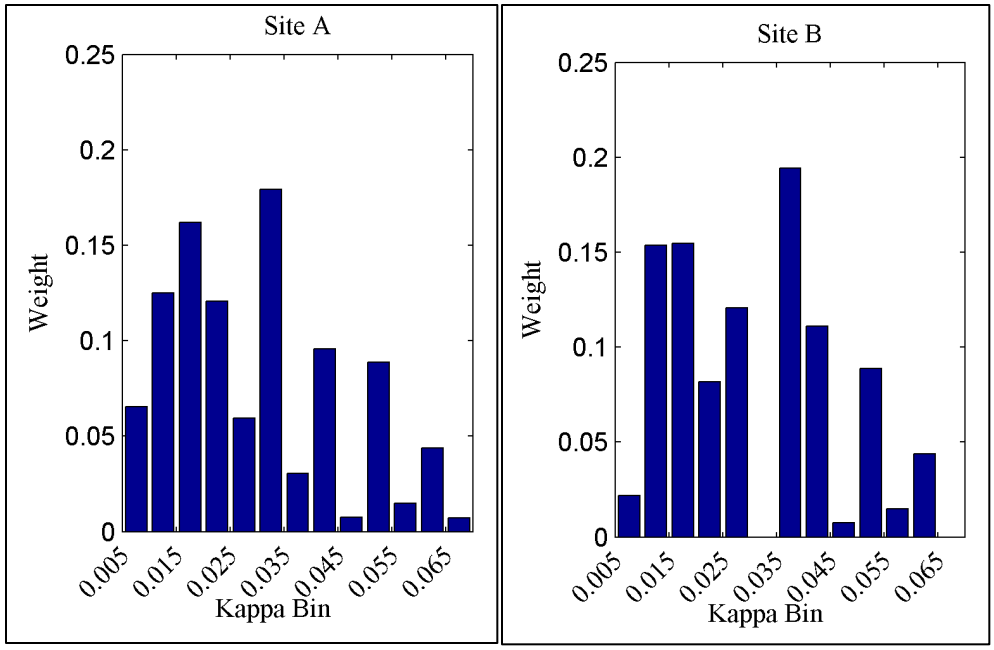

Figure 7.62. Target κ_{site} histogram and statistics at Sites A and B.

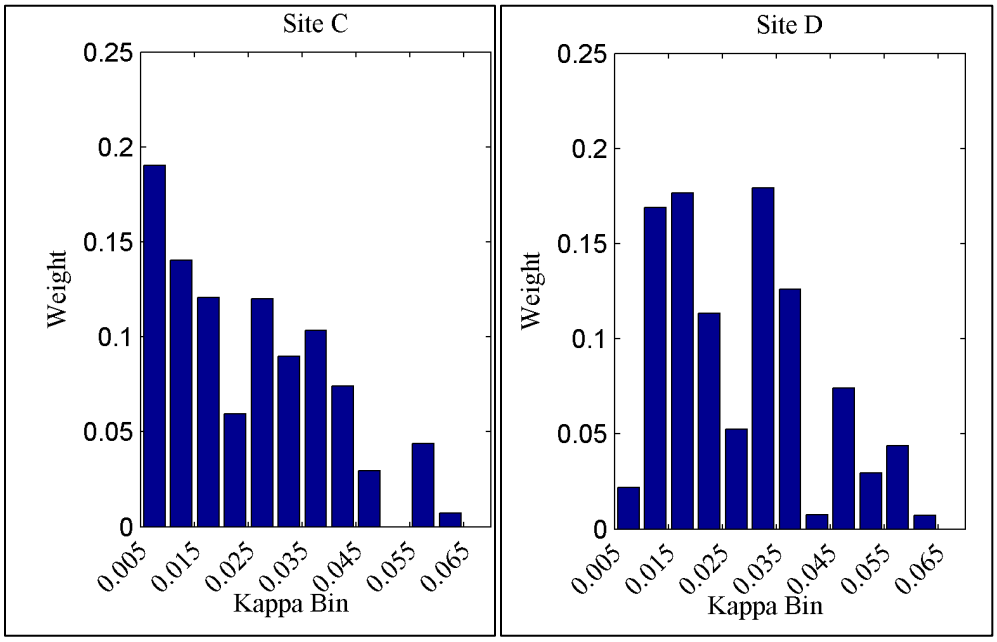

Figure 7.63. Target κ_{site} histogram and statistics at Sites C and D.

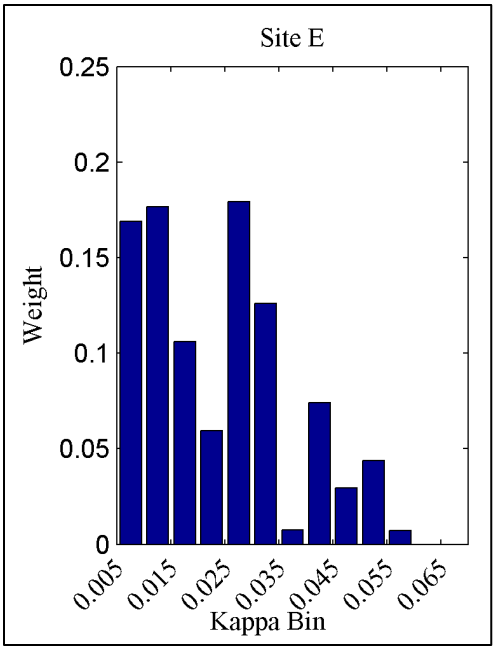

Figure 7.64. Target κ_{site} histogram and statistics at Site E.

7.3.5.4 Baserock Kappa and Damping in the SMB Stack

PSHA at the Hanford hazard calculation sites is calculated at the reference baserock horizon (top of Lolo flow). GMPEs are therefore adjusted to target $\kappa_{baserock}$. Damping in the SMB stack layers overlying the reference baserock horizon is specified such that the effective κ_{site} is maintained at each site ($\kappa_{site} = \kappa_{baserock}+\kappa_{stack}$). Similar to κ_{site}, target $\kappa_{baserock}$ can be calculated using Equation (7.13) for the logic-tree branches in Figure 7.61. Damping (ξ) in the SMB stack layers can be calculated using $\xi = 1/(2Q)$ where $Q = \gamma V_s$.

Four candidate γ values were derived using the estimates of κ_{site} at the recording stations from the inversions and the Anderson and Hough (1984) approach. To simplify the downstream site-response analysis and because the relative division of damping between the SMB stack and the baserock can be modified as long as κ_{site} is preserved, the TI Team decided to fix γ in the SMB stack to produce one set of damping properties in the stack layers. The parameter γ is fixed at 0.0345 sec/m, which is the γ value obtained from the Anderson and Hough (1984) κ_{site} estimates at the stations (Figure 7.60d). Table 7.24 presents the damping values in the SMB stack for Profiles 1 and 2 using $\gamma = 0.0345$ sec/m. Damping is on the order of 1.5 to 1.9% in the interbeds and less than 1% in the basalt layers.

Target $\kappa_{baserock}$ was calculated using $\kappa_{baserock} = \kappa_{site} - \kappa_{stack}$ and is presented in Table 7.25 for the five hazard calculation sites. This approach effectively implies different γ values for the SMB stack and the baserock such that the uncertainty in the damping in the stack is now absorbed into $\kappa_{baserock}$. It is important to note that target $\kappa_{baserock}$ values at the five hazard calculation sites cannot be used independently because they are tied to the damping properties in the SMB stack to produce the target κ_{site} at the top of SMB presented in the previous section. This approach results in inflating the target $\kappa_{baserock}$ values in order to account for the larger damping values that would have occurred in the stack using the remaining three γ values. Figure 7.65 through Figure 7.67 present the histograms of the $\kappa_{baserock}$ distribution at the five hazard calculation sites.

Table 7.24. Damping properties in the SMB stack.

Unit	Profile 1		Profile 2	
	V_S (km/sec)	ξ	V_S (km/sec)	ξ
Ice Harbor (Martindale flow top 1)	1.41	1.03%	1.77	0.82%
Ice Harbor (Martindale flow top 2)	1.67	0.87%	2.11	0.69%
Ice Harbor (Martindale flow top 3)	1.93	0.75%	2.44	0.59%
Ice Harbor (Martindale flow)	2.31	0.63%	2.91	0.50%
Levy Interbed	0.85	1.71%	0.85	1.71%
Elephant Mountain (flow top 1)	1.41	1.03%	1.77	0.82%
Elephant Mountain (flow top 2)	1.67	0.87%	2.11	0.69%
Elephant Mountain (flow top 3)	1.93	0.75%	2.44	0.59%
Elephant Mountain	2.31	0.63%	2.91	0.50%
Rattlesnake ridge Interbed	0.84	1.73%	0.83	1.74%
Pomona (flow top 1)	1.43	1.01%	1.77	0.82%
Pomona (flow top 2)	1.70	0.85%	2.11	0.69%
Pomona (flow top 3)	1.97	0.74%	2.44	0.59%
Pomona	2.52	0.58%	3.12	0.46%
Selah Interbed	0.88	1.65%	0.97	1.49%
Esquatzel (flow top 1)	1.49	0.97%	1.74	0.83%
Esquatzel (flow top 2)	1.80	0.81%	2.11	0.69%
Esquatzel (flow top 3)	2.00	0.72%	2.35	0.62%
Esquatzel	2.52	0.58%	2.95	0.49%
Cold Creek Interbed	0.82	1.76%	0.76	1.91%
Asotin (flow top 1)	1.49	0.97%	1.74	0.83%
Asotin (flow top 2)	1.80	0.81%	2.11	0.69%
Asotin (flow top 3)	2.00	0.72%	2.35	0.62%
Asotin	2.52	0.58%	2.95	0.49%
Sillusa (flow top 1)	1.53	0.95%	1.74	0.83%
Sillusa (flow top 2)	1.85	0.78%	2.11	0.69%
Sillusa (flow top 3)	2.14	0.68%	2.44	0.59%
Umatilla (Sillusa flow)	2.44	0.59%	2.78	0.52%
Umatilla (top flow 1)	1.53	0.95%	1.74	0.83%
Umatilla (top flow 2)	1.85	0.78%	2.11	0.69%
Umatilla (top flow 3)	2.14	0.68%	2.44	0.59%
Umatilla (Umatilla flow)	2.57	0.56%	2.93	0.50%
Mabton Interbed	0.83	1.75%	0.78	1.85%
Lolo (flow top 1)	1.48	0.98%	1.77	0.82%
Lolo (flow top 2)	1.76	0.82%	2.11	0.69%
Lolo (flow top 3)	2.04	0.71%	2.44	0.59%

Table 7.25. Target $\kappa_{baserock}$ at the five hazard calculation sites at Hanford.

Site	Case	Profile 1			Profile 2		
		All Sed.	Half of Sed.	No Sed.	All Sed.	Half of Sed.	No Sed.
Site A	Lower κ_{inv}	0.0322	0.0215	0.0083	0.0402	0.0258	0.0083
	Central κ_{inv}	0.0483	0.0328	0.0139	0.0598	0.0391	0.0138
	Upper κ_{inv}	0.0539	0.0368	0.0159	0.0666	0.0437	0.0158
	Lower κ_{AH}	0.0187	0.0119	0.0036	0.0263	0.0164	0.0043
	Central κ_{AH}	0.0313	0.0208	0.0080	0.0396	0.0254	0.0081
	Upper κ_{AH}	0.0509	0.0346	0.0148	0.0587	0.0383	0.0135
Site B	Lower κ_{inv}	0.0327	0.0221	0.0093	0.0405	0.0264	0.0092
	Central κ_{inv}	0.0495	0.0344	0.0159	0.0608	0.0405	0.0158
	Upper κ_{inv}	0.0554	0.0387	0.0182	0.0679	0.0454	0.0181
	Lower κ_{AH}	0.0190	0.0122	0.0039	0.0265	0.0167	0.0047
	Central κ_{AH}	0.0318	0.0215	0.0090	0.0399	0.0260	0.0090
	Upper κ_{AH}	0.0513	0.0356	0.0166	0.0590	0.0392	0.0152
Site C	Lower κ_{inv}	0.0297	0.0189	0.0058	0.0378	0.0233	0.0058
	Central κ_{inv}	0.0441	0.0285	0.0096	0.0556	0.0348	0.0095
	Upper κ_{inv}	0.0491	0.0319	0.0110	0.0618	0.0388	0.0109
	Lower κ_{AH}	0.0164	0.0100	0.0022	0.0240	0.0144	0.0028
	Central κ_{AH}	0.0286	0.0182	0.0055	0.0370	0.0228	0.0056
	Upper κ_{AH}	0.0485	0.0315	0.0108	0.0563	0.0352	0.0097
Site D	Lower κ_{inv}	0.0304	0.0210	0.0100	0.0372	0.0247	0.0099
	Central κ_{inv}	0.0454	0.0320	0.0161	0.0551	0.0371	0.0159
	Upper κ_{inv}	0.0507	0.0358	0.0182	0.0613	0.0415	0.0180
	Lower κ_{AH}	0.0170	0.0113	0.0046	0.0234	0.0151	0.0053
	Central κ_{AH}	0.0293	0.0203	0.0096	0.0364	0.0242	0.0097
	Upper κ_{AH}	0.0491	0.0347	0.0176	0.0557	0.0376	0.0161
Site E	Lower κ_{inv}	0.0272	0.0177	0.0065	0.0342	0.0214	0.0064
	Central κ_{inv}	0.0406	0.0269	0.0107	0.0505	0.0322	0.0106
	Upper κ_{inv}	0.0453	0.0301	0.0122	0.0562	0.0360	0.0120
	Lower κ_{AH}	0.0141	0.0087	0.0023	0.0206	0.0125	0.0029
	Central κ_{AH}	0.0260	0.0169	0.0061	0.0333	0.0209	0.0062
	Upper κ_{AH}	0.0460	0.0306	0.0125	0.0528	0.0337	0.0112

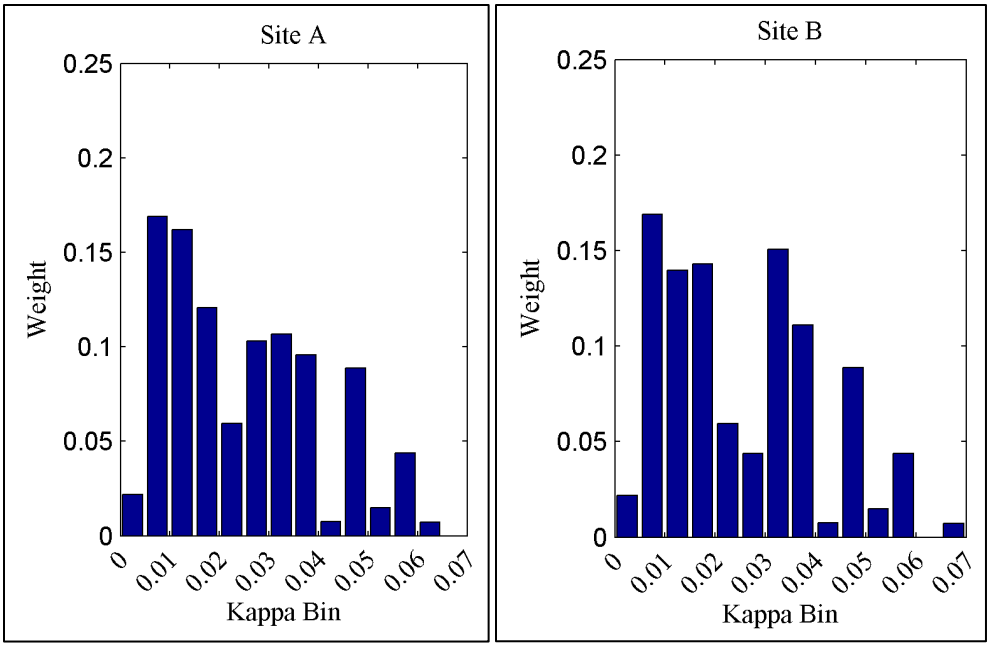

Figure 7.65. Target $\kappa_{baserock}$ histogram and statistics at Sites A and B.

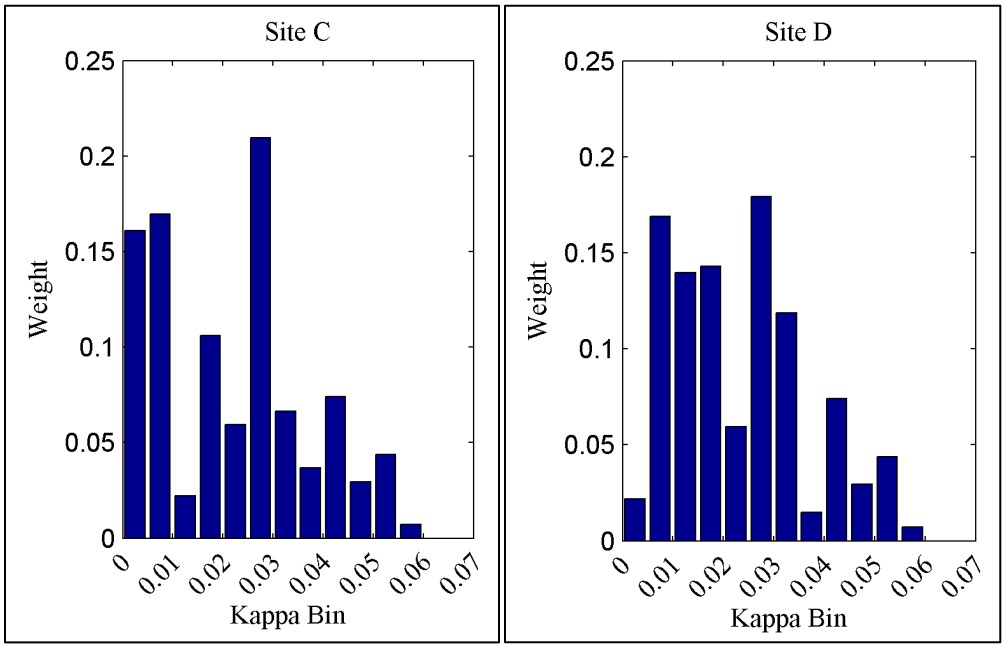

Figure 7.66. Target $\kappa_{baserock}$ histogram and statistics at Sites C and D.

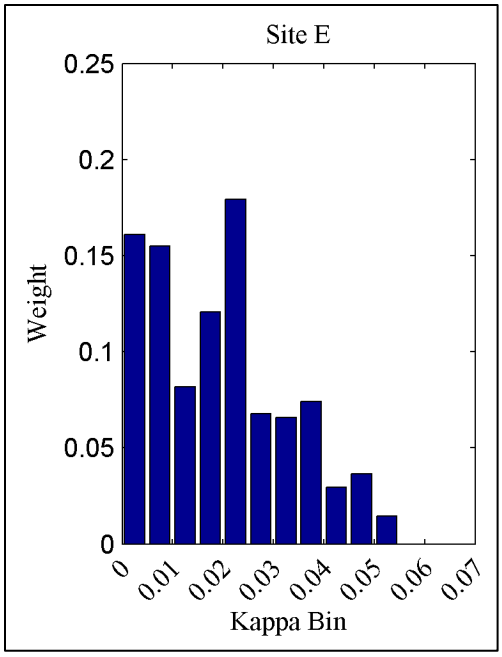

Figure 7.67. Target $\kappa_{baserock}$ histogram and statistics at Site E.

7.4 Current Ground Motion Prediction Equations and Sigma Models

The GMC model for the baserock motions consists of predictions of median spectral accelerations and their associated sigma values, from both crustal and subduction earthquakes. Knowing that repeatable site terms will be represented through both the uncertainty in the V_s-kappa adjustments (Section 9.3) and the randomizations in the site-response analyses (Section 9.6.5), the GMC TI Team decided at an early stage that the single-station sigma model would be invoked. In this section, the available databases of GMPEs for crustal and subduction earthquakes are reviewed and evaluated, as are the available models for single-station sigma.

7.4.1 GMPEs for Crustal Earthquakes

Past studies (e.g., Geomatrix 1996; Petersen et al. 2008; JBA et al. 2012) have treated eastern Washington as an active crustal region (ACR) for the purpose of calculating ground motions from crustal earthquakes, and this project adopts the same treatment. It could be argued that the region around the Hanford Site may have some elements of a stable continental region (SCR), given its distance to the plate boundary and its lower activity rate. This possibility is taken into account by means of host-to-target epistemic uncertainty in Chapter 9.0.

The number of available GMPEs for crustal earthquakes has increased substantially in recent years (see Douglas [2011] for an extensive compilation), but their quality and applicability (given the specific needs of a particular project) vary substantially. This makes a careful review of existing GMPEs, and the selection of the most suitable among them for this project, a key task, and this is the main focus of this section.

It is appropriate to clarify that although this chapter is devoted to the GMC databases, the focus is not exclusively on the compilation and collection of data but inevitably also includes elements of the evaluations that are the first part of the TI Team's work in a SSHAC Level 3 process. Even as the databases were being developed, the TI Team continuously had in mind the requirements and objectives of the project, and evaluation inevitably enters into the process so that all redundant or extraneous information can be removed from consideration at an early stage. This allows the TI Team to then focus time and effort on the data, methods, and models that were most useful and most promising for the development of the GMC logic tree.

In this context, compiling a database of GMPEs for possible consideration in the development of the GMC model necessarily involves evaluating published equations both in terms of their general inherent quality (in terms of functional form, underlying data, stability, and ability to be extrapolated) and their potential applicability to this project (in terms of the characteristics of both the region and the site). Following the precedents of Cotton et al. (2006) and Bommer et al. (2010), it was decided from the outset to adopt the approach of starting with a comprehensive global list of GMPEs and using (at least as a first cut) pre-established objective criteria to exclude GMPEs, rather than to build a list of GMPEs that might be suitable. The approach adopted is more efficient and less subject to cognitive biases.

This section begins with a brief overview of available GMPEs for ACRs. This is followed by the development, discussion, and application of exclusion criteria that were imposed in order to retain only those GMPEs that are sufficiently robust and also meet other project-specific requirements. Finally, a list of GMPEs that satisfy these requirements is presented.

For the compilation of GMPEs for ACRs, the TI Team was able to take advantage of the comprehensive global list of GMPEs published between 1964 and 2010 compiled by Douglas (2011). In addition, the TI Team identified, through a thorough literature review, a handful of models published after the period covered by this compendium. Of particular note among the recent GMPEs are the ones developed under the recently completed Pacific Earthquake Engineering Research Center (PEER) NGA-West2 project and a number of European GMPEs published in 2014 (see Douglas 2014, for an overview of the latter).

The exclusion criteria adopted by the TI Team constitute a compromise between the strict criteria of Bommer et al. (2010) and the somewhat more lenient criteria by Cotton et al. (2006), supplemented by project-specific considerations regarding V_{s30}, style of faulting, treatment of hanging-wall effects, etc. The resulting exclusion criteria are listed below.

- The GMPE was published prior to the year 2000. This is to some extent a tool of convenience, reducing the equations to be evaluated to more manageable numbers; Bommer et al. (2010) found that nearly all pre-1996 GMPEs would be eliminated by several of the other criteria anyhow. Bommer et al.'s cutoff was shifted to 2000 to maintain the same relative ages.
- The GMPE was developed using a data set with fewer than 10 earthquakes per magnitude unit or fewer than 100 records in the first 100 km. Equations failing these criteria are considered to be inadequately constrained given the current size of the global strong-motion database. One of the main consequences of applying these criteria is to exclude GMPEs derived exclusively using data from small geographical regions (in which the bias of the small data sample is interpreted, without justification, as representing a clear and systematic regional difference in ground motion behavior).

- The GMPE was developed using a data set that either starts at a magnitude greater than 5.0 or does not extend to 7.5. Such models would require excessive extrapolation to the largest magnitudes covered by the Mmax distributions in the SSC model (see Chapter 8.0).
- The GMPE was developed using a regression technique that does not distinguish between- and within-earthquake components of variability. It is well known that ignoring within-event correlation may give undue weight to some earthquakes if the numbers of recordings are unevenly distributed among earthquakes.
- The GMPE's functional form does not include nonlinear magnitude scaling. Models with linear scaling do not extrapolate realistically to larger magnitudes.
- The GMPE's functional form does not include continuous V_{s30} scaling. This is necessary to facilitate the V_s-kappa adjustments to be performed in Section 9.3.
- The GMPE's functional form neither includes a hanging-wall (HW) term nor uses Joyner-Boore (R_{jb}) as its distance metric. This criterion was later strengthened to exclude GMPEs that consider HW effects implicitly through R_{jb}, because R_{rup} GMPEs with explicit HW terms are better at capturing HW effects for a broad range of dip angle, rupture depth, and Rx, as suggested by numerical modeling (Donahue and Abrahamson 2014) and by consideration of RMS distance (Chiou et al. 2000). This issue is further discussed in Section 9.4.2.
- The GMPE's functional form does not account for style of faulting. This is important because the SSC model indicates the presence of reverse faulting, as indicated in Section 8.3.
- The GMPE was derived by adjustment (referenced or hybrid) to another region. Having to apply an adjustment to a GMPE that has already been adjusted to a different target region compounds the uncertainty associated with the adjustments; it would be preferable to start with the original host GMPE and apply one set of adjustments.
- The GMPE was not developed for the shallow crustal environment. Ground motions from subduction-zone earthquakes are treated separately (see Sections 7.4.2 and 9.2.3).
- The GMPE does not cover the frequency range of interest for the project (0.1−100 Hz) or the density of frequency sampling complicates the calculation of spectral amplitudes for the frequencies needed.
- The GMPE has been superseded by new equations by the same or similar team of authors. The rationale for this criterion is that authors would not propose a new model if the previous were considered superior.

Table 7.26 lists the GMPEs that pass the criteria regarding publication date and applicability to shallow crustal environments, provides some background information about the host region for each GMPE, and then indicates whether each GMPE fails the other criteria and why.

Only seven GMPEs pass the full suite of selection criteria, namely AC10, ASB14, ASK14, BI14, BSSA14, CB14, CY14, and DE14. Models that use R_{jb} were dropped at a later stage in the project, as indicated earlier, leaving only ASK14, CB14, and CY14 (i.e., three NGA-West2 GMPEs that use rupture distance). However, some of the models dropped here are considered in Section 9.4 in order to inform the breadth of epistemic uncertainty.

Table 7.26. Selection of Crustal GMPEs

Author(s)	Code	Region	Decision	Rationale/Comments
Pankow and Pechmann (2004, 2006)	PP04	Extensional regions	Exclude	Highest magnitude: 7.2
McVerry et al. (2006)	McVea06	New Zealand	Exclude	Highest magnitude: 7.3
Zhao et al. (2006)	Zhea06	Japan	Exclude	Highest magnitude: 7.4
Hong and Goda (2007)	HG07	WUS	Exclude	Developed for spatial correlation
Abrahamson and Silva (2008, 2009)	AS08	Worldwide (mostly WUS)	Exclude	Superseded by ASK14
Boore and Atkinson (2008) and Atkinson and Boore (2011)	BA08'	Worldwide (mostly WUS)	Exclude	Superseded by BSSA14
Campbell and Bozorgnia (2008)	CB08	Worldwide (mostly WUS)	Exclude	Superseded by CB14
Chiou and Youngs (2008a)	CY08	Worldwide (mostly WUS)	Exclude	Superseded by CY14
Cotton et al. (2008)	Cea08	Japan	Exclude	Highest magnitude: 7.3
Aghabarati and Tehranizadeh (2009)	AT09	Worldwide	Exclude	Published by mistake
Akkar and Bommer (2010)	AB10	Europe	Exclude	Superseded by ASB14
Akkar and Çağnan (2010)	AC10	Turkey	Include	
Bindi et al. (2011)	Bea11	Italy	Exclude	Highest magnitude: 6.9
Abrahamson et al. (2014b)	ASK14	Worldwide (mostly WUS)	Include	
Boore et al. (2014)	BSSA14	Worldwide (mostly WUS)	Include	Uses R_{jb} to capture HW effects
Campbell and Bozorgnia (2014)	CB14	Worldwide (mostly WUS)	Include	
Chiou and Youngs (2014)	CY14	Worldwide (mostly WUS)	Include	
Idriss (2014)	Id14	Worldwide (mostly WUS)	Exclude	No HW term
Graizer and Kalkan (2011), Graizer et al. (2013)	GK13	Worldwide (mostly WUS)	Exclude	No HW term
Bradley (2013)	BR13	New Zealand	Exclude	Adaption of NGA GMPEs to NZ
Akkar et al. (2014b,c)	ASB14	Europe	Include	Tentative inclusion: very limited data from reverse earthquakes; uses R_{jb} to capture HW effects
Bindi et al. (2014a, b)	BI14		Include	Uses R_{jb} to capture HW effects
Derras et al. (2014)	DE14	Mostly Turkish and Italian data	Include	Uses R_{jb} to capture HW effects. Retained despite unconventional (artificial neural-network) methodology used
Hermkes et al. (2014)	HE14	Europe	Exclude	An investigation of methodology, not really a mature GMPE
Bora et al. (2014)	SB14	Europe	Exclude	Mainly a methodology paper
Agustsson et al. (2008)	AG08	Iceland	Exclude	M 3.5-6.5 only, PGA and PGV only, no V_{s30} scaling
Ólafsson and Sigbjörnsson (2012)	OL12	Iceland	Exclude	Uses only data in a narrow M range; Iceland-specific attenuation
Ornthammarath et al. (2011)	OR11	Iceland	Exclude	Uses no data above 6.5

PGA = peak ground acceleration; PGV = peak ground velocity; WUS = Western United States.

7.4.2 GMPEs for Subduction Earthquakes

This section presents an overview of existing GMPEs for subduction earthquakes, along with the approach for selecting GMPEs that will be considered for the GMC model. Empirical GMPEs (i.e., those that are based only on recorded data) and GMPEs that are based on numerical simulations are reviewed separately.

7.4.2.1 Empirical GMPEs

The compilation of a database of empirical GMPEs for possible use in this project involves the evaluation of published equations in terms of their applicability for this project and their inherent quality. The former is based on whether the data used to derive the GMPE are obtained in similar tectonic environments. The latter can be judged by the ability of the equation to extrapolate outside of its data range and by its stability in the presence of additional data. The approach of Bommer et al. (2010) for selection of ground motions was adopted. This approach proposes the use of pre-established objective criteria to exclude GMPEs from a comprehensive initial list.

Candidate GMPEs are compiled from a review of the existing literature. The compilations of Douglas (2011) and Arango et al. (2012) were particularly useful in the search of existing GMPEs. The search of valid GMPEs was stopped in July 2012 (the date of WS1). The criteria adopted for exclusion of models is based on the criteria suggested by Bommer et al. (2010), with modifications to make the criteria more suitable for this project. The final criteria are listed below along with a brief explanation for their inclusion.

1. Not developed specifically for subduction-zone earthquakes or not using data from subduction-zone earthquakes. This criterion is self-explanatory; however, despite its simplicity it is not easy to apply because some models are published without specific reference to the tectonic environment of the underlying ground motion data. We excluded GMPEs that did not specifically state that the model is applicable to subduction regions or that did not explicitly state that the underlying ground motion data corresponds to subduction regions.
2. Published before 1997. Bommer et al. (2010) originally proposed to exclude equations that are more than 15 years old. At the time of application of this exclusion criteria (July 2012, during WS1) that meant excluding GMPEs published prior to 1997.
3. Superseded by more recent publication. The rationale here is that model developers would not propose a new model if the previous models were considered superior.
4. Does not distinguish between interface and intraslab earthquakes. The more mature GMPEs for subduction earthquakes (e.g., Atkinson and Boore 2003) identify clear differences in distance attenuation for intraslab and interface earthquakes. For this reason, we exclude GMPEs that do not make this distinction.
5. Frequency range is not appropriate (not enough points at long periods, maximum period less than T = 2 sec). This criterion is necessary because the GMPEs must be used to generate spectra for the entire range of periods required for this project (Section 9.1.4). The initial criterion of T = 2 sec was meant only as a soft screening criterion, because the range of periods for this project is up to T = 10 sec. However, the use of such a strict criterion would have eliminated all but one of all available GMPEs. It was considered that, if necessary, spectral accelerations could be extrapolated to longer periods.

6. Not enough data. This criterion is formalized as having less than 10 earthquakes per unit magnitude and less than 100 recordings per 100 km (considering the range of applicability of the GMPE).
7. Distance and magnitude range are too restrictive, which is interpreted based on the scenarios that are relevant for this project:
    - Interface: Magnitude applicability not up to **M** 8.0
    - Intraslab: Magnitude applicability not up to **M** 7.5
    - Distance applicability not up to 300 km.
8. Not published in peer-reviewed publication (ISI-listed journals). This latter criterion was relaxed for models that were developed within a framework that ensured a strict level of peer review (e.g., SSHAC Level 3 projects).

A comprehensive list of GMPEs up to July 2012 is included in Table 7.27 along with any applicable elimination criteria.

Hong et al. (2009) and McVerry et al. (2006) were excluded because they were published in *Earthquake Engineering and Engineering Vibrations* and the *Bulletin of the New Zealand Seismological Society*, respectively. These publications were not ISI-listed at the time of the evaluation. In addition, the Hong et al. (2009) model was developed for the specific objective of studying the orientation dependence of spectral accelerations, and was not developed with the intent of using the model for engineering applications, which further justifies its exclusion. Moreover, the intraslab data in Hong et al. (2009) are the same as those used by Garcia et al. (2005), and the interface data are from a precursor to Arroyo et al. (2010); hence, the data used in the Hong et al. (2009) model are used in other models still under consideration.

A review of Table 7.27 shows that the exclusion criteria leaves only four models (Atkinson and Boore 2003; Zhao et al. 2006; Arroyo et al. 2010; and Abrahamson et al. 2014a). The Abrahamson et al. (2014a) model (which will be referred to from now on as the "BC Hydro" model) is included despite the fact that it is not yet published because it was developed within a SSHAC framework. The GMC TI Team decided to relax criterion 6 (not enough data) to allow for the inclusion of additional models (Youngs et al. 1997; Garcia et al. 2005; Lin and Lee 2008).

Two of the models merited further scrutiny. The model by Lin and Lee (2008) uses a single-stage regression and does not properly separate intra- and inter-event standard deviation. While this was not part of the initial exclusion criteria, such separation is considered important (Bommer et al. 2010) and for this reason the Lin and Lee (2008) model is excluded. The Youngs et al. (1997) model reports only total standard deviation, but the regression analyses did account for intra- and inter-event residual computations, and hence it is not excluded on this account. The distance attenuation in the Youngs et al. (1997) model was calibrated mostly with interface data and is not well constrained for intraslab earthquakes. In summary, the Lin and Lee (2008) model, both for interface and intraslab, and the Youngs et al. (1997) model for intraslab earthquakes are also excluded. The final list of pre-selected models is shown in Table 7.28.

Table 7.27. List of evaluated subduction GMPEs (those that were not excluded by Criteria 1 and 2) and criteria for exclusion.

GMPE	Criteria for Exclusion
Youngs et al. (1997)	6 (not enough data)
Atkinson and Boore (2003)	None
Garcia et al. (2005)	6 (not enough data)
McVerry et al. (2006)	6 (not enough data for interface [IF] earthquakes, OK for intraslab [IS] earthquakes) 8 (not peer reviewed)
Kanno et al. (2006)	4 (does not differentiate IF and IS; however, uses different equations for different hypocentral depths, which is an indirect way of identifying earthquake type). This GMPE also mixes interface and crustal events
Zhao et al. (2006)	None
Lin and Lee (2008)	6 (not enough data for Interface earthquakes, OK for intraslab earthquakes)
Arroyo et al. (2010)	None
BC Hydro (Abrahamson et al. 2014a)	8 (not peer reviewed, but developed within the BC Hydro SSHAC Level 3 project; BC Hydro 2011)
Atkinson (1997)	3 (superseded by Atkinson and Boore 2003)
Schmidt et al. (1997)	4 (does not differentiate IF and IS); 6, 7 (only 67 recordings) 8 (not peer reviewed)
McVerry et al. (2000)	3 (superseded by McVerry et al. 2006); 8 (not peer reviewed)
Shabestari and Yamazaki (1998, 2000)	4 (does not differentiate IF and IS); 8 (not peer reviewed)
Kawano et al. (2000)	4 (does not differentiate IF and IS); 6, 7 (only 67 recordings) 8 (not peer reviewed)
Kobayashi et al. (2000)	3 (superseded by Zhao et al. 2006); 4 (does not differentiate IF and IS) 8 (not peer reviewed)
Takahashi et al. (2000, 2004)	3 (superseded by Zhao et al. 2006); 8 (not peer reviewed)
Sunuwar et al. (2004)	4 (does not differentiate IF and IS); 7 (Maximum magnitude = 5.6)
Cepeda et al. (2004)	5 (three frequencies only); 6 (a modification of Atkinson and Boore, 2003, that uses only one earthquake sequence)
Sakamoto et al. (2006)	4 (does not differentiate IF and IS); 8 (not peer reviewed)
Tejeda-Jacome and Chavez-Garcia (2007)	7 (Maximum magnitude = 5.2)
Yuzawa and Kudo (2008)	4 (does not differentiate IF and IS); 8 (not peer reviewed)
Hong et al. (2009)	8 (not peer reviewed)
Goda and Atkinson (2009)	4 (does not differentiate IF and IS; however, uses different equations for different hypocentral depths, which is an indirect way of identifying earthquake type)
Gupta (2010)	6 (A modification of Atkinson and Boore, 2003, using 3 earthquakes and 56 recordings)
Boroschek and Contreras (2012)	5 Only PGA and three frequencies; 6 (only 117 recordings, 13 earthquakes); 8 (not peer reviewed)

Table 7.28. Pre-selected subduction GMPEs.

Model	Code	Type[a]	**M** Range[b]		Distance Range[b] (km)		Earthquakes		Recordings	
			IF	IS	IF	IS	IF	IS	IF	IS
Youngs et al. (1997)	Y97	IF	5–8.2 (>5)	5–7.8 (>5)	8.5–551 (10–500)	45–744 (10–500)	57	26	181	53
Atkinson and Boore (2003)	AB03	IF, IS	5.3–8.3 (5.5–8.3)	4.6–7.9 (6.0–7.6)	4–518 (0–300)	34–575 (0–200)	49	30	394	161
Garcia et al. (2005)	G05	IS	NA	5.2–7.4	NA	40 − 400	NA	16	NA	277
Zhao et al. (2006)	Z06	IF, IS	5–8.3[d]		0–300[c]		269[c]		1520	1725
Arroyo et al. (2010)	A10	IF	5–8	NA	20–400	NA	40	NA	418	NA
BC Hydro (2012)	BCH	IF, IS	6.0–8.4	5.0–7.9	(<300)	(<300)	63	43	960	2590

(a) Event type for which the model is applicable. IF = interface; IS = intraslab..
(b) Range given is the range in the data used in regressions. Values in parentheses are the range of applicability of the model as claimed by the authors (if different than data range). NA = not applicable.
(c) Not reported separately for IF and IS. Near-source scaling dominated by crustal earthquakes.
(d) Does not report earthquakes separately.

7.4.2.1.1 Characteristics of Selected Models

All of the pre-selected models predict PGA and 5% damped spectral acceleration, although some use absolute spectral acceleration, some use pseudo-spectral acceleration, and for some what they use is not clear. The predicted periods for these models are shown in Figure 7.68. The component definition of the spectral acceleration varies depending on the models. Table 7.29 lists the predicted variables for the selected models. All models except Youngs et al. (1997) report within-event (ϕ) and between-event (τ) standard deviation. The BC Hydro model also reports event-corrected single-station standard deviation (ϕ_{ss}).

The predictive variables of the selected models are given in Table 7.30. All of the models use rupture distance for interface earthquakes, and some use hypocentral distance for intraslab earthquakes. For the latter, the distances are generally large enough that the differences between hypocentral and rupture distances are small enough and can be ignored. Hypocenter depth is used as a predictor variable for all the intraslab models and for some of the interface models. Most models incorporate site effects through discrete site classes. The important exception is the BC Hydro model, which incorporates site effects through the average shear-wave velocity in the upper 30 m of the profile (V_{S30}). The use of a continuous variable for the prediction of site effects is important for developing V_s-κ correction factors (Section 9.3.3).

In addition to the predictive variables listed in Table 7.30, the BC Hydro model differentiates between sites located on either side of the volcanic arc that exists inland from subduction regions. This responds to the observation of different attenuation rates in the backarc and forearc regions. This effect is also discussed by McVerry et al. (2006) and Zhao (2010). The selected models are also differentiated with respect to the geographical location of the data set used (global or regional), and on the type of the ground motion data underlying the model (Table 7.31). The only truly global models are those of Youngs et al. (1997), Atkinson and Boore (2003), and the BC Hydro model.

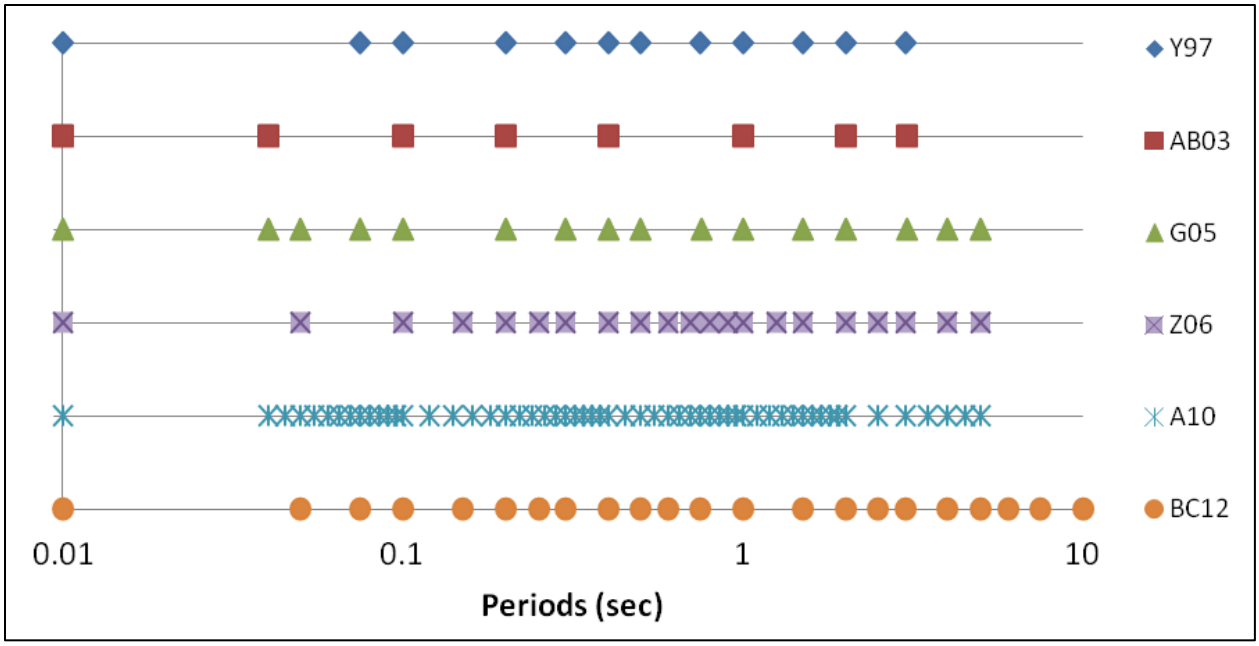

Figure 7.68. Applicable oscillator periods of the selected subduction GMPEs.

Table 7.29. Predicted variables for selected subduction GMPEs.

Model	Predicted Parameter[(a)]	Component Definition[(b)]	Sigmas
Youngs et al. (1997)	PGA, SA	GM	σ_{tot} (reported)
Atkinson and Boore (2003)	PGA, pSA	R	ϕ and τ
Garcia et al. (2005)	PGA, PGV, pSA	QM	ϕ and τ
Zhao et al. (2006)	PGA, SA	GM	ϕ and τ
Arroyo et al. (2010)	PGA, pSA	QM	ϕ and τ
BC Hydro (2012)	PGA, pSA	GM	ϕ, τ, and ϕ_{ss}

(a) PGA = peak ground acceleration. SA = spectral acceleration (5% damping); pSA = pseudo-spectral acceleration (5% damping).
(b) GM = geometric mean; QM = quadratic mean; R = random component.

Table 7.30. Predictive variables for selected subduction GMPEs.

Model	Distance Measure		Use of Hypocenter Depth		Site Response
	Interface	Intraslab	Interface	Intraslab	
Youngs et al. (1997)	R_{rup} for **M** > 7.5	R_{hyp}	Yes	Yes	Discrete (2 classes) Separate regressions
Atkinson and Boore (2003)	R_{rup} (estimated in some cases using Wells and Coppersmith, 1984)		Yes	Yes	Discrete (4 classes) Nonlinearity included
Garcia et al. (2005)	NA	R_{rup} for **M** > 6.5	NA	Yes	Rock sites (Mexico)
Zhao et al. (2006)	R_{rup} (for available EQs), R_{hyp} otherwise		Yes	Yes	Discrete (4+ classes) Based on V_{S30}, site period
Arroyo et al. (2010)	R_{rup} for **M** > 6.0	NA	No	NA	Rock sites (Mexico)
BC Hydro (2012)	R_{rup}	R_{hyp}	No	Yes	Continuous (V_{S30}) Nonlinearity included

Table 7.31. Source of data and applicable earthquake type for selected subduction GMPEs.

Model	Source	Type[(a)]	Discriminant[(b)]
Youngs et al. (1997)	Global	IF, IS	Faulting mechanism and H (H > 50 km is IS)
Atkinson and Boore (2003)	Global	IF, IS	Faulting mechanism and H, as in Youngs et al. (1997)
Garcia et al. (2005)	Central Mexico	IS	
Zhao et al. (2006)	Japan (+ 208 crustal overseas)	IF, IS, Crustal	Faulting mechanism and H
Arroyo et al. (2010)	Forearc Mexico	IF	
BC Hydro (2012)	Global	IF, IS	Faulting mechanism and H

(a) IF = interface; IS = intraslab.
(b) H = hypocenter depth.

A relevant consideration for model selection is how the models apply magnitude and distance scaling. This is an important consideration because the models may have to be extrapolated to large magnitudes and distances for application at Hanford Site. The magnitude scaling of most of the models under consideration includes cubic or quadratic terms, or is capped at large magnitudes, implying that the large-magnitude scaling is milder than for smaller magnitudes. The exceptions are the models of Garcia et al. (2005) and Arroyo et al. (2010), which only have linear magnitude scaling. Table 7.32 summarizes the magnitude scaling terms. Table 7.32 also includes a description of the geometric and anelastic attenuation terms for each of the GMPEs. Anelastic attenuation is particularly important because the absence of anelastic attenuation implies unrealistically low attenuation at long distances. Neither the Youngs et al. (1997) nor the Arroyo et al. (2010) models include anelastic attenuation.

Table 7.33 lists how each model incorporates hypocentral depth scaling. All of the models for intraslab earthquakes incorporate a linear depth scaling. Table 7.33 also lists how the model scales for intraslab earthquakes.

Table 7.32. Magnitude and distance scaling for selected subduction GMPEs.

Model	Magnitude Term $f(\mathbf{M})$	NS Saturation	Geometric Spread. Coeff (θ_1)	Anelastic Attenuation Coefficient
Youngs et al. (1997)	Linear and cubic terms	Y97	Const.	None
Atkinson and Boore (2003)	Linear (capped at large **M**)	AB03	Const.	**M** dependent
Garcia et al. (2005)	Linear	AB03	Const.	Const.
Zhao et al. (2006)	Linear and quadratic	Y97	$\theta_1 = 1$	Const.
Arroyo et al. (2010)	Linear	Complex, **M** dependent	Const.	None
BC Hydro (2012)	Quadratic Break in scaling at large **M**	Y97	**M** dependent	Const.

Table 7.33. Scaling for depth and for intraslab term for selected subduction GMPEs.

Model	Depth Scaling	H Range (km)	Scaling for Intraslab Term
Youngs et al. (1997)	Linear, constant with period	IF: H < 50 IS: H < 229	Constant term
Atkinson and Boore (2003)	Linear, capped at H = 100 km	IF: 11–59 IS: 32 (4)–100 (181)	Separate Coefficients for IF and IS
Garcia et al. (2005)	Linear (controlled by three deep earthquakes)	35–138	NA
Zhao et al. (2006)	Linear, capped at H = 125 km	IF: 10–50 IS: 40–162	Period-dependent: constant term and attenuation term
Arroyo et al. (2010)	None (Interface)	10–29	NA
BC Hydro (2012)	Linear for Intraslab None for Interface	IF: H < 50 IS: H < 194	Period-dependent: constant term and attenuation term

IF = interface; IS = intraslab; NA = not applicable.

7.4.2.1.2 Additional Considerations for Model Selection

The pre-selected models (Table 7.28) constitute a set of reliable models for consideration in this project. However, most of these models present significant shortcomings when considering application for hazard studies at Hanford. The Youngs et al. (1997) model is the oldest of the considered models and was developed with significantly less data than the Atkinson and Boore (2003) and the BC Hydro models. Moreover, the Youngs et al. (1997) interface model does not have an anelastic attenuation term, which may lead to unrealistic attenuation at large distances.

The Garcia et al. (2005) and Arroyo et al. (2010) models are both developed using only regional data and have a functional form with limited extrapolation power. For example, both of these models include only linear magnitude terms, and the Arroyo et al. (2010) model does not have an anelastic attenuation term.

The Atkinson and Boore (2003) model and the Zhao et al. (2006) models are both robust in terms of their underlying data and their functional form. However, neither of these models includes continuous

V_{S30} scaling. In addition, the Atkinson and Boore (2003) model includes predictions only up to 3 sec, which, if applied in this study, would imply the need to extrapolate for predictions at longer periods.

Additional considerations for model selection can be inferred from testing the performance of a model against particular data set. A rigorous methodology to do ground motion testing was proposed by Scherbaum et al. (2004, 2009). Two previous studies (Arango et al. 2012; Beauval et al. 2011, 2012) have performed such testing on a set of subduction models that included the BC Hydro model.

Arango et al. (2012) evaluated the applicability of GMPEs to the South and Central American subduction zones using the maximum likelihood approach of Scherbaum et al. (2004). The authors evaluated the following models: BC Hydro, Arroyo et al. (A10; 2010), Atkinson and Boore (AB03; 2003), Garcia et al. (G05; 2005), McVerry et al. (M06; 2006), Youngs et al. (1997), and Zhao et al. (Z06; 2006). For interface earthquakes, the Z06 model fits the observational data best. The Y97 model is mostly rated as intermediate (Class B and C in the Scherbaum et al. 2004, methodology). The AB03 and the M06 models perform poorly (Class D) for some subsets of the data or for some period ranges. The BC Hydro model has intermediate performance at short periods (<1 sec), and performs well (Class A) at longer spectral ordinates. For intraslab earthquakes, the BC Hydro model is the only model that consistently performs well.

Beauval et al. (2011, 2012) used the Scherbaum et al. (2009) method to evaluate regional differences in subduction ground motions using interface data from Japan, Taiwan, Central and South America, and Mexico, and intraslab data from Greece, Japan, and Taiwan. The authors conclude that the global models (BCH, Y97 and AB03) provide the best fit to all the data on average. Beauval et al. (2012) repeat their evaluation using the global BC Hydro data set (Section 7.1.3) and conclude that the best–fitting model is, unsurprisingly, the BC Hydro model, followed by the Z06 model.

All of these considerations indicate that the strongest model for subduction zones is the BC Hydro model. A simpler argument for the adoption of the BC Hydro model for this study is that this model was created after an evaluation of existing models during the SSHAC Level 3 BC Hydro PSHA study (BC Hydro 2012) concluded that none of the existing models was adequate for use in that study. Moreover, the BC Hydro data set (discussed in Section 7.1.3) was constructed by pooling together ground motion data from all previous studies, including the Youngs et al. (1997), the Atkinson and Boore (2003),and the Zhao et al. (2006) data sets. The BC Hydro model is further evaluated in Section 9.2.3.

7.4.2.2 Simulation-Based GMPEs

Subduction zones are capable of generating earthquakes of magnitudes greater than 9. Prior to the 2010 Maule (**M** 8.8) and 2011 Tohoku (**M** 9.0) earthquakes, no data had been recorded for these magnitudes. For this reason, ground motion models based on stochastic simulations were developed for estimating hazard due to interface subduction earthquakes. Simulation-based GMPEs have also been used to constrain the large-magnitude scaling of empirical GMPEs. For example, the large-magnitude scaling of the BC Hydro model is entirely controlled by simulations.

In the context of this project, simulation-based GMPEs can play various roles. First of all, these models must be given consideration for potential inclusion in the GMC logic tree. However, even if GMPEs are not considered for inclusion in the logic tree, they can be used to assess the range of epistemic uncertainty in the final GMC model for subduction earthquakes. This is particularly important when

considering that all of the models discussed previously (with the exception of the BC Hydro model) were shown to be deficient in one or more ways. Another potential use of simulation-based GMPEs is for constraining anelastic attenuation for spectral ordinates at long response periods. This would be required because of the uncertainties related to the degree of anelastic attenuation in the data-poor Cascadia subduction zone. For this purpose, the absolute values of spectral acceleration predicted by these equations may not be particularly important because the focus would be on the relative decay of these accelerations over distance, if we were to simply adopt the ratio of spectral ordinates at larger distances to those nearer the source. If, however, we wish to use the actual values of spectral acceleration at distance, then the absolute amplitudes do become important.

Only two stochastic GMPEs for response spectral ordinates that might be suitable for this application have been identified—Gregor et al. (2002) and Atkinson and Macias (2009)—and these are the main focus of the evaluation. Both of these GMPEs are exclusively for the prediction of motions from large interface earthquakes, so this exercise does not consider any models that could constrain or inform ranges of epistemic uncertainty associated with motions from intraslab earthquakes. However, the interface seismicity is the dominant contributor to the hazard at the Hanford Site. Moreover, whereas the largest earthquakes envisaged in the SSC model for the intraslab source (**M**~7.5) are covered by recordings of earthquakes such as the magnitude 7.7 El Salvador earthquake of 2001, the largest interface earthquakes (**M** 9.4) exceeds any earthquake for which there are recordings; it is precisely for such cases that the estimate of epistemic uncertainty becomes particularly important and this is where the stochastic models may be particularly helpful.

Heaton and Hartzell (1989) produced estimates of response spectra at various distances from the coast due to large-magnitude Cascadia earthquakes, but they did not derive a GMPE from their results. Neither the paper by Gregor et al. (2002) nor that by Atkinson and Macias (2009) even cites this earlier study, which may reflect the fact that despite its title indicating a specific focus on Cascadia, it is essentially about estimating the ground motions to be expected from a great earthquake (such as the 1960 **M** 9.5 earthquake) on the Chilean subduction zone. Heaton and Hartzell (1989), based on earlier work (Heaton and Hartzell 1986), conclude that great earthquakes on the south Chilean and Cascadia subduction zones would be similar. They generate ground motions for hypothetical great subduction earthquakes using empirical Green's functions, for which they adopt recordings from earthquakes in Japan and Alaska. In a sense, there is very little that is Cascadia-specific about the study.

7.4.2.2.1 Gregor et al. (2002)

This study makes use of the stochastic finite-fault model of Silva et al. (1990), which is calibrated against recordings from the **M** 8 earthquakes of 1985 at Michoacán (Mexico) and Valparaíso (Chile). The model showed very good agreement with the data for frequencies higher than 0.5 Hz but for lower frequencies—which are of greatest concern to us at Hanford—there was significant over-prediction. Gregor et al. (2002) also note that for sites at short distances, the recorded motions are over-estimated, and that this had also been found previously for megathrust earthquakes by Youngs et al. (1997).

For the hypothetical Cascadia interface earthquakes of **M** 8, 8.5, and 9, they model the sources as 9° dipping planes of 90-km width, estimating the lengths as 150, 450, and 1,100 km from Wells and Coppersmith (1994), which was derived using only crustal earthquakes and excluding subduction interface earthquakes. The dip angle is consistent with the model adopted by the SSC TI Team for Hanford, because in common with both the stochastic GMPEs, it is also derived from the model of Flück

et al. (1997). The fault lengths and widths yield areas that agree very closely with those predicted by the subduction scaling relationships of Strasser et al. (2010) for **M** 8 and **M** 8.5, but are 20% smaller for the largest earthquakes. The slip on the source is randomized with respect to rupture initiation and slip model.

The assumed geometric spreading model and the anelastic attenuation are adopted from the estimate of Atkinson (1995) for western Washington, with Q_0 at 380 and $\eta = 0.39$. This geometrical spreading model is null (no spreading) for shallow earthquakes (<10 km) and for other earthquakes a simple R^{-1} decay. The Q_0 value was randomized in the simulations, while the coefficient of frequency dependence was held constant. An important point to note here is that in her more recent model (see below), Gail Atkinson does not use or even mention this Q model but rather one for California that implies faster attenuation. The Q values around Hanford presented in the recent paper by Philips et al. (2013)—averaged over a distance of 300 km for the range of azimuths that would represent wave paths from great Cascadia earthquakes to the site (Section 7.5)—are much closer to those in Atkinson and Macias (2009).

The crustal model used to obtain amplification functions is one derived for northwestern Oregon and southwestern Washington, which may therefore be somewhat different from those that would be appropriate to the location of the Hanford Site in eastern Washington. Gregor et al. (2002) note that their crustal model is of lower velocity than the one used by Youngs et al. (1997) and that this will have led to larger crustal amplification factors in the more recent model.

The simulations are performed for soil and rock sites, the latter nominally corresponding to the CRB and a V_{S30} of just 363 m/sec, with a site kappa of 0.04 sec. Although the velocity profiles are randomized in their simulations, the average value is very low compared to the reference baserock condition adopted for the Hanford PSHA model.

The simulations were conducted for each source configuration for two lines of points perpendicular to the mid-point and end-point of the fault rupture, with points at distances of 10, 20, 50, 100, 200, and 500 km. One interesting feature of this study is that to derive a GMPE, it was necessary to apply a weighting scheme to the data from each line of points, to avoid oversaturation in the predictions. Gregor et al. (2002) note that such oversaturation was present in the nonparametric model for PGA from Cascadia earthquakes proposed by Anderson (1997). Gregor et al. (2002) argue in favor of including saturation in the magnitude scaling but not oversaturation, noting that "*from an engineering design viewpoint*" the latter "*is difficult to justify.*" Oversaturation has been seen in data from crustal earthquakes at short periods (e.g., Akkar and Bommer 2007), and it is possible that it also occurs for subduction earthquakes as one goes to very large magnitudes. A number of studies have noted that a significant part of the radiated moment from megathrust subduction earthquakes is likely to be manifest in very long-period motions (e.g., Heaton and Hartzell 1989; Zhao 2011), which would certainly contribute to saturation at least.

Gregor et al. (2002) use their simulated motions to derive GMPEs for "rock" and "soil" sites, using regression analysis with a functional form that includes nonlinear magnitude scaling and magnitude-dependent attenuation. They present coefficients at 25 response periods between 0.01 and 5.0 sec.

7.4.2.2.2. Atkinson and Macias (2009)

This study has many features in common with Gregor et al.'s (2002) general approach for developing the GMPEs. The stochastic finite-fault method of Motazedian and Atkinson (2005) is adopted and validated against recordings from the 2003 **M** 8.1 Tokachi-Oki (Japan) earthquake and four of its aftershocks. The simulations are unbiased with regard to the recordings at frequencies from 0.1 to 10 Hz, without any apparent over-estimation at short distances.

The simulations are performed for Cascadia interface earthquakes with magnitudes of **M** 7.5, 8, 8.5, and 9. The model for the subduction interface is also based on Flück et al. (1997) with a 90-km fixed fault width, although a narrower width was used at **M** 7.5 and an alternative second value of 150 km was used for the **M** 9 scenarios. Rupture dimensions were estimated using Wells and Coppersmith (1994), as well as other relationships, but the dimensions are not reported (only shown graphically). Based on analysis of recordings from a number of subduction interface earthquakes, a range of stress drops is estimated. The range has a median value of 90 bars, but values in the simulations are allowed to range from 30 to 150 bars; this uncertainty leads to a ±50% uncertainty in the simulated response spectral ordinates. The hypocentral location and slip distribution are also randomized in the simulations.

The attenuation model includes geometrical spreading proportional to R^{-1} (spherical) up to 40 km and $R^{-0.5}$ (cylindrical) at greater distances. The Q model has a value for Q_0 of 180 and $\eta = 0.45$, which are much closer to the Philips et al. (2013) values than those used by Gregor et al. (2002). The values used are those from Atkinson and Silva (2000) for California, and it is argued that the slower rates of attenuation seen in Mexico are a genuine feature of that subduction zone, and the more rapid attenuation rate in Japan is the result of domination by backarc conditions. As noted earlier, it is of interest that Atkinson and Macias (2009) do not even mention the attenuation model of Atkinson (1995) that was adopted by Gregor et al. (2002). They do note, however, that there is very considerable uncertainty in the attenuation model, which at a distance of 100 km is already a factor of 2. They conclude that deriving subduction GMPEs by combining data from several regions may not be a good idea in view of apparent regional differences in attenuation characteristics.

Simulations are performed for a range of sites across a 180° range of azimuths from the strike (in 30° intervals) and distances of 30, 60, 100, 150, 200, and 400 km. The crustal velocity model used is that for a coastal location (Victoria) and the near-surface condition is a NEHRP B/C boundary site with V_{S30} = 760 m/s, with a kappa value of 0.02 sec.

A GMPE is derived for the horizontal geometric mean spectral acceleration at 24 response periods from 0.05 to 10.0 sec, plus PGA. The functional form includes nonlinear magnitude scaling and a magnitude-dependent near-source saturation term.

7.4.2.2.3. Discussion

The two studies reviewed are both published by distinguished researchers in this field and are also published in one of the most prestigious peer-reviewed journals. In a sense, one might consider that an evaluation of whether or not the models should be used is somewhat redundant, because to completely reject them could be interpreted to imply that the review process they underwent was flawed. However, the evaluation of the models for the Hanford project is not focused on the general question of whether or

not the equations are usable, but on more specific issues. The potential usefulness of these two stochastic GMPEs to the Hanford PSHA depends on the answers to three questions:

1. Do the models capture the regional attenuation at longer distances better than the BC Hydro model?
2. Do the models capture the magnitude scaling for very large interface earthquakes not included in the BC Hydro model?
3. If the answer to either of these questions is positive, can we make use of the models in our GMC logic tree and, if so, how?

The comparison with the BC Hydro model is based on the above evaluation of empirical GMPEs, which concluded that the BC Hydro model is the strongest of all the available GMPEs.

The answer to Question 1 is that whereas the Gregor et al. (2002) model uses an attenuation model derived for the Cascadia region, the author of that model does not make use of it in later studies, Atkinson (personal communication, 2014) indicates that the values of Atkinson (1995) were superseded by Atkinson and Silva (2000). Atkinson (2005) suggests the use of California GMPE models for crustal events in Casacadia, modified only for site effects. Atkinson and Macias (2009) adopted an attenuation model for California, for reasons that are not explained or discussed at any length. Although the Q model happens to be in general agreement with that of Philips et al. (2013), the attenuation model does not appear to have been calibrated for the region; the study was focused on three sites closer to the subduction zone rather than at the distances relevant to the Hanford Site, and therefore the impact of the attenuation model was perhaps less critical. Nonetheless, what Atkinson and Macias (2009) do conclude that is highly relevant for Hanford is that there is very considerable uncertainty in the attenuation model, something that needs to be reflected in our model.

Question 2 is actually redundant because the large-magnitude scaling of the BC Hydro model is actually inferred from the stochastic GMPEs themselves, particularly the Gregor et al. (2002) model.

The responses to Questions 1 and 2 are therefore essentially negative, which renders the third question moot. However, if it were decided that either or both of these stochastic models should be used either directly in the logic tree or to make comparisons with the GMC model for interface subduction earthquakes, there would be some challenges. One of these is that in both cases the models would need to be adjusted to the Hanford reference site condition, which is very different from the "rock" of Gregor et al. (2002) and the much stiffer "firm ground" condition of Atkinson and Macias (2009). An additional challenge arises from the frequency ranges covered, although the extrapolation of coefficients at missing short periods in Atkinson and Macias (2009) is facilitated by the inclusion of a model for PGA. The limitation of the Gregor et al. (2002) model not extending to periods greater than 5 sec would be difficult to overcome.

7.4.3 Existing Models for Single-Station Sigma

This project will invoke the use of a single-station sigma within the framework of a partially non-ergodic PSHA (Rodriguez-Marek et al. 2014). The justification for the use of single-station sigma is given in Sections 9.1 and 9.5. In this section, we focus on discussing existing models for single-station sigma.

The concept of partially non-ergodic PSHA and the associated single-station sigma was first formulated by Anderson and Brune (1999), but only the recent increase in ground motion data has

allowed for the computation of single-station sigma and the development of models for this component of variability (e.g., Chen and Tsai 2002; Atkinson 2006; Morikawa et al. 2008; Lin et al. 2011; Rodriguez-Marek et al. 2011; Ornthammarath et al. 2011; Chen and Faccioli 2013; Luzi et al 2014). In this review we focus on the model by Rodriguez-Marek et al. (2013), which was developed for the Pegasos Refinement Project (PRP; Renault et al. 2010) in Switzerland, and the model developed for the Thyspunt Nuclear Siting Project (TNSP; Bommer et al. 2014) in South Africa (Rodriguez-Marek et al. 2014). The focus on these two models is justified because the Rodriguez-Marek et al. (2013) model was developed using a global data set that encompasses most of the data used in the other publications. The TNPS model is a slight update of the Rodriguez-Marek et al. (2013) model and the differences are presented and discussed.

The single-station sigma model is built from two components, the event-corrected single-station standard deviation (ϕ_{ss}; hereafter simply referred to as single-station phi) and the inter-event (or between-event) standard deviation (τ) as given by

$$\sigma_{ss} = \sqrt{\phi_{ss}^2 + \tau^2} \tag{7.15}$$

Both the Rodriguez-Marek et al. (2013) model and the TNPS model adopted between-event standard deviations computed from existing GMPEs, hence the models for this component are not discussed here, and the focus is on the models for single-station phi.

7.4.3.1 The Rodriguez-Marek et al. (2013) Model for ϕ_{ss}

This model was derived from data compiled as part of the PRP (Renault et al. 2010), and hence will be referred to as the PRP model. Data for the PRP database were provided in the form of ground motion residuals and station and earthquake metadata by different GMPE developers. The California data were provided by Dr. Norm Abrahamson. These residuals are from the Chiou et al. (2010) model for small-magnitude earthquakes and the Abrahamson and Silva (2008) model for larger-magnitude earthquakes. The Taiwan data were provided by Dr. Norm Abrahamson and are from the Lin et al. (2011) model. The remaining residuals are from publications by Edwards and Fäh (2013) for Switzerland, Rodriguez-Marek et al. (2011) for Japan, and Akkar et al. (2010) for Turkey. Station metadata for all regions except Switzerland include the average shear-wave velocity over the upper 30 m (V_{S30}).

Developers provided both total residuals of pseudo-spectral acceleration (5% damping), as well as the partition of these residuals into between-event and within-event components. These residuals are derived from GMPEs that all predict the geometrical mean of the pseudo-spectral acceleration. Depending on the original data set quality and developer choices, the residuals have been computed for different periods. Three periods (PGA, 0.3 sec, and 1 sec) are common to all the selected GMPEs. The three main residuals data sets (California, Taiwan, and Japan) are based on GMPEs using the moment magnitude (**M**) and closest distance to the rupture, which allows for comparison of magnitude and distance dependencies.

Only recordings from earthquakes recorded by at least by five stations, and from stations with at least five recordings, were used in the analysis of single-station sigma. This criterion was adopted by Rodrigiez-Marek et al. (2013) to ensure that the estimates of site and event terms are stable. Table 7.34 lists the number of recordings in each of the regions, both for the entire set of residuals provided by the developers, and for a subset of magnitude and distance of engineering interest (e.g., $M \geq 5.0$ and

$R_{rup} \leq 200$ km). The magnitude-distance distribution of the data is shown in Figure 7.69. Note that the data distribution is not even. Turkey provides a low number of recordings and contributes little weight to the model. Switzerland provides no recordings to the magnitude and distance range of interest to typical engineering projects. Taiwan has more than double the number of sites than all other regions, but the largest magnitude in the Taiwanese data set is 6.3; hence, this region does not contribute to constrain the magnitude-dependent models at large magnitudes.

Table 7.34. Number of recordings in the PRP database. The selected magnitude and distance range is $\mathbf{M \geq 5}$ and $\mathbf{R \leq 200}$ km.

	California		Switzerland		Taiwan		Turkey		Japan		All Regions	
T (s)	All M, R	Sel. M, R	All M, R	Sel. M, R	All M, R	Sel. M, R	All M, R	Sel. M, R	All M, R	Sel. M, R	All M, R	Sel. M, R
PGA	15295	936	832	0	4756	2843	145	145	3234	1137	24262	5061
0.1	0	0	3148	0	4756	2843	145	145	3234	1137	11283	4125
0.2	0	0	3514	0	0	0	145	145	3234	1137	6893	1282
0.3	15295	936	0	0	4756	2843	145	145	3234	1137	23430	5061
0.5	0	0	3145	0	4756	2843	145	145	3234	1137	11280	4125
1	15287	928	2108	0	4753	2840	145	145	3234	1137	25527	5050
3	0	0	0	0	4320	2539	100	100	0	0	4420	2639

Figure 7.70 shows the ϕ_{ss} values computed independently for each of the five regions and for all regions together. For comparison, the ergodic within-event standard deviation (ϕ) is also shown. Observe that the variability in the ergodic ϕ between regions is significantly larger than the variability of ϕ_{ss} between regions; in fact, the value of ϕ_{ss} appears to be largely region-independent. This observation is very relevant to the Hanford PSHA study because it reinforces the possibility of importing ϕ_{ss} models from other regions to the Hanford Site. To reinforce this point, Figure 7.71 shows a comparison of the ϕ_{ss} values obtained in the PRP study with those of other studies. Figure 7.71 includes results from Atkinson (2006) for California, Atkinson (2013) for the Eastern United States, Lin et al. (2011) for Taiwan, Anderson and Uchiyama (2011) for the Guerrero array in Mexico, and Abrahamson et al. (2014a) for a global data set of subduction region earthquakes. The data of Abrahamson et al. (2014a) are dominated by recordings from Taiwan and Japan. The uniformity of ϕ_{ss} values is striking; while some of these studies used similar data sets (or a subset of the data set used in the PRP study), the studies of Abrahamson et al. (2014a), Anderson and Uchiyama (2011), and Atkinson (2013) are based on data from different tectonic environments (e.g., subduction-zone earthquakes for the first two, and a SCR for the latter). Observe that an average value of $\phi_{ss} = 0.45$ is a good fit to the data across all periods. Note that σ_{ss} values have a larger variability across studies, in particular for the data set of Abrahamson et al. (2014a). This is expected because of the contribution of the between-event variability to σ_{ss} and the fact that the between-event variability is larger for data sets that include earthquakes of various tectonic regions.

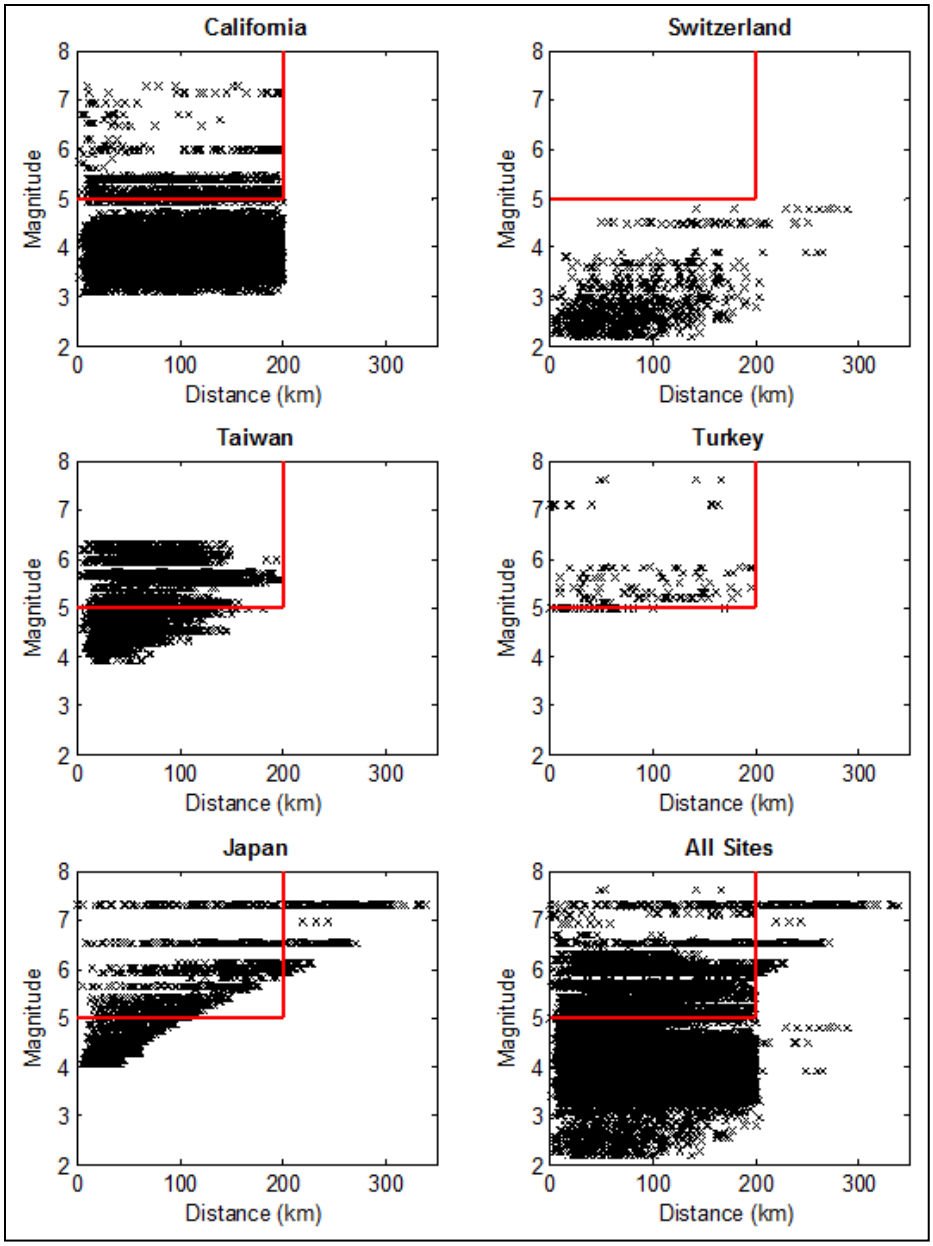

Figure 7.69. Magnitude-distance distribution of the different data sets. The red lines identify regions of typical engineering interest.

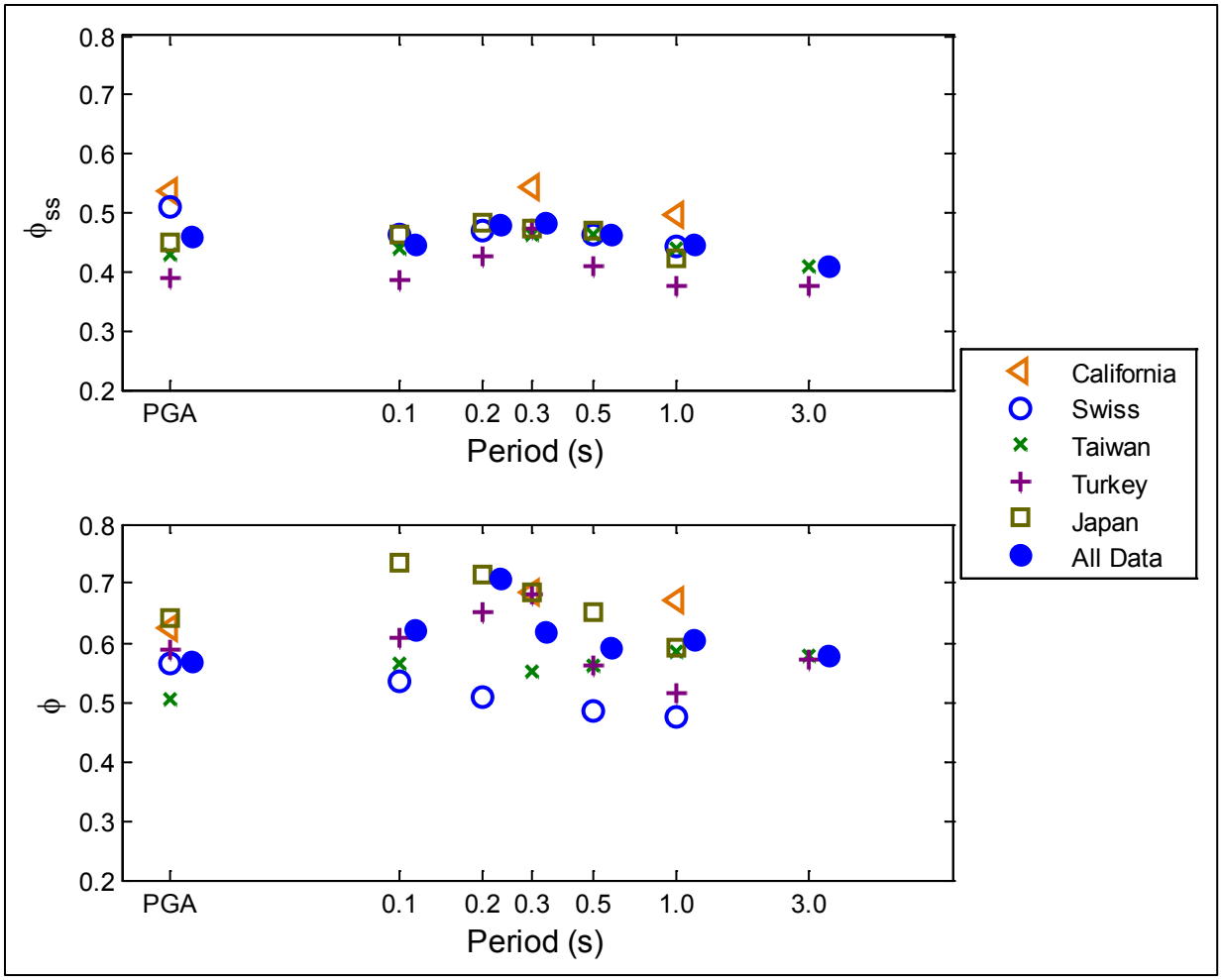

Figure 7.70. Event-corrected single-station standard deviation ($\boldsymbol{\phi_{ss}}$, top plot) and ergodic within-event standard deviations ($\boldsymbol{\phi}$, bottom plot). Standard deviations are computed for recordings with $\mathbf{M \geq 4.5}$ and $\mathbf{R_{Rup} \leq 200}$. The solid circle shows the values for the entire data set and is offset in the x-axis only for clarity.

The PRP models were based on the following observations (Rodriguez-Marek et al. 2013):

- Single-station phi shows a magnitude dependency with values decreasing from a maximum at a magnitude of about 5 to lower values at a magnitude of about 7.
- Single-station phi shows distance dependence for small magnitudes.
- There is no dependency of single-station phi on shear-wave velocity.

Based on these observations, four separate models were proposed: a constant-ϕ_{ss} model, a magnitude-dependent model, a distance-dependent model, and a magnitude and distance-dependent model. The constant ϕ_{ss} model is given in Table 7.35. All other models are briefly summarized below.

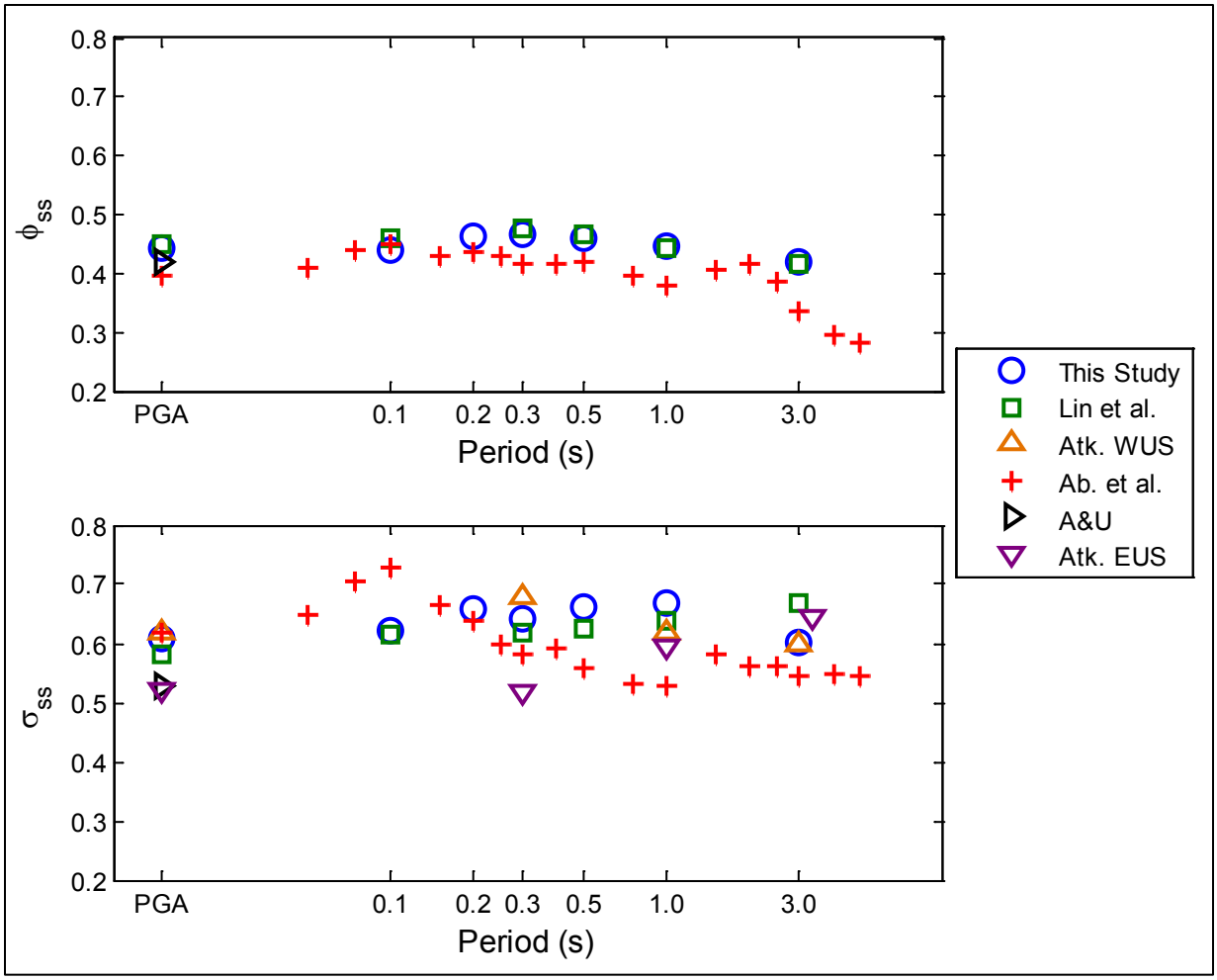

Figure 7.71. Comparison of event-corrected single-station standard deviation ($\boldsymbol{\phi_{ss}}$, top plot) and single-station standard deviation ($\boldsymbol{\sigma_{ss}}$, bottom plot) from Rodriguez-Marek et al. (2013; labeled "this study") with other published studies: Lin et al. (2011) using data from Taiwan; Atkinson (2006, denoted by Atk. WUS) using data from California; Abrahamson et al. (2014, denoted by Ab. et al.) using global data from subduction regions, but dominated by Taiwanese data; Anderson and Uchimaya (2011, denoted by A&U) using data from the Guerrero Array in Mexico; and Atkinson (2013, denoted by Atk. EUS) using data from the Charlevoix region in Canada.

7.4.3.1.1. Magnitude-Dependent Model

The magnitude-dependent ϕ_{ss} model is given by

$$\phi_{ss}(M_w) = \begin{cases} \phi_{1M} & for\ M_w < M_{c1} \\ \phi_{1M} + (\phi_{2M} - \phi_{1M})\left(\frac{M_w - M_{c1}}{M_{c2} - M_{c1}}\right) & for\ M_{c1} \le M_w \le M_{c2} \\ \phi_{2M} & for\ M_w > M_{c2} \end{cases} \quad (7.16)$$

where ϕ_{1M} and ϕ_{2M} are model parameters that correspond to a constant ϕ_{ss} at low ($M_w < M_{c1}$) and high ($M_w > M_{c2}$) magnitudes, respectively. The magnitudes that mark the transition between the constant and

the linearly varying regions (M_{c1} and M_{c2}) could not be properly constrained using the maximum likelihood regression. Moreover, a sensitivity study showed little sensitivity of the model parameters to the location of these corner magnitudes; hence M_{c1} and M_{c2} were fixed at 5 and 7, respectively. The resulting parameter values are listed in Table 7.35.

Table 7.35. Parameters for the magnitude-dependent $\boldsymbol{\phi_{ss}}$ model (Equation 7.16). For comparison, the constant $\boldsymbol{\phi_{ss}}$ value is also given.

Period (s)	Constant	Magnitude-Dependent Model			
	ϕ_{ss}	ϕ_{1M}	ϕ_{2M}	M_{C1}	M_{c2}
PGA	0.46	0.49	0.35	5	7
0.1	0.45	0.45	0.43	5	7
0.2	0.48	0.51	0.37	5	7
0.3	0.48	0.51	0.37	5	7
0.5	0.46	0.49	0.37	5	7
1	0.45	0.46	0.40	5	7
3	0.41	0.41[(a)]	0.41[(a)]	5	7

(a) For T = 3, the magnitude dependence was not well constrained and it was removed.

7.4.3.1.2. Distance-Dependent Model

The distance-dependent model is given by

$$\phi_{ss}(R_{rup}) = \begin{cases} \phi_{1R} & for\ R_{rup} < R_{c1} \\ \phi_{1R} + (\phi_{2R} - \phi_{1R})\left(\dfrac{R_{rup} - R_{c1}}{R_{c2} - R_{c1}}\right) & for\ R_{c1} \le R_{rup} \le R_{c2} \\ \phi_{2R} & for\ R_{rup} > R_{c2} \end{cases} \quad (7.17)$$

where ϕ_{1R}, ϕ_{2R}, R_{c1}, and R_{c2} are model parameters. Parameters ϕ_{1R} and ϕ_{2R} were obtained using a maximum likelihood regression and the corner distances were obtained from a grid-search algorithm. The variation of R_{c1} and R_{c2} with frequency was small; hence a reasonable value that is constant across periods was used. The parameters of the distance-dependent model are listed in Table 7.36.

Table 7.36. Parameters for the distance-dependent $\boldsymbol{\phi_{ss}}$ model (Equation 7.17). For comparison, the constant $\boldsymbol{\phi_{ss}}$ value is also given.

Period (s)	Constant	Distance-Dependent Model			
	ϕ_{ss}	ϕ_{1R}	ϕ_{2R}	R_{c1}	R_{c2}
PGA	0.46	0.55	0.45	16	36
0.1	0.45	0.54	0.44	16	36
0.2	0.48	0.60	0.47	16	36
0.3	0.48	0.61	0.47	16	36
0.5	0.46	0.57	0.45	16	36
1	0.45	0.53	0.44	16	36
3	0.41	0.53	0.40	16	36

7.4.3.1.3. Magnitude- and Distance-Dependent Model

The magnitude- and distance-dependent model is given by

$$\phi_{SS}(M, R_{rup}) = \begin{cases} C_1(R_{rup}) & for M < M_{c1} \\ C_1(R_{rup}) + \left(C_2 - C_1(R_{rup})\right)\left(\dfrac{M - M_{c1}}{M_{c2} - M_{c1}}\right) & for\ M_{c1} \le M \le M_{c2} \\ C_2 & for M > M_{c2} \end{cases} \quad (7.18)$$

where M_{c1} and M_{c2} are model parameters, C_2 is a constant, and $C_1(R_{rup})$ is given by

$$C_1(R_{rup}) = \begin{cases} \phi_{11} & for R_{rup} < R_{c11} \\ \phi_{11} + \left(\phi_{21} - \phi_{11}\right)\left(\dfrac{R_{rup} - R_{c11}}{R_{c21} - R_{c11}}\right) & for R_{c11} \le R_{rup} \le R_{c21} \\ \phi_{21} & for R_{rup} > R_{c21} \end{cases} \quad (7.19)$$

where ϕ_{11}, ϕ_{21}, R_{c11}, and R_{c21} are model parameters. The latter two parameters are given in units of kilometers. The corner distances and magnitudes were chosen to be the same as those for the magnitude- and the distance-dependent models. A maximum likelihood regression was run to obtain the values of the remaining parameters. The resulting values are listed in Table 7.37.

Table 7.37. Parameter for the distance- and magnitude-dependent $\boldsymbol{\phi_{ss}}$ model (Equations 7.18 and 7.19).

Period (s)	ϕ_{11}	ϕ_{21}	C_2	M_{c1}	M_{c2}	Rc_{11}	Rc_{21}
PGA	0.58	0.47	0.35	5	7	16	36
0.1	0.54	0.44	0.43	5	7	16	36
0.2	0.61	0.50	0.38	5	7	16	36
0.3	0.64	0.50	0.37	5	7	16	36
0.5	0.60	0.48	0.37	5	7	16	36
1	0.54	0.45	0.40	5	7	16	36
3	0.53	0.40[(a)]	0.40[(a)]	5	7	16	36

(a) These values were replaced with the constant phi value.

Figure 7.72 plots the four proposed models for all combinations of short and long distance, and low and high magnitude. Note that the "constant ϕ_{ss}" model is controlled by recordings at large distances and small magnitudes. The model parameters were not smoothed across frequency, yet the period-dependency of the models compares well with the shape of the standard deviation model of Abrahamson and Silva (2008) (Figure 7.72), with the exception of the values of ϕ_{ss} at T = 0.1 sec for some of the models. The similarity of the spectral shapes of ϕ_{ss} with those for ϕ from the Abrahamson and Silva (2008) model suggest that ϕ_{ss} can also be estimated by scaling down the ergodic phi from this model. A least-squares fit was used to find the optimum scaling parameter with respect to the magnitude-dependent model; this value was determined to be 0.79. Figure 7.72 also includes the ϕ model from Abrahamson and Silva (2008) scaled by 0.79. This choice provides a natural choice for smoothing and interpolating the model across frequencies.

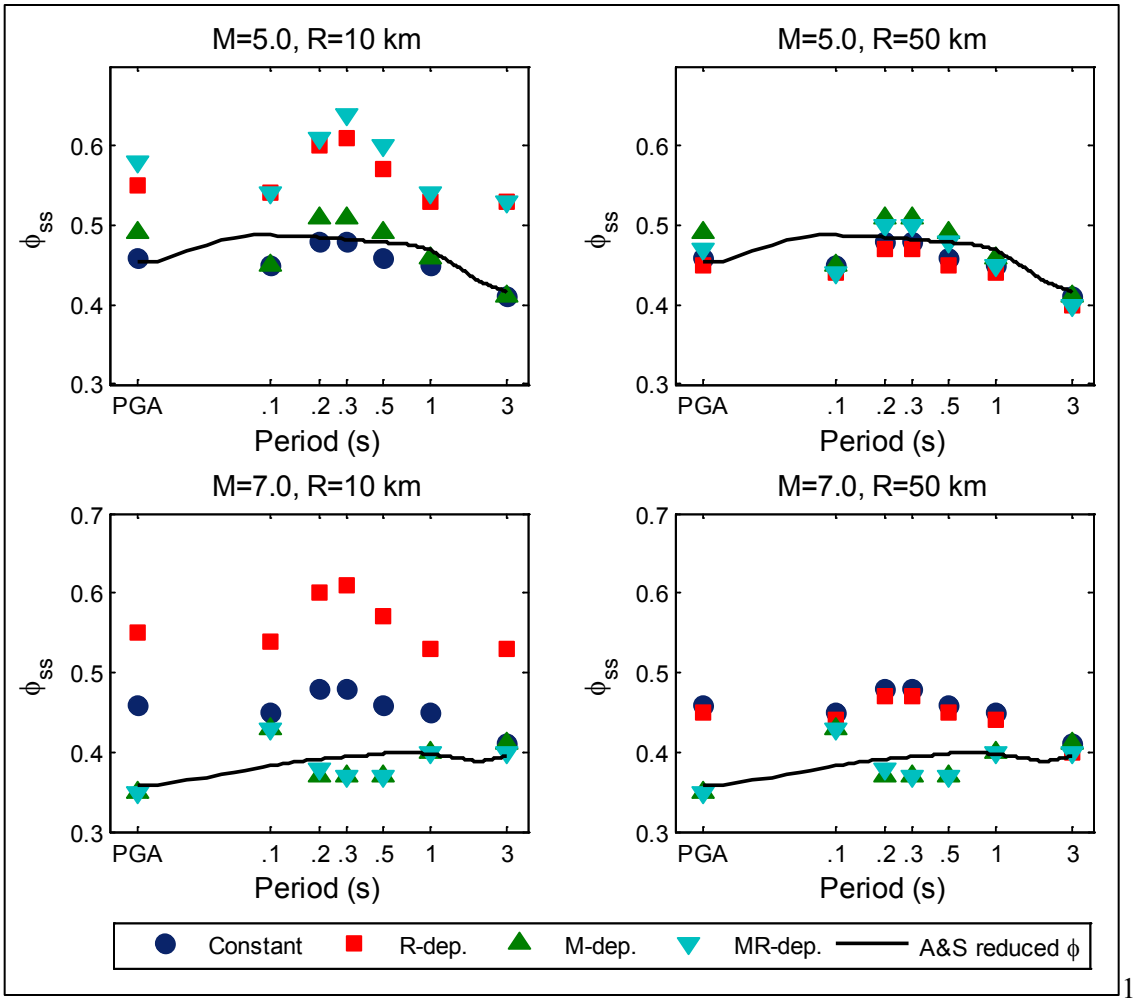

Figure 7.72. Values of $\boldsymbol{\phi_{ss}}$ from the different PRP models for all combinations of short and long distances, and low and high magnitudes. The $\boldsymbol{\phi}$ model from Abrahamson and Silva (2008) scaled by a factor of 0.79 is also shown.

7.4.3.2 The TNSP Single-Station Sigma Model

The TNSP single-station phi model is also based on the PRP data. Two sigma models were used in the TNSP project, a homoskedastic model and a heteroskedastic model including magnitude dependency only. The homoskedastic model was obtained as an average of the single-station phi across all periods (Figure 7.70), which rendered a value of $\phi_{ss} = 0.45$. The heteroskedastic model was built from the observation that the scaled Abrahamson and Silva (2008) ϕ model is a good fit to the PRP data (Figure 7.73). A scale factor of 0.8 was selected. An important difference between the TNSP and PRP models is that the distance-dependent model was not used in the TNSP project. Figure 7.74 shows the PRP distance-dependent model along with the single-station sigma computed for several distance bins. Only data from earthquakes with magnitudes between 5 and 6 are included in this figure. Observe that for the three databases shown (California, Japan, Taiwan), the only data set showing distance dependence is the Japanese data set. In fact, the distance dependence observed in the PRP database is only seen for earthquakes with magnitudes less than 5. Because the minimum magnitude of interest for the TNPS project was 5, distance dependence was not included in the TNSP single-station sigma model.

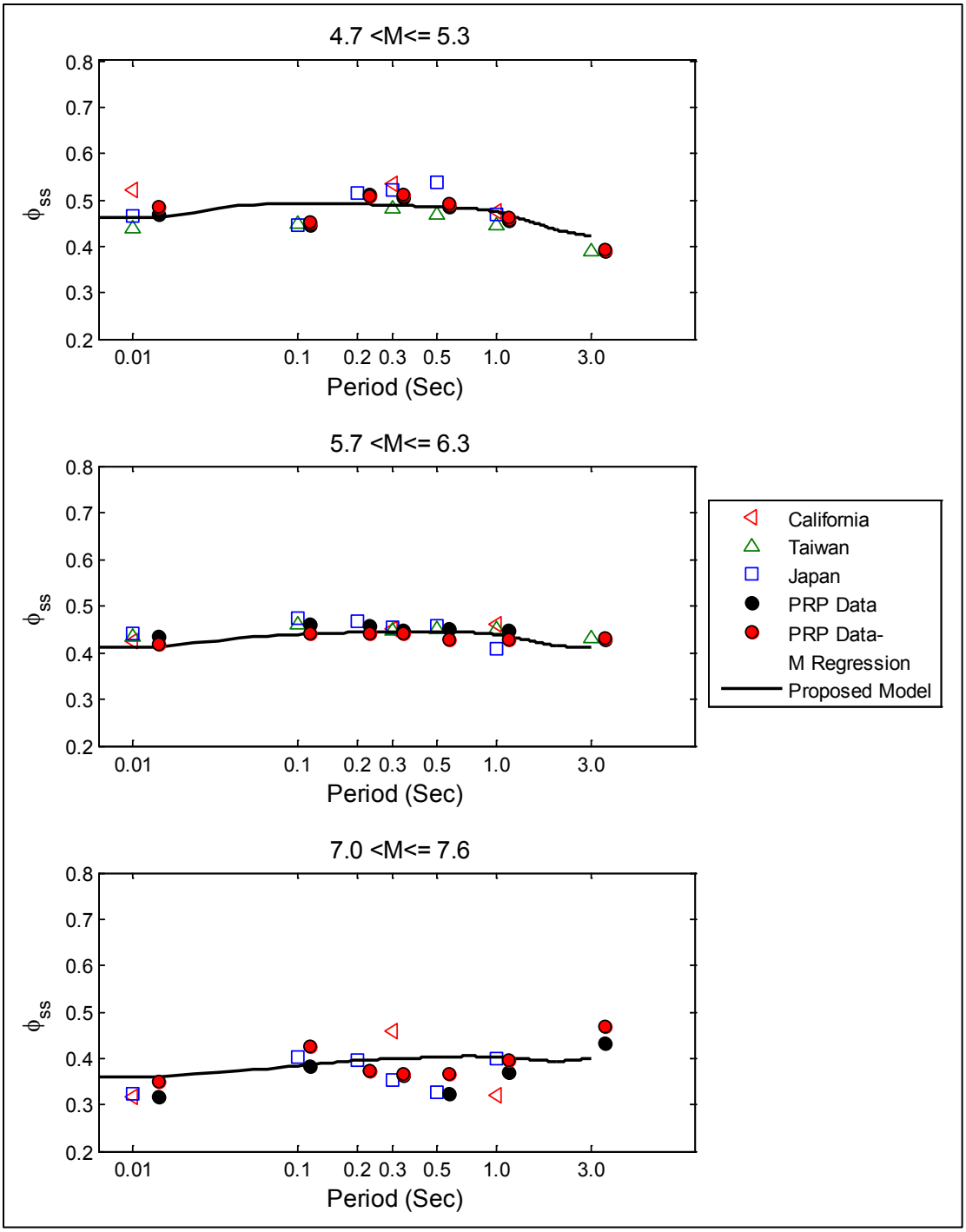

Figure 7.73. $\boldsymbol{\phi_{ss}}$ values from the PRP database for different magnitude bins (R ≤ 200 km). Data are shown separately for each of the three dominant data sets and for the entire PRP database. The red dots are the $\boldsymbol{\phi_{ss}}$ values obtained by fitting the magnitude-dependent model to the PRP residuals. The Abrahamson and Silva (2008) $\boldsymbol{\phi_{ss}}$ model scaled by 0.8 model (referred to as "proposed model") is shown for the magnitude corresponding to the center of the magnitude bin.

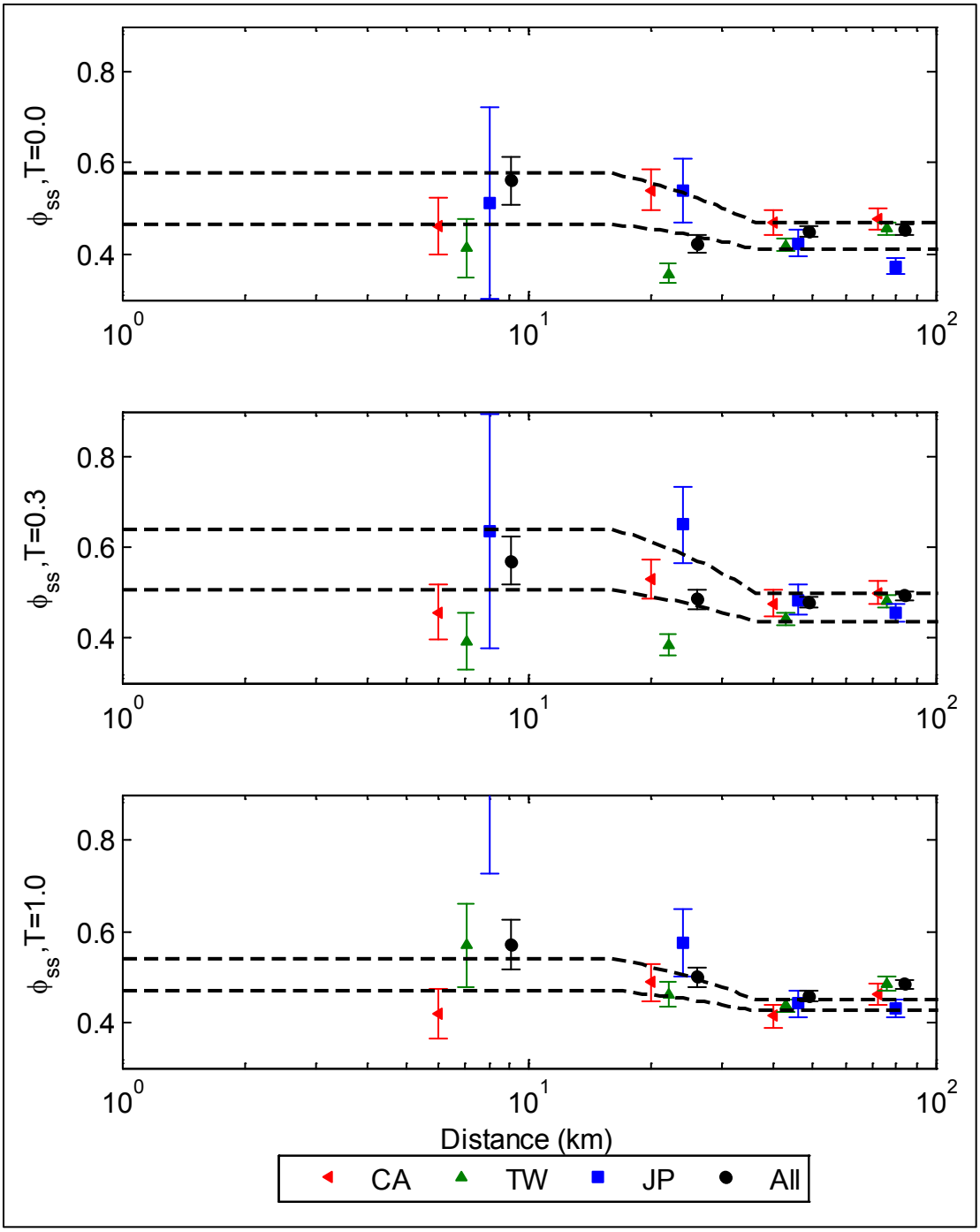

Figure 7.74. Distance dependency of $\boldsymbol{\phi_{ss}}$ in the PRP database. The band shown around each point is a one standard error band. Only residuals for recordings with magnitudes between 5 and 6 are used in this figure. The distance bins are 0 to 16 km, 16 to 32 km, 60 to 100 km, and 100 to 200 km. The plots for each region are shown with a horizontal offset only for clarity.

7.5 Q Models for Washington and California

The quality factor Q is used to represent the energy loss of earthquake waves due to *anelastic attenuation* (i.e., due to damping and scattering caused by small-scale crustal heterogeneity). Anelastic attenuation is distinct from geometric attenuation, which accounts for the reduction in amplitude as the total energy of the source motion is spread over a wave front that expands as the waves travel over longer distances. The fractional amplitude reduction caused by anelastic attenuation during one wave cycle is given by the expression $\exp[-\pi / Q]$. The effect of Q is small for distances less than 50 to 100 km but becomes important at greater distances. Q is often found to be frequency-dependent, and this dependence is typically characterized by the functional form $Q(f) = Q_0 f^{\eta}$, in which the exponent η is typically lower than unity.

This section describes the recently developed data on the regional variation of the crustal Q throughout the western United States, as documented by Phillips et al. (2014). These data are useful to this project for a number of tasks, including the estimation of parameter kappa in Appendix I and the quantification of differences in anelastic effects between Washington in California, which may be used in the development of host-to-target adjustments.

7.5.1 Ground Motion Data Used in the Q Regionalization

Phillips et al. (2014) used a very large number of recordings obtained by the USArray (sometimes called Transportable Array or TA) during the years 2004 through 2009, because the seismograph stations in this array leapfrogged through the western United States. They examined the Lg-wave phase, which is usually the strongest wave arrival at regional distances and continental ray paths. These recordings were generated by 1,139 earthquakes, with moment magnitudes 2.1 through 5.9, and were recorded at 827 stations. After correction for instrument response, the Fourier spectra of each recording was decomposed into 9 frequency bands (from 0.5 to 16 Hz), resulting in a total of 465,633 ground motion observations.

7.5.2 Inversion Method and Results

The inversion method is similar to the fitting of an empirical GMPE using least-squares regression, except that the fitting is focused on resolving regional variations in Q rather than determining GMPE coefficients. To this effect, the observed log-amplitude from each earthquake-station-frequency combination is represented as the sum of the following terms:

- a source term, which accounts for magnitude and spectral shape
- a site term, which accounts for site effects
- a geometric attenuation term of the form $0.5\log[\text{Distance}]$. The coefficient of 0.5 accounts for the geometric-decay pattern of Lg waves.
- an anelastic attenuation term, which consists of a linear combinations of the Q values from all the ray-path segments along the great-circle path between the epicenter and the site. Each ray path is discretized by dividing the study region into 0.5-degree cells.
- an epsilon term with a mean value of zero.

Because the number of records is very large, there are many ray paths crossing nearly every 0.5-degree grid cell. Also, there are many records for each earthquake and for each site. As a result, it is possible to solve for the Q value in each frequency band (or for Q_0 and η using the combined data from all bands), as well as for the source and site terms. This approach is similar to the approach used in Appendix I to investigate kappa, in the sense that it models Fourier amplitudes. In contrast, GMPEs are generally developed by modeling spectral accelerations.

Results for two frequency bands, and for Q_0 and η, are shown in Figure 7.75 and Figure 7.76, respectively. A cursory examination of these maps suggests that the values of Q are moderately higher (i.e., more efficient wave propagation) in the Hanford region than in coastal California, and become much higher northeast of Hanford. In addition to these figures, the authors made their gridded results for Q available to this project.

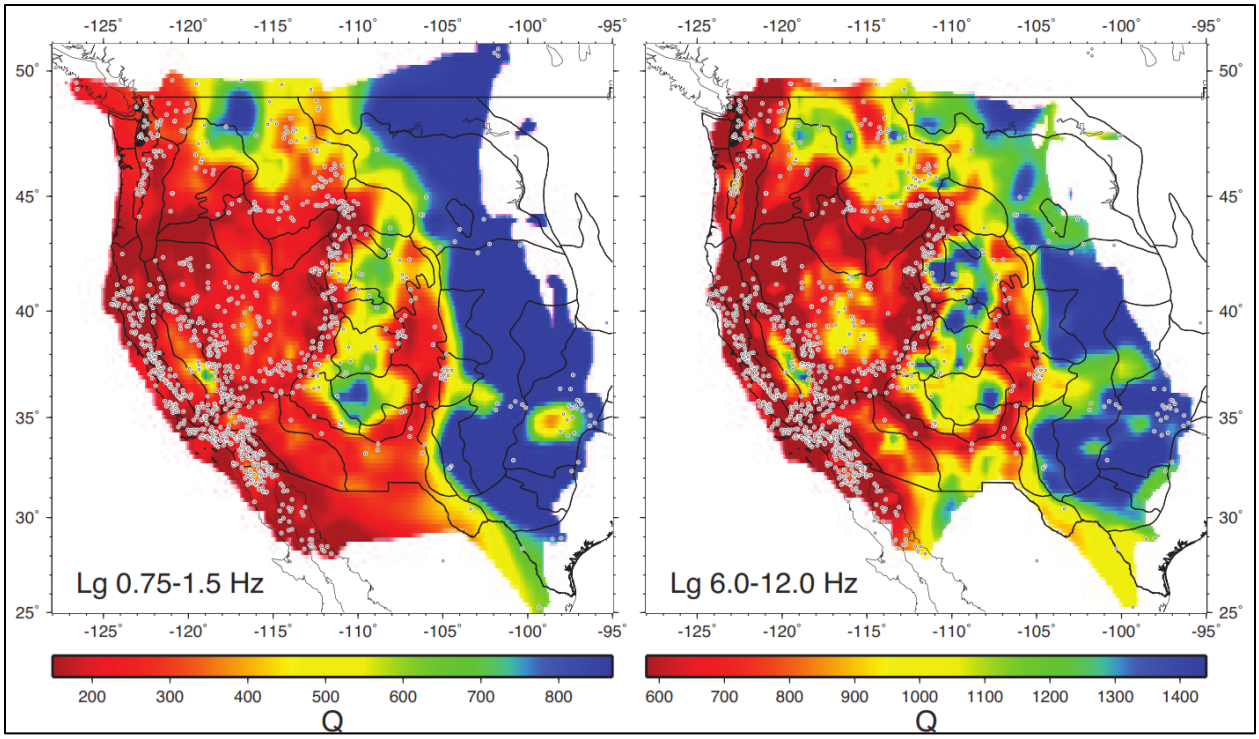

Figure 7.75. Q for two frequency bands. Results for the 0.75- to 1.5-Hz band are shown on the left and for the 6- to 12-Hz band on the right. Color bars differ; we see roughly twice the Q variation at low frequency than we see at high frequency. Geophysical provinces are outlined and events used in the inversions are represented by small dots. (Source: Phillips et al. 2014)

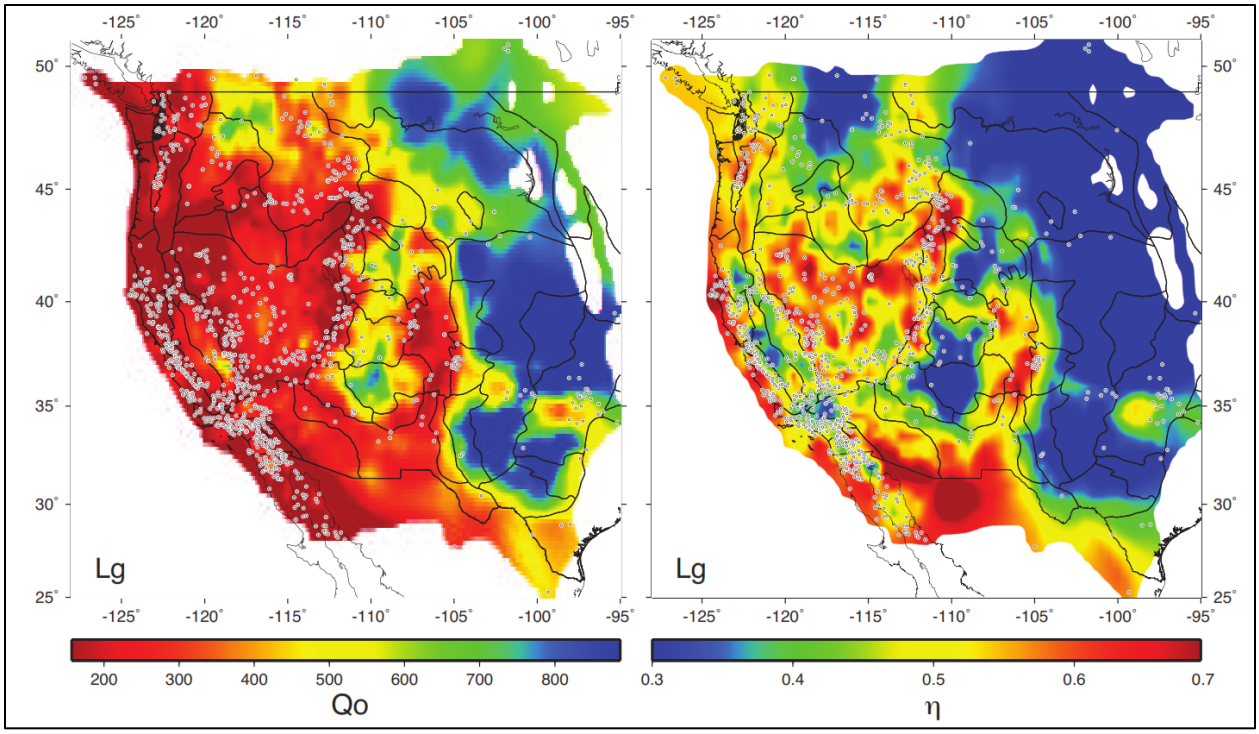

Figure 7.76. Frequency-dependent attenuation. 1-Hz Q (Qo) is shown on the left and the frequency-dependent η parameter is shown on the right. Geophysical provinces are outlined and events used in the inversions are represented by small dots. (Source: Phillips et al. 2014)

7.6 3-D Wave Propagation Effects

The Hanford Site lies within a broad and shallow basin of surface sedimentary deposits, and is also situated above a broader basin composed of the thick layer of pre-Miocene sediments that lie below the CRBs (Figure 7.13). At WS1, the GMC TI Team posed the question of whether the thick lower velocity sediment layer could produce basin effects on the ground motions. This was taken up by Dr. Art Frankel of the USGS, who was present at the workshop as a resource expert presenting considerations for the selection of GMPEs to be used in seismic hazard mapping in the Pacific Northwest. As a result of the ensuing discussions, Dr. Frankel was engaged under contract by the project to conduct investigations to explore the possibility that basin waves could be generated and lead to amplified motions. The study was presented in a report by Frankel et al. (2013).

In the terminology of a SSHAC process, Dr. Frankel was effectively engaged as a specialty contractor to conduct the exploratory analyses for the possible presence of basin effects. However, in view of the fact that Dr. Frankel himself had proposed a priori that such effects were clearly to be expected at the Hanford Site, the GMC TI Team considered it appropriate—and consistent with the SSHAC guidelines—to engage with Dr. Frankel as a proponent expert, thus critically evaluating and challenging his models and conclusions. Dr. Frankel participated in WS2, attended the third Working Meeting of the GMC TI Team, and also responded to written questions posed by the TI Team.

7.6.1 3-D Models of the Hanford Site Region

To perform the 3-D simulations of earthquake motions at the Hanford Site, the first requirement was for a 3-D model of the velocity and density structure at the Hanford Site. The required model was constructed by Thorne et al. (2014), assigning the velocities and densities to different units following the scheme summarized in Table 7.9. The model was constructed with a horizontal grid spacing of 100 m, which was interpolated by Frankel et al. (2013) to a finer mesh of 25 m; the 100-m resolution may be compared with the 70-m horizontal spacing of the velocity model constructed for an earlier study of the Seattle basin (Frankel et al. 2009). The vertical resolution of the velocity model is such that the SMB stack, including the low-velocity sediment interbeds, is represented by an "average" velocity rather than including the multiple velocity reversals (Section 7.2.6).

One particular requirement of the program used for the 3-D wave propagation modeling is that the ground surface must be flat, so the topography was suppressed while retaining the correct thickness of all of the units (Figure 7.77). The presence of surface topography can have the effect of scattering seismic waves and thus reducing the strength of the propagated motions, as was found, for example, by Ma et al. (2007) for the Los Angeles basin. Frankel et al. (2013) actually invoke the effects of surface topography for explaining the low amplitudes recorded during the shallow Wooded Island earthquakes at the edge of the Hanford Site (Section 7.6.2.1).

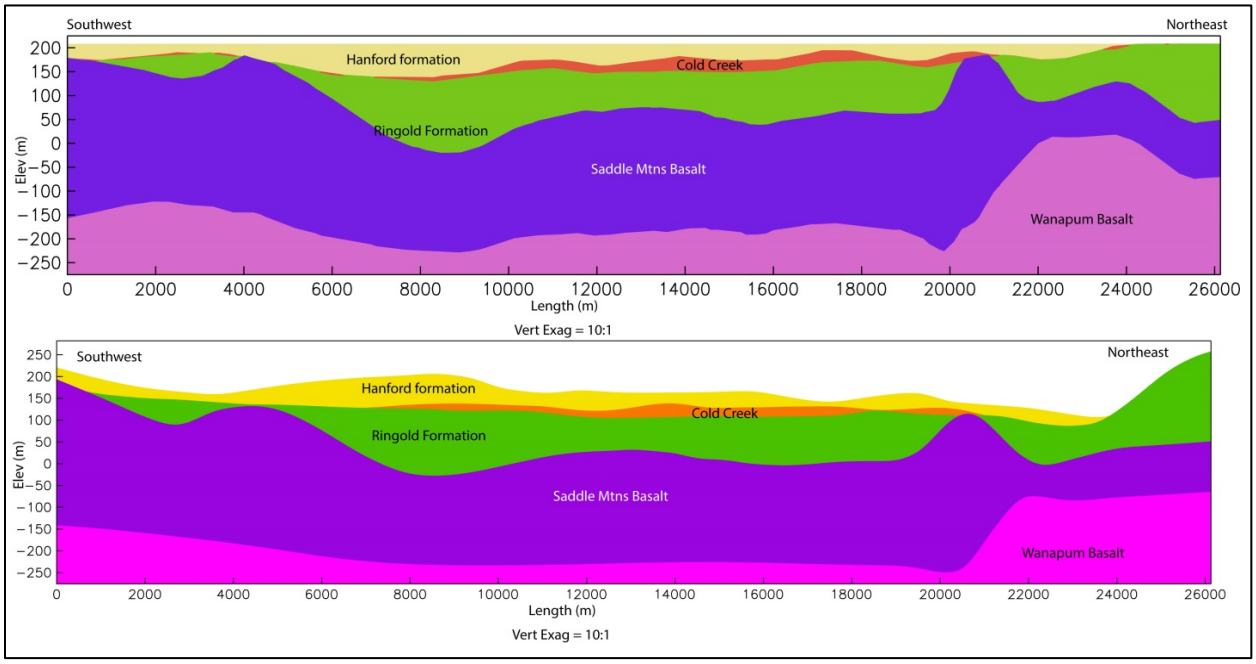

Figure 7.77. North-south section through the Hanford Site showing the original model (lower) and the model with the "zero topography" condition imposed (upper) (Source: Thorne et al. 2014).

The actual "basin" considered by Frankel et al. (2013) is only the surface sedimentary layer rather than the deeper sub-basalt sediments. Moreover, the sedimentary basin is defined as the layer above the Ringold Formation, and therefore it consists primarily of the Hanford formation sediments. The basin is thus rather thin, ranging in depth at the five hazard calculation sites from 14 m (Site C) to 39 m at Site B, only reaching greater depths (94 m) at Site A. The exclusion of the Ringold Formation from the "basin" is a result of the measured velocities in this formation at the WTP being rather high. However, only Unit

A of the Ringold Formation is present at WTP, and Unit A is much stiffer than most other units that happen to be encountered at the other locations. For example, at Site C, Units B and E of the Ringold are encountered, but these 147 m of sediments are modeled as being as hard as Unit A of the Ringold and only the thin superficial layer of the Hanford formation is treated as being part of the basin. This means that the sharp velocity contrast modeled at the base of the thin "basin" in reality is more likely the start of a step function of increasing velocities until the top of the SMBs.

A key parameter in the wave propagation model is Q_S, which is assigned on the basis of an assumed relationship between this parameter and shear-wave velocity, V_S. Figure 7.78 compares the Q_S-V_S relationship used in these simulations—which is the same model previously applied to the 3-D simulations in the Seattle basin (Frankel et al. 2009)—from which it can be immediately appreciated that the resulting Q_S values are exceptionally high. The figure also shows the alternative model used in sensitivity runs, which was modified only for V_S < 1,000 m/s, which remained higher than several other widely used models at lower V_S values.

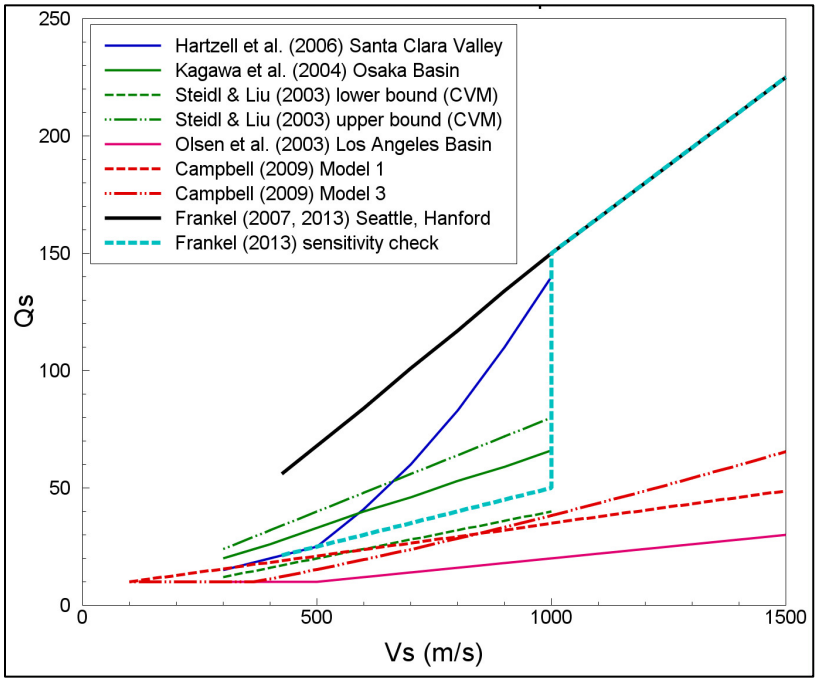

Figure 7.78. Comparison of the Q_S-V_S relationship used in the 3-D simulations for the Hanford Site with those proposed in several other studies. The Community Velocity Model values from Steidl and Liu (2003) were obtained from Hartzell et al. (2006).

The final point to note regarding the 3-D model used for the simulations is that within the sediments of the "basin" only linear soil behavior was considered regardless of the intensity of the motions.

7.6.2 Ground Motion Simulations for Selected Earthquake Scenarios

The approach adopted by Frankel et al. (2013) to explore the importance of 2-D and 3-D wave propagation effects was to compare the motions obtained from 3-D and 1-D simulations. This approach was first applied to recordings from some small earthquakes that occurred in the region of the Hanford Site, and then to hypothetical scenarios representing crustal and subduction earthquakes that could affect the site.

7.6.2.1 Validation of Simulations

The Frankel et al. (2013) study began with simulations of the recordings from the May 18, 2008 Prosser earthquake (**M** 3.27) that occurred south of the Hanford Site, and two earthquakes of the 2011 Wooded Island series located on the eastern edge of the site, with local (duration) magnitudes of 3.7 and 3.4. The Prosser earthquake had a focal depth of 18 km, the Wooded Island earthquakes depths of 1.8 and 1.4 km, respectively. The 3-D simulations were performed using the 3-D model for the site developed by Thorne et al. (2014), whereas the 1-D simulations used the same approach but a flat-layered model based on the velocity profile at the location of the recording stations. Whereas the 3-D model includes the deep velocity gradients, in the 1-D model the velocity gradients in the deeper layers were ignored and the velocities were maintained constant over the full thickness of each unit. As can be seen in Figure 7.79, the 3-D simulations were able to better reproduce the recorded signals.

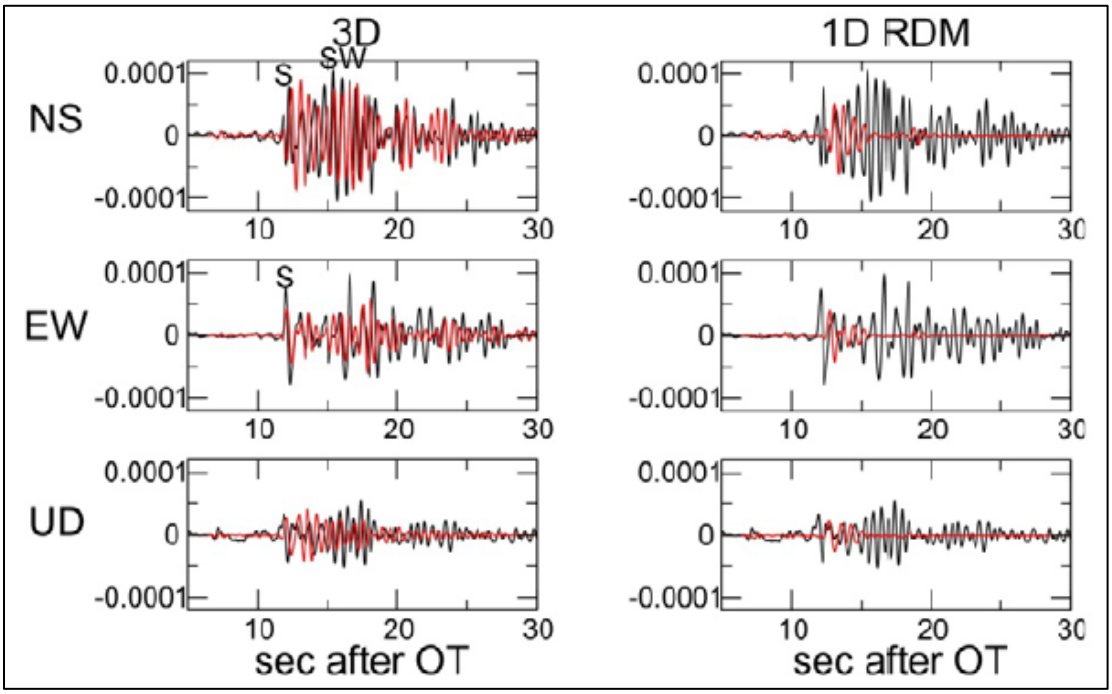

Figure 7.79. Comparison of observed (black) and simulated (red) waveforms at the H4A recording location using 3-D and 1-D simulations (Frankel et al. 2013). RDM stands for refraction-derived model, referring to the depth of the crystalline basement.

The results were also presented in terms of response spectral ordinates at oscillator periods of 0.5 and 1.0 sec (Figure 7.80). Both the 1-D and 3-D simulation underestimate the amplitudes from the Prosser earthquake, but the 3-D simulations produce motions closer to those measured. The ratio of motions from the 3-D to 1-D simulations for this case is 1.8 and 1.5 at 0.5 and 1.0 sec, respectively. Figure 7.81 shows the results for the larger of the two Wooded Island earthquakes, for which the 3-D/1-D ratios are 1.1 and 0.9 at 0.5 and 1.0 sec, respectively.

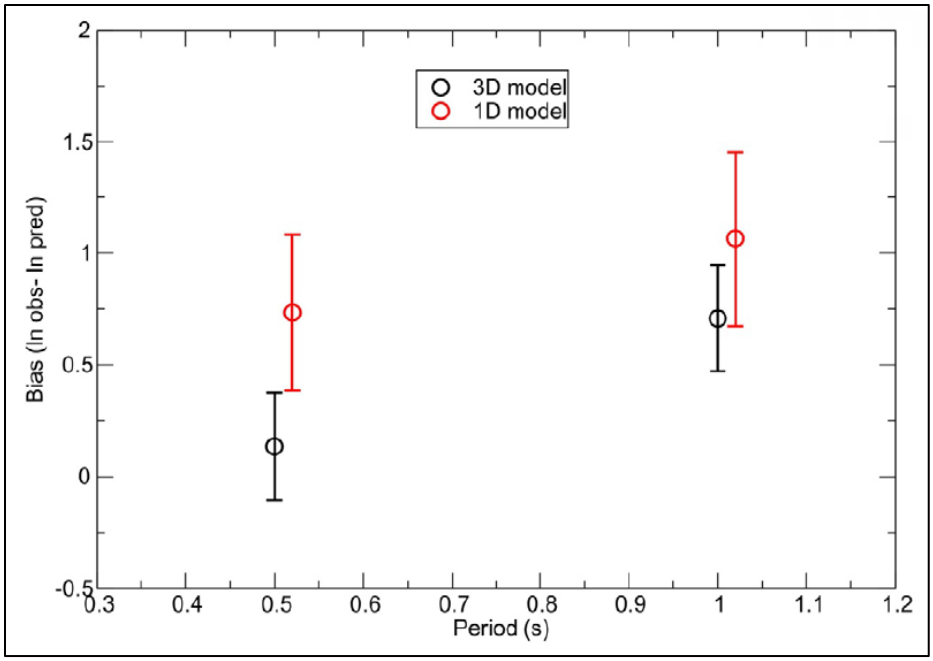

Figure 7.80. Residuals of spectral acceleration ordinates over all the Hanford Site recordings from 1-D and 3-D simulations of the 2008 Prosser earthquake (Frankel et al. 2013).

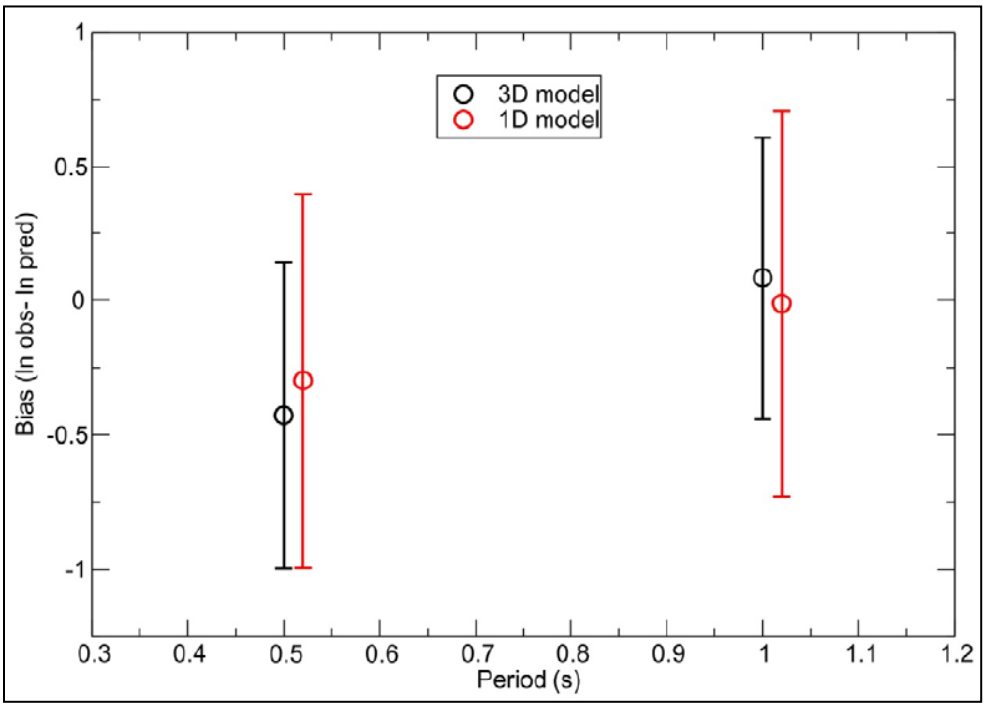

Figure 7.81. Residuals of spectral acceleration ordinates over all the Hanford Site recordings from 1-D and 3-D simulations of the September 2011 Wooded Island earthquake (Frankel et al. 2013).

The results of validation exercises were interpreted to confirm the validity of the 3-D model for the site and superior performance of the 3-D simulations in reproducing the motions in which basin waves were most clearly present. On the basis of this outcome, the 1-D and 3-D simulations were then applied to a number of earthquake scenarios considered to be relevant to the hazard at the Hanford Site, as described in the following two sections. An important distinction, however, needs to be made, which is that for these cases, the 1-D simulations were no longer performed using the same 3-D approach with a flat-layered model but a completely different approach. At each location, a velocity profile was developed from the 3-D model; on the recommendation of the TI Team, for depths greater than 3 km, V_s was taken to be equal to the value at the center of the fault rupture in order to achieve a degree of consistency between the 1-D and 3-D simulations. For each 1-D profile, Green's functions were calculated using the frequency-wavenumber integration code of Zhu and Rivera (2002).

7.6.2.2 Crustal Earthquakes

Simulations were performed for three strong earthquakes associated with ruptures on major reverse faults below the Hanford Site (Figure 7.82). These scenarios were an earthquake of **M** 6.8 on the Rattlesnake Hills west segment, another of **M** 6.7 on the east segment, and an earthquake of **M** 6.6 on the Gable Mountain fault. In each case, the rupture histories were developed following the procedure of Frankel (2009) and the 3-D wave propagation modeled using the finite difference code of Liu and Archuleta (2002).

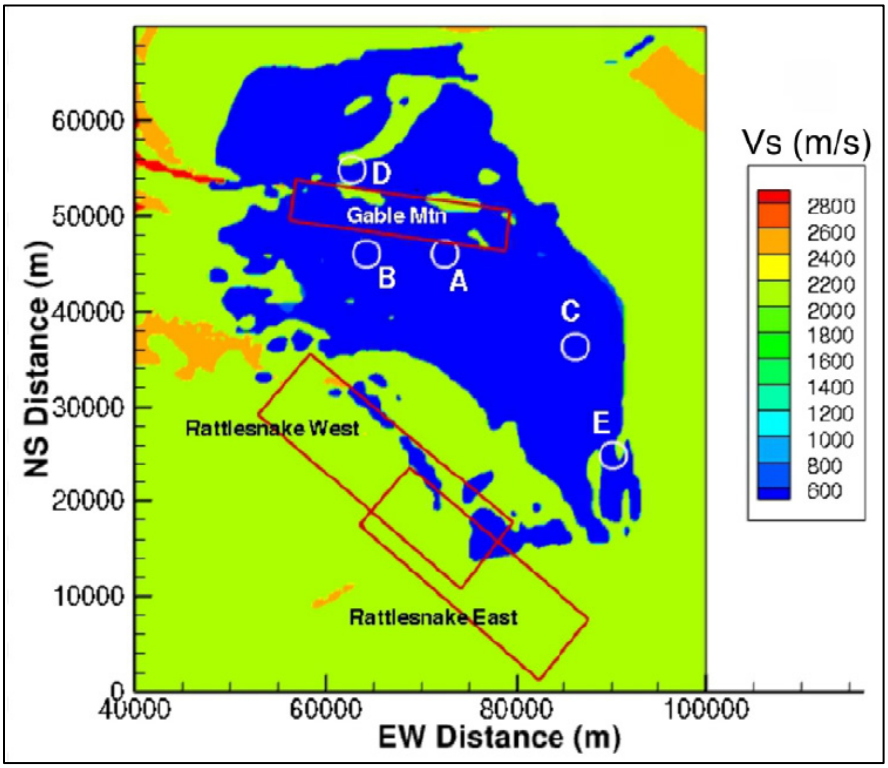

Figure 7.82. Location of three crustal earthquake ruptures modeled by Frankel et al. (2013) superimposed on a model showing shear-wave velocities. The blue area effectively marks the basin responsible for the 3-D effects to which Frankel et al. (2013) attribute amplifications of the ground motions.

For the forward simulations, the motions were developed using the 1-D and 3-D approaches at the five hazard calculation sites, and the results displayed in terms of ratios of 3-D/1-D results for response spectral ordinates at periods ranging from 0.5 to 10 sec. Figure 7.83 and Figure 7.84 show these results for two of the three crustal earthquake scenarios. These represent the end cases, the ratios from the Rattlesnake East scenario lying between those from these two scenarios.

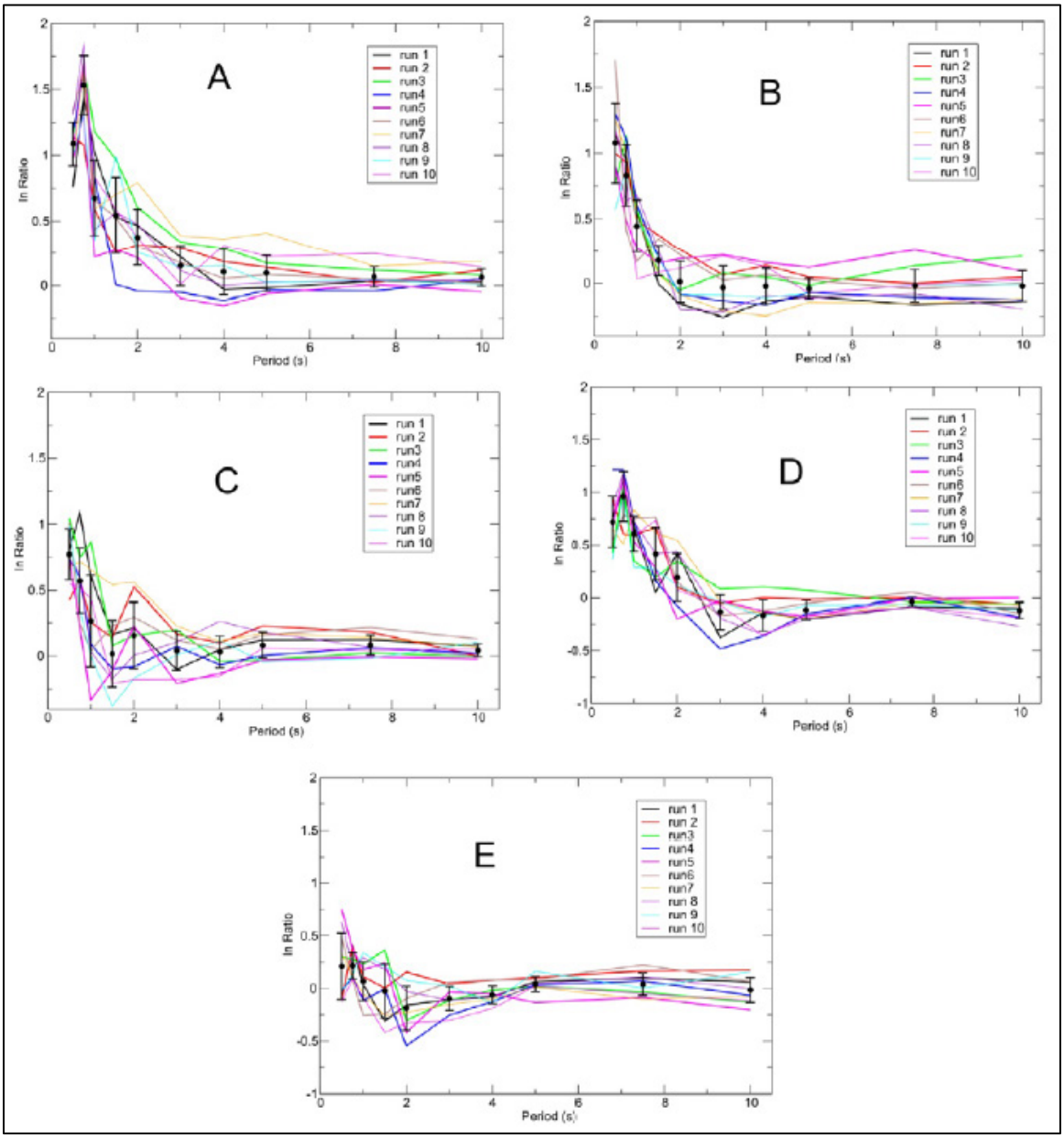

Figure 7.83. Ratios for spectral ordinates from 3-D to 1-D simulations for the M 6.8 Rattlesnake West fault earthquake (Frankel et al. 2013).

Although the actual ratios vary from one earthquake to another, and from one site to another, as would be expected, there are also persistent patterns in the results. The key observation is that for periods greater than 3 to 4 sec, the ratios are essentially equal to one, and in some cases are slightly less than unity for periods in the range of about 2 sec. The highest ratios are encountered at short periods, peaking in the

region of 0.5 to 0.75 sec, and the largest values reach 4.5 (Site A) for the Rattlesnake West earthquake and 2.7 (Site E) for the Gable Mountain earthquake.

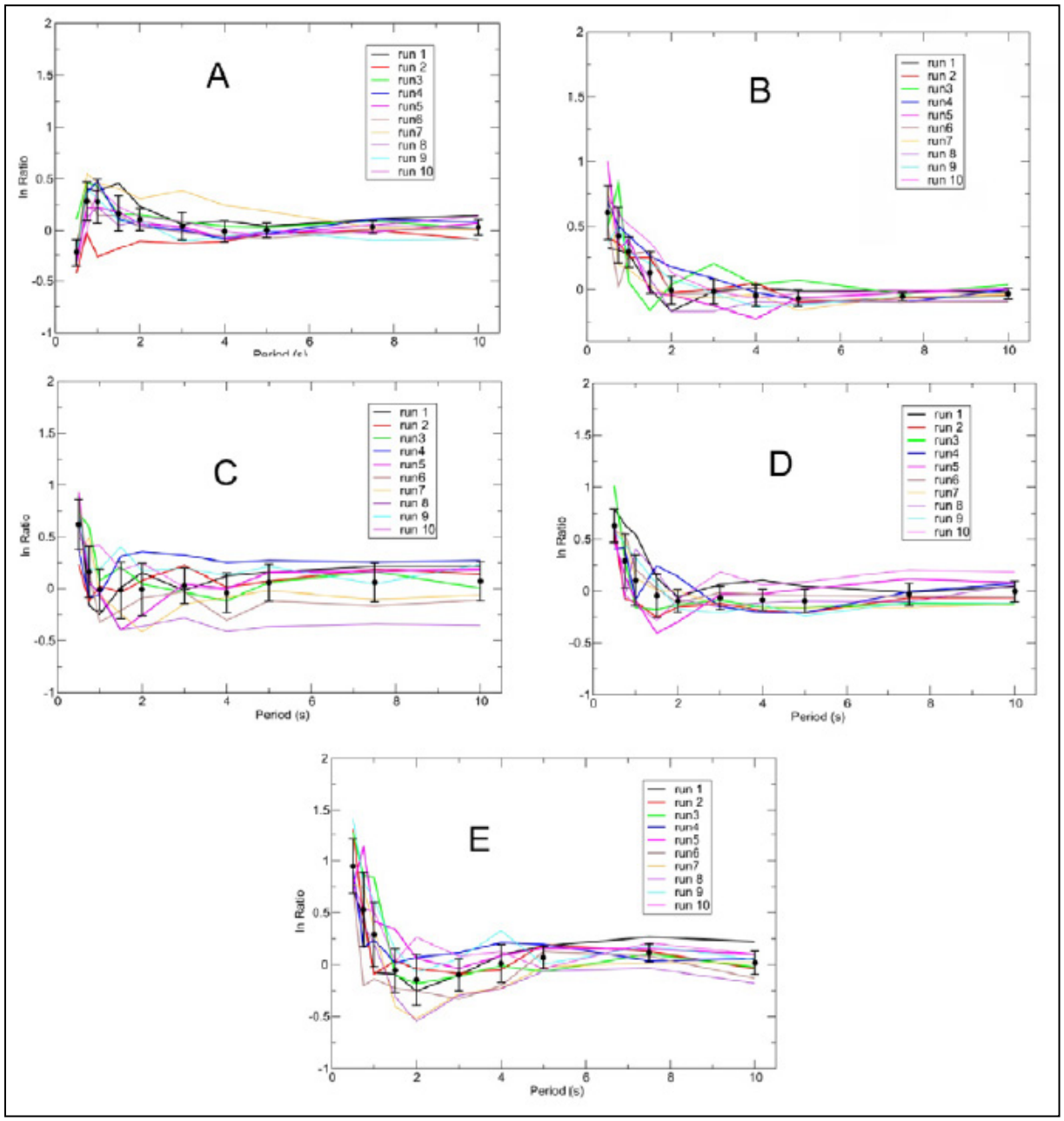

Figure 7.84. Ratios for spectral ordinates from 3-D to 1-D simulations for the M 6.6 Gable Mountain fault earthquake (Frankel et al. 2013).

7.6.2.3 Subduction Earthquake

For the simulations corresponding to a large earthquake on the Cascadia subduction zone, full simulations from the source would have required a 3-D velocity model for most of the state of Washington and even then would be computationally prohibitive. Frankel et al. (2013) therefore opted to represent this scenario by a plane wavefront at the western edge of the basin, dipping at 41° (based on the

angle of incidence of a critical reflection from the Moho). The resulting 3-D/1-D response spectral ratios (Figure 7.85) show a pattern similar to the stronger crustal earthquakes, but reaching even higher values: for Site A, the maximum ratio is encountered at a period of 0.75 sec and reaches a value of 9.5.

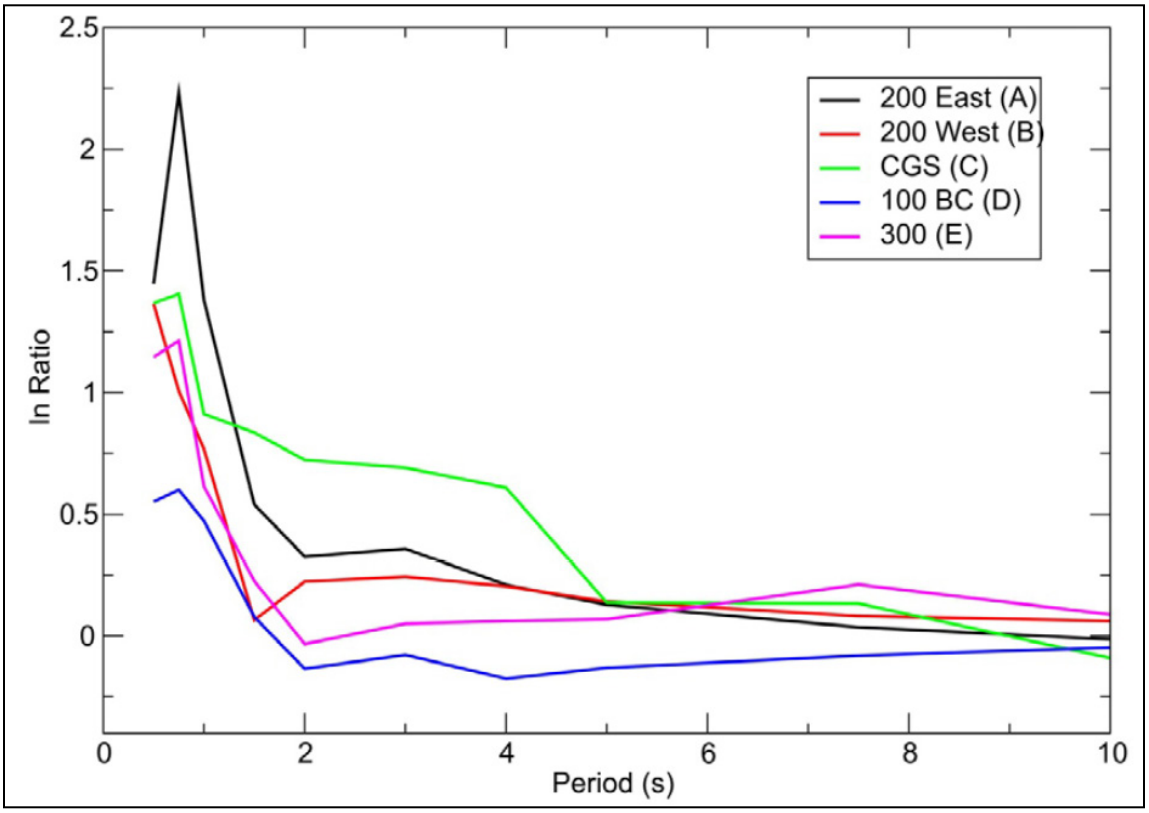

Figure 7.85. Ratios for spectral ordinates from 3-D to 1-D simulations for large Cascadia subduction earthquake (Frankel et al. 2013).

7.6.3 Assessment of the Importance of 3-D Effects

The implications of the report by Frankel et al. (2013) are that for certain combinations of earthquake source and observation location, the predicted spectral ordinates at certain response periods—particularly those from 0.5 to 2.0 sec—would need to be amplified by factors of 4 or more to account for the basin effects caused by the uppermost sediment layers at the site. However, while the GMC TI Team accepted that there is good evidence for basin-generated waves being present in some situations, there are several motivations for interpreting the calculated amplification factors with some caution. The first consideration is the fact that the 3-D model of the site probably exaggerates the strength of the velocity contrast between the basin and the underlying materials at many locations. A second, and closely related, consideration is that the velocity model for the uppermost part of model is simplified (and does not include the velocity reversals within the SMBs stack) and is defined on a relatively coarse grid that will have led to a rather smooth model (in comparison with the actual lateral variations). Thirdly, the consequence of imposing a "zero topography" condition on the model suppresses the scattering that may be produced by surface topography and creates more a continuous "basin" than is present in the original 3-D model.

Another question that inevitably arises is why the 3-D/1-D ratios calculated for the forward-modeling scenarios are so much greater than those obtained for the validation cases? When asked, Dr. Frankel indicated it was because of the shallower depths of the sources for the large earthquakes on the local faults. However, this interpretation is difficult to reconcile with the fact that much stronger basin effects were found for the Prosser earthquake (with a focal depth of 18 km) than for the very shallow Wooded Island earthquakes (which occurred close the edge of the basin). The even higher ratios calculated for the Cascadia earthquake warrant particular attention. The first observation that can be made is that the concentration of all of the wave energy from this event into a single dip angle is likely to have contributed to rather extreme results and is unlikely to represent how the wave energy would arrive at the site in the event of such an earthquake. In order to obtain additional insight into the apparently very strong amplification of the motions from a great Cascadia earthquake due to basin effects, accelerograms recorded on the Hanford Site during the 2001 Nisqually earthquake were examined. Although this earthquake was of smaller magnitude (**M** 6.8) than the largest events considered on the Cascadia subduction zone, the recordings may still be expected to show basin effects if they are genuinely so pronounced for incoming waves from such earthquakes. The velocity traces were band-passed filtered between 0.5 and 2.0 Hz using a 4th-order Butterworth filter, following the treatment applied by Frankel et al. (2002) to recordings obtained close to the source of the same earthquake. Examples of the filtered velocity traces are shown in Figure 7.86, in which it can be seen that surface waves arrive about 30 sec after the S-waves, which suggests that these are regional surface waves rather than basin waves. There is no evidence of strongly amplified waves being generated following the arrival of the S-waves.

Another issue that needs to be borne in mind is that unlike for validation exercises, in the forward-modeling simulations, different approaches were used for the 1-D and 3-D calculations. At the request of the GMC TI Team, Dr. Frankel made direct comparisons of the two approaches by comparing spectral accelerations calculated using the finite difference code and the reflectivity code for the 1-D case. The ratios of the spectral ordinates calculated at each of the five hazard calculation sites with the two approaches are shown in Figure 7.87. The ratios are close to unity, at least on average, for response periods greater than 2 sec, but vary considerably at periods of 1 sec and shorter, where the finite difference approach gives values up to 20% higher or lower than the reflectivity approach, depending on the site. Although these differences are not sufficient to explain very large 3-D/1-D ratios obtained from the simulations, they need to be considered together with the other factors that have already been expounded above.

The TI Team's interpretation of the results in Figure 7.87 is that the fluctuations of the ratios at short periods simply reflect the fact that the finite difference simulations may not be reliable at frequencies of 1 Hz and higher. The frequency range of such simulations is ultimately limited by the spatial resolution of the velocity model. In earlier studies of basin waves using the same analytical approach, such as for the Santa Clara valley (Hartzell et al. 2006) and the Seattle basin (Frankel et al. 2009), simulations were limited to an upper frequency limit of 1 Hz, despite having velocity models with superior resolution (the interpolation from a 100-m grid to a 25-m grid does not add information about the velocity structure). The GMC TI Team is of the view that the results obtained at frequencies greater than 1 Hz should be treated with caution and are probably not entirely reliable.

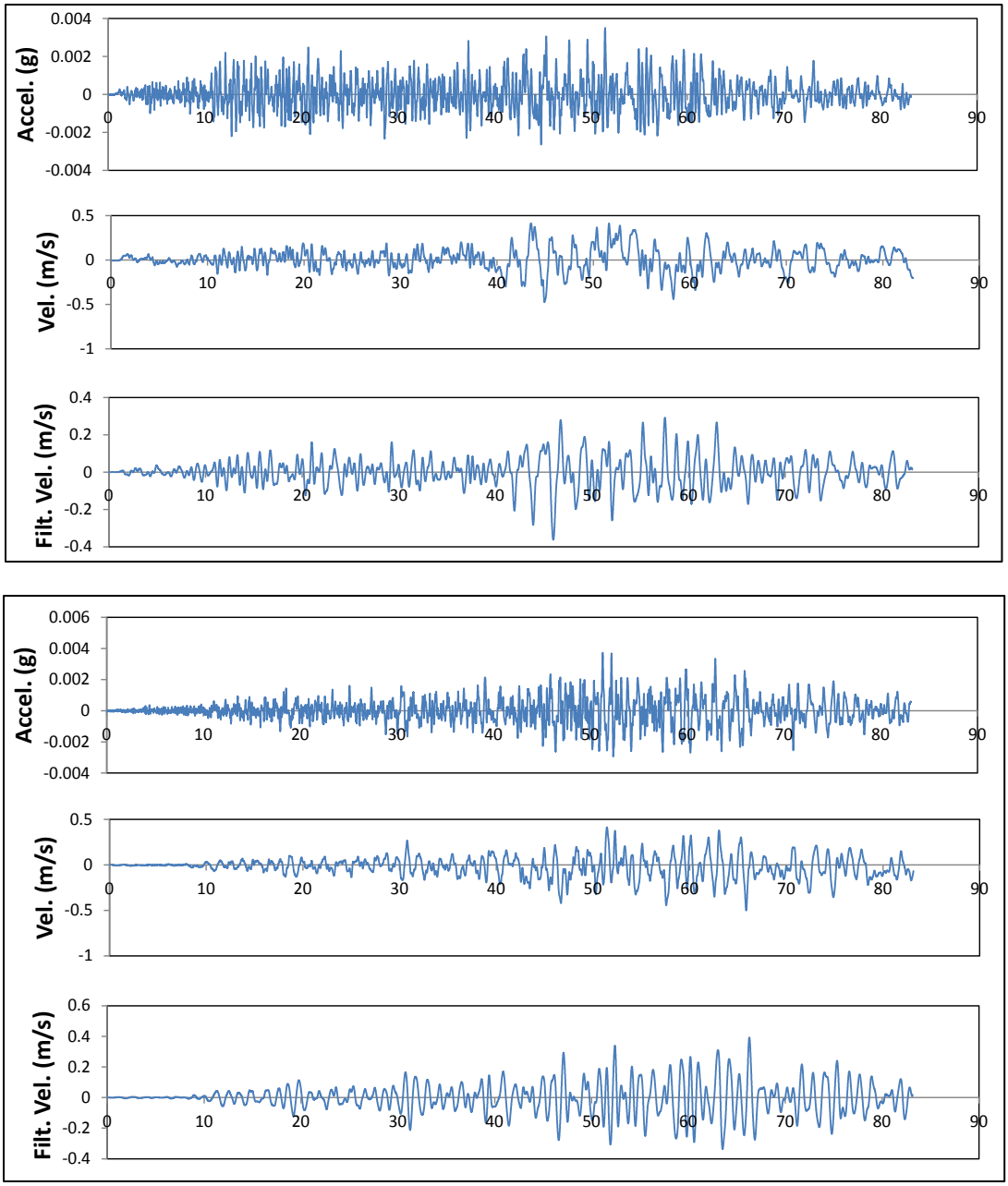

Figure 7.86. Accelerograms from the 2001 Nisqually earthquake recorded at the Hanford Site (upper: A200E, HLZ channel, lower: A400A, HLN channel). In both cases, the integrated velocity trace and the bandpass filtered velocity traces are also shown.

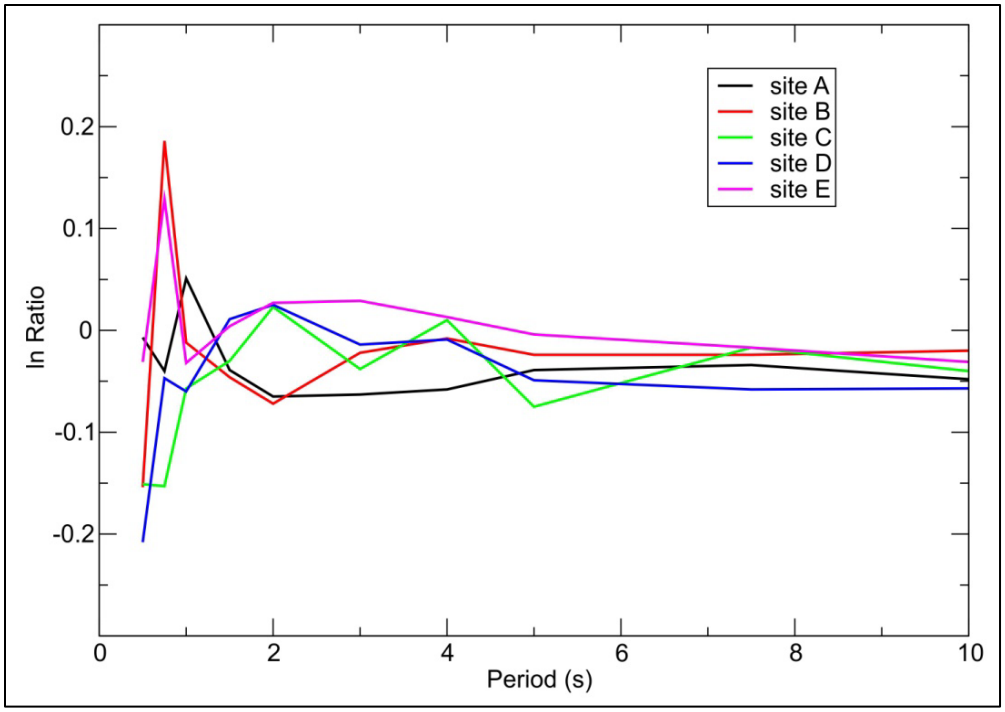

Figure 7.87. Ratios of response spectral ordinates obtained with 1-D simulations using the finite difference approach to those obtained using the reflectivity code. (Figure courtesy of Dr. Art Frankel, USGS.)

The finite difference code used is a proprietary program developed by Dr. Pengcheng Liu and is not available for inspection (the program was requested from Dr. Liu and the request was declined). Moreover, there is no available documentation of the program; the reference by Liu and Archuleta (2002) cited in Frankel et al. (2013), as well as in earlier publications making use of the same simulation code, is actually a single-paragraph abstract from an Annual Meeting of the Seismological Society of America.

In view of all of these considerations, the GMC TI Team reached the conclusion that while the presence of basin effects at the Hanford Site is accepted as a distinct possibility for many source-site combinations, the implied amplification factors found by Frankel et al. (2013) at periods of less than 2 sec are not considered reliable. The "basin" to which these amplification factors are attributed is not exceptional, in reality, neither in terms of its geometry (it is, in fact, a rather flat basin) nor in the velocity contrast between the sediments and the underlying material (when one takes into account the fact that most of the sites are not overlain by Unit A of the Ringold Formation). Therefore, any basin effects would not be expected to be markedly different from those present in the soil-site recordings of the strong-motion databases from which the selected GMPEs have been derived, given that almost by definition most soil sites are located within basins. The TI Team therefore concluded that the effect of any potential basin effects would be within the range of amplitudes implied by the ergodic standard deviations associated with the GMPEs. The TI Team decision therefore was to capture basin effects by using ergodic (rather than single-station) sigma in the modeling of spectral ordinates at those oscillator periods where such effects would be expected to manifest. However, because the amplifying effect of basin waves is attributed entirely to the suprabasalt sediments, it would not be appropriate to adjust the single-station sigma model adopted for the baserock motions (Section 9.6). The additional variability

required to encompass the potential contribution of basin effects is thus incorporated through minimum prescribed levels of variability in the site amplification functions that are to be convolved with the baserock hazard, as explained in Section 9.7.6.

7.7 Existing V/H Spectral Ratio Models

As noted at the start of this chapter, the ultimate goal of the project is to provide input to the characterization of the ground-shaking hazard at selected surface locations on the site. This characterization of the surface ground motions includes both horizontal and vertical response spectral ordinates. For reasons explained in Section 9.8.1, the vertical response spectra are to be obtained by application of V/H response spectral ratios to the horizontal response spectra. In this section of the report, available models for the V/H ratios of response spectral ordinates are reviewed and evaluated in light of the specific requirements for the Hanford Site, which are presented in the Section 7.7.1.

7.7.1 Requirements for V/H Ratios for Hanford PSHA

The horizontal response spectra that will ultimately be generated at the ground surface through convolution of the baserock hazard with site amplification functions will be defined at 20 oscillator periods ranging from 0.01 sec to 10.0 sec. Therefore, the V/H ratios also need to be defined for this same range of periods, although it is not necessary to be defined for all of the 20 target response periods (Chapter 9.0) because coefficients or actual ratios at any intermediate frequencies can be obtained from interpolation. However, for this to work well, it is necessary to include reasonably high sampling of the short-period range of the response spectrum and to include coefficients corresponding to the peak in the predicted function (Bommer et al. 2012), which for vertical spectra will tend to occur at a rather short period. Extrapolation beyond the range of periods covered by the models, however, is not advisable, particularly at the short-period end of the response spectrum.

Another consideration is that the horizontal response spectra are expressed in terms of the geometric mean of the two horizontal components, making it preferable to use V/H ratios also defined in terms of the same definition for the horizontal component of motion. However, if there were other compelling reasons to adopt ratios defined using another definition of the horizontal component—such as the larger of the two, for example—it would be reasonably straightforward to adjust for this difference using relationships between spectral accelerations defined by different treatments of the two horizontal components (e.g., Beyer and Bommer 2006; Watson-Lamprey and Boore 2007).

Because the V/H ratios are to be applied to horizontal spectral ordinates at the ground surface, they should be applicable to soil sites given that at all locations the surface deposits are sediments. In order to predict the V/H ratio at each location with increased accuracy, the ratio ideally should be defined as a function of V_{s30} and calibrated for reasonably low values, such as the 400 m/s encountered at the WTP site.

The nature of the earthquakes likely to dominate the hazard also needs to be considered when selecting the models for the V/H ratios. The crustal earthquakes, associated with the faults of the YFB, will be earthquakes of moderate-to-large magnitude occurring at relatively short distances and associated mainly with reverse ruptures. Contributions to the hazard may also come from very large interface earthquakes located at about 250 km from the site on the Cascadia subduction zone.

In the following sections, available V/H ratios—grouped into three categories—are briefly assessed in terms of their applicability to the Hanford PSHA project in light of the selection criteria listed above.

7.7.2 Ratios from Predictions of Vertical and Horizontal Components

The first category of V/H models considered are those that can be obtained from GMPEs providing separate predictions of vertical and horizontal spectral ordinates. Provided that the data sets on which the two predictions are based are consistent—which would exclude, for example, the GMPEs of Bragato and Slejko (2005), because more than twice as many records were used for the vertical component predictions as were used for the horizontal model—then ratios of the median predictions for any specific scenario can provide the required input. One limitation of this approach would arise if the variability of the V/H ratio were required, because this cannot be obtained from the variability of the individual component predictions; the strong correlation between the amplitude of horizontal and vertical components leads to much smaller variability in predictions of the ratio. Only Campbell and Bozorgnia (2003) performed the exercise of separately calculating the standard deviation of predicted V/H ratios.

Bommer et al. (2011) reviewed a number of GMPEs providing predictions of both vertical and horizontal response spectral ordinates, summarizing their key characteristics. None of these satisfies all of the requirements listed in the previous section, and most fail on multiple accounts. Of the 16 models reviewed by Bommer et al. (2011), only Abrahamson and Silva (1997) extend to periods as small as 0.01 sec—for more than half of the equations, the shortest period is 0.05 sec or greater—but its upper limit is 5 sec. If the selection criteria are limited just to the requirements of coefficients for very short periods (say 0.03 sec or less), that the equation is applicable to earthquakes of at least magnitude 7, and that the equation includes explicit V_{s30}, then all the equations considered by Bommer et al. (2011) are rejected.

More recently, a report was issued by PEER (2013) presenting preliminary versions of the vertical component models that will complement the NGA-West2 GMPEs for the horizontal components. The models satisfy all of the requirements (for crustal earthquakes) with the exception of being limited to an upper period of 3 sec. However, some of the chapters of the report only present work in progress and others state the models are to be updated and modified; it is apparent that the report was produced somewhat prematurely to address contractual obligations to project sponsors (Dr. NA Abrahamson, personal communication, 2014).

In conclusion, none of the currently available pairs of GMPEs for vertical and horizontal response spectra are particularly promising in terms of satisfying the main requirements of this application.

7.7.3 Direct Predictions of V/H Ratios

A small number of equations have been developed that directly predict the ratio of V/H spectral accelerations at several oscillator periods as functions of the same parameters generally included in GMPEs such as magnitude, style of fault, distance, and site classification. Several of these models can be rejected simply on the basis of not providing predictions at short periods, which eliminates those of Ambraseys and Simpson (1996), Ambraseys and Douglas (2003), and Kalkan and Gülkan (2004), none of which provide coefficients for periods less than 0.1 sec. Other reasons these models do not warrant

further consideration are that they each have a number of deficiencies: for example, Ambraseys and Douglas (2003) used only recordings from distances of less than 15 km, and the V/H ratios are predicted only as a function of the style of faulting.

Bommer et al. (2011) derived equations for V/H spectral ratios from a database of strong-motion accelerograms recorded in Europe and the Middle East. The upper limit on the period range is 3 sec and the equations use site classes rather than explicit V_{s30}. Another shortcoming of this model, from the perspective of potential application to the Hanford Site, is that reverse-faulting earthquakes are not well represented in the European strong-motion database, hence the model is not well constrained for the type of earthquake expected to dominate the hazard.

The more recent European model by Akkar et al. (2014a) addresses some of the limitations of the Bommer et al. (2011) model, most significantly by incorporating V_{s30} as an explicit predictor variable. The upper period limit was extended to 4 sec. However, the weak constraint for reverse-faulting earthquakes remains an issue. This is also true for the model of Gülerce and Akyüz (2013), which is a modification of the Gülerce and Abrahamson (2011) model—discussed below—to fit the strong-motion database from Turkey, in which reverse-faulting earthquakes are not strongly represented.

Tezcan and Piolatto (2012) derived a nonparametric model for predicting V/H spectral ratios, using a subset of 652 recordings from the NGA-West1 database. All of the recordings were generated by strike-slip earthquakes, which immediately makes the equations unsuitable for this application. The period range covered by the model is from 0.05 to 4.0 sec, which is another serious shortcoming from the perspective of the Hanford Site.

The most promising model is that of Gülerce and Abrahamson (2011), which was derived from the NGA-West1 database and predicts V/H response spectral ratios at 15 periods between 0.01 and 10.0 sec. The data set used and the functional form of the predictive equation are similar to those of the Abrahamson and Silva (2008) NGA-West1 GMPE. Although coefficients are provided for ratios at periods up to 10 sec, Gülerce and Abrahamson (2011) note that the usable frequency range of many recordings, as a consequence of filtering, eliminates the majority of the records from the regressions at longer periods: "*The significant drop in the number of recordings at 2.6 s indicates that the long-period predictions from this model are not well constrained by the empirical data.*" Inspection of the tabulated coefficients of the model reveals that several of the coefficients are kept constant at periods of 3 sec and greater, with only minor changes in the others; at 5, 7.5, and 10 sec, the coefficients are all identical, from which it can be inferred that the predicted ratios at longer periods were simply constrained to remain constant.

The model predicts the V/H ratios as a function of magnitude, distance, and V_{s30} (Figure 7.88). The model includes nonlinearity in the site response, which leads to very high predicted V/H ratios for large magnitudes and short distances, because the nonlinear response of softer sites diminishes the horizontal spectral ordinates but does not affect the vertical component of motion. The predictive model also includes the influence of the style of faulting, showing the pattern observed in other earlier studies that reverse-faulting earthquakes produced lower V/H ratios at short periods than other rupture mechanisms (Figure 7.89). A notable feature of the Gülerce and Abrahamson (2011) model is that it includes correlations between the residuals of the predicted V/H ratios and the horizontal period-to-period variability, which enables the construction of vertical conditional mean spectra. The only other model that also provides such correlations is that of Akkar et al. (2014a).

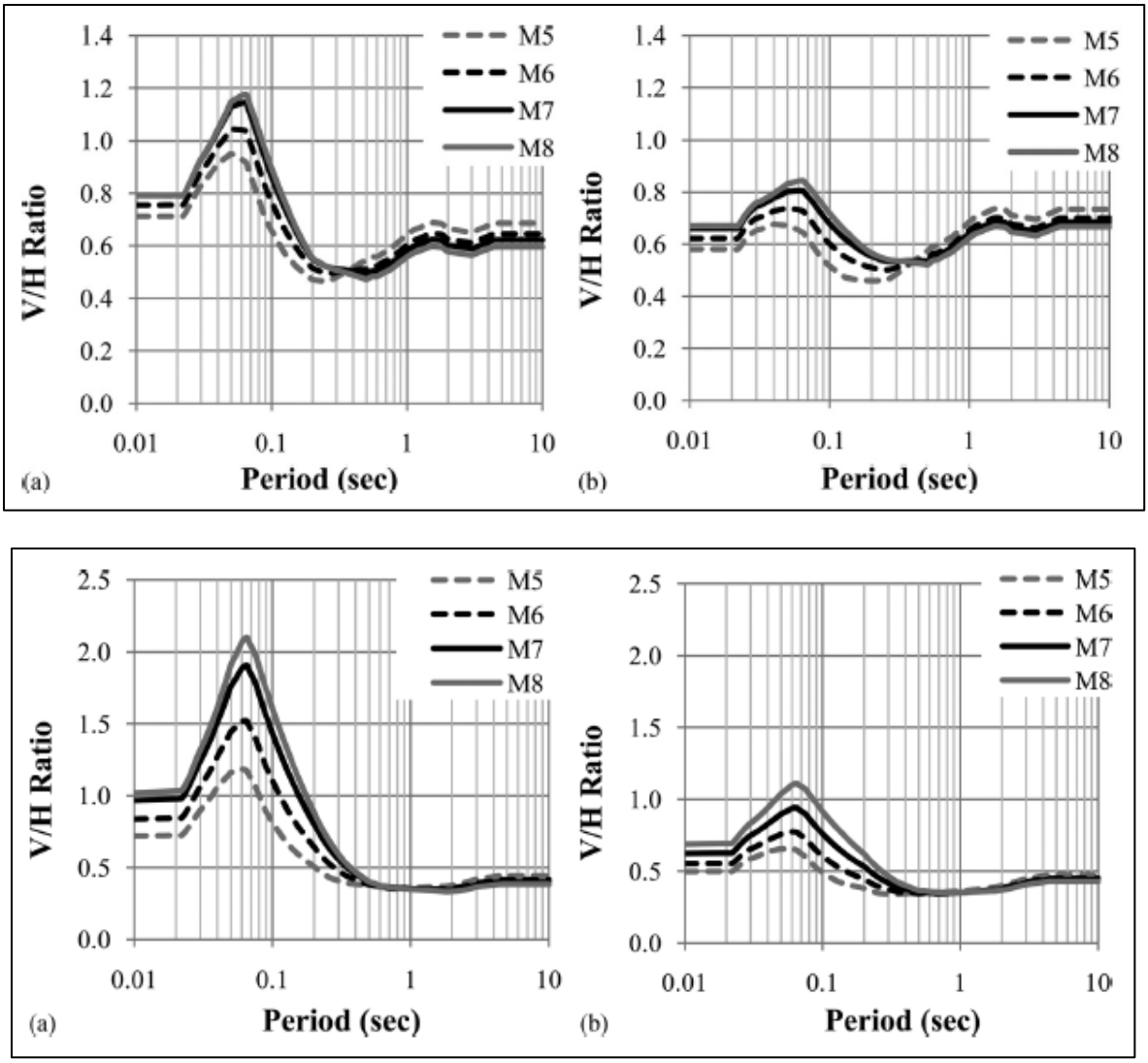

Figure 7.88. Predicted median V/H spectral ratios from the model of Gülerce and Abrahamson (2011) for earthquakes on a vertical strike-slip fault. Top row: ratios for a rock site (V_{s30} = 7 60 m/s) at rupture distances of (a) 5 km and (b) 30 km from earthquakes of different magnitudes. Bottom row: the same but for a soil site (V_{s30} = 270 m/s).

No studies have been published for the prediction of V/H spectral ratios specifically for subduction earthquakes. However, Gregor et al. (2012) explored the applicability of the Gülerce and Abrahamson (2011) equations to large subduction interface earthquakes using recordings from the **M** 8.8 Maule (Chile) earthquake of 2010 and the **M** 9.0 Tohoku (Japan) earthquake of 2011. The average residuals at different response periods for these data are shown in Figure 7.90 and Figure 7.91. The results show that at least for periods up to 1 to 2 sec, the Gülerce and Abrahamson (2011) equations perform well for these subduction earthquakes, despite the fact that the magnitudes of the earthquakes is beyond the upper limit of applicability of the model, which is stated as **M** 8 for dip-slip earthquakes. At longer periods, the Maule data are under-predicted by the equations; however, it is important to recall that the ratios for longer-period ordinates are simply assumed to be the same as those at 3 sec. Therefore, the relatively poor performance of the equations for longer-period spectral accelerations does not necessarily diminish the apparent suitability of the model based on its performance at periods of 1 sec and less.

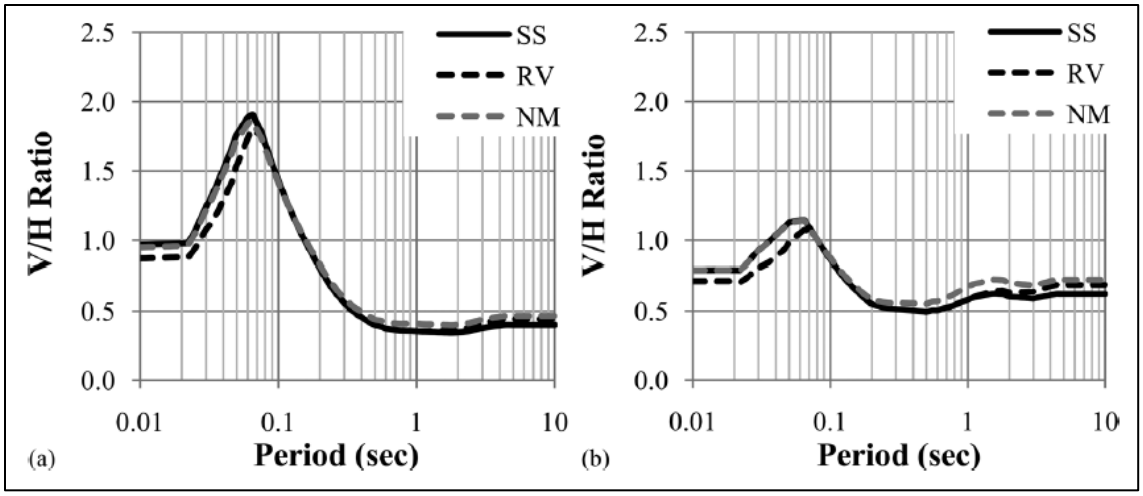

Figure 7.89. Predicted median V/H spectral ratios from the model of Gülerce and Abrahamson (2011) from an earthquakes of M 7 of different mechanisms at a rupture distance of 5 km for (a) a soil site with V_{s30} = 270 m/s and (b) a rock site with V_{s30} = 760 m/s.

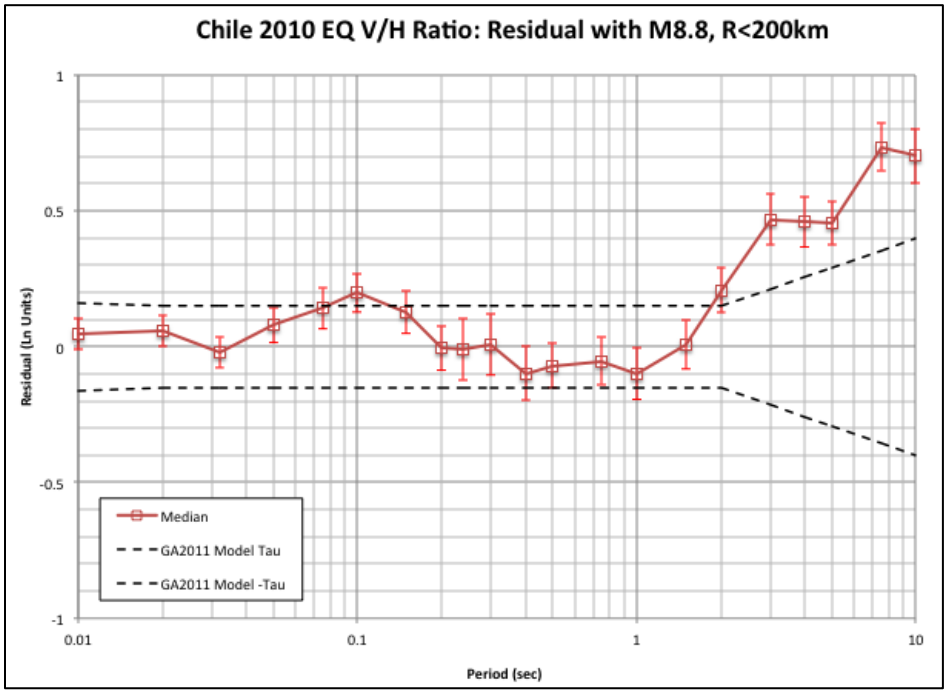

Figure 7.90. Average residuals of spectral ordinates from 31 recordings of the 2010 Maule earthquake in Chile calculated using the Gülerce and Abrahamson (2011) prediction equations (Gregor et al. 2012).

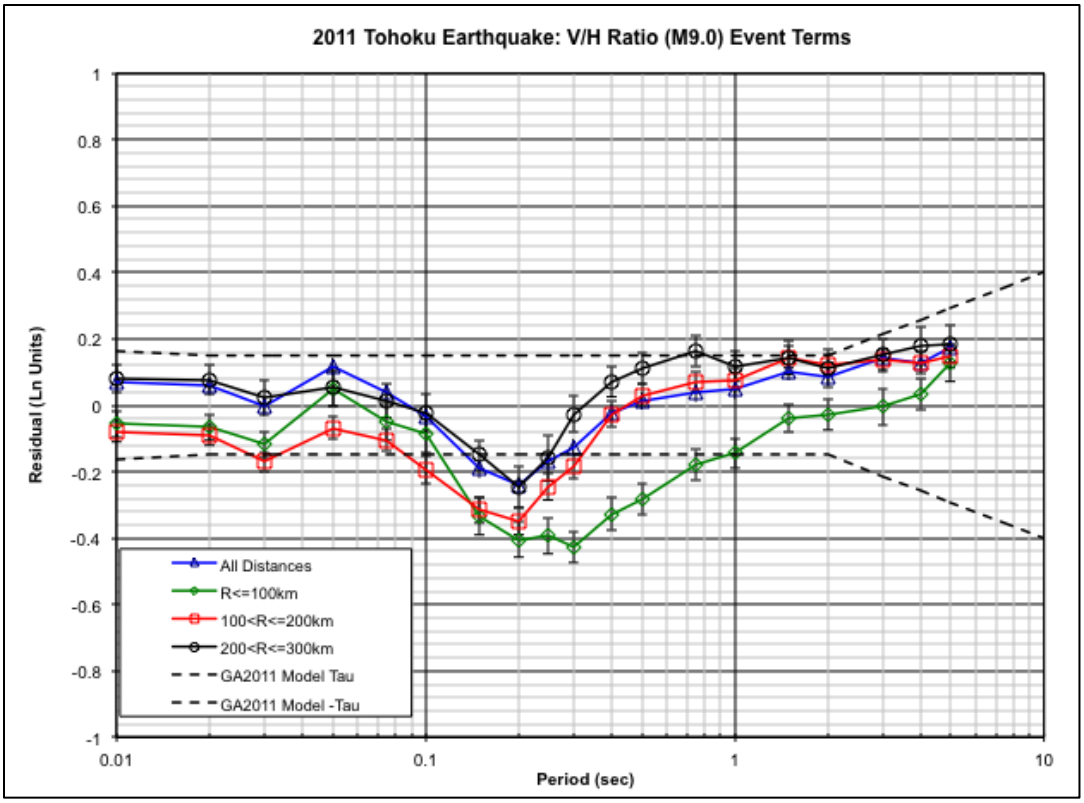

Figure 7.91. Average residuals of spectral ordinates from 360 recordings of the 2011 Tohoku earthquake in Japan, grouped in different distance ranges, calculated using the Gülerce and Abrahamson (2011) prediction equations (Gregor et al. 2012).

A point worth noting is that the distance of the Hanford Site from the Cascadia subduction zone is somewhat greater than the distance range of the Maule data in Figure 7.90. The black curve in Figure 7.91 corresponds to Tohoku recordings in the distance range of 200−300 km, which covers the distance separating the Hanford Site from Cascadia, and it is interesting to note that the residuals in this range are somewhat higher than those for the data recorded at shorter distances.

For completeness, the model of Edwards et al. (2011) for V/H spectral ratios on hard rock sites is also noted. The model was derived from a database of recordings from rock sites; small-magnitude data came from Switzerland and larger-magnitude data from Japan. The parameter chosen to characterize the sites is the QWL velocity rather than V_{s30}. The behavior represented by the resulting model is very different from that displayed in the other models reviewed herein, first by the fact that it finds almost no influence of the earthquake magnitude, and style of faulting was not considered. Distance was also found to exert only a very weak influence, but Edwards et al. (2011) proposed a correction to the V/H ratios for sites at short distances (hypocentral distance less than 30 km); this correction reduces the V/H ratios with respect to those at greater distances, which is counter to all other models, which predict higher V/H ratios at sites closer to the source.

7.7.4 Simplified Models for V/H Spectral Ratios

The models reviewed in the previous sections have the advantage of accurately capturing the influence of parameters such as magnitude and distance on the V/H response spectral ratios. Their application, however, requires that the hazard be disaggregated at the annual frequency of exceedance and oscillator period of interest in order to obtain the input values for the models. Although extensive disaggregations of the hazard are presented in this report (Section 10.3), the sponsors may wish to consider simpler models for the V/H spectral ratios, for which reason these are briefly reviewed in this section.

During many years, the few seismic design codes that did specify a vertical response spectrum simply scaled the horizontal spectrum by a factor on the order of ⅔. This approach has long been recognized as inadequate because the shape of the vertical and horizontal spectra are always different. Some seismic design codes have acknowledged this by including independent specifications of the vertical response spectrum, including Eurocode 8 (CEN 2004) and NEHRP (2009), the former based on the work of Elnashai and Papazoglu (1997) and the latter based on the model of Bozorgnia and Campbell (2004). The model of Bozorgnia and Campbell (2004) was based on the GMPEs of Campbell and Bozorgnia (2003), which covered a period range of 0.05 to 4 sec and used site classes rather than explicit V_{s30}.

In the nuclear realm, the RG 1.60 response spectrum (USAEC 1973) was the first move away from a constant V/H ratio of ⅔; it retained this value for response frequencies lower than 0.25 Hz and transitioned to a value of unity for frequencies above 3.5 Hz. A similar model was proposed more recently by Cauzzi and Faccioli (2008) who specified the ⅔ value at frequencies below 5 Hz and a value of unity for frequencies of 10 Hz and higher. Specifically to update the RG 1.60 spectral shapes for nuclear applications, McGuire et al. (2001) derived V/H ratios for rock sites in the western United States (WUS) and in central and eastern United States (CEUS), which cover the period range of interest to the Hanford project. These ratios are defined as a function of the PGA value, which is presumably a surrogate for the influence of distance and perhaps also magnitude. Figure 7.92 shows the ratios proposed by McGuire et al. (2001). The limitation of these models is that they are only calibrated to rock conditions and therefore are unlikely to be appropriate for application at soil sites such as those encountered at Hanford.

Another simplified model for constructing smoothed spectra from which V/H ratios can be inferred is that proposed by Malhotra (2006). This approach used values of PGA, peak ground velocity (PGV), and peak ground displacement (PGD) and is therefore not applicable to the Hanford Site because PGV and PGD are not part of the output from the PSHA.

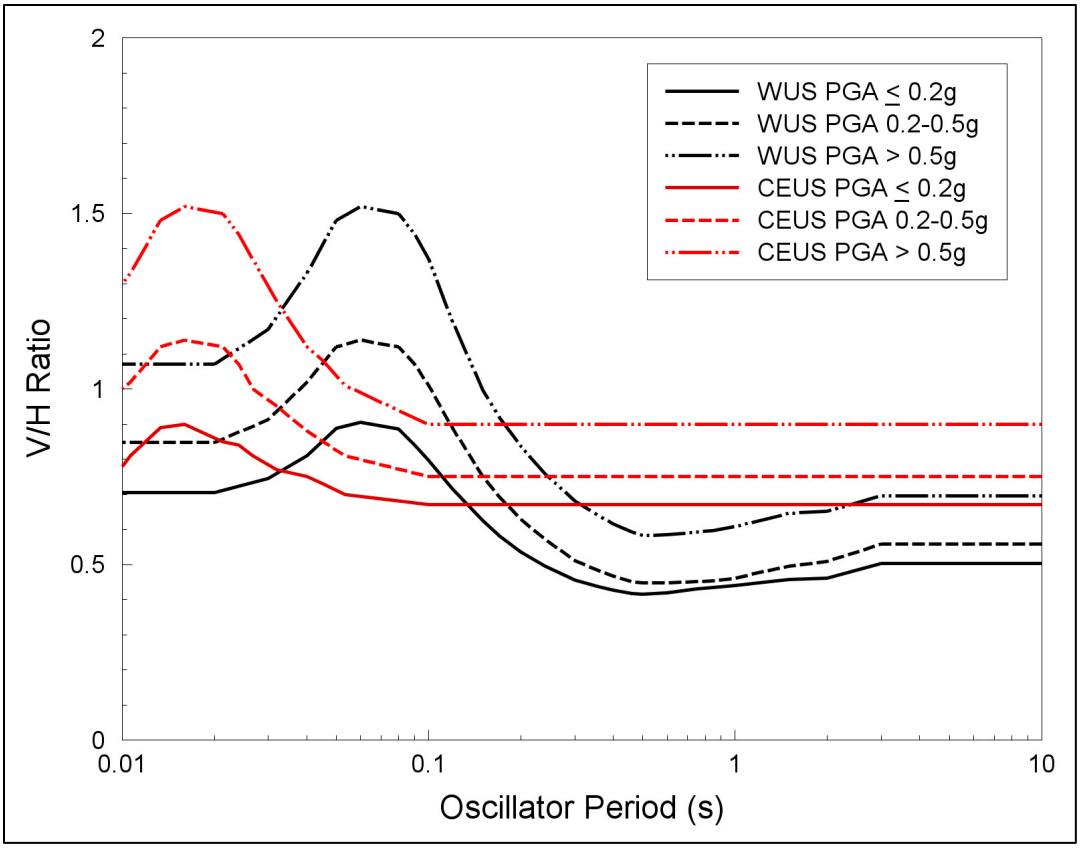

Figure 7.92. V/H spectral ratios for rock site in WUS and CEUS for different ranges of PGA as proposed by McGuire et al. (2001).

7.8 References

Abrahamson NA and WJ Silva. 1997. Empirical response spectral attenuation relations for shallow crustal earthquakes. *Seismological Research Letters* 68(1):94−127.

Abrahamson NA and WJ Silva. 2008. Summary of the Abrahamson & Silva NGA ground-motion relations. *Earthquake Spectra* 24(1):67−97.

Abrahamson NA and WJ Silva. 2009. Errata for "Summary of the Abrahamson & Silva NGA ground-motion relations." http://peer.berkeley.edu/ngawest/nga_models.html.

Abrahamson NA, N Gregor, and K Addo. 2014a. BC Hydro ground motion prediction equations for subduction earthquakes. *Earthquake Spectra* (Submitted).

Abrahamson NA, WJ Silva, and R Kamai. 2014b. Update of the AS08 Ground-Motion Prediction Equations Based on the NGA-West2 Data Set. *Earthquake Spectra* 30(3):1025-1055.

Aghabarati H and M Tehranizadeh. 2009. Near-source ground motion attenuation relationship for PGA and PSA of the vertical and horizontal components. *Bulletin of Earthquake Engineering* 7(3):609−635.

Agustsson K, BK Porbjarnadrottir, and K Vogfjörd. 2008. *Seismic Wave Attenuation for Earthquakes in SW Iceland*. Report 08005, Vedurstofa Islands Icelandic Meteorology Centre, Reykjavik.

Akkar S and JJ Bommer. 2006. Influence of long-period filter cut-off on elastic spectral displacements. *Earthquake Engineering and Structural Dynamics* 35:1145−1165.

Akkar S and JJ Bommer. 2007. Empirical prediction equations for peak ground velocity derived from strong-motions records from Europe and the Middle East. *Bulletin of the Seismological Society of America* 97(2):511−530.

Akkar S and JJ Bommer. 2010. Empirical equations for the prediction of PGA, PGV, and spectral accelerations in Europe, the Mediterranean, and the Middle East. *Seismological Research Letters* 81(2):195−206.

Akkar S and Z Çağnan. 2010. A local ground-motion predictive model for Turkey and its comparison with other regional and global ground-motion models. *Bulletin of the Seismological Society of America* 100(6):2978−2995.

Akkar S, Z Çağnan, E Yenier, Ö Erdoğan, A Sandikkaya, and P Gülkan. 2010. The recently compiled Turkish strong motion database: preliminary investigation for seismological parameters. *Journal of Seismology* 14:457−479.

Akkar S, MA Sandıkkaya, and BÖ Ay. 2014a. Compatible ground-motion prediction equations for damping scaling factors and vertical-to-horizontal spectral amplitude ratios for the broader Europe region. *Bulletin of Earthquake Engineering* 12(1):517−547.

Akkar S, MA Sandıkkaya, and JJ Bommer. 2014b. Empirical ground-motion models for point- and extended-source crustal earthquake scenarios in Europe and the Middle East. *Bulletin of Earthquake Engineering*. 12(1):359−387. DOI: 10.1007/s10518-013-9461-4.

Akkar S, MA Sandıkkaya, and JJ Bommer. 2014c. Erratum to: Empirical ground-motion models for point- and extended-source crustal earthquake scenarios in Europe and the Middle East. *Bulletin of Earthquake Engineering*. 12(1):389−390. DOI: 10.1007/s10518-013-9506-8.

Al Atik, L, A Kottke, N Abrahamson, and J Hollenback. 2013. Kappa (κ) Scaling of Ground-Motion Prediction Equations Using an Inverse Random Vibration Theory Approach. *Bulletin of the Seismological Society of America* 104(1):336−346.

Allen TI, DJ Wald, AJ Hotovec, K Lin, PS Earle, and KD Marano. 2008. An Atlas of ShakeMaps for Selected Global Earthquakes, USGS Open-File Report 2008-1236, U.S. Geological Survey, Reston, Virginia.

Ambraseys NN and J Douglas. 2003. Near-field horizontal and vertical earthquake ground motions. *Soil Dynamics & Earthquake Engineering* 23(1):1−18.

Ambraseys NN and KA Simpson. 1996. The prediction of vertical response spectra in Europe. *Earthquake Engineering & Structural Dynamics* 25:401−412.

Ancheta TD, RB Darragh JP Stewart, E Seyhan, WJ Silva, BSJ Chiou, KE Wooddell, RW Graves, AR Kottke, DM Boore, T Kishida, and JL Donahue. 2013. *PEER NGA-West2 Database.* PEER Report No 2013/03, PEER Center, University of California, Berkeley.

Anderson JG. 1997. Nonparametric description of peak acceleration above a subduction thrust. *Seismological Research Letters* 68(1):86−93.

Anderson JG and JN Brune. 1999. Probabilistic seismic hazard assessment without the ergodic assumption. *Seismological Research Lett*ers 70:19−28.

Anderson JG and SE Hough. 1984. A Model for the Shape of the Fourier Amplitude Spectrum of Acceleration at High Frequencies. *Bulletin of the Seismological Society of America* 74(5):1969–1993.

Anderson JG and Y Uchiyama. 2011. A methodology to improve ground-motion prediction equations by including path corrections. *Bulletin of the Seismological Society of America* 101:1822–1846.

Aoi S, T Kunugi, H Nakamura, and H Fujiwara. 2011. "Deployment of new strong motion seismographs of K-NET and KiK-net." In *Earthquake Data in Engineering Seismology*, Sinan Akkar, Polat. Gülkan, Torild Van Eck (eds.), Geotechnical, Geological, and Earthquake Engineering, Springer, New York.

Arango MC, F Strasser, JJ Bommer JJ, JM Cepeda, R Boroschek, DA Hernandez, and H Tavera. 2012. An Evaluation of the Applicability of Current Ground-motion Models to the South and Central American Subduction Zones. *Bulletin of the Seismological Society of America* 102(1):143–168. DOI: 10.1785/0120110078.

Arango MC, FO Strasser, JJ Bommer, DA Hernández, and JM Cepeda. 2011. A strong-motion database from the Central American subduction zone. *Journal of Seismology* 15:261−294.

Arroyo D, García D, Ordaz M, Mora MA, and SK Singh. 2010. Strong ground-motion relations for Mexican interplate earthquakes. *Journal of Seismology* 14(4):769–785.

Atkinson GM. 1995. Attenuation and source parameters of earthquakes in the Cascadia region. *Bulletin of the Seismological Society of America* 85:1327−1342.

Atkinson GM. 1997. Empirical ground motion relations for earthquakes in the Cascadia region. *Canadian Journal of Civil Engineering* 24:64–77.

Atkinson GM. 2005. Ground motions for earthquakes in southwestern British Columbia and Northwestern Washington: crustal, in-slab, and offshore events. Bulletin of the Seismological Society of America 93:1027−1044.

Atkinson GM. 2006. Single-station sigma. *Bulletin of the Seismological Society of America* 96:446−455.

Atkinson GM. 2013. Empirical evaluation of aleatory and epistemic uncertainty in Eastern ground motions. *Seismological Research Letters* 84:130−138.

Atkinson GM and DM Boore. 2003. Empirical ground-motion relations for subduction zone earthquakes and their application to Cascadia and other regions. *Bulletin of the Seismological Society of America* 93(4):1703–1729.

Atkinson GM and GM Boore. 2008. Erratum to: Empirical ground-motion relationships for subduction-zone earthquakes and their application to Cascadia and other regions. *Bulletin of the Seismological Society of America* 98:2567−2569.

Atkinson GM and DM Boore. 2011. Modifications to existing ground-motion prediction equations in light of new data. *Bulletin of the Seismological Society of America* 101(3):1121−1135.

Atkinson GM and M Macias. 2009. Predicted ground motions for great interface earthquakes in the Cascadia subduction zone. *Bulletin of the Seismological Society of America* 99(3):1552–1578.

Atkinson GM and WJ Silva. 2000. Stochastic modelling of California ground motions. *Bulletin of the Seismological Society of America* 90:255−274.

Barnett DB, BN Bjornstad, KR Fecht, DC Lanigan, SP Reidel, and CF Rust. 2007. *Geology of the Waste Treatment Plant Seismic Borehole*. PNNL-16407 (Revision 1), Pacific Northwest National Laboratory, Richland, Washington.

BC Hydro. 2012. *Probabilistic Seismic Hazard Assessment. Volume 3: Ground Motion Report*. Report No. E658 – Vol. 3, Vancouver, British Columbia.

Beauval C, F Cotton, NA Abrahamson, N Theodulidis, E Delavaud, L Rodriguez, F Scherbaum, and A Haendel. 2011. Regional differences in subduction ground motions. Presented at the 2011 CSMIP conference. Accessed at: http://www.cosmos-eq.org/technicalsession/TS2011/presentations/2011_beauval.pdf).

Beauval C, F Cotton, NA Abrahamson, N Theodulidis, E Delavaud, L Rodriguez, F Scherbaum, and A Haendel. 2012. Regional differences in subduction ground motions. *Proceedings of the 15th World Conference on Earthquake Engineering*, Lisbon, Portugal. Available at: http://www.nicee.org/wcee/.

Bechtel (Bechtel Power Corporation). 2013. *Assessment of Dynamic Geotechnical Data for the Columbia Generating Station Site*. Report prepared by Geotechnical & Hydraulic Engineering Services, Bechtel Power Corporation, Frederick, Maryland.

Beyer K and JJ Bommer. 2006. Relationships between median values and aleatory variabilities for different definitions of the horizontal component of motion. *Bulletin of the Seismological Society of America* 94(4A):1512−1522. Erratum: 2007, 97(5):1769.

Beyreuther M, R Barsch, L Krischer, T Megies, Y Behr and J Wassermann. 2010. ObsPy: A Python Toolbox for Seismology. *Seismological Research Letters* 81(3):530−533.

Bindi D, M Massa, L Luzi, G Ameri, F Pacor, R Puglia, and P Augliera. 2014a. Pan-European ground-motion prediction equations for the average horizontal component of PGA, PGV, and 5%-damped PSA at spectral periods up to 3.0 s using the RESORCE dataset. *Bulletin of Earthquake Engineering.* 12(1):391-430.

Bindi D, M Massa, L Luzi, G Ameri, F Pacor, R Puglia, and P Augliera. 2014b. Erratum to: Pan-European ground-motion prediction equations for the average horizontal component of PGA, PGV, and 5%-damped PSA at spectral periods up to 3.0 s using the RESORCE dataset. *Bulletin of Earthquake Engineering* 12(1):431−448.

Bindi D, F Pacor, L Luzi, R Puglia, M Massa, G Ameri, and R Paolucci. 2011. Ground motion prediction equations derived from the Italian strong motion database. *Bulletin of Earthquake Engineering* 9:1899−1920.

Blakely, RJ, BL Sherrod, CS Weaver, RE Wells, and AC Rohay. 2014. The Wallula fault and tectonic framework of south-central Washington, as interpreted from magnetic and gravity anomalies. *Tectonophysics* 624:32-45.

Bommer JJ, S Akkar, and S Drouet. 2012. Extending ground-motion prediction equations for spectral accelerations to higher response frequencies. *Bulletin of Earthquake Engineering* 10(2):379–399.

Bommer JJ, S Akkar, and Ö Kale. 2011. A model for vertical-to-horizontal response spectral ratios for Europe and the Middle East. *Bulletin of the Seismological Society of America* 101(4):1783−1806.

Bommer JJ, KJ Coppersmith, RT Coppersmith, KL Hanson, A Mangongolo, J Neveling, EM Rathje, A Rodriguez-Marek, F Scherbaum, R Shelembe, PJ Stafford, and FO Strasser. 2014. A SSHAC Level 3 probabilistic seismic hazard analysis for a new-build nuclear site in South Africa. *Earthquake Spectra* DOI: 10.1193/060913EQS145M (In Press).

Bommer JJ, J Douglas, F Scherbaum, F Cotton, H Bungum, and D Fäh. 2010. On the selection of ground-motion prediction equations for seismic hazard analysis. *Seismological Research Letters* 81(5):783−793.

Boore DM. 1983. Stochastic Simulation of High Frequency Ground Motions Based on Seismological Models of the Radiated Spectra. *Bulletin of the Seismological Society of America* 73(6):1865−1894.

Boore DM. 2005. *SMSIM – FORTRAN Programs for Simulating Ground Motions from Earthquakes: Version 2.3 – A revision of OFR 96-80-A*. USGS Open-File Report (A modified version of OFR 00--509, describing the program as of 15 August, 2005 [version 2.30]), U.S. Geological Survey Reston, West Virginia.

Boore DM. 2007. Some thoughts on relating density to velocity. Document on Dave Boore's web page: www.daveboore.com.

Boore DM. 2013. The Uses and Limitations of the Square-Root Impedance Method for Computing Site Amplification. *Bulletin of the Seismological Society of America.* 103:2356−2368.

Boore DM and GM Atkinson. 2008. Ground-motion prediction equations for the average horizontal component of PGA, PGV, and 5%-damped PSA at spectral periods between 0.01s and 10.0 s. *Earthquake Spectra* 24(1):99−138.

Boore DM and Bommer JJ. 2005. Processing of strong-motion accelerograms: needs, options and consequences. *Soil Dynamics and Earthquake Engineering* 25:93−115.

Boore DM and WB Joyner. 1997. Site Amplifications for Generic Rock Sites. *Bulletin of the Seismological Society of America* 87(2):327–341.

Boore DM, JP Stewart, E Seyhan, and GM Atkinson. 2014. NGA-West2 Equations for Predicting Response Spectral Accelerations for Shallow Crustal Earthquakes. *Earthquake Spectra* 30(3):1057-1085.

Boore DM, J Watson-Lamprey, and NA Abrahamson. 2006. GMRotD and GMRotI: Orientation-independent measures of ground motion. *Bulletin of the Seismological Society of America* 96:1202−1511.

Bora SS, F Scherbaum, N Kuehn, and P Stafford. 2014. Fourier spectral- and duration models for the generation of response spectra adjustable to different source-, propagation-, and site conditions. *Bulletin of Earthquake Engineering* 12(1):467−493. DOI: 10.1007/s10518-013-9482-z.

Boroschek R and V Contreras. 2012. Strong ground motion from the 2010 Mw 8.8 Maule Chile earthquake and attenuation relations for Chilean subduction zone interface earthquakes. *Proceedings of the International Symposium on Engineering Lessons Learned from the 2011 Great East Japan Earthquake,* March 1-4, 2012, Tokyo, Japan.

Bozorgnia Y and KW Campbell. 2004. The vertical-to-horizontal spectral ratio and tentative procedures for developing simplified V/H and vertical design spectra. *Journal of Earthquake Engineering* 4(4):539−561.

Bradley BA. 2013. A New Zealand-specific pseudospectral acceleration ground-motion prediction equation for active shallow crustal earthquakes based on foreign models. *Bulletin of the Seismological Society of America* 103(3):1801−1822.

Bragato PL and D Slejko. 2005. Empirical ground-motion relations for the Eastern Alps in the magnitude range 2.5-6.3. *Bulletin of the Seismological Society of America* 95(1):252−272.

Brocher TM. 2005. Empirical relations between elastic wavespeeds and density in the Earth's crust. *Bulletin of the Seismological Society of America* 95:2081−2092.

Campbell KW. 2009. Estimates of shear-wave Q and κ_0 for unconsolidated and semiconsolidated sediments in Eastern North America. *Bulletin of the Seismological Society of America* 99(4):2365−2392.

Campbell KW, YMA Hashash, B Kim, AR Kottke, EM Rathje, WJ Silva, and JP Stewart. 2014. *Reference Rock Site Condition for Central and Eastern North America: Part II – Attenuation (Kappa) Definition*. PEER 2014/12, Pacific Earthquake Engineering Center, Berkeley, California.

Campbell KW and Y Bozorgnia. 2003. Updated near-source ground motion (attenuation) relations for the horizontal and vertical components of peak ground acceleration and acceleration response spectra. *Bulletin of the Seismological Society of America* 93(1):314−331.

Campbell KW and Y Bozorgnia. 2008. NGA ground motion model for the geometric mean horizontal component of PGA, PGV, PGD and 5% damped linear elastic response spectra for periods ranging from 0.01 to 10s. *Earthquake Spectra* 24(1):139−171.

Campbell KW and Y Bozorgnia. 2014. NGA-West2 Campbell-Bozorgnia Ground Motion Model for the Horizontal Components of PGA, PGV, and 5%-Damped Elastic Pseudo-Acceleration Response Spectra for Periods Ranging from 0.01 to 10 sec. *Earthquake Spectra* 30(3): 1087-1115.

Cauzzi C and E Faccioli. 2008. Broadband (0.05 to 20 s) prediction of displacement response based on worldwide digital records. *Journal of Seismology* 12:453−475.

CEN (Comité Européen de Normalisation). 2004. *Eurocode 8, Design of Structures for Earthquake Resistance – Part 1: General rules, seismic actions, and rules for buildings*. EN 1998-1:2004, Comité Européen de Normalisation, Brussels, Belgium.

Cepeda JM, Benito MB, and EA Burgos. 2004. Strong-motion characteristics of January and February 2001 earthquakes in El Salvador. *In* WI Rose, JJ Bommer, DL López, MJ Carr, and JJ Major (eds.), Special Paper 375:405–421, *Natural Hazards in El Salvador*, Geological Society of America, Boulder, Colorado.

Chen L and E Faccioli. 2013. Single-station standard deviation analysis of 2010–2012 strong-motion data from the Canterbury region, New Zealand. *Bulletin of Earthquake Engineering* 11:1617−1632. DOI: 10.1007/s10518-013-9454-3.

Chen Y-H and C-CP Tsai. 2002. A new method for estimation of the attenuation relationship with variance components. *Bulletin of the Seismological Society of America* 92:1984–1991.

Chiou S-J, FI Makdisi, and RR Youngs. 2000. Style-of-Faulting and Footwall/Hanging Wall Effects on Strong Ground Motion, FY 1995. NEHRP Award Number 1434-95-G-2614, final report, Geomatrix Consultants, Oakland, California.

Chiou BS-J and RR Youngs. 2008a. An NGA model for the average horizontal component of peak ground motion and response spectra. *Earthquake Spectra* 24(1):173−215.

Chiou BS-J and RR Youngs. 2008b. *Chiou and Youngs PEER-NGA Empirical Ground Motion Model for the Average Horizontal Component of Peak Acceleration, Peak Velocity, and Pseudo-Spectral Acceleration for Spectral Periods of 0.01 to 10 sec*. PEER Report, Pacific Earthquake Engineering Center, Berkeley, California.

Chiou BS-J and RR Youngs. 2014. Update of the Chiou and Youngs NGA Ground Motion Model for Average Horizontal Component of Peak Ground Motion and Response Spectra. *Earthquake Spectra* 30(3):1117-1153.

Chiou B, B Youngs, NA Abrahamson, and K Addo. 2010. Ground-motion attenuation model for small-to-moderate shallow crustal earthquakes in California and its implications on regionalization of ground-motion prediction models. *Earthquake Spectra* 26:907−926.

Cotton F, G Pousse, F Bonilla, and F Scherbaum. 2008. On the discrepancy of recent European ground-motion observations and predictions from empirical models: Analysis of KiK-net accelerometric data and point-sources stochastic simulations. *Bulletin of the Seismological Society of America* 98(5):2244−2261.

Cotton F, F Scherbaum, JJ Bommer, and H Bungum. 2006. Criteria for selecting and adjusting ground-motion models for specific target regions: Application to central Europe and rock sites. *Journal of Seismology* 10(2):137−156.

Crouse CB. 1991. Ground-motion attenuation equation for earthquake on Cascadia subduction-zone earthquake. *Earthquake Spectra* 7: 210−236.

Crouse CB, KV Yogesh, and BA Schell. 1988. Ground motions from subduction zone earthquakes, *Bulletin of the Seismological Society of America* 78:1−25.

Dawood HM. 2014. Partitioning uncertainty for non-ergodic probabilistic seismic hazard analyses. PhD dissertation, Virginia Polytechnic Institute and State University, USA.

Dawood HM, A Rodriguez-Marek, J Bayless, C Goulet, and E Thompson. 2014. Processing the KiK-net strong ground motion database and compilation of metadata for GMPE development. Submitted to *Earthquake Spectra*. (Draft available upon request.)

Derras B, PY Bard, and F Cotton. 2014. Towards fully data driven ground-motion prediction models for Europe. *Bulletin of Earthquake Engineering*. 12(1):495-516. DOI: 10.1007/s10518-013-9481-0.

Donahue JL and NA Abrahamson. 2014. Hanging-Wall Scaling using Finite-Fault Simulations. *Earthquake Spectra* (In Review).

Douglas J. 2011. Ground-motion prediction equations 1964-2010. BRGM/RP-59356-FR, Bureau de Recherches Géologiques et Minières, Orléans, France.

Douglas J. 2014. Preface of special issue: A new generation of ground-motion models for Europe and the Middle East. *Bulletin of Earthquake Engineering* 12(1):307−310. DOI: 10.1007/s10518-013-9535-3.

Edwards B and D Fäh. 2013. A stochastic ground-motion model for Switzerland. *Bulletin of the Seismological Society of America* 103(1):78−98. DOI: 10.1785/0120110331.

Edwards B, V Poggi, an D Fäh. 2011. A predictive equation for the vertical-to-horizontal ratio of ground motion at rock sites based on shear-wave velocity profiles from Japan and Switzerland. *Bulletin of the Seismological Society of America* 101(6):2998−3019.

Elnashai AS and AJ Papazoglu. 1997. Procedure and spectra for analysis of RC structures subjected to vertical earthquake loads. *Journal of Earthquake Engineering* 1(1):121−155.

EPRI (Electric Power Research Institute). 1993. *Guidelines for Determining Design Basis Ground Motions*. Vol. 1-5, EPRI TR-102293, Palo Alto, California.

Flück P, RD Hyndman, and K Wang. 1997. 3-D dislocation model for great earthquakes of the Cascadia subduction zone. *Journal of Geophysical Research* 102(20):539-20,550.

Frankel AD. 2009. A constant stress-drop model for producing broadband synthetic seismograms—comparison with the Next Generation Attenuation relations. *Bulletin of the Seismological Society of America* 99:664−680.

Frankel A, DL Carver, and RA Williams. 2002. Nonlinear and linear site response and basin effects in Seattle from the M 6.8 Nisqually, Washington, earthquake. *Bulletin of the Seismological Society of America* 92:2090–2109.

Frankel A, W Stephenson, and D Carver. 2009. Sedimentary basin effects in Seattle, Washington: ground-motion observations and 3D simulations. *Bulletin of the Seismological Society of America* 99(3):1579−1611.

Frankel A, P Thorne, and A Rohay. 2013. *Three-Dimensional Ground-Motion Simulations of Earthquakes for the Hanford Area, Washington*. USGS Open-File Report 2013-1789, U.S. Geological Survey, Weston, Virginia.

García D, Singh SK, Herráiz M, Ordaz M, and JF Pacheco. 2005. Inslab earthquakes of central Mexico: Peak ground-motion parameters and response spectra. *Bulletin of the Seismological Society of America* 95(6):2272–2282.

Garcia D, DJ Wald, and MG Hearne. 2012. A global earthquake discrimination scheme to optimize ground-motion prediction equation selection. *Bulletin of the Seismological Society of America* 102:185−203.

Gardner JK and L Knopoff. 1974. Is the sequence of earthquakes in Southern California, with aftershocks removed, Poissonian? *Bulletin of the Seismological Society of America* 64(5)1363–1367.

Geomatrix. 1996. *Probabilistic Seismic Hazard Analysis – DOE Hanford Site, Washington*. WHC-SD-W236A-TI-002, Rev. 1, Westinghouse Hanford Company, Richland, Washington.

Glover DW. 1985. Crustal Structure of the Columbia Basin, Washington from Borehole and Refraction Data. A Master of Science Thesis, Geophysics Program, University of Washington, Seattle.

Goda K and GM Atkinson. 2009. Probabilistic characterization of spatially correlated response spectra for earthquakes in Japan. *Bulletin of the Seismological Society of America* 99:3003−3020.

Graizer V and E Kalkan. 2011. Modular filter-based approach to ground-motion attenuation modeling. *Seismological Research Letters* 82(1):21−31.

Graizer V, E Kalkan, and K-W Lin. 2013. Global ground motion prediction equations for shallow crustal regions. *Earthquake Spectra* 29(3):777−791

Gregor NJ, NA Abrahamson, KO Addo, A Rodriguez-Marek. 2012. Vertical to horizontal (V/H) ratios for large megathrust subduction zone earthquakes. *Proceedings of 15th World Conference on Earthquake Engineering*, Lisbon, Portugal. Available at: http://www.nicee.org/wcee/.

Gregor NJ, Silva WJ, Wong IG, and RR Youngs. 2002. Ground-motion attenuation relationships for Cascadia subduction zone megathrust earthquakes based on a stochastic finite-fault model. *Bulletin of the Seismological Society of America* 92(5):1923–1932.

Gülerce Z and NA Abrahamson. 2011. Site-specific design spectra for vertical ground motion. *Earthquake Spectra* 27(4):1023−1047.

Gülerce Z and E Akyüz. 2013. The NGA-W1 vertical-to-horizontal spectral ratio prediction equations adjusted to Turkey. *Seismological Research Letters* 84(4):678−687.

Gupta ID. 2010. Response spectral attenuation relations for in-slab earthquakes in Indo-Burmese subduction zone. *Soil Dynamics and Earthquake Engineering* 30(5):368–377.

Hashash YMA, AR Kottke, JP Stewart, KW Campbell, B Kim, C Moss, S Nikolaoy, E Rathje, and WJ Silva. 2014. Reference Rock Site Condition for Central and Eastern North America. *Bulletin of the Seismological Society of America* 104(2):684–701.

Hartzell S, S Harmsen, RA Williams, D Carver, A Frankel, G Choy, P-C Liu, RC Jachens, TM Brocher, and CM Wentworth. 2006. Modeling and validation of a 3D velocity structure for the Santa Clara Valley, California, for seismic-wave simulations. *Bulletin of the Seismological Society of America* 96(5):1851−1881.

Haskell NA. 1960. Crustal Reflection of Plane SH Waves. *Journal of Geophysical Research* 65:4147-4150.

Hayes G. 2010. Finite Fault Model. Updated Result of the Feb 27, 2010 Mw 8.8 Maule, Chile Earthquake. Accessed at http://earthquake.usgs.gov/earthquakes/eqinthenews/2010/us2010tfan/finite_fault.php.

Hayes G. 2011. Finite Fault Model. Updated Result of the Mar 11, 2011 Mw 9.0 Earthquake Offshore Honshu, Japan. Accessed at http://earthquake.usgs.gov/earthquakes/eqinthenews/2011/usc0001xgp/finite_fault.php.

Heaton TH and SH Hartzell. 1986. Source characteristics of hypothetical subduction earthquakes in the northwestern United States. *Bulletin of the Seismological Society of America* 76:675−708.

Heaton TH and SH Hartzell. 1989. Estimation of strong ground motions from hypothetical earthquakes on the Cascadia subduction zone, Pacific Northwest. *Pure and Applied Geophysics* 129(1/2):131−201.

Hermkes M, NM Kuehn, and C Riggelsen. 2014. Simultaneous quantification of epistemic and aleatory uncertainty in GMPEs using Gaussian process regression. *Bulletin of Earthquake Engineering* 12(1):449−493. DOI: 10.1007/s10518-013-9507-7.

Hong HP and K Goda. 2007. Orientation-dependent ground-motion measure for seismic hazard assessment. *Bulletin of the Seismological Society of America* 97(5):1525−1538.

Hong HP, Pozos-Estrada A, and R Gomez. 2009. Orientation effect on ground motion measurements for Mexican subduction earthquakes. *Earthquake Engineering and Engineering Vibration* 8(1):1–16.

Idriss IM. 2014. NGA-West2 Model for Estimating Average Horizontal Values of Pseudo-Absolute Spectral Accelerations Generated by Crustal Earthquakes. *Earthquake Spectra* (Submitted). (A PEER report version of this model is available at http://peer.berkeley.edu/publications/peer_reports/reports_2013/webPEER-2013-08-Idriss.pdf)

Jarchow CM, RD Catchings, and WJ Lutter. 1994. Large-explosive source, wide-recording aperture, seismic profiling on the Columbia Plateau, Washington. *Geophysics* 59(2):259–271.

JBA (Jack Benjamin & Associates), URS Corporation Seismic Hazards Group, Geomatrix Consultants, Inc., and Shannon & Wilson. 2012. *Probabilistic Seismic Hazard Analyses Project for the Mid-Columbia Dams*. Final Report prepared for the Public Utility Districts of Chelan, Douglas, and Grant Counties. Chelan County PUD, Wenatchee, Washington.

Kagawa T, B Zhao, K Miyakoshi, K Irikura. 2004. Modeling of 3D basin structure for seismic wave simulations based on available information on the target area: case study of the Osaka basin, Japan. *Bulletin of the Seismological Society of America* 94:1353−1368.

Kalkan E and P Gülkan. 2004. Empirical attenuation equations for vertical ground motion in Turkey. *Earthquake Spectra* 20(3):853−882.

Kanno T, A Narita, N Morikawa, H Fujiwara, and Y Fukushima. 2006. A new attenuation relation for strong ground motion in Japan based on recorded data. *Bulletin of the Seismological Society of America* 96(3):879–897.

Kawano H, Takahashi K, Takemura M, Tohdo M, Watanabe T, and S Noda. 2000. Empirical response spectral attenuations on the rocks with VS = 0.5 to 3.0 km/s in Japan. *Proceedings of Twelfth World Conference on Earthquake Engineering* Paper No. 0953.

Kobayashi S, Takahashi T, Matsuzaki S, Mori M, Fukushima Y, Zhao JX, and PG Somerville. 2000. A spectral attenuation model for Japan using digital strong motion records of JMA87 type. *Proceedings of Twelfth World Conference on Earthquake Engineering* Paper No. 2786.

Konno K and T Ohmachi. 1998. Ground-Motion Characteristics Estimated from Spectral Ratio between Horizontal and Vertical Components of Microtremor. *Bulletin of the Seismological Society of America* 88(1):228−241.

Last GV. 2014. *Stratigraphic Profiles for Selected Hanford Site Seismometer Stations and Other Locations*. PNNL-23126, Pacific Northwest National Laboratory, Richland Washington.

Lee C-T and B-R Tsai. 2008. Mapping Vs30 in Taiwan. *Terrestrial, Atmospheric, and Oceanic Sciences* 19(6):671:682. DOI: 10.3319/TAO.2008.19.6.671(PT).

Lin P, NA Abrahamson, M Walling, C-T Lee, B Chiou, and C Cheng. 2011. Repeatable path effects on the standard deviation for empirical ground-motion models. *Bulletin of the Seismological Society of America* 101:2281−2295.

Lin P-S and C-T Lee. 2008. Ground-motion attenuation relationships for subduction-zone earthquakes in northeastern Taiwan. *Bulletin of the Seismological Society of America* 98(1):220–240.

Liu P-C and RJ Archuleta. 2002. The effect of a low-velocity surface layer on simulated ground motion. *Seismological Research Letters* 73:267.

Ludwin RS, CS Weaver, and RS Crosson. 1991. Seismicity of Washington and Oregon. Chapter 6 in *Neotectonics of North America – The Geology of North America Decade Map Volume 1*, DB Slemmons, ER Engdahl, MD Zoback, and DD Blackwell (eds.), pp. 77–98. Geological Society of America, Boulder, Colorado.

Luzi L, D Bindi, R Puglia, F Pacor, and A Oth. 2014. Single station sigma for Italian strong motion stations. *Bulletin of the Seismological Society of America* 104(1):467−483. DOI: 10.1785/0120130089.

Ma S, RJ Archuleta, and MT Page. 2007. Effects of large-scale surface topography on ground motions, as demonstrated by the San Gabriel Mountains, Los Angeles, California. *Bulletin of the Seismological Society of America* 97(6):2066−2079.

Malhotra PK. 2006. Smooth spectra of horizontal and vertical ground motions. *Bulletin of the Seismological Society of America* 96(2):506−518.

McGuire RK, WJ Silva, and CJ Costantino. 2001. *Technical Basis for Revision of Regulatory Guidance on Design Ground Motions: Hazard- and Risk-Consistent Ground Motion Spectra Guidelines*. NUREG/CR-6728, U.S. Nuclear Regulatory Commission, Washington, D.C.

McVerry GH, Zhao JX, Abrahamson NA, and PG Somerville. 2000. Crustal and subduction zone attenuation relations for New Zealand earthquakes. *Proceedings of Twelfth World Conference on Earthquake Engineering* Paper No. 1834.

McVerry GH, JX Zhao, NA Abrahamson, and PG Somerville. 2006. New Zealand acceleration response spectrum attenuation relations for crustal and subduction zone earthquakes. *Bulletin of the New Zealand Society for Earthquake Engineering* 39(4):1−58.

Megies T, M Beyreuther, R Barsch, L Krischer, J Wassermann. 2011. ObsPy – What can it do for data centers and observatories? *Annals of Geophysics* 54(1):47−58

Morikawa N, T Kanno, A Narita, H Fujiwara, T Okumura, Y Fukushima, and A Guerpinar. 2008. Strong motion uncertainty determined from observed records by dense network in Japan. *Journal of Seismology* 12:529−546.

Motazedian D and GM Atkinson. 2005. Stochastic finite-fault modeling based on a dynamic corner frequency. *Bulletin of the Seismological Society of America* 95:955−1010.

NEHRP (National Earthquake Hazards Reduction Program). 2009. *2009 NEHRP recommended seismic provisions for new buildings and other structures: Part 1, Provisions*. National Earthquake Hazards Reduction Program. Available at: http://www.fema.gov/media-library/assets/documents/18152?id=4103.

Nigam NC and PC Jennings. 1969. Calculation of response spectra from strong-motion earthquake records. *Bulletin of the Seismological Society of America* 59:909−922.

Okada Y, K Kasahara, S Hori, K Obara, S Sekiguchi, H Fujiwara, and A Yamamoto. 2004. Recent progress of seismic observation networks in Japan: Hi-net, F-net, K-NET and KiK-net. *Earth Planets Space* 56:15–28.

Ólafsson S and R Sigbjörnsson. 2012. Near-source decay of seismic waves in Iceland. *Proceedings of the 15th World Conference on Earthquake Engineering*, Lisbon, Portugal. Available at: http://www.nicee.org/wcee/.

Ornthammarath T, J Douglas, R Sigbjörnsson, and CG Lai. 2011. Assessment of ground motion variability and its effects on seismic hazard analysis: a case study for Iceland. *Bulletin of Earthquake Engineering* 9:931−953.

Oth A, S Parolai, and D Bindi. 2011. Spectral analysis of K-NET and KiK-net data in Japan, Part I: Database compilation and peculiarities. *Bulletin of the Seismological Society of America* 101:652–666.

Palmer SP, SL Magsino, EL Bilderback, JL Poelstra, DS Folger, and RA Niggemann. 2004. Liquefaction Susceptibility and Site Class Maps of Washington State, by County. Open File Report 2004-20, Washington, State Department of Natural Resources, Olympia, Washington. Available at: http://www.dnr.wa.gov/ResearchScience/Topics/GeologyPublicationsLibrary/Pages/pub_ofr04-20.aspx.

Pankow KL and JC Pechmann. 2004. The SEA99 ground-motion predictive relations for extensional tectonic regimes: Revisions and a new peak ground velocity relation. *Bulletin of the Seismological Society of America* 94(1):341−348.

Pankow KL and JC Pechmann. 2006. Erratum: The SEA99 ground-motion predictive relations for extensional tectonic regimes: Revisions and a new peak ground velocity relation. *Bulletin of the Seismological Society of America* 96(1):364.

PEER (Pacific Earthquake Engineering Research Center). 2013. *NGA-West2 ground motion prediction equations for vertical ground motions*. PEER Report 2013/24, University of California, Berkeley, California.

Petersen MD, AD Frankel, SC Harmsen, CS Mueller, KM Haller, RL Wheeler, RL Wesson, Y Zeng, OS Boyd, DM Perkins, N Luco, EH Field, CJ Wills, and KS Rukstales. 2008. *Documentation for the 2008 Update of the United States National Seismic Hazard Maps*. USGS Open-File Report 2008-1128, U.S. Geological Survey, Reston, Virginia. Available at: http://pubs.er.usgs.gov/usgspubs/ofr/ofr081128.

Philips WS, KM Mayeda, and L Malagnini. 2014. How to invert multi-band, regional phase amplitudes for 2-D attenuation and source parameters: Tests using the USArray. *Pure and Applied Geophysics* 171(3-5):469−484. DOI: 10.1007/s00024-013-0646-1.

PNNL (Pacific Northwest National Laboratory). 2014a. "Ground Motion Data Viewer." Available at http://ec2-23-22-12-59.compute-1.amazonaws.com/, last accessed 04/22/2014, password : iris. (A copy of the file will be retained in the project records (project number 58781) at Pacific Northwest National Laboratory in Richland, Washington.)

PNNL (Pacific Northwest National Lab). 2014b. Hanford PSHA Subduction Flatfile. https://spteams1.pnnl.gov/sites/HPSHA/T5_Ground%20Motion/Forms/AllItems.aspx?RootFolde

r=%2Fsites%2FHPSHA%2FT5_Ground%20Motion%2F10%20Subduction%20Flatfile&FolderCTID=0x0120008954CF98BE1F014A94760FB5DA6282DF&View={380F803D-A245-4AAE-8D8A-79F822C8D8BE}. (A copy of the file will be retained in the project records (project number 58781) at Pacific Northwest National Laboratory, in Richland, Washington.)

Press WH, BP Flannery, SA Teukolsky, and WT Vetterling. 1986. *Numerical Recipes*. Cambridge University Press, Cambridge.

Purvance MD and JG Anderson. 2003. A Comprehensive Study of the Observed Spectral Decay in Strong-Ground Accelerations Recorded in Guerrero, Mexico. *Bulletin of the Seismological Society of America* 93:600–611.

Reasenberg P. 1985. Second-order moment of central California seismicity, 1969-82. *Journal of Geophysical Research* 90:5479−5495.

Reidel SP. 1998. Emplacement of Columbia River flood basalt. *Journal of Geophysical Research* 103(B11):27,393−27,410.

Reidel SP, VG Johnson, and FA Spane. 2002. *Natural Gas Storage in Basalt Aquifers of the Columbia Basin, Pacific Northwest USA: A Guide to Site Characterization.* PNNL-13962, Pacific Northwest National Laboratory Richland, Washington.

Renault P, S Heuberger, and NA Abrahamson. 2010. PEGASOS Refinement Project: An improved PSHA for Swiss nuclear power plants. *Proceedings of the 14th European Conference of Earthquake Engineering,* Paper ID 991. Ohrid, Republic of Macedonia. Available at: http://toc.proceedings.com/11356webtoc.pdf.

Rodriguez-Marek A, F Cotton, NA Abrahamson, S Akkar, L Al Atik, B Edwards, GA Montalva, and H. Dawood. 2013. A model for single-station standard deviation using data from various tectonic regions. *Bulletin of the Seismological Society of America* 103:3149−3163.

Rodriguez-Marek A, GA Montalva, F Cotton, and F Bonilla. 2011. Analysis of Single-Station Standard Deviation Using the KiK-net Data. *Bulletin of the Seismological Society of America* 101:1242–1258.

Rodriguez-Marek A, EM Rathje, JJ Bommer, F Scherbaum, and PJ Stafford. 2014. Application of single-station sigma and site-response characterization in a probabilistic seismic-hazard analysis for a new nuclear site. *Bulletin of the Seismological Society of America* 105(4):1601-1619.

Rohay A. 2014. *Hanford PSHA GMC database and data selection*. Technical Note, Pacific Northwest National Laboratory, Richland, Washington.

Rohay AC and TM Brouns. 2007. *Site-Specific Velocity and Density Model for the Waste Treatment Plant, Hanford, Washington*. PNNL-16652, Pacific Northwest National Laboratory, Richland, Washington.

Rohay AC and TM Brouns. 2007. *Site-Specific Velocity and Density Model for the Waste Treatment Plant, Hanford, Washington*. PNNL-16652, Pacific Northwest National Laboratory, Richland, Washington.

Rohay AC and SP Reidel. 2005. *Site-Specific Seismic Site Response Model for the Waste Treatment Plant, Hanford, Washington*. PNNL-15089, Pacific Northwest National Laboratory, Richland, Washington.

Rohay A, Reidel S, Hartshorn D, and M Valenta. 2001. Ground Motions at a Network of Strong Motion Accelerometers on the Hanford Site, Southeastern Washington, from the 28 February 2001 Nisqually Earthquake. *American Geophysical Union, Fall Meeting 2001*, Abstract S42C-0661.

Sakamoto S, Uchiyama Y, and S Midorikawa. 2006. Variance of response spectra in attenuation relationship. *Proceedings of the Eighth U.S. National Conference on Earthquake Engineering* Paper No. 471.

Scherbaum F, F Cotton, and P Smit. 2004. On the use of response spectral-reference data for the selection and ranking of ground motion models for seismic-hazard analysis in regions of moderate seismicity: The case of rock motion. *Bulletin of the Seismological Society of America* 94(6):2164–2185.

Scherbaum F, E Delavaud, and C Riggelsen. 2009. Model selection in seismic hazard analysis: An information-theoretic perspective. *Bulletin of the Seismological Society of America* 99(6):3234–3247.

Schmidt V, Dahle A, and H Bungum. 1997. Costa Rican spectral strong motion attenuation. Reduction of Natural Disasters in Central America Earthquake Preparedness and Hazard Mitigation Phase II: 1996–2000, Part 2. Technical report, NORSAR, Kjeller, Norway.

Schnabel PB, J Lysmer, and HB Seed. 1972. SHAKE, a Computer Program for Earthquake Response. Earthquake Engineering Research Center Report EERC 72-12, University of California, Berkeley, California.

Shabestari KT and F Yamazaki. 1998. Attenuation of JMA seismic intensity using recent JMA records. Pages 529–534 in *Proceedings of the 10th Japan Earthquake Engineering Symposium*, Vol. 1. As reported by Shabestari and Yamazaki (2000).

Shabestari KT and F Yamazaki. 2000. Attenuation relation of response spectra in Japan considering site-specific term. *Proceedings of Twelfth World Conference on Earthquake Engineering* Paper No. 1432.

Silva WJ and RB Darragh. 1995. *Engineering Characterization of Strong Ground Motion Recorded at Rock Sites*. EPRI TR-102262, Electric Power Research Institute, Palo Alto, California.

Silva WJ, R Darragh, C Stark, I Wong, J Stepp, J Schneider, and S Chiou. 1990. A methodology to estimate design response spectra in the near-source region of large earthquakes using the band-limited-white-noise ground motion model. *Proceedings of 4th US National Conference on Earthquake Engineering* 1:487−494.

Steidl JH and P-C Liu. 2003. Attenuation analysis of borehole data for CVM. SCEC 2003 Annual Meeting, 7-11 September 2003, Oxnard, California, p.146.

Strasser FO, MC Arango, and JJ Bommer. 2010. Scaling of the source dimensions of interface and intraslab subduction-zone earthquakes with moment magnitude. *Seismological Research Letters* 81(6):941−950.

Sunuwar L, C Cuadra, and MB Karkee. 2004. Strong ground motion attenuation in the Sea of Japan (Okhotsk-Amur plates boundary) region. *Proceedings of Thirteenth World Conference on Earthquake Engineering* Paper No. 0197.

Takahashi T, Asano A, Saiki T, Okada H, Irikura, K, Zhao JX, Zhang J, HK Thio, Somerville PG, Fukushima Y, and Y Fukushima. 2004. Attenuation models for response spectra derived from Japanese strong-motion records accounting for tectonic source types. *Proceedings of Thirteenth World Conference on Earthquake Engineering* Paper No. 1271.

Takahashi T, Kobayashi S, Fukushima, Y, Zhao JX, Nakamura, H., and PG Somerville. 2000. A spectral attenuation model for Japan using strong motion data base. *Proceedings of the Sixth International Conference on Seismic Zonation*.

Tejeda-Jácome J and FJ Chávez-García. 2007. Empirical ground-motion estimation equations in Colima from weak motion records. *ISET Journal of Earthquake Technology* 44(3–4):409–420.

Tezcan J and A Piolatto. 2012. A probabilistic nonparametric model for the vertical-to-horizontal spectral ratio. *Journal of Earthquake Engineering* 16:142−157.

Thordarson T and S Self. 1998. The Roza member, Columbia River Basalt Group: A gigantic pahoehoe lava flow formed by ondogenous process? *Journal of Geophysical Research* 103(B11):27,411−27,441.

Thorne PD, AC Rohay, and SP Reidel. 2014. *Development of a basin geologic and seismic property model used to support basin-effects modeling for the Hanford Probabilistic Seismic Hazard Analysis*. PNNL-23305, Pacific Northwest National Laboratory, Richland, Washington.

USAEC (U.S. Atomic Energy Commission). 1973. *Design Response Spectra for Seismic Design of Nuclear Power Plants*. Regulatory Guide RG 1.60, Washington, D.C.

USGS (U.S. Geological Survey). 2014. STREC: SeismoTectonic Regime Earthquake Calculator. Available at https://github.com/usgs/strec, last accessed 4/26/2014.

Van Houtte C, S Drouet, and F Cotton. 2011. Analysis of the Origins of κ (kappa) to Compute Hard Rock to Rock Adjustment Factors for GMPEs. *Bulletin of the Seismological Society of America* 101(6):2926−2941.

Watson-Lamprey JA and DM Boore. 2007. Beyond Sa_{GMRotI} : Conversion to Sa_{Arb}, SA_{SN}, and Sa_{MaxRot}. *Bulletin of the Seismological Society of America* 97(5):1511−1524.

WCC (Woodward-Clyde Consultants). 1981. Task E2-5: Wave Propagation and Ground Motion Modeling. Washington Public Power Supply System Nuclear Project Nos. 1 & 4, Hanford FSAR Geological Support. Prepared for Washington Public Power Supply System by WCC, San Francisco, California.

Wells DL and KJ Coppersmith. 1994. New empirical relationships among magnitude, rupture length, rupture width, rupture area, and surface displacement. *Bulletin of the Seismological Society of America* 84:974−1002.

Youngs RR. 2007. *Updated Site Response Analyses for the Waste Treatment Plant, DOE Hanford Site, Washington*. PNNL-16653, GMX-9995.002-001, Pacific Northwest National Laboratory, Richland, Washington.

Youngs RR, S-J Chiou, WJ Silva, and JR Humphrey. 1997. Strong ground motion attenuation relationships for subduction zone earthquakes. *Seismological Research Letters* 68(1):58–73.

Yuzawa Y and K Kudo. 2008. Empirical estimation of long-period (1–10 sec.) earthquake ground motion on hard rocks. *Proceedings of Fourteenth World Conference on Earthquake Engineering* Paper No. S10-057.

Zhao JX. 2010. Geometric spreading functions and modeling of volcanic zones for strong motion attenuation models derived from records in Japan. *Bulletin of the Seismological Society of America* 100(2):712–732.

Zhao JX. 2011. Magnitude scaling in ground-motion prediction equations for response spectra from large subduction interface earthquakes from Japan. In: *Proceedings of 4th IASPEI/IAEE Symposium on Effects of Surface Geology on Seismic Motion*, UC Santa Barbara, August 23-26, 2011. Available at: http://esg4.eri.ucsb.edu/sites/default/files/4.4%20Zhao.pdf.

Zhao JX, J Zhang, A Asano, Y Ohno, T Oouchi, T Takahashi, H Ogawa, K Irikura, HK Thio, PG Somerville, Y Fukushima, and Y Fukushima. 2006. Attenuation relations of strong ground motion in Japan using site classification based on predominant period. *Bulletin of the Seismological Society of America* 96(3):898−913.

Zhu L and L Rivera. 2002. Computation of dynamic and static displacement from a point source in multi-layered media. *Geophysical Journal International* 148:619−627.